Rydberg atom ensembles under dephasing and dissipation: from single- to many-body dynamics

SIBALIC, NIKOLA

Rydberg atom ensembles under dephasing and dissipation: from single- to many-body dynamics

Nikola Šibalić

Abstract

This thesis explores the effects of decoherence and dephasing on single- and many-body dynamics of spin-systems. A particular realisation of the spin systems that the work focuses on are highly excited, Rydberg states of atoms.

A software library ARC (Alkali Rydberg Calculator) for calculating properties of Rydberg states in alkali metals is presented, with particular attention to the multi-atom and multi-level effects that influence many-body dynamics in realistic systems, and properties related to terahertz imaging with alkali atom Rydberg states.

Dressed-state electromagnetically induced transparency (EIT) is proposed as a way of preparing uniform-phase spin-waves in ladder excitation schemes, making the collective excitation storage insensitive to motional dephasing. Proof of concept dressed state EIT experiments are presented. Strong resonant dressing is also theoretically analysed as a way of preparing velocity superposition of spin-waves. The developed theoretical model is in a good agreement with existing experimental data on single-photon many-atom quantum beats in diamond excitation schemes.

By modelling the strongly driven Rydberg ensembles, many-body dynamics of driven-dissipative spin systems is analysed. Working in the limit of strong dephasing, the effects of fluctuations, the shape of interaction potential, spatial correlations and motion on non-equilibrium phase diagrams and the occurrence of bistability are examined. An ensemble averaged mean field model is introduced as an exact solution for completely uncorrelated ensembles. It is shown that the van der Waals interaction does not allow the occurrence of bistability, for which a finite dipolar core is required. The short-range interaction potential shape is found to have a profound influence on non-equilibrium phase diagrams, controlling the size of fluctuations in the dynamics. For a frozen system, several methods for identifying and quantifying bistable phases are introduced, and phase diagrams are reconstructed. It is shown that the temperature of external degrees of freedom, i.e. spin motion, can drive a non-equilibrium transition into the bistable phase.

Rydberg atom ensembles under dephasing and dissipation: from single- to many-body dynamics

Nikola Šibalić

A thesis submitted in partial fulfilment
of the requirements for the degree
of Doctor of Philosophy

Department of Physics
4th July 2017

Contents

List of Figures

Declaration

I confirm that no part of the material offered has previously been submitted by myself for a degree in this or any other University. Where material has been generated through joint work, the work of others has been indicated.

Nikola Šibalić
In Durham, on 4th July 2017

Acknowledgements

Throughout the course of this long research project, I had fantastic opportunity to meet, interact with and learn from a diverse group of people.

I was lucky to have as my supervisors Kevin Weatherill and Charles Adams, that gave me both support and freedom in pursuing various new ideas.

Discussions with Massayuki Kondo, Riccardo Faoro, Hannes Busche, Dan Whiting, Chris Wade, Alistair Bounds, James Keaveney, Tom Billam, Liz Bridge, Dani Pizzey, Natalia Melo, Paul Huillery, Christoph Vaillant, Nicholas Chancellor, Ifan Hughes, Stephen Hopkins, Robert Potvliege, Matt Jones, Joschka Roffe, Nicholas Spong, Will Hamlyn, Dominic Reed and Ryan Hanley were important for all my work, providing space for checking ideas, and learning about new ideas and approaches. In particular, without detailed checks and proof-reading of this thesis by Lucy Downes, it would contain many more mistakes.

I greatly enjoyed many discussions with Thomas Pohl, during our collaborative work. He and his group provided great hospitality during my stay at MPIPKS. Discussions with Jon Pritchard greatly improved many details of the ARC project, while without help of Tom Billam, Atom calculator wouldn't be online. Without patience and cheerfulness of Massayuki Kondo, many perfect optical alignments would have never been reached.

Many people from the group, as well as wider University, contributed in indirect ways to this thesis, over the last three and a half years. I enjoyed spending time with them on cinema and theatre trips, swing dancing, food trips, orienteering, board games, documentary movie projections, and many more, as well as discussions following these activities on topics ranging from physics to anything else in this world. All these moments immensely enriched my time here.

Even the longest of journeys starts with a first step. At the beginning of my physics journey, I had some great teachers, Snežana Nemeš and Nataša Čaluković.

Finally, without continuous support all these years by my mother and grandmother, nothing of this would happen.

Thank you all.

Dedicated to Sanja Popović

Foreword

Making the world more easily understandable.

When one shoots a cannon ball, as it flies, many complex processes happen. As it spins around and precesses, air streams exert forces on its surface and, in turn, air starts to move in turbulent vortexes. And yet, to a good approximation, this amazingly complicated real world example can be reduced and engrasped in our minds as a simple motion along a parabolic path.

At the same time, there is a suggestion that some systems cannot be computationally reduced[1]. That is to say, they themselves implement a minimum amount of computation necessary to predict their dynamics. Today many systems are reduced to this category by companies which use statistical analysis of big datasets to try to guide their decision-making, giving impression that almost all problems can be solved with enough data and raw computational power.

Physics is still amazingly good in taking seemingly complex phenomena and reducing it to the conceptually tractable problem. That is immensely important, because, as we have learned from the limitations of the human brain[2], it is rare to find something more useful to humans than a phenomena that can be described discussing only half a dozen ideas at a time. Indeed, by careful stacking ideas in a hierarchy of abstraction levels, we've build all the reliable structures in our society.

Guerilla fighting science is maybe the best description of the process of doing physics. For a given problem, we try very different theoretical approaches and numerical tools, in process of identifying best concepts that facilitate understanding of the problem. When we turn to the experiment, we happily misuse latest products of technology, to control and extract data from various systems. Socially, physicists are incredibly diverse group, in both ways of thinking and ways of doing things. That makes scientific discussions hard, but also rewarding experiences.

I am grateful for having the opportunity to enjoy these activities, and hope that this thesis will allow easier understanding of a few phenomena.

[1] computational irreducibility is a term coined by Steven Wolfram in *A New Kind of Science*, Ch. 12, Champaign, IL: Wolfram Media (2002)

[2] George A. Miller, "The Magical Number Seven, Plus or Minus Two: Some Limits on Our Capacity for Processing Information", *Psychological Review* **63**, 81 (1956)

Introduction

CHAPTER 1

Observing modern physics research in the realm of energy and length scales relatively easily accessible on Earth, one can make a very rough approximation, and identify at least two big groups of problems currently attracting significant attention.

The first one is concerned with making better devices that will clearly expose, use and control underlying physics to achieve new goals. Specifically, we are interested in limits of measurement and control. For that, a perfect control of very few particles or photons at a time is of crucial importance. An example is development of devices for performing quantum logic operations, communication and quantum enhanced measurements. In order to realise such devices, basic storage, state control and production protocols at single-particle or single-photon level have to be developed. While we have fundamental understanding of the basic processes for most of the approaches, it remains an open question how best to combine, control and model the systems to achieve ultimate goals.

The second group of problems deals with predictions about many-body systems. Here, our predictive power and understanding are limited, particularly for non-equilibrium systems, both quantum and classical ones. Developing a better understanding and some common ideas for treating these systems is of huge significance. On the one hand the majority of real-world systems are non-equilibrium. A noteworthy example is abnormalities in cell differentiation, affecting more than a third of the population during their lifetime and often grouped under common name cancer. These can be very-well understood as a many-body non-equilibrium system transitioning between the attractors of dynamics [1]. On the other hand, unexplored non-equilibrium phenomena may be harnessed for future technologies.

A dominant idea over the last decades is that understanding, tools and modelling (see Fig. 1.1) that allows solving of these two groups of problems will emerge through a construction of well-controlled quantum systems. That process has many steps. With electromagnetic radiation being a fast, high-capacity information carrier, and matter medium providing long-term storage and strong interactions, mapping information between the two is crucial. That was achieved with both probabilistic (heralded) [2] and deterministic (adiabatic) [3, 4] control schemes. As a matter media of choice, atoms, ions [5, 6], molecules [7] and quantum degenerate ultra-cold atoms [8] have all been used, as well as artificial spin systems [9] like nitrogen-vacancy centres [10], rare-earth doped crystals [11], superconducting circuits [12] and nano-fabricated quantum dots [10, 13]. Interactions between the internal degrees of freedom (spins) in the matter media are sometimes direct, provided as a contact interaction as in the case of Bose-Einstein condensates [14] and ultra-cold atoms on lattices [8, 15]. However, most of the considered systems have spins at

large separations, necessitating mediation of interactions via electromagnetic fields.

In order to control interactions between the spins, as well as information encoded in electromagnetic field modes, atom coupling with selected electromagnetic field modes has to be enhanced and/or suppressed [16, 17]. To achieve enhanced coupling between the two, one commonly used approach is geometric confinement of spins and light in cavities [18, 19], at the surface of nano-fibres [20], inside hollow-core fibres [21], and above planar waveguides [22]. Alternatively, spins can have enhanced atom-light coupling strength, as in the case of atoms excited to high-lying electron energy levels, also called Rydberg states [23], or polar molecules [7]. In the non-confined matter media, like solid-state materials or atomic ensembles, directionality of the light output is achieved through storage of this spatial information in a shared excitation (superposition) of many particles in the medium, in a so-called spin-wave. An additional benefit of the collective storage of information is robustness of created states against single-particle loss and decoherence [24].

It is worth noting that while this progress brought huge focus on quantum systems, i.e. systems that can exhibit quantum superposition, particularly non-local, or whose behaviour is critically dependant on quantum fluctuations and indistinguishably of particles or excitations, there are interesting, and not fully understood effects that can be explored in classical systems too. For example, while vortex formation can be observed and analysed in matter-fields in Bose-Einstein condensates, it can also be seen in light fields [25]. This is because the phenomena ultimately depends on a field description of matter or light, and therefore can be explored in the two systems of vastly different technological complexity. Similarly, topologically protected transport, being characteristic of delocalized waves in lattice potentials, can be realized in light and acoustic systems, as well as electron or atom matter-wave systems.

The program of solution as outlined above has one major obstacle to overcome in any real-world application: dephasing and dissipation mechanisms that occur in the chosen matter medium (spin-system).

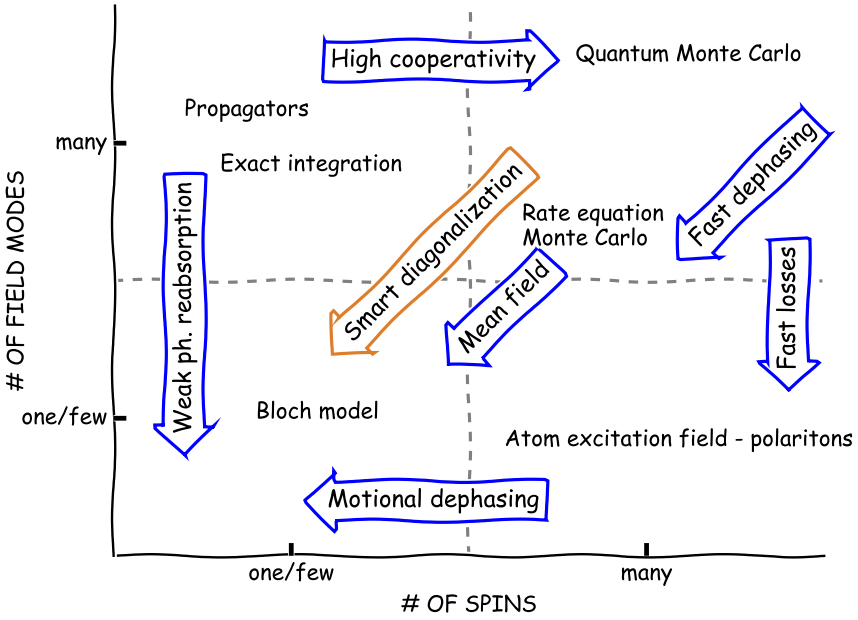

Figure 1.1: Landscape of theoretical modelling. Depending on the minimum number of field modes and spins that we have to consider in a system, very different theoretical models and solution approaches are typically used. The top right rectangle corresponds to many-body physics. Arrows indicate some typical reasons for changing solution approach. For example, we will use exact integration/diagonalization of interactions for two strongly interacting atoms in chapter 2. However, if photons emitted in deexcitation of any spin in the systems are not likely to be reabsorbed (weak ph. reabsorption arrow), exciting some other spin in the system, this often allows effective treatment of the system within single a spin picture. Similarly, motional dephasing and fast dephasing of coherences, to be discussed in chapters 3 and 4 respectively, can simplify dynamics of the system and allow usage of a different theoretical framework.

1.1 Dephasing

Dephasing, also called decoherence, usually occurs due to a coupling of the system to its environment that perturbs the system's energy levels. This causes accumulation of additional phases by the system in time, but doesn't change the system's state. Depending on the self-correlation time of the external perturbation, the impact of this perturbation can sometimes be reduced.

If the correlation time of the coupling term to the environment is long compared to the time required to perform spin-flip operations, one can perform spin-echo protocols [26], and their continuous analogue for decoupling the system's dynamics from the environment called "bang-bang" control [27]. This is used, for example, in long correlation-time environments, like nitrogen-vacancy centres in diamonds [28], or static stray magnetic and electric fields [29]. An alternative route to reduce dephasing, that can be applied even in short correlation-time environments, is to engineer the environment such that its coupling to the system is reduced in the first place. For example, both coupling to vibration modes in solids and associated phonon fields, and coupling to microwave/terahertz black-body photons in electromagnetic fields, can be suppressed by reducing the number of field excitations through environment cooling, or alternatively by removing the unwanted modes through geometric constrains on the fields, achieved by enclosing the environment in optical [16, 17, 30, 31] or acoustic cavities [32]. Finally, note that well-defined off-resonant coupling to the environment that gives rise to phase shifts but maintains the system's state, can be exploited in well-controlled systems to perform non-demolition measurements on quantum systems [33–35].

For environment-induced perturbations much faster than the typical times required to perform spin-flip operations, there is usually no solution for overcoming them. Examples include atomic collisions, laser noise, and molecular dephasing in Rydberg molecules [36], where many close lying molecular resonances broaden the energy level. Usually these are accounted for by an additional dephasing term in open-system ensemble dynamics, where they provide a limit on how much quantum phenomena we can expect in the system. As we will see in Chapter 4, this is also a significant simplification factor in theoretical modelling of the systems, providing us with a clear limit where we can treat many thousands of particles in numerical simulations, since the dephasing ensures that coherences reach steady states much more quickly than populations. Interestingly, however, there are special cases of fast inhomogeneous noise, when in spite of the fast perturbations we can still see clear evidence that individual particles evolve under quantum dynamics that continuously drives them between the discrete states. As we will see in Section (5.1.2), this allows for fully quantum dynamics to be recovered even in the presence of dephasing mechanisms, in the limit when the time-correlation of perturbative level shifts is very short compared to the coherent driving frequencies, while the average pertubative level shifts are stable in time.

Finally, there is a third type of dephasing that is not due to random events causing perturbations, fast or slow, but due to the normal, easily-tractable dynamics of the system *ensemble*. Examples are Doppler broadening, and a related phenomena for stored excitations of a motional dephasing of collective atomic excitations. This type of dephasing can, in principle, be fully accounted for by theory, and to a significant degree controlled, as we will see in Chapter 3.

1.2 Dissipation

Dissipative mechanisms describe couplings to the environment that induce energy level transitions within the system. A familiar example is spontaneous decay of the excited atomic energy levels due to coupling to the vacuum modes of the electromagnetic field. Processes like these can be reduced in a similar way to dephasing, by removing free field modes for corresponding decays (i.e. modes resonant with the spin-system). This is done by setting boundary conditions on the field by enclosing the system in a cavity [16, 17, 30–32]. However, there are additional possible dissipative processes, like inelastic (non-adiabatic) atomic collisions. Dissipative processes are particularly hard to control when excited system states can decay to many different states. For example, to prevent such situations laser cooling of atoms is done on closed transitions. Since similar transitions in molecules usually don't exist due to much more complex energy schemes, direct laser cooling of molecules is much harder, and can be done only if additional lasers are added to speed up dissipative processes that drive population from unwanted excited levels back to the cooling energy-level loop. In Rydberg atomic states, these additional decays can also be important for many-body physics, since unwanted excitation of many nearby levels can, under the right conditions, trigger avalanche effects that drastically change the dynamics [37, 38].

Dissipation also leads to strong projective measurements of the system, and as such can be used for a system's state preparation. Photon absorption and measurement in a detector can be seen as an extremely well controlled case of dissipation that allows, among the other things, entanglement swapping [39] and quantum eraser protocols [40], and essentially all the experiments in quantum optics that use post-selection/heralding. An example of this will be discussed in Chapter 3. Even when this leaked information about the system is not directly measured by the experimentator, but is written somewhere in the environment's degrees of freedom, dissipation still constitutes a projective measurement. An early example from atomic physics is optical pumping, which induces stochastic loss of population in all the unwanted levels, leaving a couple of so called dark states untouched. After a long enough time, all the atoms will be stochastically projected onto dark states, where they stay and population accumulates. Prepared states can be hyperfine or magnetic Zeeman levels, subradiant states, dark states giving rise to electromagnetically induced transparency (EIT), or a more general class of states called decoherence-free states [41–45].

Finally, we note a relation between dissipation and dynamics of coherences. In the simplest example of spontaneous emission in a typical ensemble treatment using density matrix formalism, coherences are washed away by decays, and thus dissipation also seems to decohere the system. This is, however, only true in the ensemble average picture. Individual decay processes map fully coherently the state probability amplitudes. It is the undetermined timing between decay processes that in ensemble average, treated in density-matrix picture, reduces coherences. Preserving of coherences in spontaneous emission will be crucial for the results of the Chapter 3 that analyse the case of time-resolved measurements (photon-counting). The particularly important example of this is when there is no information about the exact emitter in the system, giving rise to collective emission processes. These are responsible for correlations in photon-pair emission directions in spontaneous

double-Λ four-wave mixing schemes, directionality of heralded quantum memories and single-photon sources [46], as well as phase locking between non-interacting emitters [47].

1.3 Short history of Rydberg atomic physics

The introduction so far described two big questions that we ultimately aim to contribute to, and two important factors whose implications will be all important for the further discussion. Although most of the results in this thesis are quite general and applicable to a wide variety of systems, the stimulation to think about these questions was provided by a specific matter system that we had in the laboratory: an atomic caesium thermal vapour contained in a spectroscopic cell, where alkali vapour can be excited with a cascade of lasers to high-lying Rydberg states. In order to position our work within the wider developments in Rydberg physics, we will now give a short general overview of some of the main developments in the field. This motivates the main questions of this thesis, while more detailed context for each of the results will be provided in the subsequent chapters.

In the 19th century, spectroscopy provided many observations of absorption and emission lines. Although there was regularity in their appearance, numerous attempts to explain spectral series failed. One more successful attempt was Balmer's equation explaining one of the series in the hydrogen spectrum. However, it couldn't reproduce many other observed spectral features. In 1888, Johannes R. Rydberg (1854-1919) presented a formula that could explain a wide range of spectroscopic series. In modern notation and interpretation it states that the transition wavelength λ_{ab} between two energy levels a and b in an atom is

$$\frac{1}{\lambda_{ab}} = \mathrm{Ry}\left(\frac{1}{n_a^2} - \frac{1}{n_b^2}\right) \tag{1.1}$$

where n_a and n_b are reduced principal quantum numbers of the energy levels, and Ry is the (Rydberg) constant of proportionality. This provided some crucial input for the development of early atomic theory by Niels Bohr at the beginning of 20th century. All the spectral lines from highly excited atomic states, as they approach ionization limit, follow this equation. This is true even for complex non-hydrogenic atoms, since the ionic core will have similar character as the hydrogen system.

These high-lying states are called Rydberg states. They have big electron wavefunctions, scaling as n^2 with principal quantum number n, whose radius is ~ 1 μm for $n = 100$. This leads to n^2 scaling of strong dipolar coupling strengths for transitions between nearby states. This was recognized in the 1980's as a resource for performing precise far-infrared (terahertz) and microwave electrometry [48–52]. The Rydberg states are also very sensitive to applied static electric and magnetic fields, and exploration of their complex level diagrams in external fields also attracted significant attention. Partly because this was seen as a system exhibiting "quantum chaos" [53] but also because electric fields can be used to tune transitions between states, allowing, for example, controllable preparation of states with a high orbital angular momentum - so-called circular states [54]. Experimentally, access to high-lying states was provided by tunable dye-lasers [55]. The Rydberg states have long lifetimes, which increase as n^α, where α is between 3 and 5, making

them difficult targets for direct optical observation via fluorescence. Still, they were efficiently detected in a state-selective manner in these early experiments through state-selective field ionization [56].

At around the same time, understanding of light fields that contain only a few field excitations was improved. From the original photon concept introduced by Einstein in 1905 [57], the whole field of quantum optics developed. Initial laser systems [55, 58], were developed in semiconductor technology [59], that provided compact, simple and stable long-term operation. This allowed a lot of interesting atom-light interaction proposals to be tested [60, 61], including schemes for slowing and storing light through interference effects in multilevel atom-field interaction schemes [61, 62].

Initial explorations of Rydberg atom interactions [63–65] culminated in pioneering experiments combining strong Rydberg interactions and well-controlled atom-light interactions [66]. This demonstrated that nonlinearity in the collective excitation of atomic media can indeed be controlled with individual photons exciting single Rydberg states as suggested in early theoretical works [67]. This paved the way for experiments demonstrating interactions between individual photons in mesoscopic atomic clouds [68–70], demonstrations of deterministic dissipative manipulation at single-photon level [71] and even interactions between photons in spatially separated optical channels [70, 72]. Simultaneously, there was a push in exploring atom-atom interactions as a way to prepare exotic new states. In a few-spin limit, bounding of ground state atoms to a Rydberg atom through scattering of atoms in the density cloud of a highly excited electron in the Rydberg-atom have been demonstrated [36, 73]. Molecular attractive potentials have been used to allow binding between two Rydberg atoms [74], as well as to enhance atomic interactions between dressed ground-states [75]. This brings excitement since tunable, switchable, long-range interactions can be exploited for quantum-logic gates [23], as well as many-body state preparation [75–78]. Prospects for controllable exploration of many-body physics are particularly exciting. Some proposals for preparation of crystalline phases through adiabatic tuning of external driving [76] have been demonstrated in experiments that have single-atom resolution [79]. However, initialization of unity filled lattices through preparation of Mott insulators [15], as well as optical resolving of the individual single-atom optical lattice sites [80], are both achieved in very complicated, hard-to-replicate setups. In addition, standing wave lattices have limited tunability of interatomic spacing and geometries. An alternative approach for creating spatially well defined atomic spin ensembles uses optical tweezers, where tightly focused red-detuned laser beams provide traps whose maximum filling is limited to one atom per trap, due to collisions within the small trapping volume [81–83]. Until recently indeterministic filling of these traps prevented preparation of unity-filled arrays with big spin-numbers [84]. This has been resolved by fast real-time experimental control, allowing imaging and shuffling of filled traps, so that arbitrary 1D [85] or 2D [86] patterns can be formed deterministically.

While the future trend is likely to change in favour of site-resolved experiments, at the moment the majority of experiments that report many-body phenomena in Rydberg gases do so through indirect measurements of population dynamics. Among them was observation of bistability of Rydberg population in thermal vapour experiments in Durham [87]. That, and related findings of aggregate growth [88] and bimodality in full counting statistics of Rydberg populations [89, 90], motivated

one of the questions explored in this thesis, namely when and why one can expect to observe bistability in many-body interacting Rydberg systems. On the other hand, stimulated by a pioneering work in Durham [91, 92] and Stuttgart [93, 94] on coherent dynamics in thermal-vapour cells, we were interested to explore possibilities for control of Rydberg thermal vapours in few-excitation limits, which constituted the other main question. Working in thermal cells, dephasing and dissipation were very important factors from the very start of our considerations, and this thesis explores their consequences both on many-body dynamics, in the limit of many excitations, and on collective and single atom effects, in the limit of single excitation.

1.4 Thesis layout

Rydberg properties are explored in Chapter 2, providing microscopic understanding behind the elementary processes that will appear throughout the rest of this thesis. As part of efforts to establish tools for quantitative treatment of the atomic properties, an open-source Python library, Alkali Rydberg Calculator (ARC), was developed, accompanied by extensive documentation and examples. In addition to that, a web application was also developed, to allow quick access to relevant numbers, as well as automated scheduling, storing and retrieving of more complex calculations. This is now a resource available word-wide at `https://atomcalc.jqc.org.uk`.

Motional dephasing effects in the limit of few excitations, where we try to establish control of atom and light states, are explored in Chapter 3. Here we go beyond single- or two- particle models by considering collective excitations of the atomic medium (spin-waves), but we don't include inter-atomic interactions. We introduce a new scheme for creating uniform-phase spin-waves, by using a dressed-state as a proxy for EIT. We show that the usual storage protocol, combining EIT and adiabatic following, can be easily generalized for usage in a new four-level scheme, achieving a number of benefits along the way. This is followed by a proof-of-concept experimental demonstration. Exploring further influences of spin-wave motional dephasing and limits of state control, detailed theoretical analysis of an experiment on cascade photon-pair emission from diamond schemes in thermal vapours is presented. Full microscopic treatment is in very good agreement with the experimental data, and provides additional insight into the details of the process that forms a single-excitation interferometer between two collective excitations moving with two selected velocities within a thermal vapour. In both examples, strong resonant dressing of the atomic states provides a valuable experimental tool for coherent control.

Going into the limit of ensembles with many, densely packed excitations requires accounting for inter-particle interactions. In Chapter 4, we abstract away all the microscopic details and keep just the effective spin model, but account for inter-particle interactions. Exploring this model in the strongly dissipative limit, we will show that phase transitions in this driven-dissipative system crucially depend on the form of the interaction potential. Advanced parallel simulations also allow us also to explore effects of motion, that washes away spatial excitation correlations in the system. This uncovered a temperature-driven non-equilibrium transition to the bistable regime. The findings are corroborated by deriving a mean-field model that is an exact solution in the well defined limit of rapid atomic motion (i.e.

hot atomic ensemble). The derived mean field model has qualitatively different predictions compared to the simplified mean field models used in the literature for similar treatments, as it properly accounts for fluctuations in dynamics. Agreement between a mean field treatment and full many-body dynamics is confirmed through intensive numeric simulations. The importance of short-range details of the inter-spin interaction, usually not of qualitative value for thermal-equilibrium systems, is highlighted for these driven-dissipative systems, where it controls fluctuations of the system's dynamics.

Finally, in Chapter 5 we show short-term outlook of the presented research, as well as possible long-term developments.

1.5 Publications arising from this work

- N. Šibalić, J. D. Pritchard, C. S. Adams and K. J. Weatherill, ARC: An open-source library for calculating properties of alkali Rydberg atoms, *Computer Physics Communications* accepted for publication, arXiv:1612.05529 [95]
  GitHub: https://github.com/nikolasibalic/ARC-Alkali-Rydberg-Calculator
  Online atom calculator: https ://atomcalc.jqc.org.uk
- D. J. Whiting, N. Šibalić, J. Keaveney, C. S. Adams and I. G. Hughes, Single-photon interference due to motion in an atomic collective excitation, *Phys. Rev. Lett.* **118**, 253601 (2017) [96]
- C. G. Wade, N. Šibalić, N. R. de Melo, J. M. Kondo, C. S. Adams and K. J. Weatherill, Real-time near-field terahertz imaging with atomic optical fluorescence, *Nature Photonics* **11**, 40 (2017) [97]
- N. Šibalić, J. M. Kondo, C. S. Adams and K. J. Weatherill, Dressed-state electromagnetically induced transparency for light storage in uniform phase spin-waves, *Phys. Rev. A* **94**, 033840 (2016) [98]
- N. Šibalić, C. G. Wade, C. S. Adams, K. J. Weatheril and T. Pohl, Driven-dissipative many-body systems with mixed power-law interactions: Bistabilities and temperature-driven non-equilibrium phase transitions, *Phys. Rev. A* **94**, 011401(R) (2016) [99]
- J. M. Kondo, N. Šibalić, A. Guttridge, C. G. Wade, N. R. De Melo, C. S. Adams and K. J. Weatherill, Observation of Interference effects via four photon excitation of highly excited Rydberg states in thermal cesium vapor, *Opt. Lett.* **40**, 5570 (2015) [100]
- C. G. Wade, N. Šibalić, J. Keaveney, C. S. Adams and K. J. Weatherill, Probing an excited-state atomic transition using hyperfine quantum beat spectroscopy, *Phys. Rev. A* **90**, 033424 (2014) [101]

Related publications:

- N. R. De Melo, C. G. Wade, N. Šibalić, J. M. Kondo, C. S. Adam and K. J. Weatherill, Intrinsic optical bistability in strongly-driven Rydberg ensemble, *Phys. Rev. A* **93**, 063863 (2016) [102]
- B. Zlatković, A. J. Krmpot, N. Šibalić, M. Radonjić and B. M. Jelenković, Efficient parametric non- degenerate four-wave mixing in hot potassium vapor, *Laser Phys. Lett.* **13**, 015205 (2016) [103]

Rydberg atomic states: energy level structure and dynamics

CHAPTER 2

This chapter describes the properties of alkali atom Rydberg states, as well as ways of controlling atom dynamics. We will firstly discuss some order-of-magnitude estimates to provide a feeling for the relative importance of various processes, which will be described in detail in the following sections. The sections follow the development of the Alkali Rydberg Calculator (ARC), a Python library developed to facilitate quantitative work with alkali Rydberg atoms. In addition, we will highlight some specific situations which will be of interest for discussion in the following chapters. This establishes both a common framework for all the developments, and points out limiting cases where common approximations breakdown, requiring additional processes to be taken into account. Finally, we will use ARC to provide simple analysis of experiments on terahertz imaging.

2.1 Overview: scaling and estimates

For highly-excited electrons in neutral atoms, the positive attractive core can be treated as hydrogenic central potential $\sim 1/r$, with several correcting factors accounting for the core structure. For example, the energies of the states can be expressed with a standard Rydberg series equation (1.1), by replacing the principal quantum number n with scaled principal quantum number $n_* = n - \delta_{n,\ell,j}$ reduced by the quantum defect $\delta_{n,\ell,j}$ for the corresponding state $|\psi\rangle = |n,\ell,j\rangle$. The typical radial extent $\langle\psi|r|\psi\rangle$ of these states scales as n_*^2 [Fig. 2.1(a)]. These electron wavefunctions, that reach $\langle r\rangle \sim 6500\ a_0$ (~ 350 nm) for $n \sim 70$ in caesium, produce dipole matrix elements for transitions between neighbouring states that scale also as n_*^2, reaching values of $\sim 5700\ a_0 e$ for 70 $S_{1/2} \to 70\ P_{3/2}$ in Cs. If two atoms are close to each other, one in the $|nS\rangle$ state and the other in the $|nP\rangle$ state, a photon emitted in this $|n\ S\rangle \to |n\ P\rangle$ transition of one atom can be reabsorbed by the other atom. The coupling strength $V_{\rm dd}$ for this resonant dipole-dipole interaction scales as n_*^4 [Fig. 2.1(b)], reaching $V_{\rm dd}/h \sim 40$ MHz for two atoms separated by 5 μm for the same transition in Cs. At the same time, much smaller overlap with energetically distant states, and smaller number of vacuum modes for energetically close states (that are typically $\Delta \propto n_*^{-3}$ far away in energy), means that these states have lifetimes $1/\Gamma$ that scale as n_*^α, where α is between 3 and 5 depending on the orbital angular momentum of the state. For Cs 70 $S_{1/2}$, the radiative lifetime of ~ 0.3 ms is reached in cold (black-body radiation free) environment.

Comparing the interactions between neighbouring atoms with the vacuum coupling

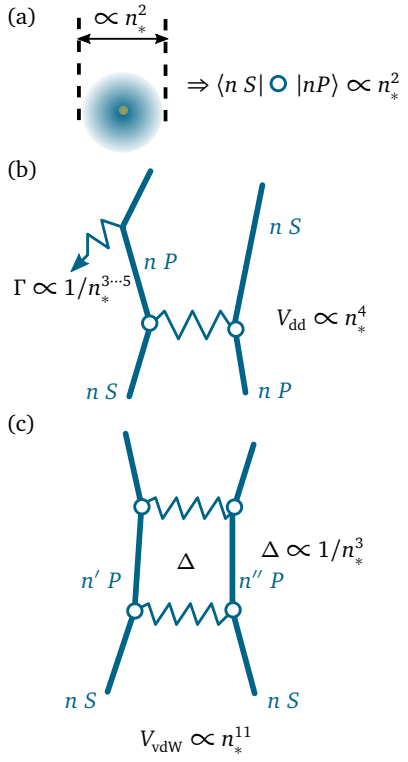

Figure 2.1: Rydberg states' interaction scaling with a principal quantum number n. (a) Increased size of the wavefunctions leads to enhanced electromagnetic coupling between the neighbouring states, causing strong resonant dipole-dipole $V_{\rm dd}$ interactions (b) between dipolar coupled states $n\ S$ and $n\ P$ (solid lines). At the same time, coupling of the system to the environment, given by the rate Γ, is reduced, allowing the system to enter the *strong coupling regime* $V_{\rm dd} \gg \Gamma$. Even the states that in the first order are coupled only to energetically forbidden states (c), characterised with energy defect Δ, can be coupled in the second order with van der Waals interactions $V_{\rm vdW}$, that also has strong scaling $\propto n_*^{11}$ with scaled principal quantum number n_*.

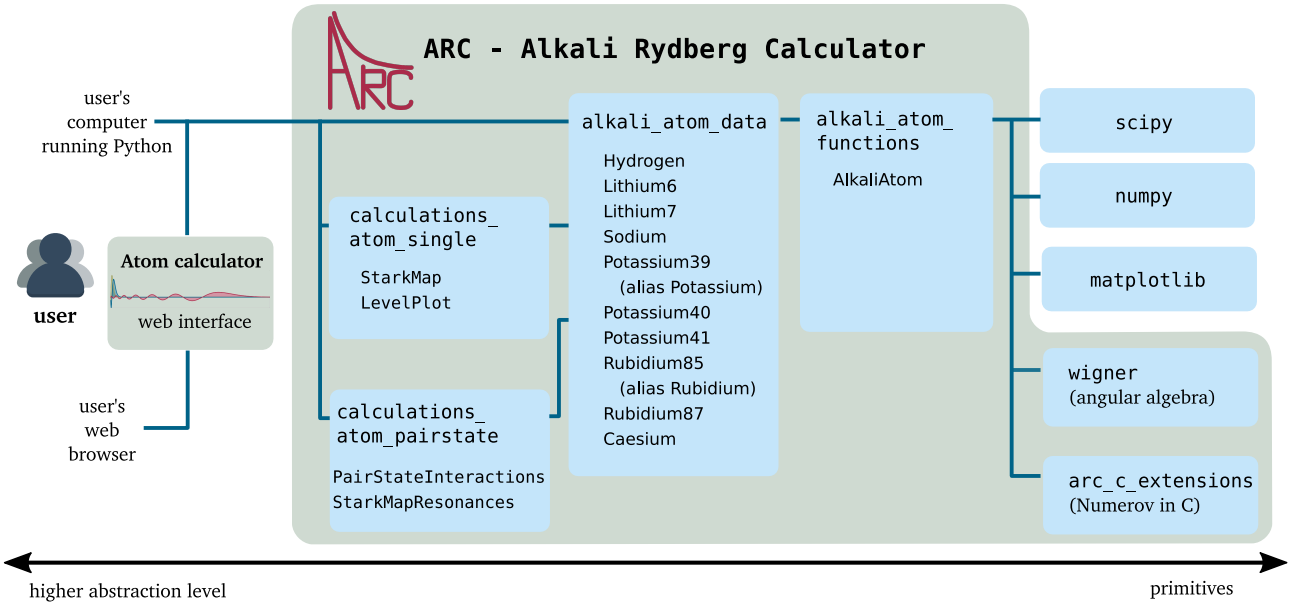

Figure 2.2: Overview of Alkali Rydberg Calculator (ARC) modules. The object-oriented structure of this Python module reflects a hierarchy of abstraction levels in atomic-physics calculations. This allows quick access to relevant data and functions, facilitating development of new calculations, for users starting both from low-level atomic properties implemented in `alkali_atom_functions.AlkaliAtom`, and from high-level concepts like pair-state diagrams and Förster resonances, implemented in `calculations_atom_pair_state`. Numerically intensive primitives, like Numerov integration, are C coded Python extensions.

to the environment, we see that even for experimentally well controllable interatomic distances of several μm, the strong coupling regime $V_{\mathrm{dd}} \gg \Gamma$ is reachable. Even non-resonant interactions [Fig. 2.1(c)] exhibit strong scaling ($\propto n_*^{11}$) and comparable absolute strengths. Crucially, since this is an atomic system, we have a system with fixed, reproducible properties. We will see later an example of how this can be used in electrometry. This also means that properties can be relatively easily calculated and even adjusted with external fields, making atoms in Rydberg states perfect building blocks for exploring many-body physics. Since a single atom in a Rydberg state can offset other highly-excited states of neighbouring atoms more than the typical transition linewidths, over μm-distances that are individually addressable through, for example, focused optical ($\lambda \sim 1\mu$m) driving fields, there has been an interest in using them as a platform for quantum information processing [23]. Finally, coherent mapping of weak optical fields into collective atomic excitations through electromagnetically induced transparency [104], allowed strong effective interactions between optical photons to be achieved using these strong atom-atom interactions [105].

Advanced research of Rydberg atomic states requires efficient quantitative analysis and predictions. In order to allow both quick quantitative estimates, and easy building up of more complex calculations and their visualisations, we have developed the Alkali Rydberg Calculator (ARC), an open-source Python library that combines theoretical calculation models and necessary experimental data into a single research resource. The hierarchical nature of the library (Fig. 2.2) organises calculations at several abstraction levels, allowing the user access to information and a platform for further development at the level of interest for any given project. To facilitate its use, we provided detailed documentation, and took care that all the naming conventions

reflect closely the physical content of calculations.

2.2 Energy levels and electron wavefunctions

Binding energies $E_{n,\ell,j}$ of Rydberg states $|n,\ell,j\rangle$ annotated by their principal quantum number n and orbital ℓ and total j angular momentum can be expressed using the Rydberg-Ritz formula [106] as

$$E_{n,\ell,j} = -\frac{\mathrm{Ry}}{(n-\delta_{n,\ell,j})^2}, \tag{2.1}$$

where Ry is the Rydberg constant corrected for the reduced mass $\mathrm{Ry} = M/(M+m_e)\times \mathrm{Ry}_\infty$ where M is mass of the ion core and m_e is the electron mass. Quantum defects $\delta_{n,\ell,j}$ are given by

$$\delta_{n,\ell,j} = \delta_0 + \frac{\delta_2}{(n-\delta_0)^2} + \frac{\delta_4}{(n-\delta_0)^4} + \ldots, \tag{2.2}$$

where δ_0, δ_2, ... are modified Rydberg-Ritz coefficients obtained by fitting Eq. (2.1) to the precise measurements of energy levels [106–115]. The energy levels obtained in this way (Fig. 2.3) don't include hyperfine splitting, and they correspond to the centre of gravity of the hyperfine-split lines. Hyperfine structure for high-lying states scales as $\sim 1/n_*^3$ [116], and is about several MHz for caesium states with $n \sim 30$ [117], which is usually negligible in experiments.

In addition to the energies of the states, in order to calculate coupling between the states due to the interaction with external electromagnetic field, we need to know the electron wavefunctions ψ. These can be obtained by numerical integration of the time-independent Schrödinger equation in a central potential $V(r)$ of the ion core with mass M, in a centre of mass frame of reference where the electron reduced mass is $\mu \equiv m_e M/(m_e+M)$

$$\left[-\frac{\nabla^2}{2\mu} + V(r)\right]\psi(r,\theta,\phi) = E_{n,\ell,j}\psi(r,\theta,\phi). \tag{2.3}$$

For motion in central (i.e. angular independent) potentials the solutions for the wavefunction can be factorised into a radial part $R(r)$ and angular part whose solutions are spherical harmonics $Y_{\ell,m}(\theta,\phi)$. Replacing $\psi = R(r)Y_{\ell,m}(\theta,\psi)$ in Eq. (2.3) we obtain an equation for the radial part of the wavefunction

$$\left[-\frac{1}{2\mu}\left(\frac{\mathrm{d}^2}{\mathrm{d}r^2} + \frac{2}{r}\frac{\mathrm{d}}{\mathrm{d}r} - \frac{\ell(\ell+1)}{r^2}\right) + V(r)\right] R(r) = E_{n,\ell,j}R(r). \tag{2.4}$$

State energies $E_{n,\ell,j}$ can be obtained from experimentally measured values [Eq. (2.1)]. The central potential for high orbital angular momentum states $\ell > 3$ is effectively the hydrogen-core potential $V(r) = 1/r + V_{so}$ (in Hartree atomic units), with addition of $V_{so} = \alpha^2 \mathbf{L}\cdot\mathbf{S}/(2r^3)$ accounting for the (relativistic) spin-orbit interaction . However low-angular momentum states have finite probability to penetrate and probe the ion-core more closely, which requires modifications to the potential form. For these states ($\ell \leq 3$) the model central potential $V(r)$ is taken in the following form (Marinescu *et.al.* [118])

$$V(r) = -\frac{Z_\ell(r)}{r} - \frac{\alpha_C}{2r^4}\left[1 - e^{-(r/r_C)^6}\right] + V_{so}(r), \tag{2.5}$$

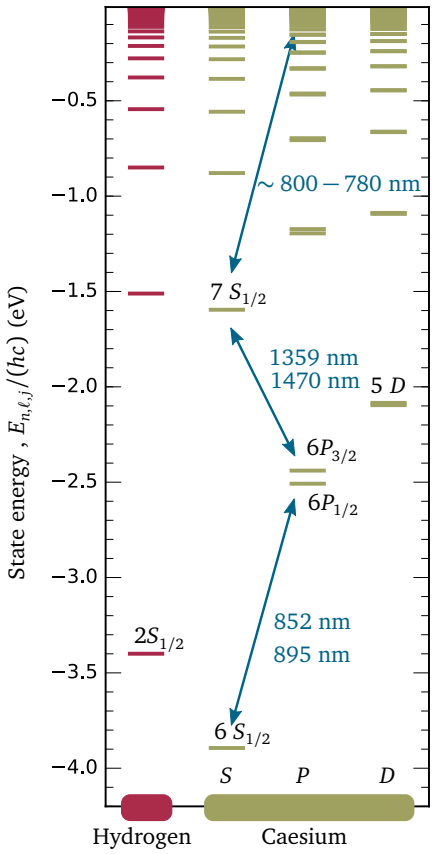

Figure 2.3: Comparison of energy levels of hydrogen and caesium. Wavelengths for some common transitions used in caesium for reaching high-lying states are highlighted (blue arrows).

REMINDER: In Hartree atomic units $m_e = e = \hbar = 1/(4\pi\varepsilon_0) = 1$. Speed of light is $c = \alpha^{-1}\frac{e^2}{4\pi\varepsilon_0\cdot\hbar}$, where $\alpha \approx 1/137$ is the *fine-structure* constant.

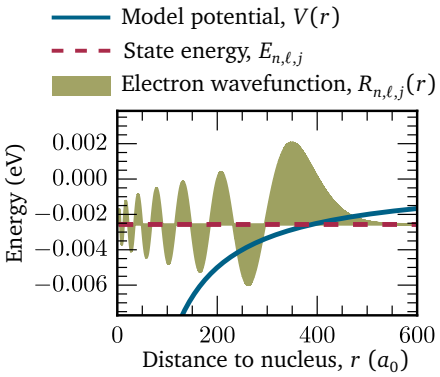

Figure 2.4: Numerically calculated radial wavefunction. Example of Numerov integration of radial wavefunction $R_{n,\ell,j}(r)$ for caesium 18 $S_{1/2}$ state.

where α_C describes the static dipole polarizability of the positive ion core, while the effective ion core charge $Z_\ell(r)$ that an electron feels is expressed as

$$Z_\ell = 1 + (Z-1)e^{-a_1 r} - r(a_3 + a_4 r)e^{-a_2 r}, \tag{2.6}$$

where Z is the nuclear charge. Parameters $a_1, \ldots a_4, r_C$ are obtained from parametric fits of one-electron energy levels [118]. With this all the terms in Eq. (2.4) are fixed, and one can convert it into a purely second-order differential equation (see Appendix A.1 for details) that can be efficiently numerically integrated with the Numerov algorithm [119, 120] to find $R(r)$. Integration is performed from the outer limit inwards, since we know the initial condition $R(r) \to 0$ for $r \to \infty$. Following Ref. [121], integration starts at $r_o = 2n(n+15)$, which is much larger than the classical turning point, and continues inwards down to $r_i = \sqrt[3]{\alpha_C}$. Sometimes, for some $\ell > 3$ states, divergence occurs before r_i is reached. That is detected by the implemented algorithm, and integration is stopped at the nearest node of the wavefunction before divergence occurs.

The obtained radial wavefunctions $R_{n,\ell,j}(r)$ (Fig. 2.4) can be used for calculation of dipole and quadrupole matrix elements, as required for calculations of single-atom energy levels due to external applied fields, as well as pair-state energy level diagrams under strong inter-atomic interactions. The complete wavefunctions, with both angular and radial dependence, are

$$|n,\ell,j,m_j\rangle(r,\theta,\phi) = R_{n,\ell,j}(r) \sum_{m_\ell + m_s = m_j} \langle l,s,m_\ell,m_s|l,s,j,m_j\rangle Y_{\ell,m_\ell}(\theta,\phi), \tag{2.7}$$

where $\langle l,s,m_\ell,m_s|l,s,j,m_j\rangle$ are Clebsch-Gordon coefficients, s is electron spin and m_s its projection.

These wavefunctions can become so big for high-lying states, that in dense samples they can encompass several other ground-state atoms. The big electron wavefunction provides then a background scattering potential for the ground-state atoms, which sometimes can sustain bound states [122]. In the cold samples this allows formation of so called Rydberg molecules [36, 73, 123]. This binding lowers the energy of (Rydberg state atom)-(ground state atom) system, producing additional resonances that are red-detuned to the usual excitation transition to the Rydberg state. In the high-density limit, even multiple ground-state atoms can be bound in this electron potential [123], producing at the end a mean-field level shift and line-broadening, limiting the Rydberg state coherence time in dense samples.

2.3 Interaction with electromagnetic field

The Hamiltonian for an atom interacting via its valence electron with an electromagnetic field described with vector potential $\hat{\mathbf{A}}(r)$ in space without free charges can be written as

$$\begin{aligned}\mathscr{H} &= \frac{(\hat{\mathbf{p}}-e\hat{\mathbf{A}})^2}{2m} + V(\hat{\mathbf{r}}) + e\phi(\hat{\mathbf{r}}) + \hat{H}_{\text{free}} \\ &= \underbrace{\frac{\hat{\mathbf{p}}^2}{2m} + V(\hat{\mathbf{r}})}_{\equiv \hat{H}_0} \underbrace{- \frac{e}{m}\hat{\mathbf{A}}\cdot\hat{\mathbf{p}}}_{\equiv \hat{H}_{\text{int}}} + \frac{e^2}{2m}\hat{\mathbf{A}}^2 + \hat{H}_{\text{free}},\end{aligned} \tag{2.8}$$

where in the second line we fixed the gauge to be Coulomb in space without free charges ($\phi = 0$, $\nabla\cdot\hat{\mathbf{A}} = 0 \Rightarrow [\hat{\mathbf{A}}, \hat{\mathbf{p}}] = 0$). We can identify $\hat{H}_0$ as a free-atom Hamiltonian, and $\hat{H}_{\text{int}}$ atom-light interaction Hamiltonian. The term proportional to $\hat{\mathbf{A}}^2$ will be neglected in the remaining calculations, since it just adds to the energy of the field proportionally to the number of dipoles. The last term H_{free} is the free-field energy. By using $[\hat{x}, \hat{H}_0(\hat{x}, \hat{p}_x)] = [\hat{x}, \hat{p}_x]\partial\hat{H}_0/\partial\hat{p}_x = i\hbar\hat{p}_x/m$, we obtain $\hat{\mathbf{p}} = -im\hbar^{-1}[\hat{\mathbf{r}}, \hat{H}_0]$. Hence, we can write the coupling between the two atomic states $|a\rangle$ and $|b\rangle$ due to H_{int} as

$$\langle a, f_1|\hat{H}_{\text{int}}|b, f_2\rangle = \langle a, f_1|-\frac{e}{m}\hat{\mathbf{A}}\cdot\frac{im}{\hbar}[\hat{\mathbf{r}}, \hat{H}_0]|b, f_2\rangle, \tag{2.9}$$

where f_1 and f_2 mark the state of the photon field. We will assume now that we are working with a plane-wave field, which can be factorized into vector and scalar parts $\hat{\mathbf{A}} = \hat{\varepsilon}\,\hat{A}$, where $\hat{\varepsilon}$ denotes the polarization of the field. Further expanding the spatial dependence of the plane wave in the vicinity of the atom nucleus ($r = 0$) to the lowest order (constant term) $\hat{A}(\hat{\mathbf{r}}) \approx \hat{A}(0)$, we can write the atom-field interaction element as

$$\begin{aligned}\langle a, f_1|\hat{H}_{\text{int}}|b, f_2\rangle &\approx -\langle f_1|\hat{A}|f_2\rangle\cdot\langle a|i\frac{\hbar\omega_b - \hbar\omega_a}{\hbar}\hat{\varepsilon}\cdot\hat{\mathbf{r}}e|b\rangle \\ &= \langle f_1|\underbrace{-i\omega_{ab}\hat{A}}_{=-\partial A/\partial t = E}|f_2\rangle\langle a|\hat{\varepsilon}\cdot\hat{\mathbf{r}}e|b\rangle.\end{aligned} \tag{2.10}$$

This is atom-light coupling in the dipole (E1) approximation.

2.3.1 Transition matrix elements

Electric dipole transitions between atomic states occur due to couplings of the form $\mathscr{H} = -e\hat{\mathbf{r}}\cdot\hat{\varepsilon}_q$, where $\bar{\mathbf{r}}\cdot\hat{\varepsilon}_q = \sqrt{4\pi/3}\,Y_{1,q}$ couples σ^-, π and σ^+ transitions for spherical harmonics $Y_{1,q}$ with $q = -1, 0, 1$ respectively ($\bar{\mathbf{r}}$ is the unit vector in the direction of $\mathbf{r}$).

We will first consider matrix elements in the basis $|n, \ell, m_\ell\rangle$ that neglects the fine-structure. The matrix element can be factorised into a part that couples radial parts of the wavefunction, and a part that couples to the angular parts of the wavefunction

$$\begin{aligned}\langle n', \ell', m_{\ell'}|\hat{\mathbf{r}}\cdot\hat{\varepsilon}_q|n, \ell, m_\ell\rangle &= \sqrt{\frac{4\pi}{3}}\overbrace{\int_0^{+\infty} R^*_{n',\ell',m_{\ell'}} r R_{n,\ell,m_\ell}\, r^2 \mathrm{d}r}^{\equiv \mathscr{R}_{n\ell\to n'\ell'}} \\ &\quad\cdot\int_0^{\pi}\mathrm{d}\theta\int_0^{2\pi}\sin\theta\;\mathrm{d}\phi\; Y^*_{\ell',m_{\ell'}}Y_{1,q}Y_{\ell,m_\ell}.\end{aligned}$$

The radial matrix element $\mathscr{R}_{n\ell\to n'\ell'}$ can be calculated from the wavefunctions ob-

tained in Sec. (2.2), returned by the ARC function `getRadialMatrixElement`. For numerical calculations, instead of $(0,+\infty)$ formal bounds, the integration bounds are finite $(r_\mathrm{i}, r_\mathrm{o})$ as outlined in Sec. (2.2). The product of the three spherical harmonics[1] can be expressed via Wigner 3-j (or Clebsch-Gordon) coefficients as

REMINDER: Eq. (3.8.73) in Ref. [125]:

$$\int_0^{\pi} \mathrm{d}\theta \int_0^{2\pi} \sin\theta \ \mathrm{d}\phi \ Y_{l_1,m_1} Y_{l_2,m_2} Y_{l_3,m_3} = \sqrt{\frac{(2l_1+1)(2l_2+1)(2l_3+1)}{4\pi}} \cdot \begin{pmatrix} l_1 & l_2 & l_3 \\ 0 & 0 & 0 \end{pmatrix} \begin{pmatrix} l_1 & l_2 & l_3 \\ m_1 & m_2 & m_3 \end{pmatrix}$$

$$\begin{aligned} \langle n',\ell',m_{\ell'}|\hat{\mathbf{r}}\cdot\hat{\varepsilon}_q|n,\ell,m_\ell\rangle &= (-1)^{\ell'-m_{\ell'}} \begin{pmatrix} \ell' & 1 & \ell \\ -m_{\ell'} & q & m_\ell \end{pmatrix} \langle n'\ell'||r||n\ell\rangle, \\ \langle n'\ell'||r||n\ell\rangle &\equiv (-1)^{\ell'} \sqrt{(2\ell'+1)(2\ell+1)} \begin{pmatrix} \ell' & 1 & \ell \\ 0 & 0 & 0 \end{pmatrix} \mathscr{R}_{n\ell\to n'\ell'}, \end{aligned} \tag{2.11}$$

where the introduced quantity $\langle n'\ell'||r||n\ell\rangle$ is the *reduced matrix element*, returned by the ARC function `getReducedMatrixElementL`.

Calculating these dipole matrix elements in the fine basis $|n,\ell,j,m_j\rangle$ requires expansion of wavefunctions in the uncoupled basis $|n,l,m_l,m_s\rangle$ as in Eq. (2.7) since for these states we can directly calculate dipole matrix elements as demonstrated above. As a consequence of this, summation over four 3-j coefficients will occur giving rise to 6-j Wigner coefficient $\{\ldots\}$. The final result is

$$\begin{aligned} \langle n',\ell',j',m_{j'}|\hat{\mathbf{r}}\cdot\hat{\varepsilon}_q|n,\ell,j,m_j\rangle &= (-1)^{j'-m_{j'}} \begin{pmatrix} j' & 1 & j \\ -m_{j'} & q & m_j \end{pmatrix} \langle n',\ell',j'||r||n,\ell,j\rangle, \\ \langle n',\ell',j'||r||n,\ell,j\rangle &\equiv (-1)^{l'+s+j+1} \sqrt{(2j'+1)(2j+1)} \\ &\quad \cdot \begin{Bmatrix} j' & 1 & j \\ \ell & s & \ell' \end{Bmatrix} \langle n'\ell'j'||r||n\ell j\rangle. \end{aligned} \tag{2.12}$$

The dipole element and reduced dipole matrix element in the J basis can be obtained from ARC using the `getDipoleMatrixElement` and `getReducedMatrixElementJ` functions. The numerically obtained radial wavefunctions $R_{n,\ell,j}$ [Sec. (2.2)] also allow calculation of a radial matrix element for quadrupole coupling, that will appear in calculations of coupling matrix elements in static magnetic fields [Sec. (2.4.2)] and atom-atom interactions [Sec. (2.5.1)], as (`getQuadrupoleMatrixElement`)

$$\mathscr{R}^{Q}_{n\ell\to n'\ell'} = \int_{r_\mathrm{i}}^{r_\mathrm{o}} R_{n',\ell',j'}\ r^2\ R_{n,\ell,j}\ r^2\ \mathrm{d}r. \tag{2.13}$$

The accuracy of calculated dipole-coupling strengths through numerical integration of the wavefunctions in the model potential can be checked with experimental measurements of C_3 and C_6 [126–128], putting an upper boundary of relative accuracy at $\sim 10^{-2}$. For low-lying states that are closer to the core, the relative accuracy deteriorates, and is of the 10^{-1} level for transitions from the ground state. More advanced theoretical models have been developed for calculation of dipole matrix elements of these lower-lying states [129, 130]. These values are tabulated in the files used by the ARC library, and can be directly queried by the `getLiteratureDME` method. Calculations will use these values by default if they exist for required transitions, since the expected relative accuracy of these more advanced approaches is 10^{-2} or better.

[1] We use the Condon-Shortley phase convention [124] for spherical harmonics.

2.3.2 Lifetimes

The lifetime $1/\Gamma_{n,\ell,j}$ of the alkali atom population in the state $|n,\ell,j\rangle$ due to radiative transitions can be calculated by finding the transition rate $\Gamma_{n,\ell,j}$ from $|n,\ell,j\rangle$ to all the other states $|n',\ell',j'\rangle$ as

$$\Gamma_{n,\ell,j} = \sum_{n',\ell',j':\ E(n',\ell',j')<E(n,\ell,j)} A_{n\ell j\to n'\ell'j'} + \sum_{n',\ell',j'} A_{n\ell j\to n'\ell'j'}\bar{n}_\omega. \tag{2.14}$$

Here the first summation includes spontaneous decays to states with energies $E(n'\ell',j')$ lower than the considered state $|n,\ell,j\rangle$. The second term in the summation includes transitions to all the states, including ones with higher energies, induced by the black-body radiation at finite temperature T of the environment. Average per-mode occupation number $\bar{n}_\omega$ of black-body photons with the correct energy $\hbar\omega = |E(n',\ell',j') - E(n,\ell,j)|$ is given by the Bose-Einstein distribution

$$\bar{n}_\omega = \frac{1}{\exp[\hbar\omega/(k_B T)]-1}. \tag{2.15}$$

Finally Einstein A coefficients [131] account for vacuum coupling to all the available EM field modes for each of the given transitions

$$A_{n\ell j\to n'\ell'j'} = \frac{4\omega^3}{3c^3}\frac{\max(\ell,\ell')}{2\ell+1}\mathscr{R}^2_{n\ell j\to n'\ell'j'}. \tag{2.16}$$

As an example, Figure 2.5 shows transition rates from caesium 25 $S_{1/2}$ states to other n $P_{1/2,3/2}$ states. As we will see in the next Sec. (2.3.3), coupling strengths between neighbouring states differing by δn in principal quantum number go down $\propto \mathscr{R}^2_{n\ell j\to n'\ell'j'}$ as δn increases. Yet decays to the ground states, if allowed by the selection rules, still dominate due to higher number of vacuum modes $\propto \omega^2$ and stronger vacuum coupling $\propto \omega$. For low-angular momentum states, that can decay to ground states, this gives total scaling of Rydberg state lifetimes as n_*^3 (Fig. 2.6). Interestingly, even at a room temperature $T \sim 300$ K, black-body radiation redistributes population to the states close in energy [Fig. 2.5 and Fig. 2.6(a)], both below and above the ground state, contributing ~10–80% to the total state depopulation

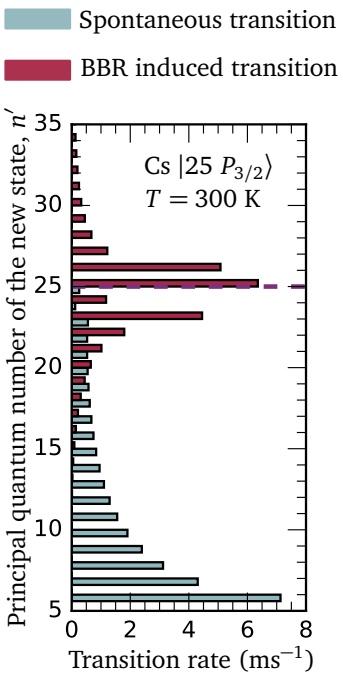

Figure 2.5: Black-body induced transition rates. Transition rates for caesium 25 $P_{3/2}$ state (dashed line) to $|n\ S_{1/2}\rangle$ and $|n\ D_{3/2,5/2}\rangle$ states. At 300 K there is a significant contribution of black-body radiation (BBR) induced transitions (red), both to lower- and higher-lying states.

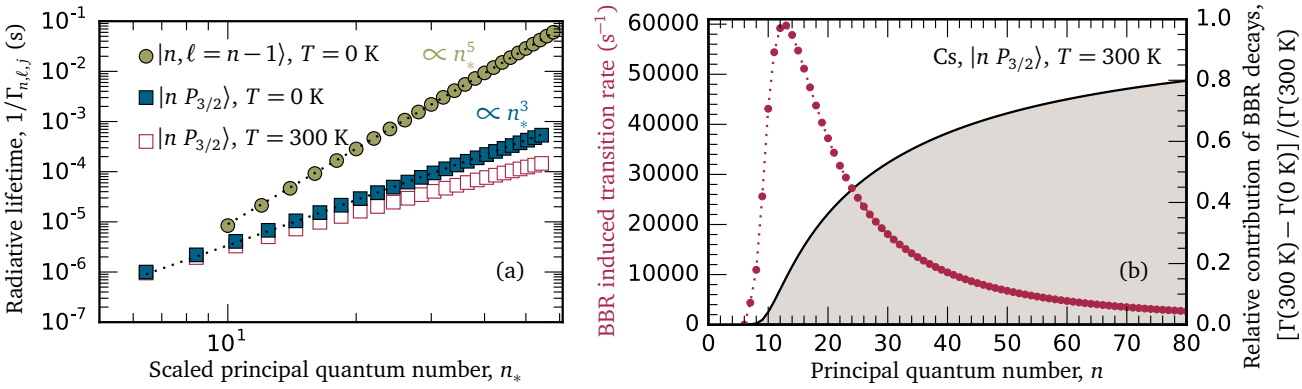

Figure 2.6: Scaling of radiative lifetimes and black-body radiation (BBR) induced transitions. Radiative lifetimes of caesium states (a), exhibiting scaling $\propto n_*^3$ (dotted line) for a low orbital angular momentum states (solid squares), and $\propto n_*^5$ (dotted line) for a high orbital angular momentum states (circles). BBR induces significant changes in the radiative lifetime, shown on the example of n $P_{3/2}$ states at 300 K (open squares). While rates of BBR induced transition are reduced for higher-lying states (b), BBR-induced transitions actually become the dominant factor in radiative decays of high-lying states.

rate [Fig. 2.6(b)]. We note that this factor is quite an important practical consideration since even in cold, collision-free, atomic ensembles, this redistributes the initial population excited to a single Rydberg state, among all the nearby states, even the higher lying ones. For $n\,S$, $n \sim 30$ states this happens at time scales of $\sim 10\ \mu$s, leaving a fraction of population of the order of several % in states close in energy, as detected in early experiments [132–135]. This can fundamentally change processes occurring in the samples, by turning on resonant dipole-dipole interactions, requiring inclusion in theoretical analysis of the experiments [37, 38]. We will discuss possible implications in Chapter 4. For higher lying states [Fig. 2.6(b)] black-body rates can be about an order of magnitude lower than the peak BBR-induced depopulation rates at room temperature that occur for states with principal quantum number $n \sim 10-12$. Finally we note that black-body induced transition between bound states and the continuum, i.e. black-body induced photoionization [136], can also contribute to the finite lifetime of the states. For example, for sodium 17 D states at room temperature (300 K) the calculated ionization rate [133, 137] is $\sim 10^3$ s^{-1}. The longest lived Rydberg states are high orbital angular momentum states $\ell = n-1$, also called "circular" states [Fig. 2.6(a), circles]. Due to the selection rules for orbital angular momentum, they have only one decay path to the states with principal quantum number $n-1$, which gives rise to lifetime scaling of n_*^5 [ω^3 goes down as $(1/n_*^3)^3$, while the rate of dipolar coupling goes up as $(n_*^2)^2$].

The lifetimes calculated here include only single-atom processes. In experimental samples one typically has a large number of atoms that opens up the possibility of additional processes. For random ensembles at finite temperature we have collisional processes, for which cross-section σ [as we will see in Sec. (2.6)] typically scales as the wavefunction size $\sigma \sim \pi\langle r^2\rangle \propto n_*^4$, reaching 1 μm^2 for $n \sim 80$. For example, atoms in $n \sim 25$ moving with the typical average 1D speed $\bar{v}$ of atoms in thermal vapour (MOT) of 200 m/s (10^{-2} m/s), and typical number densities $\mathcal{N}$ of about $10^{10...13}$ cm^{-3} (10^{10} cm^{-3}) the Rydberg-Rydberg collision rate $\bar{v}\sigma\rho_{\mathrm{R}}$ is about $10^{4...7}$ s^{-1} (1 s^{-1}), assuming that the Rydberg state population has number density ρ_{R} of the same order of magnitude as the initial ground-state atoms ($\rho_{\mathrm{R}} \sim \mathcal{N}$). The collisions result in collisional broadening of lines, population redistribution among different states, and ionization of some of the Rydberg atoms. Electrons produced in ionization typically have average velocities $\bar{v}_{\mathrm{e}}/\bar{v} \sim 10^{2...3}$ higher than ions and atoms, but similar cross-sections for collisions with Rydberg states [138]. This can result in ionization avalanche *in the time domain* [138], since creation of fast electrons can speed-up the state redistribution process. These processes happen even in the absence of external driving - i.e. they will happen even if the atom excitation is done in a pulsed regime. The addition of external driving during collisional processes, as in the case of continuous laser excitation, can open up new two-atom mechanisms for decay, even in the case of off-resonant excitation where light assisted collisions can occur, as we will discuss in Sec. (2.5.2).

2.3.3 Exciting Rydberg states

Coupling strengths between the ground state and high-lying states with principal quantum numbers differing n typically scale as $n_*^{-3/2}$. As a consequence, for direct ground state-Rydberg state 5 $S_{1/2} \xrightarrow[297\ \mathrm{nm}]{0.003\ a_0 e}$ 60 $P_{3/2}$ transition one needs intensities $\sim 10^5$ W/cm^{-2} in order to achieve Rabi frequencies of the order of $2\pi \times 10$ MHz,

and requires driving at UV wavelengths of ∼300 nm[38]. Values above and below arrows in transition indicate reduced dipole matrix element $\langle j'||er||j\rangle$ and transition wavelength respectively. More commonly used schemes use excitation with two driving fields, one typically in the near infrared (NIR) and the other in the blue part of the spectrum. For rubidium the corresponding transitions are $5S_{1/2} \xrightarrow[780\text{ nm}]{5.96\ a_0 e} 5P_{3/2} \xrightarrow[480\text{ nm}]{0.01\ a_0 e} 60S_{1/2}$. For caesium the corresponding transition is $6\ S_{1/2} \xrightarrow[455\text{ nm}]{0.576\ a_0 e} 5P_{3/2} \xrightarrow[1061\text{ nm}]{0.02\ a_0 e} 60S_{1/2}$. Blue driving coherent fields are typically generated in a chain, by frequency-doubling in second harmonic generation (SHG) crystals that are pumped with several watts of infrared light originating from NIR extended cavity diode lasers (ECDL) amplified in tapered amplifiers (TA). The second step in the transition still requires intensities of $\sim 10^4$ W/cm^{-2} to achieve coupling Rabi frequencies of the order of several MHz. Crucially, with one- and two-photon ladder excitation schemes, one cannot fulfil the usual Doppler-free condition $\sum_i \mathbf{k}_i = 0$ due to mismatch in excitation laser wave vectors $\mathbf{k}_i$, which has fundamental implications on the nature of the collective Rydberg excitations as we will see in Chapter 3.

The simplest ladder-system excitation scheme that achieves Doppler-free condition uses three laser beams. Wave vectors $\mathbf{k}_i$ of the three driving fields can be added in a triangular configuration, summing them to zero. Example of two such schemes in caesium used for the experimental results in Sec. (3.2) of this thesis are $6S_{1/2} \xrightarrow[852\ nm]{6.324\ a_0 e} 6P_{3/2} \xrightarrow[1470\ nm]{6.479\ a_0 e} 7S_{1/2} \xrightarrow[1394\ nm]{0.975\ a_0 e} 8P_{1/2}$ and $6S_{1/2} \rightarrow 6P_{3/2} \rightarrow 7S_{1/2} \xrightarrow[795\ nm]{0.021\ a_0 e} 23P_{3/2}$. Three photon coupling strengths using S states as a penultimate state have slightly weaker coupling strengths (Fig. 2.7 diamonds), in spite the used S states being higher up in the energy then P states in two-photon scheme. This is because the S state wavefunction, mostly centred around the nucleus, has smaller overlap with more weakly bound P states than the S and P wavefunctions in the inverse situation (Rydberg S states and P initial states) is actually better. Yet, in spite of similar requirements on the laser powers, this situation can be considered simpler since it doesn't require an SHG crystal for generating the last driving field in the excitation, and instead uses just a TA. Further improvement in requirements on driving fields powers comes with four driving fields, where we gain in coupling strength by approaching the Rydberg states gradually (Fig. 2.7 circles). An example of this scheme is $6\ S_{1/2} \rightarrow 6P_{3/2} \rightarrow 7S_{1/2} \xrightarrow[1769\ nm]{0.093\ a_0 e} 52D_{3/2}$ transition, used in Ref. [100].

Driving fields in most cases originate from master lasers that are NIR extended cavity diode lasers (ECDL) whose cavity lengths and driving currents are locked to the spectroscopic reference for the relevant transitions, while their temperature is actively stabilised [139, 140]. Typically this achieves laser linewidths that are of the order of ∼ 100kHz. Sometimes one wants to achieve smaller phase noise — for example for optically induced single-spin operations [127], narrow driving of forbidden transitions [141, 142] or for coherent effects like EIT where ultimate linewidth is limited by the combined laser linewidth [143]. Achieving narrow combined linewidth is significantly harder in the ladder-excitation schemes compared to the Λ schemes used for observation of coherent phenomena between the atomic ground states. In the latter case, all the driving fields can be derived from a single laser, with some combination of stable acousto- and electro-optic modulator induced frequency shifts (of up to several GHz) and injection locking [144], or alternatively, with direct relative-phase measurement and feedback of two independent lasers [145]. This

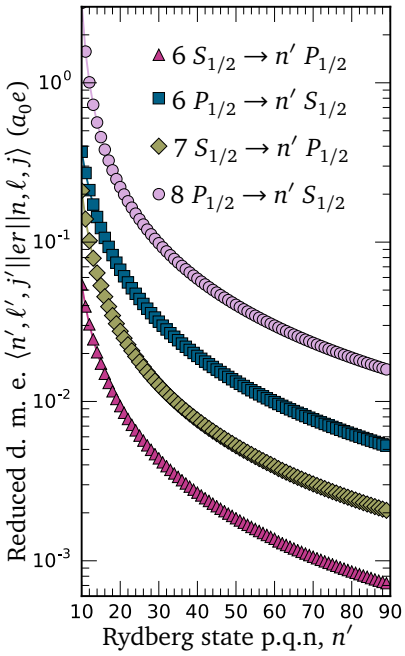

Figure 2.7: Comparison of coupling strengths to Rydberg state in multi-step ladder driving schemes in caesium. Reduced dipole matrix elements (d.m.e) for coupling to Rydberg states with principal quantum number (p.q.n) n' for different initial states, reached in single, two, three and four-driving field ladder excitation schemes.

renders the system insensitive to phase drifts of the master laser. This approach is not possible in the ladder excitations schemes due to a big discrepancy in the wavelengths used for excitation. Therefore one has to try to reduce the absolute phase drift of each laser independently, and the remaining phase drifts characterised by the laser linewidths K_i will all contribute as uncorrelated random variables to the total phase noise, giving linewidths of $K = \sum_i K_i$ for ground state-Rydberg state driving. Laser linewidths down to 1 Hz can be achieved by locking to ultra-stable, temperature stabilised, high-finesse cavities [141, 146, 147].

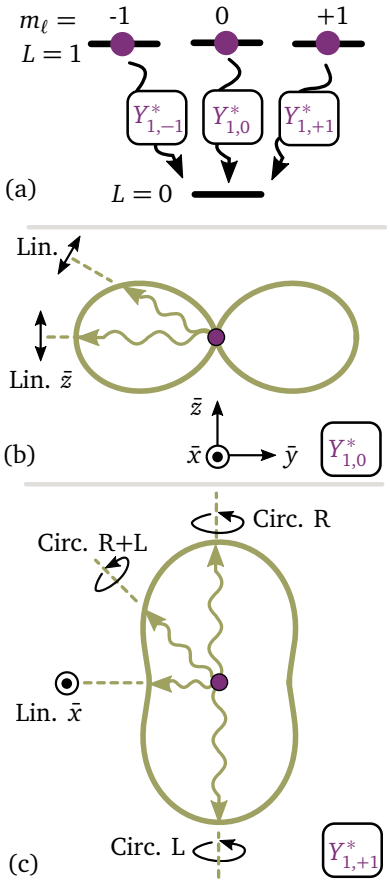

Figure 2.8: Spatial fluorescence patterns from single-atom decays in the far-field. (a)Level scheme of an excited atom decaying under dipolar coupling $\propto \langle L = 0, m_\ell = 0|Y^*_{1,q}|L = 1, m_\ell\rangle$, $q = 0, \pm 1$ into the vacuum modes. Solid line (yellow) on (b) and (c) are polar plots of fluorescence *intensity* in $\bar{y} - \bar{z}$ plane for $q = 0$ and $q = +1$ decays respectively. The scale is same on both plots, and the fluorescence pattern is $\bar{z}$-axially symmetric. Polarisation of emitted light in several example directions (wavy lines) is labelled Lin., Circ. R, Circ. L, corresponding to linear, right-hand circularly polarised and left-hand circularly polarised respectively.

2.3.4 Atomic contribution to the electromagnetic field

Excited single atoms emit fluorescence whose spatial profile depends on the angle θ between the quantization axis and the direction of observation. For π transitions the fluorescence intensity profile[2] is $\propto \sin^2\theta$, while for $\sigma^\pm$ it is $\propto (1+\cos^2\theta)/2$, as shown in Fig. 2.8.

For a medium of many emitters that all have well-defined relative phase, inherited for example from the external driving field, we calculate the effect of their re-radiated field on a propagating driving field by calculating the dynamic polarizability $\mathbf{P} = \sum_{q=0,\pm1} \int \mathrm{d}\omega \left[\mathscr{P}_q(\omega,\mathbf{r})\varepsilon_q \exp(-i\omega t) + \mathscr{P}^*_q(\omega,\mathbf{r})\varepsilon^*_q \exp(+i\omega t)\right]$ of the medium, where q indexes possible polarisations $\varepsilon_0 = \bar{\mathbf{z}}$, $\varepsilon_{\pm1} = (\bar{\mathbf{x}} \pm i\bar{\mathbf{y}})/\sqrt{2}$. This polarizability arises from individual dipoles $\langle e\hat{\mathbf{r}}\rangle$, where $\langle \ldots \rangle = \mathrm{Tr}[\rho \ldots]$ over the density matrix ρ of the ensemble at the corresponding location $\mathbf{r}$ in space. Assume that in the frequency range of interest there is only one resonance, for example ground-state excited state resonance $|\mathrm{g}\rangle \longleftrightarrow |\mathrm{e}\rangle$. For a medium with atom number density $\mathscr{N}$ that is dilute enough that we can neglect inter-atomic interactions, we obtain

$$\begin{aligned}\mathscr{P}_q(\omega,\mathbf{r}) &= \frac{\mathscr{N}}{\pi}\int \mathrm{d}\omega\; e^{i\omega t}\langle e\hat{\mathbf{r}}\cdot\varepsilon_q\rangle \\ &= \mathscr{N}\mu^{(q)}_{\mathrm{ge}}\rho_{\mathrm{eg}}(\omega,\mathbf{r}),\end{aligned} \tag{2.17}$$

where $\mu^{(q)}_{\mathrm{ge}} \equiv \langle \mathrm{g}|e\mathbf{r}\cdot\varepsilon_q|\mathrm{e}\rangle$ is the corresponding dipole matrix element and $\rho_{\mathrm{eg}}(\omega,\mathbf{r})$ is the corresponding coherence element of the ω frequency component in the Fourier transform of the density matrix. Note that this density matrix frequency component is usually obtained by solving atom dynamics for ρ_{eg} in a basis where the excited state is rotating $\hat{U} = \exp(i\omega t|\mathrm{e}\rangle\langle\mathrm{e}|)$, which is typically done when the probe field also has frequency ω (for example, see Sec. 2.4.3).

For a weak driving field $\mathbf{E} = \varepsilon[\varepsilon_p \exp(i\mathbf{kr} - i\omega t) + \varepsilon^*_p \exp(-i\mathbf{kr} + i\omega t)]/2$, with amplitude ε and polarisation ε_p, in the solution of atom dynamics for ρ_{eg} we can keep only term linear in $\mathbf{E}$. This allows for the medium's response to the applied electric field to be described by a single *constant* value of susceptibility $\chi(\omega)$, defined with

$$\mathbf{P} = \varepsilon_0 \frac{\varepsilon}{2}[\chi\varepsilon_p \exp(i\mathbf{kr} - i\omega t) + \chi^*\varepsilon^*_p \exp(-i\mathbf{kr} + i\omega t)]. \tag{2.18}$$

For an isotropic atomic medium $\mathbf{P} \parallel \mathbf{E}$, so χ is a complex scalar. Eq. (2.18) and Eq. (2.17) can be solved for χ analytically in simpler systems, see for example

[2] Remember that radiation of a classical dipole $\mathbf{p}$ is $\mathbf{E}(\mathbf{r},t) = \frac{\mu_0}{4\pi r}\{\bar{\mathbf{r}}\times[\bar{\mathbf{r}}\times\ddot{\mathbf{p}}(t-r/c)]\}$, see e.g. Eq. (11.56) in Ref. [148].

Ref. [149]. In general we can directly numerically calculate χ from $\rho_{\rm eg}$ obtained in solving atomic dynamics. If the polarisation of the field is $\varepsilon_p = \varepsilon_q$, then we can define the driving Rabi frequency $\Omega \equiv \langle {\rm e}|e\hat{\mathbf{r}}\cdot\varepsilon_p\varepsilon|{\rm g}\rangle/\hbar = \mu_{\rm eg}^{(q)}\varepsilon/\hbar$, and combine Eq. (2.17) and Eq. (2.18), to obtain susceptibility

$$\begin{aligned}\chi(\omega) &= \frac{2\,\mathscr{N}\,\mu_{\rm ge}^{(q)}\,\rho_{\rm eg}(\omega)}{\varepsilon_0\,\varepsilon} \\ &= -\frac{2\,\mathscr{N}\,|\mu_{\rm eg}^{(q)}|^2}{\varepsilon_0\,\hbar\,\Omega}\,\rho_{\rm eg}(\omega).\end{aligned} \tag{2.19}$$

When the propagating field and continuous atomic medium have respectively electric field amplitude ε and polarizability amplitude $\mathscr{P}$ that slowly change[3] in space and time, in the vicinity of the frequency $\bar{\omega}$ (corresponding wave vector $\bar{k} = \bar{\omega}/c$), we can write Maxwell equations for the plane-wave electric field propagating in the z direction as (see Appendix A.2)

$$\frac{\partial\varepsilon}{\partial z} + \frac{1}{c}\frac{\partial\varepsilon}{\partial t} = \frac{i\bar{k}}{\varepsilon_0}\mathscr{P}. \tag{2.20}$$

Using susceptibility $\chi(\delta\omega)$ at $\omega \equiv \bar{\omega} + \delta\omega$ to express polarizability $\mathscr{P} = \varepsilon_0\chi(\delta\omega)\frac{\varepsilon}{2}$ in terms of electric field amplitude ε, we can obtain

$$\varepsilon(z,t) = \int {\rm d}(\delta\omega)\;\varepsilon(z=0,\delta\omega)e^{-i\;\delta\omega\;t}e^{i\;z\{\;\delta\omega/c+\bar{k}\;{\rm Re}[\chi(\delta\omega)]/2\;\}}e^{-z\;\bar{k}\;{\rm Im}[\chi(\delta\omega)]/2}. \tag{2.21}$$

In this slowly-varying envelope limit, we see from the solution that the real part of the susceptibility matrix causes a phase shift, effectively changing the refractive index n as $n = 1+{\rm Re}[\chi(\delta\omega)]/2$, while the imaginary part leads to attenuation of the forward propagating signal. Intensity of the probing field $I(z)$ will be exponentially attenuated as $I(z) = I(0)\exp(-\alpha\,z)$ upon propagation for distance z, where the attenuation coefficient is $\alpha = \bar{k}\;{\rm Im}(\chi)$. Finally, dispersion of the susceptibility $\frac{\partial\chi}{\partial\omega}$ changes the group velocity

$$v_{\rm g} = \frac{\partial\omega}{\partial k} = \frac{c}{1+\frac{\bar{\omega}}{2}{\rm Re}\left(\frac{\partial\chi}{\partial\omega}\right)}. \tag{2.22}$$

Highly dispersive media ${\rm Re}\left(\frac{\partial\chi}{\partial\omega}\right) \gg 1$, can significantly reduce probe pulse propagation speeds.

2.3.5 Detecting Rydberg states

Detection of atom population in relatively low-lying ($\lesssim 30$) Rydberg states is possible directly though observing fluorescence of decaying Rydberg states [150], using a monochromator to resolve transitions from individual states. This becomes harder for higher-lying states due to their longer lifetimes (Sec. 2.3.2), however field-ionization can be used as a state selective Rydberg population detection method [151]. The method relies on the fact that higher-lying Rydberg states require lower applied DC electric fields to ionise [56]. Therefore the populations of all the Rydberg states can

[3] Formally, slowly-varying conditions are $|\bar{\omega}\mathscr{P}| \gg |\partial\mathscr{P}/\partial t|$, $|\bar{k}\mathscr{P}| \gg |\partial\mathscr{P}/\partial z|$, $|\bar{\omega}\varepsilon| \gg |\partial\varepsilon/\partial t|$ and $|\bar{k}\varepsilon| \gg |\partial\varepsilon/\partial z|$.

be recorded by applying an electric field ramp, and measuring the ion signal in time. Nowadays ion signals are typically detected on multi-channel plates (MCP) detector, which, in addition to recording total number of ions, can provide spatial resolution of the detected ions. By accounting for the particle trajectories, this information can be used to deduce the original spatial distribution of Rydberg atoms [152] down to 1 μm spatial resolution [128]. Such a measurement of Rydberg atom distances after some variable time following the Rydberg state excitation, allowed direct observation of repulsive van der Waals inter-atomic forces [128, 153].

Recently, Rydberg states have been detected in coherent detection schemes by probing locations of EIT and EIA features with laser transmission (Sec. 2.4.3), in two [63, 66, 91, 92], three [98, 154] and four-step [100] excitation schemes. These coherent detection schemes have also been extended to systems for imaging spatial distributions of Rydberg states in cold atomic samples [155, 156]. New opportunities opened in experiments in controllable atomic arrays [85, 86], whose geometries are more flexible than those of the lattices achieved through Mott insulator preparation [38]. Exquisite level of coherent control [84] allows population transfer between Rydberg states and ground states by performing optical π pulses, where ground-state trapped atoms can be imaged directly by fluorescence imaging with single-site resolution.

2.4 Tuning the state energies and properties

The single-atom energy levels can be tuned by admixing other states via applied DC and AC external fields. Changing the composition of the unperturbed bare-states also changes their properties, allowing states to acquire permanent dipole moments or become coupled to previously forbidden states. Calculations of single-atom properties like this are implemented in the ARC module `calculations_atom_single`.

2.4.1 Static electric field: state polarizability and Stark maps

Calculation of energy-level shifts in constant external electric fields (Stark shifts) is important for both precision electrometry, and tuning atomic interactions to Förster resonances (Sec. 2.5) which allow use of strong resonant dipole-dipole interactions between the atoms. Energies and states can be found by finding eigenstates of the Hamiltonian for an electric field ε applied along the $\hat{z}$-axis (in Hartree atomic units)

$$\mathscr{H} = H_0 + \varepsilon\,\hat{z}, \tag{2.23}$$

where H_0 is the unperturbed atomic Hamiltonian. The coupling terms $\langle n,\ell,j,m_j|\varepsilon\hat{z}|n',\ell',j',m_{j'}\rangle$ have the same form as dipole matrix elements [Eq. (2.12)] for $q=0$. Therefore only $\Delta m_j = 0,\ \Delta\ell = \pm 1$ states will be coupled together. Low angular momentum states $\ell \lesssim 4$ are non-degenerate, and in low field their level shift will be dominated by the second-order perturbative corrections $\alpha_0\varepsilon^2/2$ to the state energy quantified by the scalar polarizability

$$\alpha_0 \approx 2\sum_{n'\ell'j\neq n\ell j}\frac{\left|\langle n,\ell,j,m_j|\hat{z}|n',\ell',j',m_{j'}\rangle\right|^2}{E(n',\ell',j')-E(n,\ell,j)}. \tag{2.24}$$

In low fields, scalar polarizability scales as $\alpha_0 \propto n_*^7$.

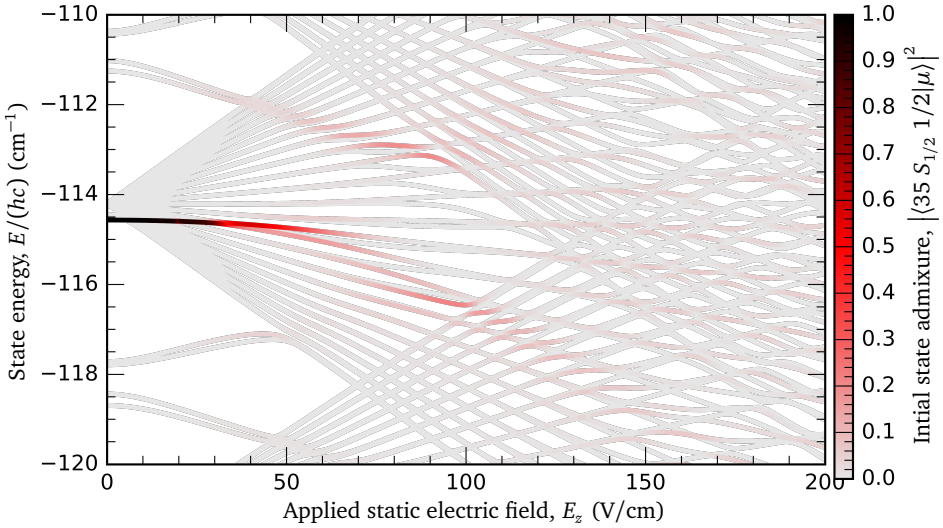

Figure 2.9: Atom energy levels in applied static electric field (Stark map). Caesium 35 $S_{1/2}$ $m_j = 1/2\rangle$ state is admixed to other atom eigenstates $|\mu\rangle$ due to the external static electric field E_z, leading to energy shifts. ARC package in interactive use allows "on-click" exploration of unperturbed states admixed in eigenstates.

For stronger fields, due to strong state admixing, this second-order correction doesn't give good predictions any more, and one has to numerically diagonalize the Hamiltonian [Eq. (2.23)]. Following the approach of Zimmerman *et.al* [121], this is implemented in the `StarkMap` class in ARC. The basis $\{|n', \ell', j', m_{j'}\rangle, \ldots\}$ has to be selected based on the principal quantum number n of the state we are interested in and the applied field, but typically states with $|n - n'| \leq 5$ and, due to strong state admixing of states with different orbital angular momentum (see Fig. 2.9), states with $|\ell - \ell'| \lesssim 20$ need to be included for convergence of results. Knowledge of state compositions obtained from diagonalization is also important because laser coupling strength will be strongly modified by admixing. The ARC class `StarkMap` can show the Stark maps as interactive graphs, where users can choose states by clicking on them and explore their composition. Default colour highlighting of the states, as seen on Fig. 2.9, shows the contribution of the original target state $|n, \ell, j, m_j\rangle$ to other states. One can also set an optional argument `drivingFromState` and specify an initial state from which to drive transitions. ARC will then calculate colour highlighting of states based on initial state dipole coupling to the obtained Stark eigenstates.

This calculation method has been applied in strong electric fields for the calculation of complex Rydberg Stark manifolds, showing very good agreement with experimental measurements [157].

2.4.2 Static magnetic field

The Hamiltonian for an atom interacting with static magnetic field $\mathbf{B}$ can be written as (in SI units, neglecting free field energy)

$$\mathscr{H} = \frac{(\hat{\mathbf{p}} - e\hat{\mathbf{A}})^2}{2m} + V(\hat{r}) + e\hat{\phi} + \mu_\mathrm{B}\mathbf{B}\,(g_\mathrm{S}\,\hat{\mathbf{S}} + g_\mathrm{I}\,\hat{\mathbf{I}}) + H_\mathrm{HFS}, \tag{2.25}$$

where g_S and g_I are gyromagnetic factors corresponding to the magnetic field interaction with valence electron spin $\hat{\mathbf{S}}$ and nuclear spin $\hat{\mathbf{I}}$, and $\mu_\mathrm{B} \equiv e\hbar/(2m_\mathrm{e})$ is the Bohr magneton. The hyperfine interaction term H_HFS can be neglected for Rydberg states [116]. We can fix the gauge for space without free charges $\phi = 0, \nabla \cdot \hat{\mathbf{A}} = 0$. Setting $\hat{\mathbf{A}} = -\frac{1}{2}\hat{\mathbf{r}} \times \mathbf{B}$, we can extract an interaction Hamiltonian (similarly to Eq. 2.8)

$$H_{\rm int} = \underbrace{-\frac{\mu_{\rm B}\mathbf{B}}{\hbar}(\hat{\mathbf{L}} + g_S\,\hat{\mathbf{S}} + g_I\,\hat{\mathbf{I}})}_{\equiv H_{\rm P}} + \underbrace{\frac{e^2}{8m_e}(\mathbf{B}\times\hat{\mathbf{r}})^2}_{\equiv H_{\rm D}}. \tag{2.26}$$

Terms with linear ($H_{\rm P}$) and quadratic ($H_{\rm D}$) dependence on magnetic field B are paramagnetic and diamagnetic terms respectively. For magnetic fields directed along the z axis, the matrix elements of $H_{\rm P}$ are easily calculated by expanding states in an uncoupled ℓ basis with Eq. (2.7). On the other hand, the diamagnetic term can be rewritten as

$$H_{\rm D} = \frac{e^2}{8m_{\rm e}}B^2\,\hat{r}^2\,\sin^2\hat{\theta}, \tag{2.27}$$

where angle $\hat{\theta}$ measures direction of $\hat{\mathbf{r}}$ relative to the quantization axis. The non zero elements of $H_{\rm D}$ are those for which $\Delta l = 0, \pm 2$, and $\Delta m = 0$. Explicit forms of the matrix elements are [158]

$$\langle nlm|\hat{r}^2\sin^2\theta|n'lm\rangle = 2\frac{l^2+l-1+m^2}{(2l-1)(2l+3)}\,\mathscr{R}^Q_{n\ell\to n'l}\ , \tag{2.28}$$

$$\langle nlm|\hat{r}^2\sin^2\theta|n'(l+2)m\rangle = \left[\frac{(l+m+2)(l+m+1)(l-m+2)(l-m+1)}{(2l+5)(2l+3)^2(2l+1)}\right]^{1/2} \cdot\ \mathscr{R}^Q_{n\ell\to n'(\ell+2)}\ . \tag{2.29}$$

The ratio of paramagnetic to diamagnetic terms is $H_{\rm P}/H_{\rm D} \sim 10^{5-6}\ {\rm T}/(B\ n_*^4)$. For atomic ground states and low-lying states the diamagnetic term is negligible, however it becomes more important for higher-lying states due to the quadrupole matrix element scaling as n_*^4, becoming equal to the paramagnetic term for $B \sim 1$ T and $n \sim 20-30$.

The hyperfine interaction in Eq. (2.25) is

$$H_{\rm HFS} = \frac{A_{\rm HFS}}{\hbar^2}\mathbf{I}\cdot\mathbf{J} + \frac{B_{\rm HFS}}{\hbar^4}\frac{3(\mathbf{I}\cdot\mathbf{J})^2 + 3/2\,(\mathbf{I}\cdot\mathbf{J}) - I(I+1)\,J(J+1)}{2I(2I-1)\,J(2J-1)}, \tag{2.30}$$

where $A_{\rm HFS}$ and $B_{\rm HFS}$ are experimentally determined magnetic dipole and electric quadrupole interaction constants. Hyperfine structure is negligible for Rydberg states as it scales as $H_{\rm HSF} \propto 1/n_*^3$ [116], however, it has to be included for low-lying states, since ground state hyperfine splittings are of the order of several GHz for alkali atoms. Static magnetic fields are a useful experimental tool as they can isolate transitions, allowing experimental situations to be more tractable. This is also true for hot atoms, since relatively cheap and compact permanent magnets can provide static fields of the order of $0.6-0.7$ T, which induces splitting of the spectra over tens of GHz range, allowing addressing of individual transitions, since separations between transitions can be bigger than the room-temperature Doppler widths. Applications will be discussed in Sections (3.3) and (5.1.1).

2.4.3 Dressing

Finally, we will discuss the important case of atom energy-level tuning due to coherent driving with AC electromagnetic fields. Two crucial elements that allow rich applications of this approach are (i) the existence of resonances for particular frequencies of the driving, allowing much more precise and state-selective admixing compared to schemes with static fields; and (ii) the existence of long-coherence driv-

ing field sources (lasers, MW and THz generators) that can prepare superpositions of atomic states with well defined relative phases, allowing exploration of interference phenomena in atom-light interactions [104, 159], both within single atoms and in spatially extended atomic-ensembles. Particular examples will be discussed in Chapter 3, but here we will introduce the basic concepts.

To start, consider an atom with two dipole-coupled levels, ground state $|\mathrm{g}\rangle$ and excited state $|\mathrm{e}\rangle$, separated in energy by $\hbar\omega_{\mathrm{ge}} = \langle \mathrm{e}|\mathscr{H}|\mathrm{e}\rangle - \langle \mathrm{g}|\mathscr{H}|\mathrm{g}\rangle$. The atom moves with velocity $\mathbf{v}$ relative to the classical, coherent driving field with electric field $\varepsilon_{\mathrm{d}}(\mathbf{r}) = \varepsilon\cos(\mathbf{k}\cdot\mathbf{r} - \omega_L t)$ of amplitude ε and frequency ω_{L} propagating along the wave vector $\mathbf{k}, k \equiv \omega_{\mathrm{L}}/c$. Neglecting the second-order Doppler effect (relativistic), the atom-light Hamiltonian ($\hbar = 1$) is

$$\mathscr{H}_{\mathrm{AL}} = \omega_{\mathrm{ge}}|\mathrm{e}\rangle\langle\mathrm{e}| + (\Omega^*|\mathrm{g}\rangle\langle\mathrm{e}| + \Omega|\mathrm{e}\rangle\langle\mathrm{g}|)\frac{1}{2}\left[\mathrm{e}^{i(\mathbf{k}\cdot\mathbf{v}\ t-\omega_L t)} + \mathrm{e}^{-i(\mathbf{k}\cdot\mathbf{v}\ t-\omega_L t)}\right], \tag{2.31}$$

where we have assumed electric-dipole coupling between atoms and field with Rabi frequency $\Omega = \langle \mathrm{e}|e\hat{\mathbf{r}}\cdot\varepsilon|\mathrm{g}\rangle$. We can switch to a suitable basis that rotates as $\hat{U} = \exp[i(\omega_{\mathrm{L}}t - \mathbf{k}\cdot\mathbf{v}t)|\mathrm{e}\rangle\langle\mathrm{e}|]$ and find the Hamiltonian in that basis $\hat{U}\mathscr{H}_{\mathrm{AL}}\hat{U}^\dagger + i\frac{\mathrm{d}\hat{U}}{\mathrm{d}t}\hat{U}^\dagger$. After applying the rotating wave approximation (RWA), that neglects rapidly oscillating factors in the new Hamiltonian, we find

$$\mathscr{H}_{\mathrm{RWA}} = -\Delta|\mathrm{e}\rangle\langle\mathrm{e}| + \left(\frac{\Omega}{2}|\mathrm{e}\rangle\langle\mathrm{g}| + \mathrm{H.c.}\right), \tag{2.32}$$

where $\Delta \equiv \omega_{\mathrm{L}} - \mathbf{k}\cdot\mathbf{v} - \omega_{\mathrm{ge}}$ is the Doppler-shifted driving field detuning from the transition resonance[4] . The eigenenergies of the system are $E_\pm = (-\Delta \pm \sqrt{\Delta^2 + \Omega^2})/2$. For far detuned driving $\Delta \gg \Omega$, eigenstates are weakly admixed, causing a ground state off-set in energy (AC Stark shift) of $\Omega^2/(4\Delta)$. For resonant driving $\Delta = 0$ eigenstates $|\pm\rangle = (|\mathrm{g}\rangle \pm |\mathrm{e}\rangle)/\sqrt{2}$ (dressed states) are symmetric and antisymmetric superpositions of bare states $|\mathrm{g}\rangle$ and $|\mathrm{e}\rangle$ with eigenenergies $\pm\Omega/2$ split by the Rabi driving frequency Ω. An example is resonant dressing of two Rydberg states by a microwave or terahertz field. Since admixed states $|\pm\rangle$ will have strong permanent dipole moments, interactions between the atoms separated by R will be of a long range $\propto R^{-3}$ type [160]. Off-resonant dressing in the Rydberg state manifold (i.e. with microwave and terahertz fields), with weak state-selective and interatomic-distance dependant admixing control, can provide even more refined shaping of interaction potentials [161].

Now we will consider a slightly more complicated system that has an additional state $|\mathrm{a}\rangle$ (Fig 2.11) with energy ω_{a} relative to the ground state $|\mathrm{g}\rangle$. We'll also add an additional driving field $\varepsilon_{\mathrm{C}}\cos(\mathbf{k}_{\mathrm{C}}\cdot\mathbf{r} - \omega_{\mathrm{C}}t)$ with electric field amplitude ε_{C} and frequency ω_{C} ($k_{\mathrm{C}} = \omega/c$), and introduce coupling to the environmental modes allowing decay of state $|\mathrm{e}\rangle$ with rates Γ_{g}, Γ_{a} (Fig 2.11). The additional state is easily incorporated into the Hamiltonian, expressed in the $\{|\mathrm{g}\rangle, |\mathrm{e}\rangle, |\mathrm{a}\rangle\}$ basis as

$$\mathscr{H}_{\mathrm{RWA}} = \begin{pmatrix} 0 & \Omega/2 & 0 \\ \Omega/2 & -\Delta & \Omega_{\mathrm{c}}/2 \\ 0 & \Omega_{\mathrm{c}}/2 & -\Delta_{\mathrm{C}} \end{pmatrix}, \tag{2.33}$$

[4]For simple cases like this, it is possible to choose a coordinate system such that the Hamiltonian is a time-independent. In more complicated cases when this is not true, one has to use a Floquet basis, which is for time-periodic differential analogous to Bloch waves for spatially periodic differential equations.

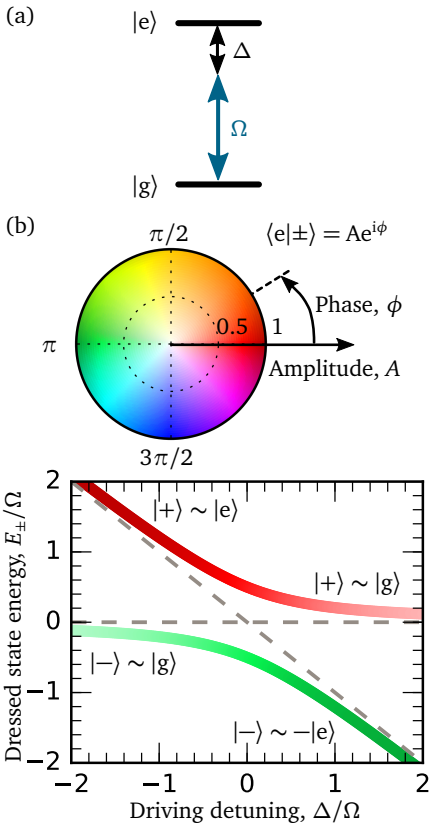

Figure 2.10: State composition and relative phase of dressed states. (a) Two-level system driven by driving field with Rabi frequency Ω, detuned Δ from transition. (b) Dressed states $|\pm\rangle$ are eigenstates of driving Hamiltonian (Eq. 2.32). Colour wheel maps amplitude and phase, relative to the ground state, of the excited state admixture.

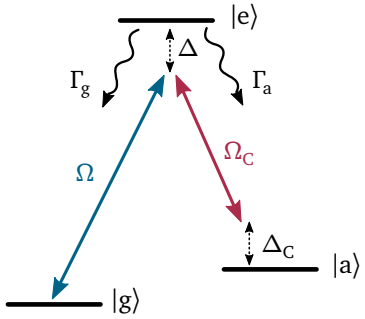

Figure 2.11: Energy level diagram of a considered three state system. Two long-lived states $|\mathrm{g}\rangle$ and $|\mathrm{a}\rangle$ are coupled via decaying state $|\mathrm{e}\rangle$ with two fields with the Rabi frequencies Ω and Ω_{C} that have corresponding one- and two-photon detunings of Δ and Δ_{C} respectively.

where $\Omega_c = \langle a|e\hat{r}\cdot\varepsilon|e\rangle$ is a second (control) field Rabi frequency, and $\Delta_C \equiv \omega_L - \omega_C - (\mathbf{k}-\mathbf{k}_C)\cdot\mathbf{v} - \omega_a$ is the two-photon detuning of the control driving laser. For the moment, we will neglect decays, and analyse dynamics only as governed by $\mathscr{H}_{RWA}$ [Eq. (2.33)]. A particularly clean solution is obtained for resonant driving $\Delta = \Delta_C = 0$, when we obtain three eigenstates, one of them completely decoupled from the time-evolution under the applied Hamiltonian $\mathscr{H}_{RWA}|D\rangle = 0$,

$$|D\rangle = (\Omega_C\,|g\rangle - \Omega\,|a\rangle)\,/\sqrt{\Omega^2+\Omega_C^2}. \tag{2.34}$$

Since this state $|D\rangle$ doesn't contain a contribution from state $|e\rangle$ that can decay, adding dissipation Γ_g, Γ_a doesn't have an effect on it. This dissipation-less state is called a *dark state*. Intuitive understanding can be obtained if we look at the probability amplitude redistribution in the small time δt due to evolution under $\mathscr{H}_{RWA}$. Amplitudes of the two bare states are adjusted such that their driving will map exactly the same amount $\Omega\delta t\ \Omega_C = \Omega_C\delta t\ \Omega$ of their state amplitude to the probability amplitude of the bright state $|e\rangle$, however their well-defined, opposite phases will interfere destructively, preventing change of the state $|e\rangle$ population. An interesting case is also the limit of $\Omega_C \gg \Omega$, when $|D\rangle \to |g\rangle$. Diagonalizing only part of the Hamiltonian, keeping the upper left corner corresponding to the $|g\rangle$ state unchanged (*semi-dressed picture*), we find two eigenstates $|\pm\rangle = (|e\rangle \pm |a\rangle)/\sqrt{2}$ in analogy to the previously discussed two-level system. Depending which one of the $|\pm\rangle$ states we couple to with the field Ω, the probability amplitude for $|a\rangle$ will pick phase of 0 or π with respect to $|e\rangle$, producing opposite phases for probability amplitudes of state $|a\rangle$. We will see direct consequences of this in Chapter 3. This also implies that for weak dressing $\Omega_C \ll \Gamma_a, \Gamma_g$, when we can *simultaneously* couple to $|a\rangle$ over both $|\pm\rangle$ states, these two excitation paths will interfere destructively and state $|a\rangle$ will not be excited.

To account for spontaneous decay of state $|e\rangle$ we have to include mixed states in our description by analysing the evolution of the system's density matrix $\hat{\rho}$. The evolution equations can be obtained by calculating the evolution of both system and environment that, starting from an initial state $\rho_{system}\bigotimes\rho_{env}$, becomes entangled over time due to coupling of the system to the environment. Tracing over environmental degrees of freedom, and assuming the that environment has short memory[5], we obtain the following master equation for the time evolution of the density matrix

$$\frac{d\hat{\rho}}{dt} = \underbrace{-i[\mathscr{H}_{RWA},\hat{\rho}] + L[\hat{\rho}]}_{\equiv\mathscr{L}[\hat{\rho}]}, \tag{2.35}$$

where $L[\hat{\rho}] = \sum_\alpha (L_\alpha\hat{\rho}L_\alpha^\dagger - \frac{1}{2}L_\alpha^\dagger L_\alpha\hat{\rho} - \frac{1}{2}\hat{\rho}L_\alpha^\dagger L_\alpha)$ is the *Lindblad superoperator*, where the terms $L_0 = \sqrt{\Gamma_g}|g\rangle\langle e|$, $L_1 = \sqrt{\Gamma_a}|a\rangle\langle e|$ describe decay of the state $|e\rangle$. This can also be seen as the action of the *Liouville superoperator* $\mathscr{L}[\ldots]$ on the system density matrix. We can formally solve Eq. (2.35) as $\rho(t) = \exp(\mathscr{L}t)\rho(0)$. Complex eigenvalues Λ_i of $\mathscr{L}$ determine accumulated phase $\mathrm{Im}(\Lambda_i)t$ during evolution time t, and decay of eigen-vectors with rate $-\mathrm{Re}(\Lambda_i)$ as the system reaches steady state whose eigen-value is zero.

It is of practical importance to explore time scale on which steady states, like

[5] Environment has very short correlation time, i.e. it is Markovian; in our case "very short" means that photons leave local environment (from where they can be reabsorbed) on much faster time-scale then atom-field coupling strength.

the dark state described in the specific case by Eq. (2.34), are reached. If one considers atoms flying into, and out of the driving field, as in the case of a laser beam in thermal vapour, atoms initially in the ground state will in general have only partial overlap with the dark state $|\langle g|D\rangle|^2 \neq 1$. Therefore, initially atoms will absorb light, and the dark state will be eventually populated through stochastic decay (fluorescence) of bright states, with atomic population being optically pumped to the dark state. The time scale for this pumping to happen depends on the overlap of initial and dark states, decay rates and Rabi driving strengths. If it is longer than the average atom transit time through the driving field, e.g. when using narrowly focused laser beams, increased probe *absorption* will be observed in the probe transmission signal even with the laser on resonance for the EIT peak [162], because this transient atomic evolution happens on time-scale comparable to the atom transit time through the beam. An effective way to account for the finite transit time through the driving region in the formalism above, is to introduce additional Lindblad operators $L_{\tau,\beta} = \sqrt{1/\tau}|g\rangle\langle\beta|$ producing decay of all the excited states $|\beta\rangle$ to the ground state with rates corresponding to the average transit time τ. An alternative way of dark states creation that doesn't rely on dissipation is by employing a time-changing Hamiltonian, where one starts with a dark state that matches the initial state of the atoms $|D\rangle = |g\rangle$. This corresponds to $\Omega_c \gg \Omega_p$ in the previously discussed three level scheme. With this Hamiltonian change, the dark state is adiabatically changed to some other state-composition, preparing the system state deterministically in principle. This will be discussed further in Sec. (2.6).

A steady state solution for the considered three level system (Eq. 2.33) evolved under Eq. (2.35) can be found as a steady-state density matrix ρ. As we have seen in Sec. 2.3.4, the real and imaginary parts of coherences in the weak probe regime, are directly proportional to the real and imaginary parts of the susceptibility for the probe field (Eq. 2.19), which is shown on Fig. 2.12. Strong dressing ($\Omega_C = 4\Gamma$) splits the resonance into two, in the so-called *Autler-Townes splitting*. For $\Omega_C \lesssim \Gamma$, we see more than just a split transition: we see the *interference* between the two resonances. The dashed line shows the expected excitation profile if this were just two levels spaced by Ω_C. We can clearly see that well defined relative phase for two excitation paths in the coherent driving scheme causes significant change. The highly dispersive properties of an atomic medium within the EIT window cause slow group velocities for probe propagation. This, in combination with adiabatic (Sec. 2.6) changing of Ω_C, allowed slowing down and stopping of light in experiments [163, 164].

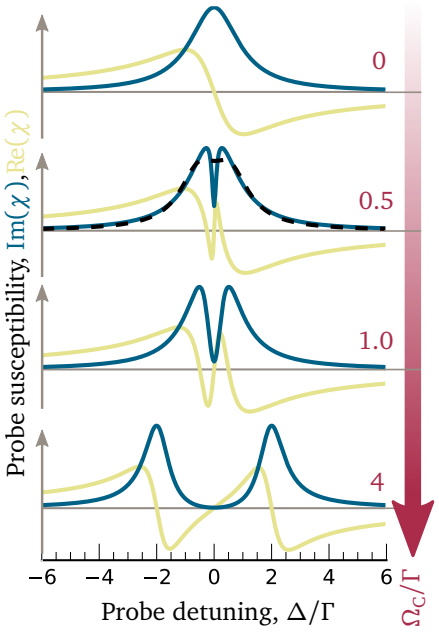

Figure 2.12: Electromagnetically induced transparency and Autler-Townes splitting. The dashed line for $\Omega_C = 0.5\ \Gamma$ is the best fit of two Lorentzians centred at $\Delta = \pm\Omega_C/2$. The discrepancy between that fit and the full calculation highlights the importance of interference between two dressed levels for obtaining a narrow EIT window. Parameters: $\Omega_p = \Gamma/100$, $\tau = 20\ \Gamma^{-1}$. The scale for all plots is the same, absolute y-scale depends on atom number density in the medium.

2.5 Two and more atoms

Up to now we have been focusing on properties of single, isolated atoms. Now we will consider what happens when two atoms are close to each other, and see how we can analyse level shifts and other changes that occur then. Insights into this will help us understand collisional processes and additional effects that can occur when many-body systems are driven.

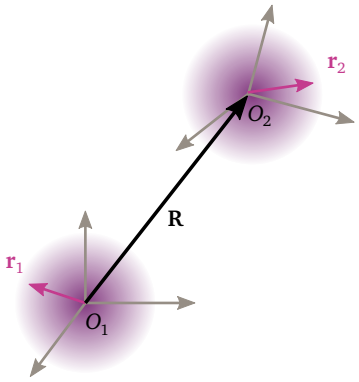

Figure 2.13: Two charge distributions (violet). Grey lines indicate two arbitrarily oriented coordinate systems used for description of the two charge distributions.

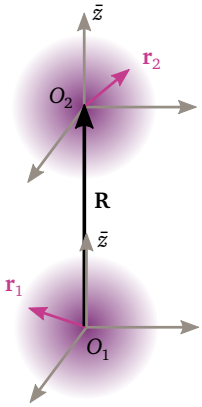

Figure 2.14: Particular orientation of two coordinate systems centred at O_1 and O_2 (grey). For this orientation inter-particle interactions can be expanded in a simple form (Eq. 2.38).

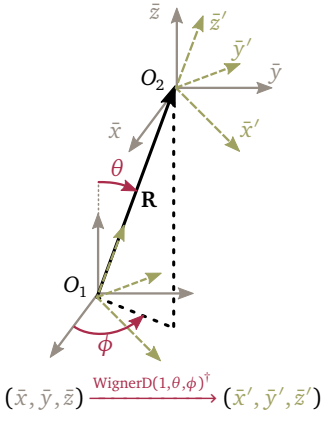

Figure 2.15: Changing the coordinate system. Application of WignerD matrix rotates states, expressed initially in two arbitrary parallel coordinate systems defined by unit-vectors $(\bar{x},\bar{y},\bar{z})$ (solid grey), giving their components in new basis $(\bar{x}',\bar{y}',\bar{z}')$ (dashed yellow) where atoms are separated along $\bar{z}'$-axis. This reduces calculations for the general case of atomic orientation, with states given in parallel coordinate systems, to the case shown on Fig. 2.14.

2.5.1 Interactions

For two atoms separated by a distance R, when $kR \ll 1$, where k is the wave vector of the possible radiative fields originating from each of these atoms, inter-atomic interactions can be calculated based on electrostatic interactions between the two atomic charge distributions [165], neglecting the retardation effects. Consider two charge distributions (Fig 2.13), each with total charge of one (e), indexed with $i = 1, 2$, with respective centres of gravity O_1 and O_2 separated by $\mathbf{R} > 0$ so that they are not overlapping. If $\mathbf{r}_i$ measures location of the charge with respect to the origin O_i then the potential due to charge distribution $i = 1$ at location $\mathbf{R}$ can be expanded (Laplace expansion) in terms of spherical harmonics

$$\phi(R) = \frac{1}{|\mathbf{R}-\mathbf{r}_1|} = 4\pi \sum_{L_1=0}^{\infty} \frac{r_1^{L_1}}{(2L_1+1)R^{L_1+1}} \sum_{m=-L_1}^{+L_1} Y^*_{L_1,m}(\bar{\mathbf{r}}_1) Y_{L_1,m}(\bar{\mathbf{R}}). \tag{2.36}$$

The interaction potential between the charges $V = r_2\phi(\mathbf{R}+\mathbf{r_1})$ can be expanded [166], in the case of non-overlapping charges $r_1 + r_2 < R$, in Taylor series

$$V(R) = \sum_{L_1,L_2=1}^{\infty} \frac{V_{L_1,L_2}(\mathbf{r}_1,\mathbf{r}_2)}{R^{L_1+L_2+1}}, \tag{2.37}$$

where $L_1 + L_2 = 2, 3, 4$ corresponds respectively to dipole-dipole, dipole-quadrupole and quadrupole-quadrupole coupling. In the case when the coordinate systems at O_1 and O_2 are parallel (Fig. 2.14), and displaced with respect to each other along the z axis, i.e. $\mathbf{R} = R\bar{z}$, the form of V_{L_1,L_2} is especially simple [165]

$$V_{L_1,L_2} = \frac{(-1)^{L_2}4\pi}{\sqrt{(2L_1+1)(2L_2+1)}} \cdot \sum_{m=-L_<}^{L_<} \sqrt{\binom{L_1+L_2}{L_1+m}\binom{L_1+L_2}{L_2+m}}\, r_1^{L_1} Y_{L_1,m}(\bar{\mathbf{r}}_1)\, r_2^{L_2} Y_{L_2,m}(\bar{\mathbf{r}}_2), \tag{2.38}$$

where $L_< \equiv \min(L_1, L_2)$ and the $\binom{n}{k} = n!/[k!(n-k)!]$ are binomial coefficients. States and energies of two interacting atoms can be then calculated by considering the Hamiltonian for two interacting atoms $\mathscr{H} = \sum_{i=1,2} \hat{H}_0^{(i)} + \hat{V}$, where $\hat{H}_0^{(i)}$ are uncoupled, single-atom Hamiltonians. A suitable basis is the one formed from linear combinations of atomic eigenstates in the fine-splitting regime $\{|n_1,\ell_1,j_1,m_{j_1},n_2,\ell_2,j_2,m_{j_2}\rangle,\ldots\}$. Matrix elements that occur in calculations of the form $\langle n_1',\ell_1',j_1',m_{j_1}'|\hat{r}_1^L Y_{L_1,m}(\hat{\theta},\hat{\phi})|n_1,\ell_1,j_1,m_{j_1}\rangle$ can be then calculated in the same fashion as Eq. (2.12). In practice, it is often convenient to think about the system in the basis where quantization axis $\bar{z}$ points in the direction of the applied external magnetic or electric field, or where $\bar{z}$ is directed in the plane of the electric field, perpendicularly to the linearly polarised EM field, or along the propagation direction of the drive field, for a circularly polarised EM field. The general orientation $\mathbf{R}$ of the two atoms in such a coordinate system, can be described with the polar and azimuth angles θ and ϕ (see Fig. 2.15). We can reduce this general case to the $(\theta = 0, \phi = 0)$ case, for which V_{L_1,L_2} has a simple form [Eq. (2.38)], by rotating the coordinate system. This is done by applying Wigner-D matrices

WignerD$(j_1,\theta,\phi)\bigotimes$WignerD$(j_2,\theta,\phi)$ to states expressed in the original pair-state basis, to obtain state-vectors in the rotated pair-state basis (Fig. 2.15), with $\bar{z}'$ direction oriented along **R**. As mentioned above, this multipole expansion analysis is correct as long as charges don't overlap. This starts to happen below the so called Le Roy radius [167], which can be calculated from the knowledge of the wavefunctions Eq.(2.7) as $R_{\rm LR} = 2(\langle\hat{r}_1^2\rangle^{1/2} + \langle\hat{r}_2^2\rangle^{1/2})$. This can be calculated in ARC by calling the `getLeRoyRadius` method of `PairStateInteractions`. For example, the Le Roy radius for two Caesium atoms in n S state is ~ 0.1 μm for $n \sim 20$, and reaches 1 μm for $n \sim 60$, marking minimum inter-atomic distance for this interaction calculation is valid.

Before we proceed in analysing a realistic case, let's discuss a simple system of two two-state atoms, where the pair state[6] $|r_1, r_2\rangle$ interacts via a potential V with the pair state $|r_1', r_2'\rangle$ whose relative energy difference (energy defect) is $\Delta \equiv E(r_1', r_2') - E(r_1, r_2)$. In the $\{|r_1, r_2\rangle, |r_1', r_2'\rangle\}$ pair-state basis the interaction Hamiltonian is

$$\mathscr{H} = \begin{pmatrix} 0 & V \\ V & \Delta \end{pmatrix}. \tag{2.39}$$

The eigenenergies of the system are $E_\pm(R) = (\Delta \pm \sqrt{\Delta^2 + 4V(R)^2})/2$. Let's also assume that the states $r_1 \longleftrightarrow r_1'$ and $r_2 \longleftrightarrow r_2'$ are dipole coupled in which case the interaction potential has the form $V = C_3/R^3$, where C_3 is constant for a given pair-state combination and atom orientation. In this case at short distances $R \ll R_{\rm vdW}$, the energy shift of the states will be $\propto C_3/R^3$, which is long-range in 3-dimensional systems since it decays with the same power-law as the system dimension. At long distances $R \gg R_{\rm vdW}$ the potential has the short-range form of $\sim -C_6/R^6$, where $C_6 = C_3^2/\Delta$. The cross-over distance is the van der Waals radius $R_{\rm vdW} \equiv \sqrt[3]{|C_3/\Delta|}$ at which $V(R_{\rm vdW}) = \Delta$. This cross-over distance can be changed by adjusting Δ, which can be done by external fields [see Sec. (2.5.3)] for example. One special case of interest is when $\Delta = 0$, which occurs when $r_1 = r_2'$ and $r_2 = r_1'$. In this case, two atoms initially in state $|r_1, r_2\rangle$ will oscillate between this state and $|r_2, r_1\rangle$ with frequency set by V.

In realistic situations at long inter-atomic separations, when there are no single resonantly coupled states, there are many pair-states $|r_1', r_2'\rangle$ with energy defects Δ'. The level shift of the initial state at long-distances R, $V(R) \ll$ Min$[\Delta']$, can be calculated in the second-order perturbation. Typically the dominant contribution is from dipole-coupled pair-states, causing an interaction shift of $-C_6/R^6$, where

$$C_6 = \sum_{r_1', r_2'} \frac{\left|\langle r_1' r_2' | V(R) | r_1 r_2\rangle\right|^2}{\Delta'}. \tag{2.40}$$

For Eq. (2.40) to converge, only pair-states with small energy defect $|\Delta'| < \Delta$ and strongly coupled states ($|n_1 - n_1'| < \delta n, |n_2 - n_2'| < \delta n$) have to be included, where typically Δ is several $h \cdot 10$ GHz, and $\delta n \sim 5$. All calculations of pair-state interactions are implemented in ARC class `PairStateInteractions` and a perturbative calculation of C_6 is implemented as `getC6perturbatively`. This can be used for example to calculate C_6 for various orientations of interatomic axis **R** with respect to the quantization z-axis, illustrating the anisotropy of interactions (Fig. 2.16).

[6] We've introduced r as short hand notation for n, ℓ, j, m_j.

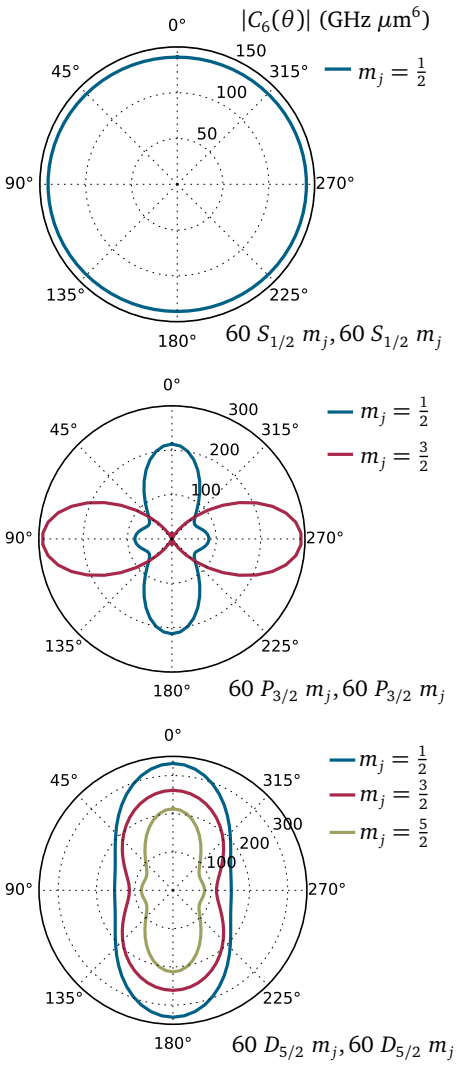

Figure 2.16: Anisotropy of van der Waals interactions. Calculated for rubidium $n = 60$ $\ell = S, P, D$ states

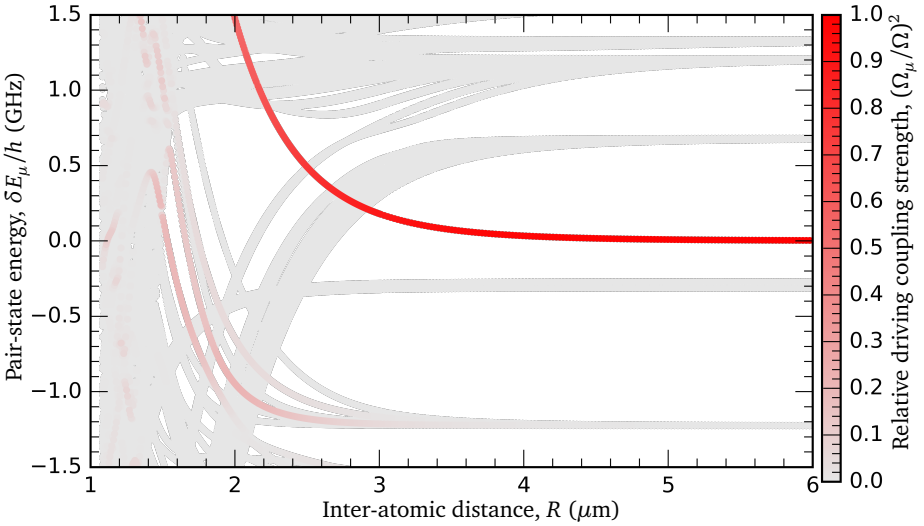

Figure 2.17: Pair-state energies obtained by diagonalising the interaction Hamiltonian. Pair-state energies δE_μ relative to the the unperturbed rubidium target $|60\,S_{1/2}\,1/2, 60\,S_{1/2}\,1/2\rangle$, pair-state. Highlighting is done based on the coupling of pair states $|\mu\rangle$, obtained in diagonalising the interaction Hamiltonian, to the state where one of the atoms is already in the target state and the other atom is in $|5P_{3/2}\,3/2\rangle$ state, with driving field coupling to the σ^- transition (set by `drivingFromState` argument in ARC), $\Omega_\mu = \langle\mu|e\mathbf{r}\cdot\varepsilon_q|60\,S_{1/2}\,1/2, 5\,P_{3/2}\,3/2\rangle + \langle\mu|e\mathbf{r}\cdot\varepsilon_q|5\,P_{3/2}\,3/2, 60\,S_{1/2}\,1/2\rangle$, $q=-1$. This driving field coupling is normalised with coupling Ω to the maximally coupled state, which in this case is the target state.

For short inter-atomic separations, down to the minimum distance given by the Le Roy radius $R_{\rm LR}$, it is necessary to do numeric diagonalization of the Hamiltonian $\mathscr{H} = \sum_{i=0,1}\hat{H}_{0,i} + \hat{V}(R)$ in the pair-state basis for all interatomic distances R of interest. The basis considerations are the same as for the perturbative calculations, except that now we will be including higher order orbital angular momentum states $\ell = 0,\ldots,\ell_{\rm max}$, due to the strong admixing of states. Typically, for calculation of S state interactions we include $\ell_{\rm max}\sim 4$. For each distance R we find only $n_{\rm eig}$ eigenstates with eigenenergies closest to the set pair-state energy (relative to the initial pair-state) by using an efficient ARPACK [168] routine through a Numpy [169] interface.

An example of calculations obtained by diagonalizing $\mathscr{H}$ in the basis of ~ 2300 states in this way is shown in Fig. 2.17. By default, only dipole-dipole interactions are included in $V(R)$, but interactions up to the quadrupole-quadrupole term [up to $L_1+L_2\leq 4$ in Eq. (2.38)] can be turned on by setting the optional parameter `interactionsUpTo=2` during the initialization of `PairStateInteractions`. Quadrupole couplings can be important for short-distance structure of the level diagrams [88, 170], where they can affect the formation of short-range potential wells, which can supporting bound states [74]. Similarly to the Stark maps, default state colour highlighting is done proportionally to the contribution of the original state in the obtained eigenstates. Specifying the optional argument `drivingFromState` can again be used to obtain highlighting relative to the dipole coupling strength from a pair state where one of the atoms is already in the target state, and the other is in the state given in the `drivingFromState` argument. On a computer, obtained level diagrams can be explored in the form of interactive graphs, showing contribution of different states, which is non-trivial and experimentally important information due to strong state admixing.

After diagonalization, C_3 and C_6 interaction coefficients can be obtained by fitting of the energy level shifts, which is done in the methods `getC3fromLevelDiagram` and `getC6fromLevelDiagram` respectively. They will perform a fit to the eigenenergies of the state that contains the largest admixture of the target state. A method `getVdwFromLevelDiagram` for finding a cross-over distance between van der Waals and resonant dipole-dipole interactions, i.e. van der Waals radius $R_{\rm vdW}$ is also provided. As can be seen in Fig. 2.18 even after including the full pair-state interac-

ARC NOTE: `drivingFromState` is an array $[n,\ell,j,m_j,q]$, where n,ℓ,j,m_j specifies the state, and the q specifies the transition that is driven by the external field, with $q=-1,0,1$ corresponding to σ^-, π and σ^+ transitions.

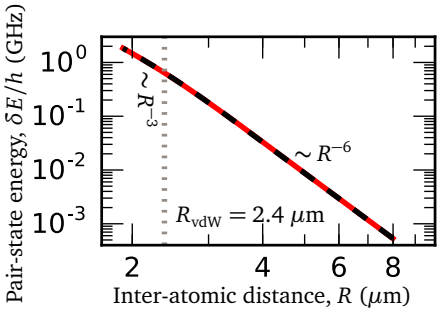

Figure 2.18: Cross-over between $\sim R^{-3}$ and $\sim R^{-6}$ interactions. Pair-state energy obtained from the interaction diagonalization (solid red) is fitted to the simple potential obtained from simplified Hamiltonian [Eq. (2.39)] (dashed black). The cross-over distance is given by the van der Waals radius $R_{\rm vdW}$ (vertical dotted line).

tion potential, we obtain the $E_{\pm}(R)$ function from the simplified model discussed before. This will be one reason for choosing a particular form of model interaction potential in Chapter 4.

2.5.2 Discussion of features: blocking and facilitating dynamics

We will now highlight several features seen in Fig. 2.17. For resonant laser excitation $\Delta = 0$, we see that the probability for excitation of the two atoms into the Rydberg state rapidly changes once the interatomic distance R goes below the so-called *blockade radius* $R_B \equiv \sqrt[6]{C_6/\Gamma}$. For simple resonant excitation of the Rydberg states, $\Gamma = \Gamma_{\text{state}} + \Gamma_{\text{drive}}$ is a combination of laser linewidth Γ_{drive} and natural linewidth Γ_{state} due to the state decay. In the presence of a single Rydberg excitation, below the blockade radius, the driving laser is effectively decoupled from the Rydberg state of the other atom, and no additional Rydberg excitations will be formed. In the limit of strong driving of atomic ensembles, this causes saturation of resonant excitation [171] of the Rydberg states, setting a limit on the maximum number of closely packed Rydberg atoms. As a consequence of this, fluctuations of the number of excitations[7] will be reduced compared to the situation of individually excited non-interacting atoms [172]. A strong blockade can also be used for preparation of symmetric collective excitations [67, 84], where atoms are in a coherent superposition where only one of them is excited. Finally note that in this case, although C_6 is typically anisotropic (Fig. 2.16), due to the rapid level shift $\propto R^{-6}$, the blockade is still spherical to a very good approximation, as long as C_6 doesn't cross zero for a particular angle. The other important case of the blockade occurs when the Rydberg state is used as a second stable state, to open an electromagnetically induced transparency window. In this case, Γ will be determined by the width of the EIT window. For vanishing control field, in the limit of an infinitely long-lived Rydberg state, this will be determined by finite combined laser linewidth (as discussed in Sec. 2.3.3) and motional induced dephasing (to be discussed in Chapter 3). For atoms closer than the blockade radius under EIT conditions, the presence of a single Rydberg excitation will decouple the Rydberg level of the other atom from the control field, destroying the EIT condition for that atom and causing probe absorption [66].

For off-resonant Rydberg excitation $\Delta \neq 0$ we see that the presence of a single Rydberg state excitation can increase the probability of exciting another atom. For example on Fig. 2.17 for $\Delta > 0$ at the so called facilitation radius $R_\Delta \equiv \sqrt[6]{\Delta/C_6}$, the laser will be resonant with the pair-state that corresponds to the two-Rydberg excitation at a distance R_Δ. This marks in space around a single Rydberg excitation a spherical shell of radius R_Δ and thickness $\delta R_\Delta \approx \Gamma\, R_\Delta^7/(6\, C_6)$, determined by the linewidth of transition Γ, in which there is a high probability of exciting another atom. Note that this shell can be very thin. For example in the Rb 60 $S_{1/2}$ pair-state, for detuning of $\Delta = 2\pi \times 200$ MHz ($2\pi \times 20$ MHz), even a relatively broad transition of $\Gamma = 2\pi \times 3$ MHz will result in shell thickness of only ~ 7 nm (0.3 μm). In thermal atomic vapours (see Sec. 2.8) at room temperature atoms traverse this distance in only 0.04 ns (1 ns), which means that typically effective dephasing due to a time-dependant level shift will be relatively big $\sim 1-10$ GHz. Even if one includes

[7] usually expressed through Mandel-Q parameter $Q \equiv \frac{\langle N_e^2\rangle - \langle N_e\rangle^2}{\langle N_e\rangle} - 1$, where N_e is the number of excitations, and angle brackets indicate averaging over experimental or simulation runs. For resonant excitation of the Rydberg gas the variance of the number of excitations N_e is sub-Poissonian $Q < 0$.

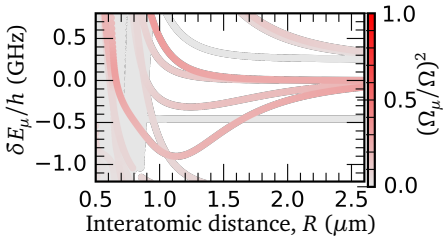

Figure 2.19: Avoided crossings create potential wells in pair-state interaction energies. Pair-state energies relative to the $|43P_{3/2}m_j = 1/2, 43P_{3/2}m_j = 1/2\rangle$ pair-state energy in rubidium with highlighting corresponding to driving π transitions from $5\,S_{1/2}m_j = 1/2$ state. Based on figure 1. in Ref. [75]. Labels are the same as in Fig. 2.17.

Doppler broadening by setting $\Gamma \sim 2\pi \times 300$ MHz, facilitation sphere thickness averaged over all the thermal velocity classes would be still about 0.9 μm. Note that full pair-state diagonalization reveals that, due to strong state admixing, there can be additional states in the blockade region that are coupled to the driving field [173], as can be seen in Fig. 2.17 at distance $R \approx 1.5$ μm. However, these states are usually weakly coupled and, more importantly, the thickness of the facilitation sphere they create will be much smaller, as it occurs at $R < R_\Delta$ while facilitation sphere thickness scales[8] with radius at which occurs as R^7. Therefore additional resonances are usually orders of magnitude smaller [99].

One particular case when the facilitation due to additional resonances is more prominent is the case of avoided crossings. An example is the avoided crossing that occurs around $(\Delta E/h, R) \approx$(500 MHz,1.5 μm) on Fig. 2.17 in the blockaded region. An avoided crossing will make the facilitation sphere thicker for that particular detuning, resulting in a clearly observable peak in excitation [170, 174]. Some of these resonances are deep enough to support bound states [175]. Avoided crossings can also cause potential wells like the one on Fig 2.19, that can be used for control of interactions e.g. in state dressing approaches [75], since they can increase coupling in well-defined intervals of inter-atomic distances, again effectively acting as thick facilitation spheres.

Finally, we note that when facilitation occurs due to *attractive* interactions, it opens a loss mechanism. This is because an off-resonant laser will now excite strongly attractive pairs of atoms that will move into the regions of dense pair-state and strong mixing, where state redistribution and ionization can happen. This is true even for low-lying states, where it is responsible for *light-assisted collisions* [176, 177].

2.5.3 Tuning of interaction potentials

Stark tuned Förster resonances

The energy defects of the pair-states Δ control the distance R_{vdW} at which cross-over between long-range, resonant dipole-dipole $V(R) \sim R^{-3}$ and off-resonant dipole-dipole (i.e. van der Waals) interactions will occur, as discussed earlier in Sec. (2.5.1). Static external electric fields can be used to offset pair-state energies via induced Stark shifts [Sec. (2.4.1)]. The special case when a given pair of dipole-dipole coupled pair-states has negligible energy defect $\Delta/V(R) \to 0$ is called a Förster resonance, and corresponds to the case when resonant long-range interactions ($\propto R^{-3}$) are obtained [71, 178–182].

Finding resonant states and values of electric field for which these resonances occur can be done with the `StarkMapResonances` class of ARC. It takes as initialization arguments two atom types[9], their initial target states, and energy window, and then performs a Stark map calculation in the pair-state basis. Since pair-state interactions $V(R)$ [Eq. (2.38)] can couple target pair-state to states that differ in projection of total angular momentum by $\Delta m_j = 0, \pm 1$, it is necessary to calculate Stark maps for up to nine different manifolds corresponding to all possible combinations (m'_{j1}, m'_{j2}) for dipole-coupled states. After diagonalization, only pair states which are in the

[8] This analysis assumes that C_6 for all states is of the similar order of magnitude for all dipole coupled states, which is usually true.

[9] Atom types can be different to allow for heterogeneous mixtures of atoms.

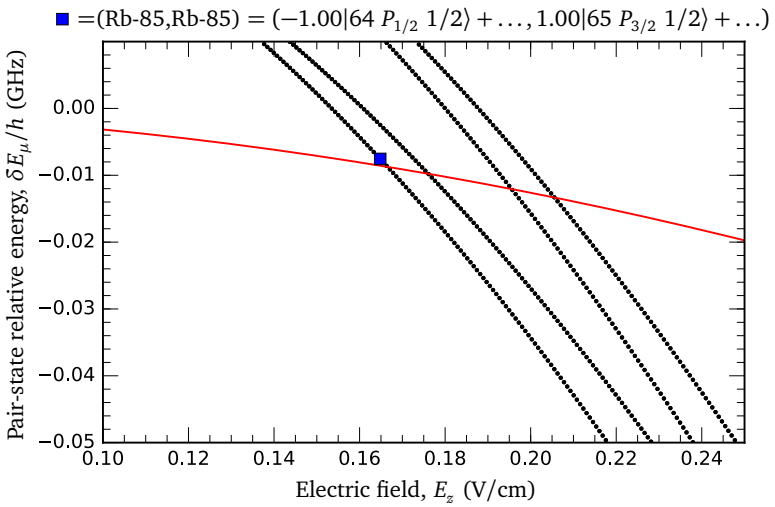

Figure 2.20: Automatic search for Förster resonance. ARC automatically searches within a set range of electric fields and pair-state energies for resonances with the given pair-state. An example calculation here shows pair-state energies relative to the unperturbed pair-state $|66\ S_{1/2}\ m_j = 1/2, 64\ S_{1/2}\ m_j = 1/2\rangle$ of two rubidium-85 atoms. This pair-state (solid red) in electric-field $E_z \approx 0.165$ V/cm becomes resonant with another Stark-shifted state. In interactive use of ARC users can select resonant states to see their composition, here shown marked by a blue square, that corresponds to an almost pure $|64\ P_{1/2}\ m_j = 1/2, 65\ P_{3/2}\ m_j = 1/2\rangle$ pair-state. These resonances have been detected in Ref. [71].

specified energy window are considered, discarding the pair-states that are not dipole coupled. Since electric field leads to strong admixing of basis pair-states, the algorithm identifies states as dipole coupled if the basis state with dominant contribution in the obtained eigen-state is coupled to the target pair-state provided in the initialization. That pair-state is also admixed by the electric field, but can be found as the state with the largest initial state fraction. Finally the interactive routine allows users to select states, see plots with resonances, and identify state composition (Fig. 2.20).

Dressing

Coupling of states with AC fields, discussed in the single atom context in Sec. (2.4.3), can be used for tuning pair-state interaction potentials. In this context, we can highlight two distinct cases of off-resonant dressing and resonant dressing.

Off-resonant dressing can be used to admix the Rydberg state into the ground state, introducing interactions between new ground eigenstates [183]. A driving field with Rabi frequency Ω tuned $\Delta \gg \Omega$ off-resonance from the $|g\rangle \leftrightarrow |r\rangle$ resonance, acting on a single atom, gives rise to a ground eigen-state $|\tilde{g}\rangle \sim |g\rangle + \varepsilon|r\rangle$, where $\varepsilon = \Omega/(2\Delta)$ is the admixture of the Rydberg state $|r\rangle$. This admixing causes the usual AC Stark shift [Sec. (2.4.3)], given here for red-detuned driving ($\Delta < 0$) as

$$\delta_{\mathrm{AC}} = \frac{-\Delta - \sqrt{\Delta^2 + \Omega^2}}{2}. \tag{2.41}$$

Note that even when the admixed Rydberg state has a finite lifetime τ_r, it has a small impact on the ground eigen-state lifetime $\tau_{\tilde{g}} = \varepsilon^2 \tau_r$, as typically $\varepsilon \ll 1$.

Interactions between the Rydberg states will cause changes to this AC Stark shift. For example, this can be easily calculated in the simple case of two two-level atoms interacting with van der Waals interactions $V = -C_6/R^6$ [Fig. 2.21(a)]. The system Hamiltonian in the pair-state basis $\{|g,g\rangle, |r,g\rangle, |g,r\rangle, |r,r\rangle\}$ is ($h = 1$, RWA)

$$\mathscr{H} = \begin{pmatrix} 0 & \Omega/2 & \Omega/2 & 0 \\ \Omega/2 & -\Delta & 0 & \Omega/2 \\ \Omega/2 & 0 & -\Delta & \Omega/2 \\ 0 & \Omega/2 & \Omega/2 & -(2\Delta - V) \end{pmatrix}. \tag{2.42}$$

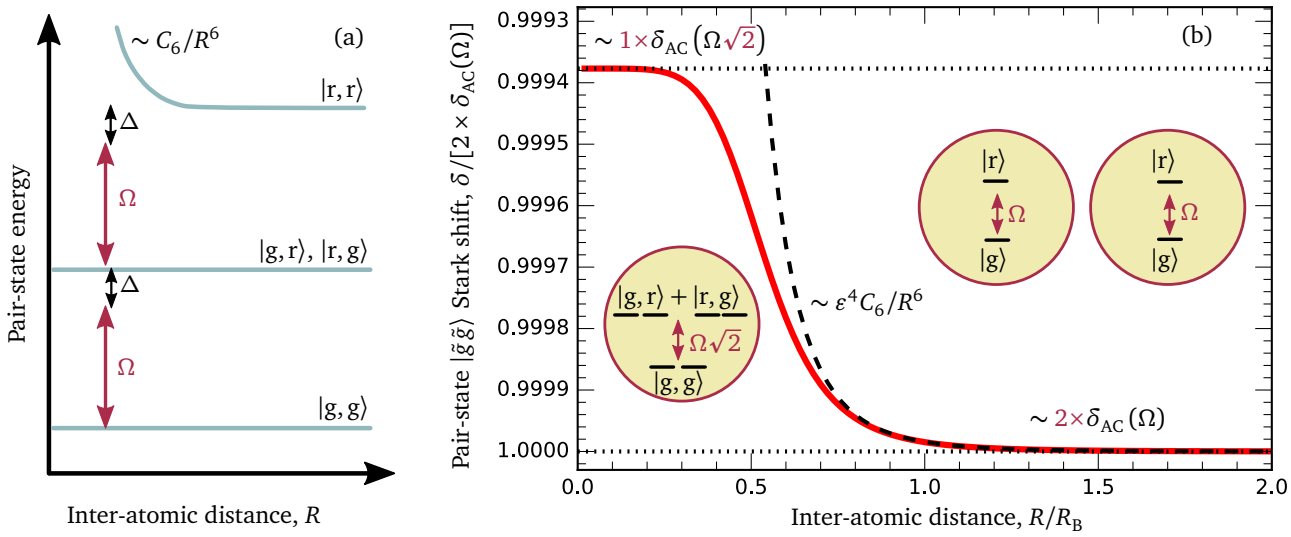

Figure 2.21: Effective potential between ground-state atoms due to Rydberg state admixing in off-resonant dressing. (a) Pair-state energy diagram where two ground $|g\rangle$ state atoms at distance R are dressed by Δ off-resonant field with Rabi frequency Ω that admixes Rydberg state $|r\rangle$ into new ground eigen-state $|\tilde{g}\rangle \sim |g\rangle + \varepsilon|r\rangle$. Rydberg states are interacting with van der Waals interactions C_6/R^6. The new ground pair-state will have AC Stark shift $\delta = E(\tilde{g},\tilde{g}) - E(g,g)$ relative to the unperturbed ground-state [solid red (b)]. At large distances $R \gg R_B \equiv \sqrt[6]{|C_6|/\Omega}$ AC Stark shift approaches Stark shift value $2\times\delta_{AC}(\Omega)$ (dotted line) for two independently dressed atoms [(b) right inset] with Rabi driving field Ω. Below $R \lesssim R_B$ atoms start feeling repulsive van der Waals interactions (dashed line), with interaction strength scaled down by ε^4, the probability that both atoms are simultaneously in the excited state. However, deeply in the blockaded region $R \ll R_B$ only one atom can be excited, at the same time we don't know which one. This limit can be seen as dressing of the superatom consisting of two atoms [(b) left inset], with enhanced driving $\Omega\times\sqrt{2}$ between ground and singly excited, symmetric collective state. Indeed the Stark shift δ saturates in this limit at value of a *single* superatom Stark shift $\delta_{AC}(\Omega\sqrt{2})$ (dotted line). Calculation parameters $\Delta = 20\,\Omega$.

Diagonalizing this Hamiltonian, we obtain the AC Stark shift of the $|\tilde{g},\tilde{g}\rangle$ pair-state, shown in Fig. 2.21(b). The effect of the interactions can be seen as an effective pair-state interaction soft-core potential $V_D(R)|\tilde{g}\tilde{g}\rangle\langle\tilde{g}\tilde{g}|$ whose amplitude is

$$\mathrm{Max}[V_D(R)] = 2\delta_{AC}(\Omega) - \delta_{AC}(\Omega\sqrt{2}) \approx \frac{\Omega^4}{8\Delta^3}. \tag{2.43}$$

More complex Rydberg level energies, arising e.g. due to avoided resonances (Fig. 2.19), can cause reduction of Δ over a range of inter-atomic distances R, leading to localised stronger dressing, as discussed in Ref. [75].

Dressing, both resonant and off-resonant, can also be done in the Rydberg state manifold with microwave and terahertz fields, where it can be exploited for fine-tuning of Rydberg interaction potentials [160, 161].

2.6 Adiabatic and non-adiabatic transitions

All discussion up to now was analysing static situations, where distances, laser drivings and other external fields don't change in time. Now we will consider what happens when that is not the case.

Almost all Hamiltonian eigenstates calculated so far actually change in time, for example because atoms move, changing the inter-atomic distance R and hence the underlying Hamiltonian over time. Also, time-dependant external fields are,

together with direct coherent driving and dissipative pumping mechanisms, one of the main practical ways of quantum state preparation and state manipulation. If the Hamiltonian changes slowly, so that the minimal gap between the energy of the selected state and the rest of the Hamiltonian eigenstates Δ is much bigger than the speed of the eigen-energy E change in time t such that $|\Delta|^2 \gg \hbar\, \mathrm{d}E/\mathrm{d}t$, the system state will stay in the instantaneous eigenstate. This is so-called *adiabatic following* [184]. This is the basic mechanism behind state preparation in STIRAP protocols, including many-body state preparation [76, 79] and adiabatic quantum computing [185]. For changes of the Hamiltonian in finite time, there will always be a "leakage" of system state from the instantaneous eigen-state to other states. For two-level systems, this is quantified through the Landau-Zener equation[186, 187] which states that a fraction $\exp[-2\pi|\Delta|^2/(\hbar\, \mathrm{d}E/\mathrm{d}t)]$ of the the state after transition will leak to the non-instantaneous eigenstate. This is the basic mechanism leading to collisional state redistributions of atomic population [188], including ionization [189, 190]. For example, Rydberg autoionization process in dense samples can be seen [138] as initial creation of ions and electrons in Rydberg-Rydberg collisions. For collisions to occur, mixing and non-adiabatic transfer has to occur, which requires two atoms to come close to the dense region of energy-levels, so-called energy-level "spaghetti" region, that occurs for example on Fig. 2.17 for $R < 2\ \mu$m. This distance scales typically as the Le Roy radius $\propto n_*^2$, making Rydberg-Rydberg and Rydberg-electron cross-sections $\propto n_*^4$.

2.7 Additional multi-atom effects

In the discussion so far we have had no more than two atoms. It is reasonable to ask whether knowing all two-atom processes allows for understanding processes in many-body systems, in a sense that they are just summations of the two level terms? While that is true in the case of an elementary Hamiltonian (Eq. 2.38), for some other concepts that we like to think about, like interaction-induced state level-shifts, that is not always the case. That can be important in writing effective Hamiltonians [191, 192]. For example, in the case of three atoms shown on Fig 2.22(a), it can be that dipole $\hat{V}$ (Eq. 2.37) allowed coupling $|pp\rangle \to |ss'\rangle$ is forbidden since the energy defect is too big $\Delta_2 = E(ss') - E(pp) \gg V$. Therefore the effective interaction Hamiltonian $\sum_{i<j} W_{ij}(R)|pp\rangle\langle pp|$ could be written as two atoms in state p interacting via the second-order term giving rise to van der Waals interactions $W_{ij} = -V(R)^2/\Delta_2 = -C_3^2/(\Delta_2\, R^6)$. For two atoms within a blockaded volume (Sec. 2.5.2), we might naively expect that addition of the third atom in the blockade volume doesn't change anything. However as we can see on Fig 2.22(b) the three-atom process has energy defect $\Delta_3 = E(ss'p') - E(ppp)$ and in principle can even be resonant. In the limit of $\Delta_3 \ll V$, the eigenstates will be strong admixtures of $|ppp\rangle$ and $|ss'p'\rangle$. Writing an effective interaction Hamiltonian in the basis that includes only p states doesn't make sense any more, and blockade can be broken [193] by exciting the $|ss'p'\rangle$ state [192], even though each atom pair, taken separately, might be blockaded. This process can be seen as a three-body Förster resonance [194]. In the case when the three-photon process is not resonant $\Delta_3 \gg V$, it will introduce state admixing in the second order $\sim V^2/\Delta_3^2$, that would in principle add a fourth-order three-body correction to the effective Hamiltonian $\sum_{i<j<k} W_{ijk}|ppp\rangle\langle ppp|$. Similarly, four-body [195] and

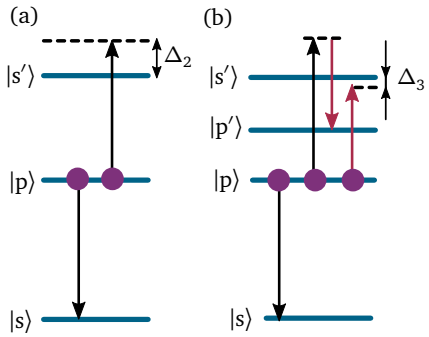

Figure 2.22: Three atom processes. In situations when two-atom processes (a) are energetically forbidden, three-atom processes (b) can be resonant. Horizontal lines are *single* atom energy levels.

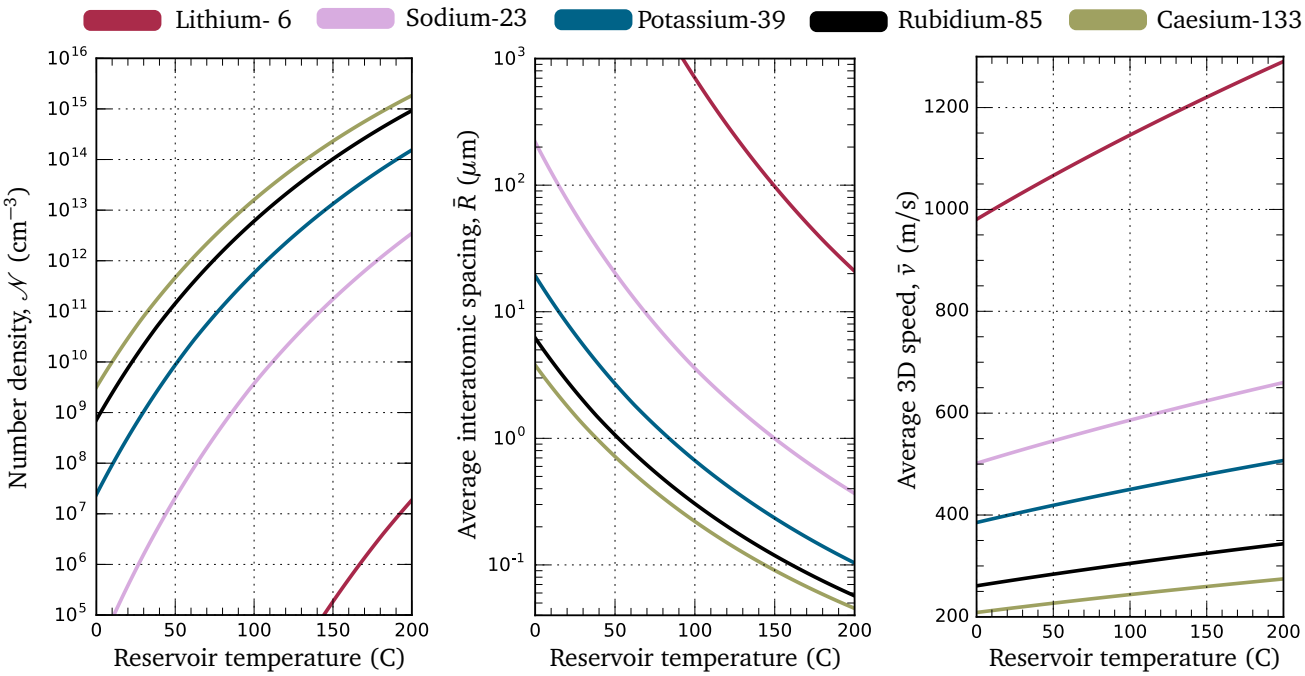

Figure 2.23: Comparison of alkali atomic vapour properties. The vapour pressure is set by the metal reservoir temperature, that should be the point in the cell with the lowest temperature.

higher-order resonances can occur.

2.8 Atomic thermal vapours

Thermal vapours of atoms are used both as experimental systems for investigation, and to provide spectroscopic reference standards for lasers in experiments investigating other systems (e.g. cold atom samples). ARC contains vapour pressure data [196] for Na, Li, K, Rb and Cs (`getPressure`), and allows easy access number densities (`getNumberDensity`), average interatomic distances (`getAverageInteratomicSpacing`), atomic speeds at given temperatures (`getAverageSpeed`), etc. A comparison of alkali metal properties is shown on Figure. 2.23.

2.9 ARC implementation

The Alkali Rydberg Calculator (ARC) library, described in Ref. [95] and used throughout this thesis for calculations is a part of a project that includes:

WWW address `https://github.com/nikolasibalic/ARC-Alkali-Rydberg-Calculator`

- **ARC code**, open-source code (BSD-3) hosted on GitHub [197]. This is a collection of theoretical calculation methods and relevant experimental data, organised in an object-oriented structure with clear hierarchy following the physical decomposition of the calculation problems. The choice of Python as a programming language provides easy integration with many other tools, and facilitates further development and expansions in a multi-user research environment.

WWW address `http://arc-alkali-rydberg-calculator.readthedocs.io`

- **Documentation** hosted online on Read the Docs [198]. It is generated auto-

matically from code comments (docstrings) using the Python Sphinx package that outputs hyper-linked .html and .pdf, cross-referenced directly to the source code.

- **"An Introduction to Rydberg atoms with ARC"**, an interactive IPython notebook that explores Rydberg physics quantitatively with the ARC package. This provides many examples of use, and benchmarks the package against literature. This is accessible from the documentation.

  WWW address: see "Getting started with ARC" section of the online documentation

- **Atom calculator** is a web-application hosted on a dedicated server, that provides access to a subsection of ARC functionality. Answers for quick calculations are provided immediately, while ones that require more lengthy calculations are scheduled, and users are notified via email once the results are available. All results of long calculations are stored in a growing database, allowing quick access to all previous calculations. The aim is to increase accessibility of common atomic-physics quantities and provide quick estimates. Generated codes can be downloaded as "on-demand-examples" of using the ARC package, which is also useful for more complicated calculations for which users have to check convergence themselves if they want more than quick estimates.

  WWW address: `https://atomcalc.jqc.org.uk`

We will now note several details on the implementation of the library. Numerov integration of the wavefunctions in the model potential, the origin for the majority of the coupling constants used in the rest of calculation, is an intensive numeric calculation that was implemented in the C language as a hard-coded Python Numpy extension. This combines the quickest possible integration with a directly returned Numpy array used in the rest of the library. Everything else is implemented in pure Python to allow easy changes and relies on Scipy and Numpy packages [169] that provide wrappers for optimized numerical methods (often hard-coded in FORTRAN). Memoization of results is used throughout to provide significant performance improvement. For example, all calculated dipole and quadrupole matrix elements are saved in an in-program SQL database (SQLite). Not being a client-server database, this doesn't have good support for concurrency, but has a quick response time. Many angular coupling factors, such as Wigner-nJ coefficients and WignerD matrices are also memorized and reused. Thanks to this, the generation of sparse interaction matrices in 2000 basis-state space takes on the order of a minute on a modern computer ($\sim$ 3 GHz CPU). Now we will focus on interfacing this library. Within Python, since calculations are implemented as classes, they are easily saved and reused with the Python Pickle library. Also, full documentation provides details on all the internal variables and methods of the ARC classes that can be interfaced if modules are built on top of them, or if one wants to take and reuse only part of them, e.g. interaction matrices and basis states. For other interfaces, calculations can be directly exported as .csv files.

The online interface, Atom calculator (Fig. 2.24), has been in itself a challenging computational project. In order to provide 1-to-1 compatibility with the standalone ARC library and allow easy updates of the used library, user queries are parsed with a combination of regular expressions, and corresponding Python code is generated in response. If the code can be quickly executed (e.g. calculation of dipole matrix elements), it is executed on the server and results are returned to the user within

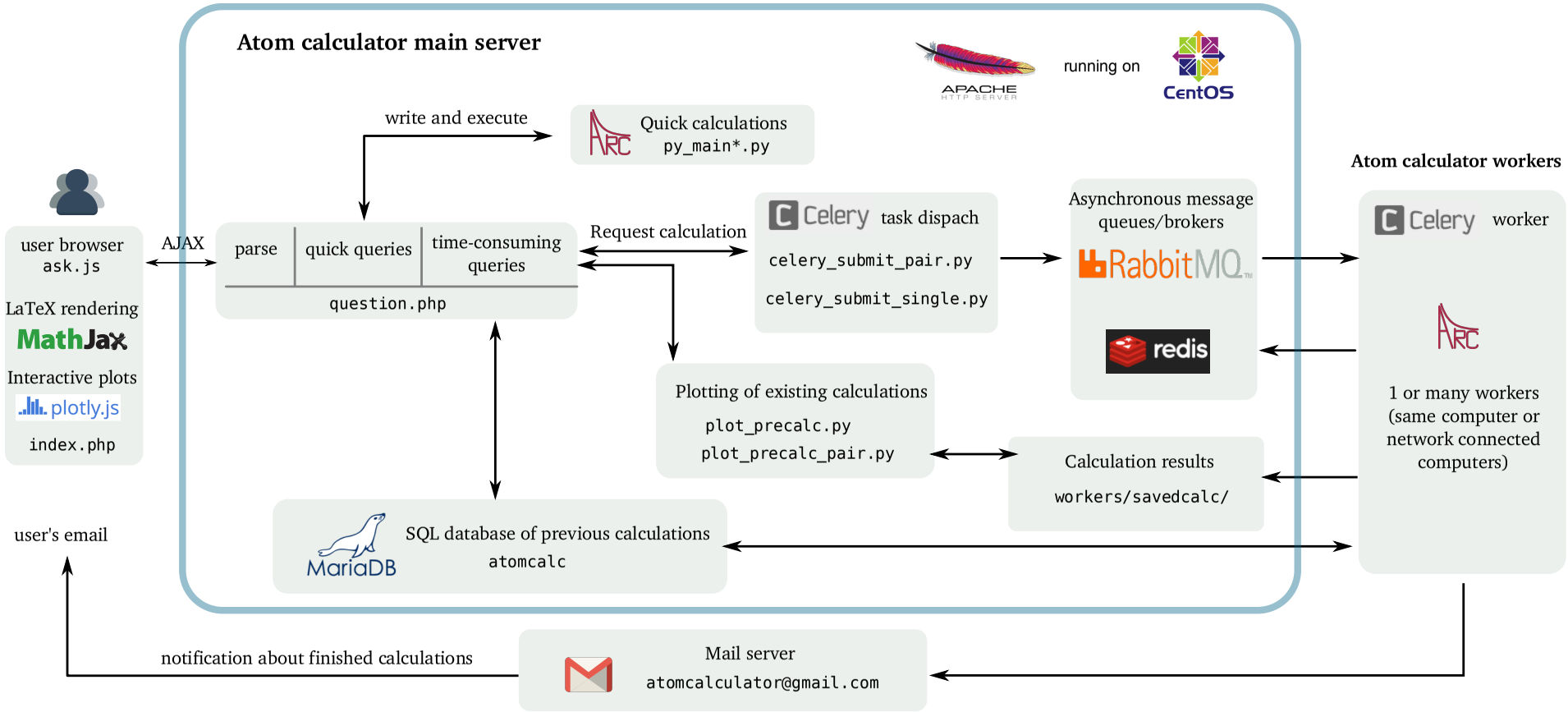

Figure 2.24: Atom calculator architecture. Users land on `index.php` page which provides in-browser interactive plotting and LaTeX rendering. JavaScript `ask.js` script is used to asynchronously (AJAX) query the main server. Questions are analysed by `quesiton.php`, and depending on time required for answering the question and aveability of previously calculated results, calculations are done immediately, retrieved from the database of old slowly-executed calculations, or new request for calculation is submitted. This new requests are processed with Celery Python module using asynchronous task queues, which are used for communication with separate worker processes that perform slow calculations. Once scheduled calculation is done, user receives the email notification, and the result is added to the database of slowly executed calculations for the benefit of all users. Note that the same framework can be used for any other wider-community relevant calculations.

several seconds. However, for lengthy calculations (e.g. pair-state interaction potentials, Stark maps, angular dependence of C_6) this cannot be done. In that case the Server will check the SQL database (MariaDB) that stores details of previous calculations, to see if the requested calculation, or anything similar, has been done in the past, and if it does exist, it will be offered to the user for immediate access. If, however, the requested calculation doesn't exist, users can submit an academic email address to schedule a job. The server then submits this job to the queue. The queue is implemented as a job queue for distributed computing in the Python Celery module, with RabbitMQ and Redis based communication layer. This is necessary since computation is done by separate worker process(es) that can in principle be on another machine. Workers take jobs from the queue, perform calculations, save their results in a shared folder, and update the MySQL database. Finally, workers connect to the email server and send a message to the user about a finished calculation with a corresponding link. On the user-side, MathJax and Plotly JavaScript libraries are used for equation rendering and data representation in the form of high-quality interactive plots. The architecture is summarised on Fig. 2.24. The final implementation uses a two-core virtual CentOS machine, allowing simultaneous running of server and worker processes. In terms of lines of code, it is the same order of magnitude as the ARC package itself, and includes JavaScript, PHP and Python segments, as well as HTML and CSS for web interface structure and design.

▷ For more information see
MariaDB - `www.mariadb.com`
Celery - `www.celeryproject.org`
RabbitMQ - `www.rabbitmq.com`
Redis - `www.redis.io`
MathJax - `www.mathjax.org`
Plotly - `www.plot.ly/javascript/`

2.10 An application: analysis of THz imaging

In the final section of this chapter, we will consider some of the Rydberg properties in the context of a recently demonstrated application [97]. The potential of Rydberg atoms for detection of microwave (MW) and terahertz[10] fields, has been recognised in early experiments [48, 50, 52]. For example, authors in Ref. [48] excited atoms in a atomic beam to a high-lying state $|r_1\rangle$, where big dipole matrix elements $\propto n_*^2$ between nearby states would make the medium optically dense for incoming black-body radiation in the narrow spectral range corresponding to the transition $|r_1\rangle \rightarrow |r_2\rangle$ where $|r_2\rangle$ is Rydberg state with higher energy. Atomic population in different Rydberg states can be detected with state-selective ionization (Sec. 2.3.5) providing readout of incoming radiation intensity. The ultimate detection sensitivity limit of this approach is given by the noise due to the collisional and black-body radiation induced population redistribution of $|r_1\rangle$. Authors of Ref. [50] managed to control the black-body radiation by enclosing the interaction region of the atomic beam in a cooled ($\sim$ 14 K) box which included metallic meshes in the holes for beam input that were dense enough to prevent penetration of the MW radiation from the hot atom source. This background shielded detection region was then used for directly measuring microwave radiation from black-body sources at different temperatures, using the same approach as in Ref. [48].

More recently, the intensity of a coherent source was measured with all-optical methods in a Rydberg vapour. Coherent MW driving between the two Rydberg states induced dressing of the state, and the corresponding Autler-Townes splitting can be detected if the transition to either of the Rydberg states is probed with a laser scan [160, 199]. However, the glass cell reflects microwaves, producing a

[10] Note that in the early papers the terahertz part of the spectrum was referred to as far-infrared (FIR) [48] or submillimetre [50] radiation.

Material	n	α (cm^{-1})
Silica	1.96	0.62 - 7.8
Pyrex	2.1	7 - >90
BK7	2.5	14 - >90
SF7	3.5	43 - >90
PTFE	1.44	1.4 - 2.8
HDPE	1.53	1.4 - 2.8

Table 2.1: Refractive indexes n and absorption coefficients α for common glasses and polymers for EM radiation in range 0.5-2 THz. All materials exhibit stronger absorption at higher frequencies. Data for glasses is from [201] and for polymers from [202].

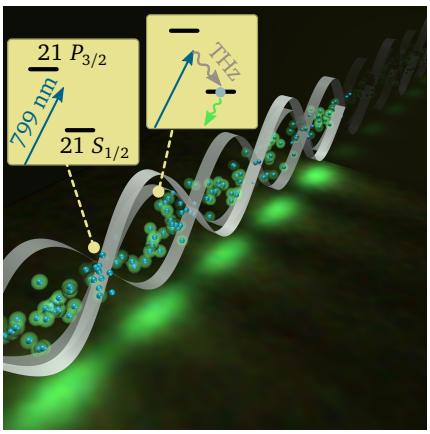

Figure 2.25: Two-photon optical-terahertz excitation of the Rydberg atomic states maps intensity of the terahertz standing wave into the fluorescence pattern of the Rydberg atoms. Atoms (blue dots) in the off-resonant laser beam can be excited (green spherical clouds) to Rydberg state if they are in the areas where field of terahertz standing wave (grey oscillating strip) is non-zero, as the two-photon resonance condition is fulfilled (insets). Image below illustration is experimental data from C. Wade [97].

complicated interference pattern in the measurement volume [200] that, due to the integral nature of all-optical detection via transmission measurements, cannot be directly detected in a single measurement. Also the interference pattern has to be known in order to correctly model the Autler-Townes splitting spectra.

In recent experiments by C. Wade *et.al.* [97] that interference pattern was converted to optical domain and measured along the laser beam in a single shot, by spatially imaging atomic fluorescence. Thermal caesium vapour enclosed in a quartz glass cell was used as active medium (for details of the experimental setup, see Ref. [97]). The choice of glass is crucial for efficient sampling of terahertz radiation, since other common glasses with higher ionic fraction have order of magnitude higher absorption coefficients (Table 2.1). Common polymers used for THz lenses (PTFE, HDPE) have similar absorption coefficients as Silica glass. PTFE with maximal usable temperature up to ~ 250 °C and low thermal conductivity, can also be used as an insulator for vapour-cell ovens if minimum absorption is needed. Alkali metals have a number of transitions in the THz regime featuring strong coupling [Fig. 2.26(a)], that forms a dense frequency comb in the terahertz window (0.3-3.0 THz) of the EM spectra, allowing measurement of radiation electric field amplitude via Autler-Townes splitting, as described in the previous paragraph. Measurements are relative to the fixed atomic standard that, in principle, can be absolutely calibrated. If both laser and THz driving are detuned from resonance ~ 200 MHz a new regime emerges. Due to reflections of the THz wave typically a standing wave will form (Fig. 2.25). In the nodes of the THz field, the laser driving is off-resonant with Rydberg transitions and therefore no atoms will be excited to this highly excited state. This is different compared to the previously discussed techniques in Ref. [48, 50], where states could be always populated through collisional processes, introducing a background signal[11]. In the points in space where there is a non-zero THz field present, the combination of optical and THz fields with equal detunings (Fig. 2.25, inset) will drive two-photon stimulated Raman transition to the Rydberg state $|r\rangle$. The natural lifetime of that state is 4 μs, but the population from that state will be redistributed through BBR and collision induced processes to other states, most of them capable of decaying in the visible spectrum. On these time scales hot atoms (~ 60 °C) can travel distances of ~ 1 mm before they emit fluorescence in the visible spectrum. Crucially, since the experiment uses a three-step ladder excitation scheme, the only atoms that can be excited to the Rydberg state will be those selected by the resonance condition of the lasers. If the laser beams are not too strong so as to induce additional dressings, and if they are set on resonance with the zero-velocity class, the atoms' velocity in the direction of the laser beam will be significantly reduced (~ 5 m/s) compared to the average velocity in the transverse direction (~ 200m/s). This means that after excitation the atom motion will *not* smear the fluorescence pattern *in the direction of laser beam propagation*, thus maintaining high-resolution record of THz driving field in the fluorescence pattern. At the same time lower-lying Rydberg states that have strong THz transitions, have lifetimes of the order of $\sim 1-10$ μs. That sets an ultimate theoretical limit on maximum frequency of THz field amplitude modulation at $\sim$100 kHz, if intensity changes are to be resolved in time. Realistic rates are also limited by the finite exposure time required to capture an image with good signal to noise ratio. This depends on the fluorescence intensity, the detection acceptance

[11] Note that for very dense vapours collisional redistributions and light-assisted collisions will ultimately cause populating of high lying states [203].

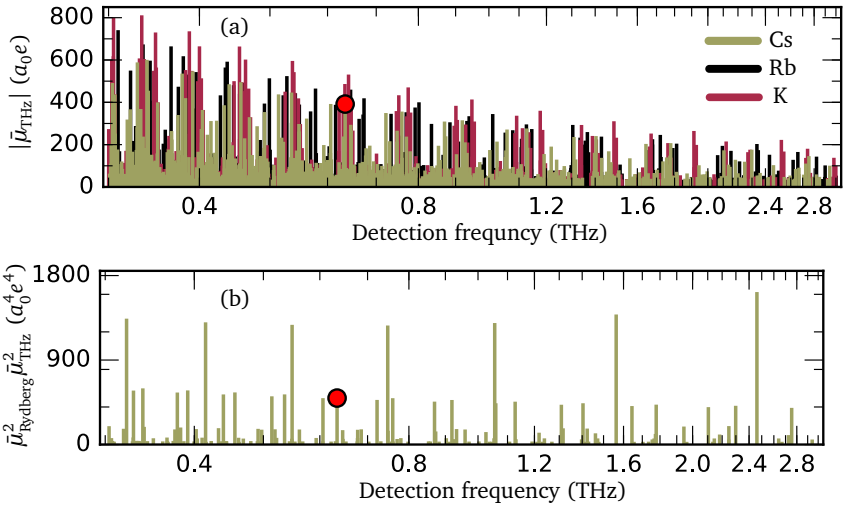

Figure 2.26: Relative sensitivity of alkali metals to terahertz radiation. (a) For resonant detection of coherent radiation measured via Autler-Townes splitting of the Rydberg-state excitation resonances, reduced dipole matrix elements $|\bar{\mu}_{\mathrm{THz}}| = |\langle \mathrm{r}_1||er||\mathrm{r}_2\rangle|$ for terahertz transitions between the Rydberg states $|\mathrm{r}_1\rangle \leftrightarrow |\mathrm{r}_2\rangle$ gives relative sensitivities in the terahertz range. For off-resonant imaging schemes, the fluorescence rate will depend on both coupling between the Rydberg states $\bar{\mu}_{\mathrm{THz}}$ and coupling from the lower excited state to the Rydberg state $\bar{\mu}_{\mathrm{Rydberg}}$ as $\bar{\mu}^2_{\mathrm{Rydberg}}\bar{\mu}^2_{\mathrm{THz}}$ (for the *fixed* Rydberg laser intensity), calculated on (b) for example of caesium excitation from the lower excited state $7\,S_{1/2}$, as in Ref. [97] (THz transition used there is highlighted with a red dot).

angle and efficiency, and dark-noise. Rates of ~ 12 Hz have been demonstrated with the standard consumer photo-camera [97], which is already good for real-time applications.

The excitation rate of Rydberg states in the off-resonant laser beam will be proportional to the square of the two-photon Rabi frequency $(\Omega_{\mathrm{o}}\Omega_{\mathrm{THz}}/\Delta)^2$ where Ω_{o} and Ω_{THz} are the Rabi frequencies of the optical and terahertz transitions respectively. The initial Rydberg population will then be proportional to the square of the corresponding dipole matrix elements. For all possible caesium transitions from Fig. 2.26(a), that quantifies relative sensitivities for resonant probing of the fields, Fig. 2.26(b) quantifies this relative Rydberg excitation rates for the off-resonant fluorescence imaging. The ultimate intensity of the fluorescence depends also on the lifetimes and decay channels of the state. The resolution of this method in the axial direction is limited by the residual Doppler-velocity of the excited atoms in that direction to $\sim 20\ \mu$m (theoretical estimate of lower bound). In the other two dimensions (in the radial direction) resolution is limited by the size of the probing laser beam, similarly to Ref. [200].

As can be seen on Fig. 2.26(b), this method as it stands offers narrowband detection, which has limited discrete tunability, achieved by changing the principal quantum number of the state. Detuning the excitation laser offers limited continuous tunability, since for bigger detunings Δ the two-photon transition rate is quickly diminished, while for smaller detunings the direct single-photon excitation of the states will cause a background signal. In principle, fluorescence from directly excited P states will have different frequencies than decays from S states populated in a Raman transition, but quick population redistribution processes will quickly contaminate all the fluorescence channels. A viable alternative for expanding detection ranges is by using Stark shifts of the state (Sec. 2.4.1), as in Ref. [48]. For example, scalar polarizability of the 21 $P_{3/2}$ $m_j = 1/2$ and 21 $S_{1/2}$ $m_j = 1/2$ caesium states are $\alpha_0^{(P)}$ =1.36 MHz cm^2/V^2 and $\alpha_0^{(S)}$ =0.08 MHz cm^2/V^2 respectively, providing tuning of $\alpha_P - \alpha_S = 1.28$ MHz cm^2/V^2 with an applied electric field, i.e. S to P resonance shift of 6.4 GHz through application of an electric field of 100 V/cm. In stronger fields, one has to take care of the strong state admixing (Sec. 2.4.1) that would not only change coupling constants, but also possibly allow driving of two-photon transitions to states that are normally forbidden by the ℓ selection rules for the dipole operator of the unperturbed atomic states.

2.11 Summary

The ARC project can be seen as an experiment on the ways to increase accessibility and portability of the knowledge of Rydberg atom properties. It was inspired by the day-to-day needs of research in the field of Rydberg atoms. Although a lot of results about Rydberg properties have been published in traditional ways in the form of various journal articles, the space of possibilities was too big to be exhausted with several specific examples. This extent also prevents simple tabulation of all the results. Existing on-line databases and computational engines provide neither all the necessary information, nor a framework upon which one can build new calculations. At the time work on ARC started, the only solution was tedious error-prone assembly of relevant data and re-use of existing theoretical frameworks. We hope that this project can provide the initial kernel for a community-developed framework, and inspire more well-documented scientific open-source libraries. Novel aspects are mostly not in the theoretical approach, which follows established state-of-the art methods, but in the implementation and organization. Success of projects like this can be best measured by the number of users, and in particular number of future extensions built with these tools, which remains to be seen in the future. In building this computational "brick" of theoretical methods and experimental data we tried to follow good practices of successful open-source development. Often neglected work of writing the documentation, and organising architecture of the program was found to be very good practice in clarifying all details of the theoretical reasoning. Finally, we note that open-source computational formats like .ipynb will probably allow much more effective sharing of theoretical and experimental results in the future, allowing readers of publications hands-on exploration of models, including parameter changes. This is a significant improvement over the traditional model of several example plots. Providing computational notebooks like IPython as a supplement to papers would provide quicker and deeper understanding of both theoretical and experimental results, a good example being recent results on gravitational wave detection [204]. That could be not just an effective way of sharing knowledge among specialists in the field, but also allow easier wider dissemination of knowledge. If an effort is made to provide relatively common interfaces for various calculations, results published in that way can be used directly as active computational libraries in other projects. We hope that the ARC library, along with other similar recent projects [205], will provide some drive in that direction.

Spin-wave motion

CHAPTER 3

In this chapter we discuss ways to control motional dephasing of collectively stored excitations. In Sec. 3.2 we present a dressed-state EIT scheme for a four-level ladder system both experimentally and theoretically. The four-level system can be mapped, through strong-resonant dressing of the states, to an effective three-level system which supports converting of optical excitations into uniform-phase spin waves with adiabatic protocol. A readout efficiency in well-defined spatial channels, for excitations stored in this type of spin-waves, is insensitive to the motional dephasing. In addition, the three-step excitation scheme produces momentum kick-free and Doppler-free excitation giving narrow resonances in thermal vapours. The scheme achieves spatial selectivity of the atom-light interaction region for *all three* driving fields within the atomic medium. We present proof-of-concept experimental demonstration of the generalised EIT scheme in the caesium thermal vapour, for $6\,S_{1/2} \rightarrow 6\,P_{3/2} \rightarrow 7\,S_{1/2} \rightarrow 8\,P_{1/2}$ excitation path. Results of exciting the higher-lying $23\,P_{3/2}$ state in the Doppler-free geometry are also presented, where we were able to observe bistability within this small excitation region volume of $\approx (36\ \mu\text{m})^3$. In Sec. 3.3 we present a theoretical model of an experiment where a spin-wave with a non-trivial motional state has been formed. We highlight the importance of strong dressing for coherent control (i.e. including relative phases of excitations) of motional degrees of freedom, and perform detailed derivation of the expected experimental signals. The theoretical prediction matches well with experimental data across the wide range of parameters. The model reveals interference, at a single-photon level, of the light emitted from two spin waves moving at two different velocities. Detailed theory provides insight into conditions for the observation of such phenomena at the single-photon level, clarifies some of the processes contributing to the background signal and allows future generalizations.

3.1 Introduction: collective storage of excitations

We have seen in the previous chapter (Sec. 2.5.2) that the presence of a single Rydberg state excitation can dominate all other experimentally relevant energy scales in its neighbourhood having a radius on the micrometer scale . Volumes of that size can contain big numbers ($\sim 10^{0\ldots3}$) of atoms, and can even be individually optically resolved [64, 72]. This represents potential for non-linear optics, provided that one can map strong Rydberg-Rydberg interactions into optical and NIR photons (wavelength $\sim 400-1600$ nm).

The desired mapping is provided by electromagnetically induced transparency (see Fig. 3.1) that uses the ground and long-lived Rydberg state for storing part of the

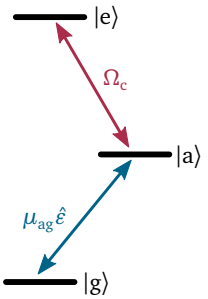

Figure 3.1: Example level system for EIT mapping of the weak field $\hat{\epsilon}$ into atomic degrees of freedom. Weak field $\hat{\epsilon}$ is dipole μ_{ag} coupled to the atomic system where a classical control field with Rabi frequency Ω_c controls the transparency window and group velocity.

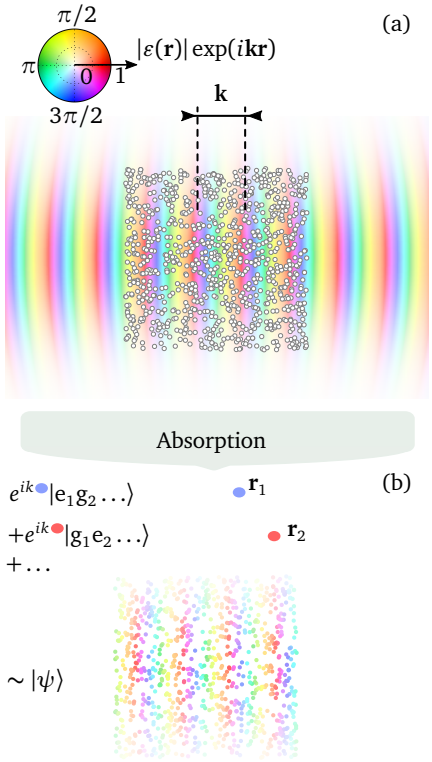

Figure 3.2: Spin-wave formation in collective absorption. (a) Ensemble of ground state $|g\rangle$ atoms irradiated with probe field whose amplitude $|\varepsilon(\mathbf{r})|$ and total phase picked up in transfer to the excited state $|e\rangle$ are mapped in space with the colour wheel. If in the absorption process there is no information about which atom absorbed the excitation, the collective excitation of the atomic ensemble (b) will be a superposition of probabilities that atoms at locations $\mathbf{r}_j$ are excited. The spatial phase of the formed state, spin-wave $|\psi\rangle$, records directionality of the input field and allows retrieval in well defined direction.

light-field excitation [4, 206]. EIT opens a transparency window (Fig. 2.12) whose high dispersion means (Sec. 2.3.4) that the group velocity of the light pulses is slow. Pulses are therefore compressed inside the medium, with excitation originally in the $\hat{\varepsilon}$ field mode now coherently coupled to the atomic degrees of freedom, admixing Rydberg state character to the optical excitation. For dense media[1] , discrete atomic degrees of freedom can be replaced by a field, and the excitation can be formally described as a polariton [4, 206], i.e. a coherent superposition of excited matter field and light field. The ratio of light-matter character of excitation is adjustable in time through adiabatic variation (Sec 2.6) of the control field (Ω_c in Fig. 2.12). This admixing of Rydberg atomic character into optical excitation [207] allowed observation of strong non-linearities [66, 68], including photon bunching due to effective attractive interactions between excitations in 1D [69]. However, with everything happening "in-flight" of the excitation through the medium, with limited interaction time and variable localization of the excitation, building more involved schemes can become difficult, both experimentally and theoretically.

Optical excitation can be completely mapped into the atomic degrees of freedom in two ways. One way is adiabatic turn-off of the control field Ω_c that in principle can deterministically map the excitation pulse to a polariton that in this limit becomes purely atomic excitation [164, 206, 208], with no contribution of the field $\hat{\varepsilon}$. Alternatively, one can stochastically prepare the medium. For example, short laser pulses can stochastically excite atoms, however unless some additional mechanism limits the maximum number of excitations (as suggested in Ref. [209]), one cannot create a non-Poissonian excitation number distribution in this way, and therefore no non-classical light sources. For deterministic single-excitation preparation, spontaneous emission can be used as in DCZL protocol [2], where single-decay events are detected and used as a herald for the preparation of a singly-excited state. These are probabilistic methods since exact timing of the state preparation is unknown and, in contrast to EIT methods, they cannot be used for coherent manipulation of weak light pulses, although they can provide an initial, non-classical source of such pulses [210]. In all the cases, there is a lack of information about which atom within the medium is excited. The prepared atomic *collective* excitation state is called a *spin-wave* (Fig. 3.2), which can be written for a case of a single-excitation for plane-wave excitation fields as

$$|\psi\rangle = \frac{1}{\sqrt{N}} \sum_{j=1}^{N} \exp(i\mathbf{k}\cdot\mathbf{r}_j)|g,\ldots,e_j,\ldots\rangle. \tag{3.1}$$

This excitation is a coherent superposition state, made of the sum of the probability amplitudes for the events that any j-th atom, out of a total of N atoms, has been excited to the Rydberg[2] state $|e\rangle$. The relative phase of these different excitation absorption events at atom-locations $\mathbf{r}_j$ depends on the sum of all wave-vectors $\mathbf{k} \equiv \sum_l \mathbf{k}_l$ whose corresponding field modes l have been involved in coupling $|g\rangle$ and $|e\rangle$ states in the storage procedure. This state is robust against single-spin decoherence and loss, being an example of so-called W states [24]. Light excitation stored in this way in the Rydberg manifold allows for long interaction times, has

[1] media is dense, for requirements of continuum approximation applied here, if $\mathcal{N}\ \sigma\ \delta z \gg 1$, where $\mathcal{N}$ is atom number density, σ is the characteristic cross-section of the EM field mode, and δz is the characteristic distance over which slowly-varying envelope (Sec. 2.4.3) of the atomic polarizability and propagating electric field change.

[2] or, alternatively, the other stable state used in storage protocol

strong interactions since light mode excitation is completely mapped into the Rydberg atomic state, and provides localization of excitation in space and time that allows building of more complicated control protocols. Finally, at the end of such a control protocol, light can be retrieved in a well defined spatial mode due to constructive interference of the emission events from different atoms making up the collective spin-wave $|\psi\rangle$. This allowed filtering of stored excitation pulses by successfully retriving only excitations stored in singly-excited atomic clouds [211], their manipulation during the storage time with applied AC fields [212], realization of dissipative single-photon transistors [71, 213] and measurement of both strong [blockade, Sec. (2.5.2)] and weak [214], dephasing-induced interactions between two light excitations stored in two separate optical channels [72]. For readout of the excitation in a well-defined direction, a phase grating [Fig. 3.2(b)] imprinted in relative atomic phases $\mathbf{k}\cdot\mathbf{r}_i$ should be preserved. However, the atomic ensemble[3] used in these storage experiments (also called quantum memories) has Boltzmann distributed velocities due to the finite temperature of the ensemble. Because of the atomic motion, the lifetime for successful readout in the initially defined direction is limited by the time $(k\bar{v})^{-1}$ required for atoms to smear out the phase grating under thermal motion with average velocity $\bar{v}$ (Fig. 2.23). This process is called *motional dephasing*.

3.2 Uniform phase spin-waves

In early light-storage experiments, initial excitation of the optical field $\hat{\varepsilon}$ was stored in the Zeeman levels of the ground state [164], or hyperfine states of the ground state [217]. In both cases, the energy distance between the two states used for storage, which is also the energy difference of probe and control fields, is maximally of the order of few GHz. With nearly co-propagating probe and control fields [Fig. 3.3(a)], typically at an angle of about $\sim 1^\circ$, the imprinted spin-wave has a period of $\Lambda \equiv 2\pi/|\mathbf{k}_p - \mathbf{k}_c|$ that can be on the order of 100 μm or up to two orders of magnitude larger, depending on alignment precision, reaching the microwave wavelengths which corresponding to inter-state $|g\rangle \leftrightarrow |e\rangle$ transition. In an alkali vapour medium, diffusion of the atoms can be reduced by adding a buffer gas, reducing motional dephasing. Typical lifetimes reached in thermal vapours are of the order of ~ 100 μs [217, 218], limited by the diffusion of the atoms out of the beam and collisional dephasing ($\sim$ 1 ms). The longest storage time reached for excitation storage in ground-state atoms to date, was achieved in cold samples. The atomic motion was reduced by using a 1D optical lattice with 3.2 μm period in the direction of the formed spin-wave whose period of is ~ 35 μm. With the help of additional dynamical decoupling [27] that cancels dephasing from nearly-static external fields, storage lifetimes of 16 s were reached [29].

For excitation storage in the Rydberg state the situation is, however, much worse. Typical storage schemes use combination of blue and red laser driving giving, even in the optimal counter-propagating orientation of the probe and control fields [Fig. 3.3(b)], spin-waves on the order of $\Lambda \sim 800$ nm. In thermal vapours, where the average thermal velocity is $\bar{v} \sim 200-300$ m/s, this gives rise to lifetimes of $\Lambda/\bar{v} \sim 1$ ns [219]. Remedies for motional dephasing are limited in these schemes

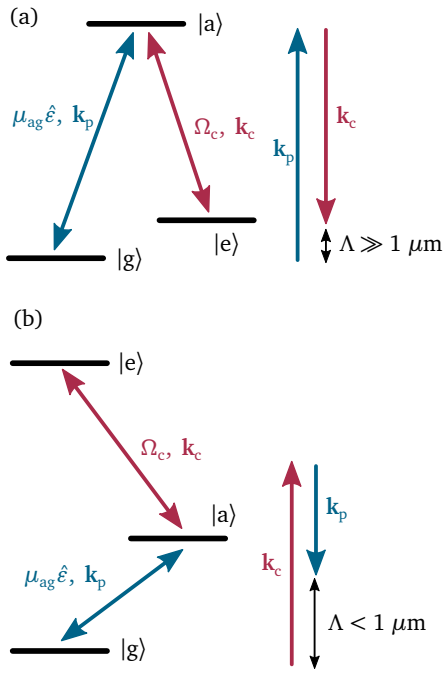

Figure 3.3: Comparison of ground state and Rydberg state two-photon collective excitation storage. (a) For storing excitation between two ground state hyperfine or Zeeman sub-levels, drive wave vector mismatch $|\mathbf{k}_p - \mathbf{k}_c| \equiv (2\pi)/\Lambda$ is typically small, making spin-waves with long wavelength ($\Lambda \gg 1$ μm). (b) Storage in Rydberg state, due to wavelength mismatch between the two fields, limits spin-wave period to $\Lambda < 1$ μm.

[3] Note that realisations of the spin ensemble other than atomic vapour medium can be used. For example solid state realisation can be done with rare earth doped crystals [11, 215, 216], however atomic vapours medium has some technological advantages to be discussed in Sec. 3.3.1.

since buffer gas cannot be added as it has strongly perturbing effects on high-lying states, giving rise to line broadening and shifts [220]. In cold atoms, with absolute temperatures six orders of magnitude lower, and corresponding velocities three orders of magnitude lower, lifetimes are $\sim 1\ \mu s$ [211, 212]. Here the application of optical lattices for reduction of atomic motion is not effective in reducing motional dephasing since the lattice period cannot be much smaller than the spin-wave period.

Here we propose an excitation storage approach based on the ladder scheme with three fields. The fields' propagation directions $\mathbf{k}_l$ can be oriented in a plane such that their wave-vectors cancel $\left|\sum_l \mathbf{k}_l\right| = 0$ [see Fig. 3.4(c)]. In this configuration each atom will pick-up the same phase, independent of its spatial location $\mathbf{r}_j$ within the driving field, creating a spin-wave with uniform phase. A phase-grating [Fig. 3.2(b)] determining the readout direction is imprinted then only when the readout laser pulses are applied. The efficiency of selecting a spatial direction for the readout is therefore unaffected by the motional dephasing during the storage time. The pulse amplitude can be distorted, since it is stored in relative amplitudes of the atom excitation within the medium. However, the relevant length-scale over which variation of the pulse amplitude is stored, determined by the initial length of the compressed light pulse in the medium, is typically orders of magnitude bigger than $1\ \mu$m. Therefore, loading of atoms into optical 1D lattice effectively stops atomic motion over that scale, preventing pulse distortion. Of course, just orienting three laser beams in a Doppler-free geometry as on Fig. 3.4(c) doesn't allow controllable mapping of excitation between light field and atoms. In the following, we present such a protocol.

3.2.1 Generalised EIT for 4 level systems

Consider a four-level ladder system driven by three coherent fields, denoted as probe, dressing and control, shown on Fig. 3.4(a). Their respective intensities are given by the coupling Rabi frequencies Ω_p, Ω_d and Ω_c. With respective field detunings Δ_p, Δ_d and Δ_c, the coherent dynamics of the system is described in the $\{|1\rangle, |2\rangle, |3\rangle, |4\rangle\}$ basis with Hamiltonian ($\hbar = 1$)

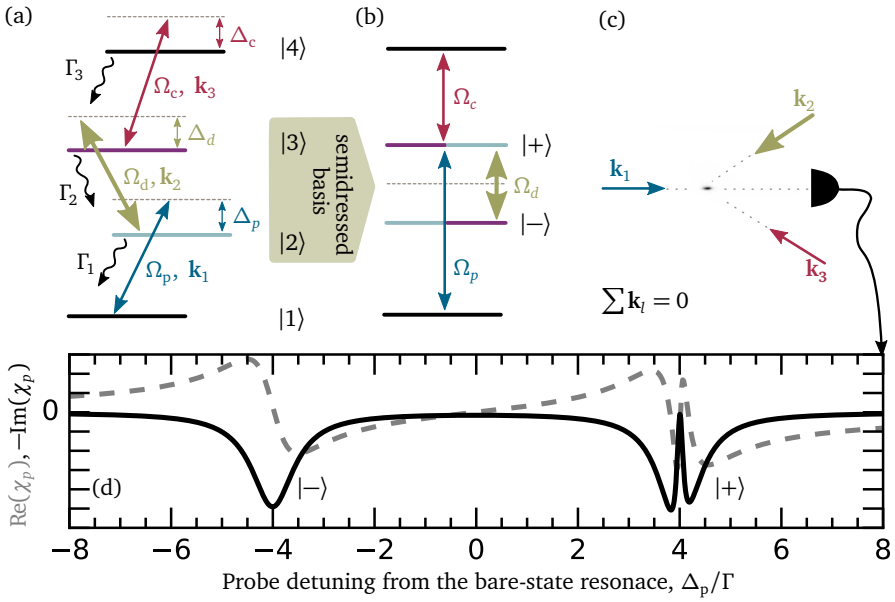

Figure 3.4: Dressed state electromagnetically induced transparency in Doppler-free (uniform-phase spin-wave) configuration. (a) Bare-states level diagram of the system driven by three coherent fields. (b) Levels in semi-dressed picture. With three driving fields oriented in plane as in (c), Doppler-free condition is fulfilled, and collective excitation of the ensemble of such four-level systems into state $|4\rangle$ will form uniform-phase spin-wave. Simultaneously, for $\Delta_p = -\Delta_c = \Omega_d/2$ highly dispersive EIT window opens for probe light (d), theoretically calculated here for $\Gamma_1 = \Gamma_2 \equiv \Gamma$, $\Gamma_3 = 0$, $(\Omega_d, \Omega_p, \Omega_c)/\Gamma = (8, 0.1, 0.5)$ and $(\Delta_d, \Delta_c)/\Gamma = (0, -4)$ for a stationary four-level system.

$$\mathscr{H} = \begin{pmatrix} 0 & \Omega_\mathrm{p}/2 & 0 & 0 \\ \Omega_\mathrm{p}/2 & -\Delta_\mathrm{p} & \Omega_\mathrm{d}/2 & 0 \\ 0 & \Omega_\mathrm{d}/2 & -\Delta_\mathrm{p}-\Delta_\mathrm{d} & \Omega_\mathrm{c}/2 \\ 0 & 0 & \Omega_\mathrm{c}/2 & -\Delta_\mathrm{p}-\Delta_\mathrm{d}-\Delta_\mathrm{c} \end{pmatrix}. \tag{3.2}$$

In addition to the coherent driving, dissipation affecting the system is described by the Lindblad superoperator $L[\ldots]$ acting on the system's density matrix $\hat{\rho}$ as $L[\hat{\rho}] = \sum_\alpha \left(L_k \hat{\rho} L_\alpha^\dagger - \frac{1}{2} L_\alpha^\dagger L_\alpha \hat{\rho} - \frac{1}{2}\hat{\rho} L_\alpha^\dagger L_\alpha\right)$. Spontaneous decays with rates Γ_i, $i = 1,2,3$ are included with $L_i = \sqrt{\Gamma_i}|i\rangle\langle i+1|$. Overall, the system's dynamics is governed by the master equation $\frac{\mathrm{d}}{\mathrm{d}t}\hat{\rho} = -i[\mathscr{H}, \hat{\rho}] + L[\hat{\rho}]$. As discussed in Sec. 2.4.3, solving this in the case when all three beams are resonant will give rise to electromagnetically induced absorption, instead of transparency. We have to identify parameters for EIT to occur.

In the following, we focus our attention to the parameter regime where the middle driving field, resonant with the unperturbed transition $|2\rangle \to |3\rangle$, $\Delta_\mathrm{d} = 0$, introduces strong dressing $\Omega_\mathrm{d} \gg \Omega_\mathrm{p}, \Omega_\mathrm{c}$ of the two intermediate states. The probe field will then see an Autler-Townes split resonance [Fig. 3.4(d)], corresponding to the two states $|+\rangle$ and $|-\rangle$, that appear in the semi-dressed basis [Fig. 3.4(b) and Sec. 2.4.3]. Consider the situation where the probe and control fields are *both detuned from the bare-state resonances* $\Delta_\mathrm{p} = -\Delta_\mathrm{c} = \Omega_\mathrm{d}/2$, so that they are resonant with one of the semi-dressed states $|+\rangle$ or $|-\rangle$. This engineered dressed-state resonance can then be used in combination with control Ω_c and probe light Ω_p to open a narrow transparency window [Fig. 3.4(d)]. Typically, state $|4\rangle$ would be a long-lived Rydberg state, whose decay (Sec. 2.3.2) is much weaker compared to that of the two intermediate states $\Gamma_3 \ll \Gamma_1 \approx \Gamma_2$. To a very good approximation a dark state $|D\rangle$ is formed, which can be obtained by diagonalising the system Hamiltonian (Eq. 3.2). In the limiting worst case $\Omega_\mathrm{p} = \Omega_\mathrm{c}$, when atoms are in an equal-weighted superposition of the ground $|1\rangle$ and excited state $|4\rangle$, we can obtain a clean expression for the dark state

$$|D\rangle = (|1\rangle - \xi|2\rangle - \xi|3\rangle + |4\rangle)/N, \tag{3.3}$$

$$\xi \equiv \frac{-\Omega_\mathrm{d} + \sqrt{\Omega_\mathrm{c}^2 + \Omega_\mathrm{d}^2}}{\Omega_\mathrm{c}}, \tag{3.4}$$

where N is a normalization factor, and ξ characterises the admixture of the bright (radiatively coupled) states $|2\rangle$ and $|3\rangle$. In the limit of strong dressing the contribution of the bright states $2\xi \approx \Omega_\mathrm{c}/\Omega_\mathrm{d} \ll 1$ is negligible. This is similar to the double-dark resonance schemes explored in 4-level Λ-like systems [221]. The benefit of using the engineered state for excitation becomes apparent if one considers momentum-kick free, Doppler-free excitation. In contrast to typical two-photon driving schemes to highly excited states that, as discussed in the introduction, cannot fulfil the Doppler-free condition, this can be achieved with three fields arranged in a plane [Fig. 3.4(c)]. Additional advantages will be discussed in the following sections.

Intuitively, how EIT arises in this situation can be seen in a similar way as for the usual three-level EIT scheme discussed in Sec. 2.4.3. One can expect that one of the eigenstates of $\mathscr{H}$ (Eq. 3.2) has dominant composition of $a_1|1\rangle + a_2|4\rangle$, so that in a time δt, evolution under $\mathscr{H}$ adds $a_1 \cdot \Omega_\mathrm{p}\delta t$ and $a_2 \cdot \Omega_\mathrm{c}\delta t$ to the manifold consisting

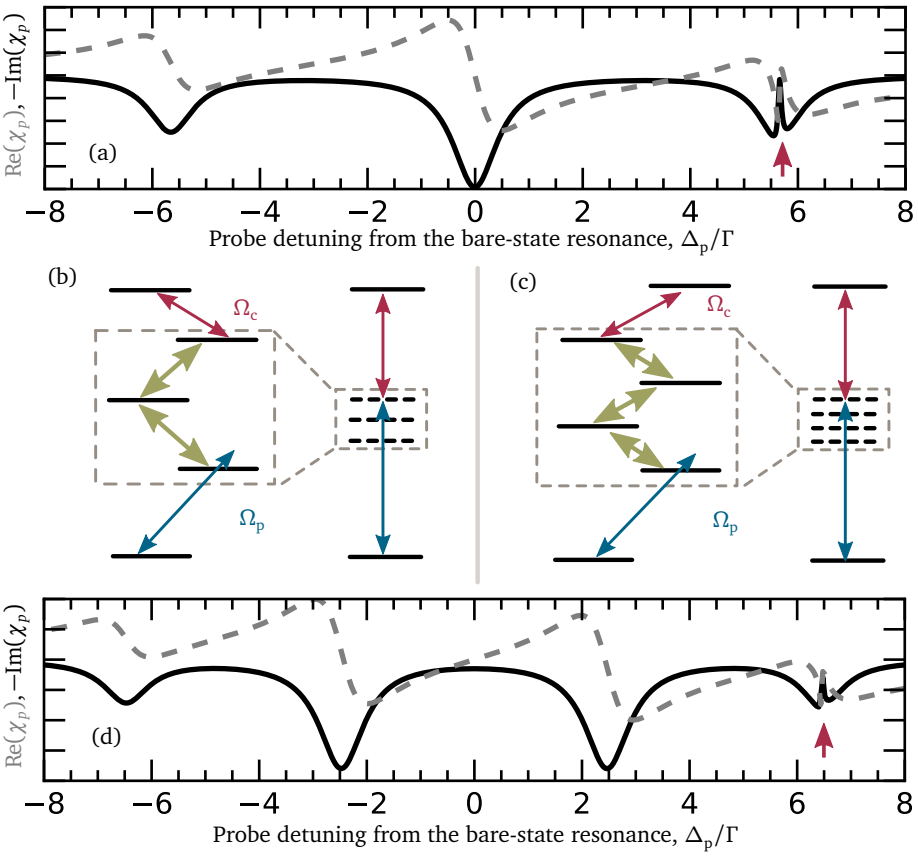

Figure 3.5: Generalisation of dressed-state EIT for N-middle levels. Example configuration for the five- (b) and six-level (c) system, shown in bare and semi-dressed basis. With all dressing beams resonant (yellow) $\Delta_{d,i} = 0$, and much stronger then probe and control fields $\Omega_{d,i} \gg \Omega_c, \Omega_p$ narrow transparency window opens when probe and control are resonant with one of the states in the semi-dressed basis. For example for $\Omega_{d,i} = 8\Gamma$, $(\Omega_p, \Omega_c)/\Gamma = (0.1, 0.5)$, narrow transparency window opens for for $\Delta_p = -\Delta_c = 5.65\ \Gamma$ for five-level system (a) and $\Delta_p = -\Delta_c = 6.45\ \Gamma$ in six-level system (d). Arrows (a,d) highlight the transparency window.

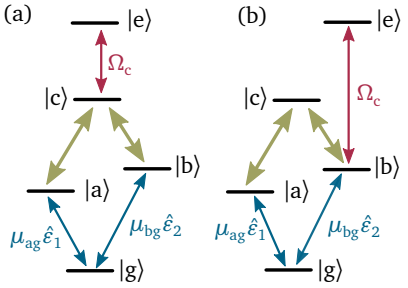

Figure 3.6: Extension of the dressed-state EIT scheme for coupling between bi-chromatic polaritons. (a) A uniform spin-wave between states $|e\rangle$ and $|g\rangle$, from light excitation $\hat{\mathcal{E}}_1$ stored over $|g\rangle \rightarrow |a\rangle \rightarrow |c\rangle \rightarrow |e\rangle$ levels, can be phase-matched for retrieval as field $\hat{\mathcal{E}}_2$ of different frequency, by retrieving over $|e\rangle \rightarrow |c\rangle \rightarrow |b\rangle \rightarrow |g\rangle$. This modified diamond schemes is also interesting for exploring the influence of EIT on the efficiency of the four-wave mixing process. For continuous coupling of two propagating bi-chromatic fields $\hat{\mathcal{E}}_1$ and $\hat{\mathcal{E}}_2$ the scheme shown on (b) is particularly interesting although the spin-wave between $|g\rangle$ and $|e\rangle$ is not uniform-phase. That is because phase matching of spin waves formed over transitions $|g\rangle \rightarrow |a\rangle \rightarrow |c\rangle \rightarrow |b\rangle \rightarrow |e\rangle$ and $|g\rangle \rightarrow |b\rangle \rightarrow |e\rangle$ can be done only by adjusting the propagation direction of the two dressing fields on transitions $|a\rangle \rightarrow |c\rangle$ and $|c\rangle \rightarrow |b\rangle$, allowing co-propagation of the two fields $\hat{\mathcal{E}}_1$ and $\hat{\mathcal{E}}_2$. Using Rydberg state for $|e\rangle$ would additionally open the possibility for non-trivial couplings between the two bi-chromatic quantum fields.

of the middle two states $|2\rangle$ and $|3\rangle$. If the coherent driving Ω_d between these two states is strong enough to coherently mix these two contributions, there has to exist a combination of the amplitudes a_1 and a_2 that will in this mixing destructively interfere in the amplitude for excitation of the middle manifold. Following this effective image, one would expect that if we have a middle manifold consisting of a ladder of N states $|m_1\rangle \xrightarrow{\Omega_{d,1}} |m_2\rangle \xrightarrow{\Omega_{d,2}} \ldots \xrightarrow{\Omega_{d,N-1}} |m_N\rangle$, all of them coupled with strong dressing fields $\Omega_{d,i}$ resonant with the unperturbed transitions, EIT would again appear if we tune probe and control laser to one of the dressed states. That is indeed the case, as we show on Fig. 3.5, where the calculation is performed with three and four middle states, amounting to a total of five and six states respectively. Finally, we note that these multi-level schemes can also be interesting because they open up interesting possibilities for coupling multiple weak (quantum) fields (Fig. 3.6), where a total system's polariton that forms would have two quantum EM field modes with very different frequencies. Bi-chromatic quantum field interfacing can be interesting in several contexts, as different energies can be used as a frequency encoded qubits [222] or for interfacing and entanglement of heterogenous quantum systems with different resonant frequencies. Some possibilities will be discussed in Sec. 3.3.5.

3.2.2 Doppler free excitation

As noted in the introduction, Rydberg state excitation with three field wave-vectors $\mathbf{k}_i$ oriented in a Doppler-free configuration, excites atoms with the same relative phase $\sum_i \mathbf{k}_i \cdot \mathbf{r} = 0$ independently of the atomic positions $\mathbf{r}$ within the medium. The phase grating determining the output mode is now set only by the readout control

beams. Any atomic motion before application of the readout control beams (during the storage time) does not affect the retrieval efficiency [223]. Since only readout beams set the direction of the output mode, the output mode *direction* can also be changed by changing the readout beams direction. Also, since all the schemes that produce a uniform-phase polariton have the same form of stored spin-wave, one can use two different dressed states, one for storage and one for readout, to change the *frequency* of the readout pulse [Fig. 3.6(b)]. Both of these features can be important for realizing quantum interconnects [224]. Finally, note that in EIT achieved under Doppler-free conditions all the atom-velocity classes contribute to the signal, in contrast to other methods where Doppler-free signals are achieved by velocity-selective techniques, standard saturation spectroscopy being the simplest example [225].

We will now focus on extended storage lifetime, which was the original motivation for pursuing uniform-spin waves. Rydberg-vapour based single-photon sources [209] are a prominent example in which prolonged storage of excitations in the atomic degrees of freedom can improve operation. Recently demonstrated memories, where light was stored as a Rydberg excitation in a thermal vapour, had lifetime of the readout efficiency of only 1.2 ns[219], limited by motional dephasing of the spin-wave imprinted in their two-step excitation process. With the proposed Doppler-free excitation, the lifetime of this atom-vapour memory would be limited to the transit time of atoms through the excitation region defined by the size of the laser beams. Taking parameters in Ref. [219] as an example, for Rubidium vapour at 140 °C and a laser waist of 35 μm, two orders of magnitude longer lifetime ($\sim$ 100 ns) is expected.

The longer storage time can be used to obtain an effectively bigger blockaded volume. Namely, to obtain single photons from the output, one can rely on strong Rydberg blockade that dephases states with more than two excitations on the time scale of the excitation laser pulse [209, 219], or, in continuous excitation schemes, scale $1/\gamma$ defined by transition linewidth γ (typically dominated by laser linewidth). The dephasing occurs due to atom-atom interactions (see Sec. 2.5) that introduce additional level shifts C_α/r^α for two atoms at distance r, where $\alpha = 3$ for resonant dipole-dipole interactions, or $\alpha = 6$ for non-resonant van der Waals interactions. For short pulses the excitation linewidth $\Gamma = 1/T$ will be determined by the pulse duration T. During the excitation time T any two atoms in blockade radius $R_\mathrm{B} = \sqrt[\alpha]{C_\alpha/\Gamma}$ (Sec. 2.5.2) would acquire a phase shift $> \pi$ relative to the phase of the exciting pulse. That prevents creation of excited atom-pairs within the blockaded volume. In order to achieve strong enough interactions so that only a single excitation can be created within it, the excitation volume has to be small $\sim R_\mathrm{B}^3$. The longer storage lifetime, achievable with uniform-phase spin-waves, can provide another mechanism for filtering out cases in which only a single excitation is stored within the medium. In this *weak-blockade* regime, multiple excitations will be created within the storage medium, however, any spin-waves containing two or more excitations will dephase during the storage time [214]. This is because each excited atom-pair $\{j_1, j_2\}$ with superposition amplitude $a_{j_1 j_2}$ in the initially stored spin-wave $|\psi\rangle = \sum_{j_1 \neq j_2} a_{j_1 j_2} |\mathrm{g}, \ldots, \mathrm{e}_{j_1}, \ldots, \mathrm{e}_{j_2} \ldots\rangle$ will acquire an additional phase $a_{j_1 j_2} \xrightarrow{\tau} \exp(i\ \tau\ C_\alpha / r_{j_1 j_2}^\alpha)\ a_{j_1 j_2}$ during the storage time τ. The phase for each term will be uncorrelated, depending on the particular atom-pair distance $r_{j_1 j_2}$,

which would dephase the initial two-excitation (or more) spin-wave $|\psi\rangle$, preventing readout in a well defined output mode. For an atomic excitation cloud of size d, this decoupling of multi-photon excitations from the output mode would happen after $\sim d^{\alpha}/C_{\alpha}$ (in units $h = 1$). For example, if the medium excitation is performed in 1 ns, a waiting time of $\tau = 100$ ns would increase the excitation volume from which we expect to retrieve only single-photon output by an factor of 100 or 10, for dipole-dipole and van der Waals interactions respectively. This corresponds to the increased effective blockade radius by a factor of 4.6 and 2.1 respectively. Finally, note that recent experiments which demonstrated interactions between photons in two separated optical channels [72] relied on the weak-blockade regime for effective photon-photon interactions.

3.2.3 Coherent transfer: STIRAP over dressed states

For wider applications of the three-photon scheme it is desirable to have coherent manipulation protocols allowing for deterministic storage and retrieval [4, 206], in addition to the obtained uniform-phase spin waves. In the previous section we discussed only stochastic excitation that cannot deterministically perform storage, and a weak-blockade regime where it was not possible to deterministically store only spin-waves containing only a single excitation. Off-resonant Doppler-free driving schemes have been proposed [226] for deterministic, coherent control of populations, however it's difficult to achieve strong Rabi driving frequencies in multi-level ladder schemes due to weak dipole-matrix elements and a requirement that lasers are detuned from intermediate states in order to avoid populating them. Protocols relying on direct coherent driving also require precise control of driving power and time duration of driving. Finally, they cannot be used for manipulation of weak fields.

Adiabatic following (Sec. 2.6) offers a good alternative, relaxing constraints on precise pulse duration and power while allowing deterministic atomic state preparation, as well as mapping of weak quantum fields [4, 206] into excitation of atomic media. The usual two-field, three-level STIRAP protocol has been used to transfer atomic population to the Rydberg states [227], and it can be generalized for use with an engineered dressed state as a mediator. The protocol is shown in Fig. 3.7 (left inset). We keep laser detunings as in Sec. 3.2.1, with probe and control fields resonant with one of the dressed states, and the dressing field resonant with the unperturbed transition between the two middle states. Keeping the dressing field Rabi frequency Ω_{d} fixed, and pulsing txhe control and probe laser beams achieves population transfer between the ground and the Rydberg state [Fig. 3.7 (right inset)] without significantly populating any of the *two* intermediate states. To achieve efficient transfer two requirements have to be satisfied: (i) the dressing driving has to be stronger than the probe or control driving $\Omega_{\mathrm{d}} \gg \Omega_{\mathrm{c}}, \Omega_{\mathrm{p}}$ [228] [Fig. 3.7]; and (ii) the usual three-level STIRAP adiabaticity condition should be satisfied $\Gamma/(T\Omega^2) \ll 1$ [229], where Ω is the control [$\mathrm{Max}(\Omega_{\mathrm{p}}, \Omega_{\mathrm{c}})$] pulse intensity, Γ is the decay constant of the two middle (dressed) states, and T is the switching time of the two pulses.

The combination of adiabatic following and the existence of a narrow transparency window (Sec. 3.2.1) that allows pulse slowing down and compression, implies that this scheme can be used as a simple generalization of the three-level storage protocols [4, 206] offering the discussed benefits of uniform-phase spin-wave excit-

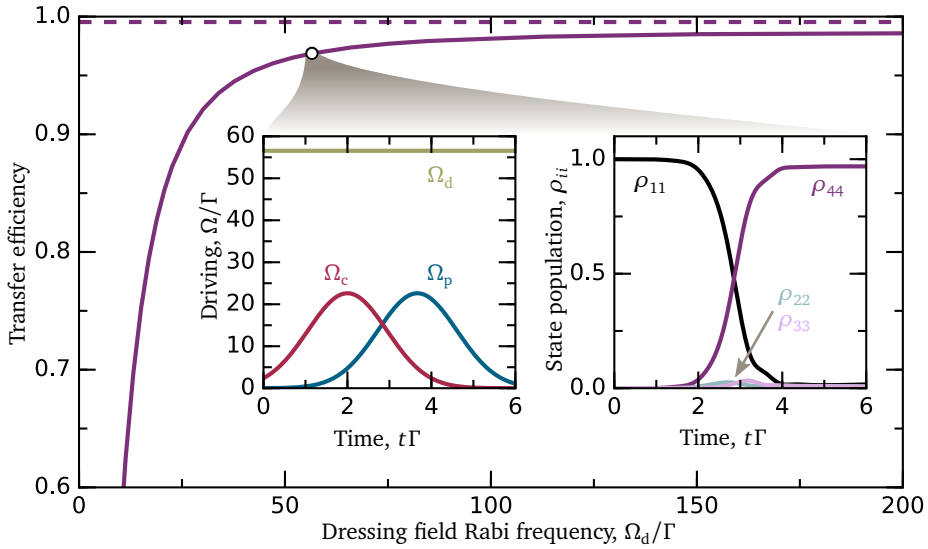

Figure 3.7: Deterministic state preparation with generalised STIRAP in a four-level ladder system. Transfer efficiency to the excited state $|4\rangle$ (solid line) compared to that of the three-level scheme (dashed line) for the same control and probe pulses (left inset). High efficiency is achieved for strong dressing of the two middle states with the generalised STIRAP protocol for four-level ladder scheme (insets). States $|1\rangle$ and $|4\rangle$ are assumed to be long-lived, while the decay rate of each of the two middle states is Γ.

ation (Sec. 3.2.2). In the strong driving limit where both probe and control fields can be considered as classical driving fields, extended storage times can allow for testing of proposals that exploit Rydberg-Rydberg interactions within the blockade volume for deterministic preparation of many-body states containing only a single excitation [230]. These protocols require localization of the excitation region within a sphere of blockade radius R_B. Such tight localization of the excitation can provided by this scheme, as will be discussed in the following Section 3.2.4. Finally, note that the described adiabatic following protocol is only efficient for cold atoms, since in hot atoms the Doppler effect dephases the system *during* adiabatic following, significantly reducing the transfer efficiency. This is because while the dark state [Eq. (3.3)] is Doppler-free, the Doppler-free condition holds only for the ground $|1\rangle$ and Rydberg $|4\rangle$ state, not for the two intermediate states over which the transfer happens.

3.2.4 Spatial localization of excitation within the atomic medium

The noncollinear orientation of the three driving fields provides, in addition to Doppler-free excitation, a well-localized excitation volume whose size is determined by the overlap of all three beams. Since both probe and control beams are detuned from the bare-state resonance, the medium is *transparent* for them everywhere except in the common overlap region, which is the only place where the population of atoms in the Rydberg and ground states is changed. Using strong resonant dressing to provide an engineered state over which interaction happens in this noncollinear multi-drive field scheme allows excitation and probing of well-localized regions in any selected location *within* the atomic medium whose size can be down to micrometer distances if all the beams are tightly focused.

Well localized excitation of atomic vapours confined in spectroscopic cells in this scheme, in combination with Doppler-free features, is promising for electrometry applications in the microwave and terahertz regions (see Sec. 2.10), allowing for sub-wavelength imaging of fields in the vicinity of the field-perturbing structures that are either immersed in the atomic vapour or placed next to the spectroscopic cell [231]. Localization of excitations can also allow probing of atom-surface interactions [232] with patterned surfaces [233] inserted inside the vapour cells, and explorations of

non-equilibrium phase transitions [87] in small volumes.

The scheme can also be used in cold-atom ensembles to provide excitation of only a tiny fraction of the bigger cloud, e.g. in Rydberg experiments where one wants to perform excitation in volumes with linear dimensions of several micrometers characteristic of a Rydberg blockade, for state preparation [67, 230] or single-ion creation [234]. In particular, this can be used within larger cold atom clouds not requiring previous preparation of small cold-atom ensembles. Similarly in cold-atom arrays, the scheme can be used for single-site addressing [80, 83, 235–237] in two-dimensional (2D) and three-dimensional (3D) lattices. For ensembles held in 2D lattices, the addressing can be done by moving only the dressing laser focus, keeping the probe and control beams, that illuminate the whole lattice, unchanged.

ACKNOWLEDGEMENTS: Experimental results in this section are obtained in collaboration with Massayuki Kondo. The author designed experiment, and collaboratively performed setting-up of experiment, and measurements.

3.2.5 Experimental demonstration of dressed-state EIT

This section presents experimental demonstration of the proposed EIT scheme. As an atomic medium, an evacuated quartz cell filled with caesium is used. To increase the atomic vapour pressure within the 2 mm optical path length inside the cell, it is heated in a PTFE insulated enclosure with ceramic heaters up to 50 °C, corresponding to an atom-number density of $4.6 \cdot 10^{11}$ cm^{-3}. The four caesium states selected for the ladder scheme are $6\,S_{1/2}\ F=4 \to 6P_{3/2}\ F=5 \to 7S_{1/2}\ F=4 \to 8P_{1/2}\ F=3,4$, coherently driven by three laser beams with corresponding wavelengths 852 nm, 1470 nm and 1394 nm respectively. The first two lasers (ECDL) are locked to the transition using a Doppler-free signal provided by polarisation spectroscopy [154, 238]. The third control laser is not actively stabilised, however since it is a single-chip based distributed feedback laser (DFB) its short-term drift and linewidth are below 1 MHz. The weak 852 nm probe beam is set $2\pi \times 500$ MHz off-resonance from the transition, outside the usual Doppler-broadened profile (FWHM $\sim 2\pi \times 700$ MHz for Cs at 50 °C). The strong second laser beam ($P_\mathrm{d} = 4.1$ mW) on $6P_{3/2}\ F=5 \leftrightarrow 7S_{1/2}\ F=4$ resonance dresses the corresponding transition by Rabi frequency $\Omega_\mathrm{d} \approx 2\pi \times 1$ GHz bringing the dressed state into resonance with the detuned probe field.

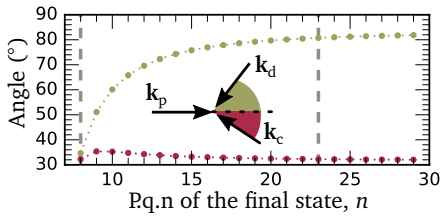

Figure 3.8: Relative angles for three driving fields (shown in inset) in the Doppler-free ladder excitation scheme. Calculated for caesium $6\,S_{1/2} \to 6\,P_{3/2} \to 7\,S_{1/1} \to n\,P_{1/2}$ excitation scheme. Similar angles are obtained for driving to $n\,P_{3/2}$ state. Two principal quantum numbers (p.q.n) of final states used in this chapter are highlighted with vertical dashed lines.

The three laser beams for the ladder excitation are focused down to beam waists ($1/e^2$ intensity) of $(w_p, w_d, w_c) = (6, 28, 29)$ μm and overlapped in plane at a common focal point inside the cell. To achieve Doppler-free configuration (Fig. 3.8), the dressing and control beams are focused at an angle of 34° and 32° respectively, relative to the direction of the probe beam (Fig. 3.9). This requires focusing of dressing and control beams through a 1.25 mm thick quartz cell wall at an angle, instead of the usual normal-incidence conditions. That introduces astigmatism [239], offsetting the foci in the sagittal and tangential planes by as much as ~ 0.2 mm. This is compensated by additional quartz windows (AC1 and AC2 in Fig. 3.9), of the same thickness and at the same incident angle, but now in the beam's sagittal plane, i.e. rotated 90° around propagation direction with respect to the glass window. The correction windows are fixed in single-piece 3D printed mounts that keep them fixed at the correct angles.

Alignment of the three tightly focused beams is quite challenging. Initial alignment is done in identical empty quartz cell, allowing almost exactly the same beam propagation to be achieved as with the filled experimental cell. A corner of the empty cell is removed, so that a razor blade can be inserted inside. A piezo-actuated

translation stage is continuously driven by a saw-tooth voltage, knife-edging the beam by moving ≈ 100 μm, and providing real-time information on the beam focal point location. With the blade set at an angle to all three beams, it is possible to simultaneously obtain a signal from all three beams, and perform fine alignment of their focal points in all three dimensions. The empty cell is then replaced with the caesium-filled experimental cell. Since the probe beam is off-resonant for the undressed transition probe beam absorption occurs only at location where the second strong laser dresses the atomic levels. This causes fluorescence at 852 nm that is imaged through the interference filter on a CCD camera from the side of the cell to find beam overlap between the first and the second laser. With the three laser beams overlapped, upon scanning of the control laser over resonance, reduction of 852 nm fluorescence can be observed. It is also possible to replace third fibre-coupled laser output with 1470 nm laser driving $6P_{3/2} \rightarrow 7S_{1/2}$ or 794 nm laser driving $6P_{3/2} \rightarrow 8S_{1/2}$, both of which can induce dressing and associated fluorescence to help with visually (with CCD camera) locating beam position inside the vapour cell.

A theoretical prediction for the probe absorption is presented in Fig. 3.10(a). The steady state for model's dynamics described in Sec. 3.2.1 is calculated with a simple four level system, excluding hyperfine states F and different coupling constants for all possible m_F sub-levels. The model does include averaging over atom-velocity classes in two-dimensional plane (defined by the laser beams propagation directions), each with the corresponding Doppler shift of driving-field detunings, for Boltzmann velocity distribution at 50 °C. Decay rates $\Gamma_{1...3}$ are taken to match the natural lifetimes of 6 $P_{3/2}$, $7S_{1/2}$ and $8P_{1/2}$ states respectively (Sec. 2.3.2). Additionally, each of the states decays to the ground state with rate $\Gamma_\tau = 1/\tau$ due to the finite transit time τ. The transparency peak that opens on one of the dressed state [$|+\rangle$ on Fig. 3.10(a)] does not reach full transparency, being limited in visibility by the transit time (see Sec. 2.4.3 for discussion on the time required to populate the dark state).

The experimentally obtained level splitting is shown in Fig. 3.10(b-d). An avalanche photodiode (APD) records the probe beam absorption through the 2 mm thick vapour that includes ∼ 100 times smaller common interaction region defined by the overlap of the three focal points. In the interaction region, a dressing beam induces Autler-Townes (AT) splitting of the $6P_{3/2} \rightarrow 7S_{1/2}$ resonance, which additionally broadens

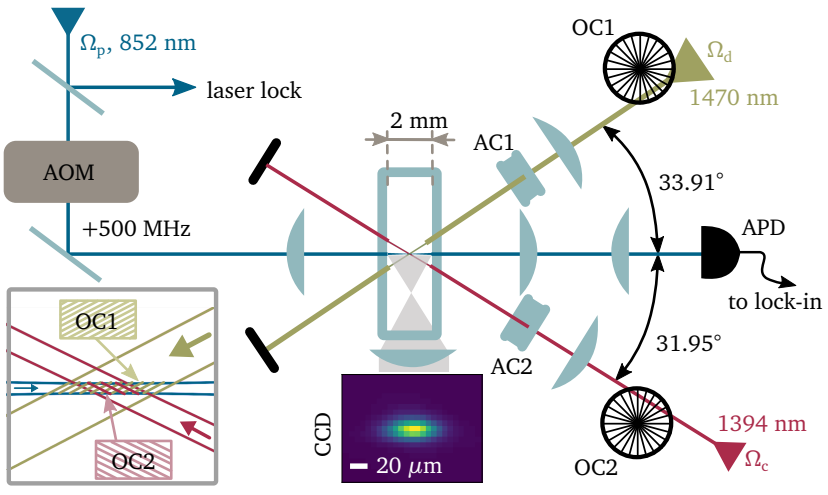

Figure 3.9: Schematics of experimental setup for demonstrating dressed-state EIT in Doppler-free configuration. The probe beam, offset with acousto-optic modulator (AOM) from the atomic resonance by +500 MHz, passes through 2 mm of caesium vapour and its transmission is recorded on an avalanche photodiode (APD). Dressing (1470 nm) and control (1394 nm) laser beams pass through the achromatic lenses and astigmatism correction plates (AC1 and AC2) before reaching a common focus inside the vapour cell. There, the frequency-shifted probe field becomes resonant with the dressed-state transition, causing strong 852 nm fluorescence imaged through the interference filter on the camera (CCD) from the side of the cell. The dynamics from the beam-overlap region (zoom-in shown in the bottom left inset) can be extracted by performing transmission detection locked-in to the modulation of dressing or control fields, provided by optical chopper wheels OC1 and OC2 respectively.

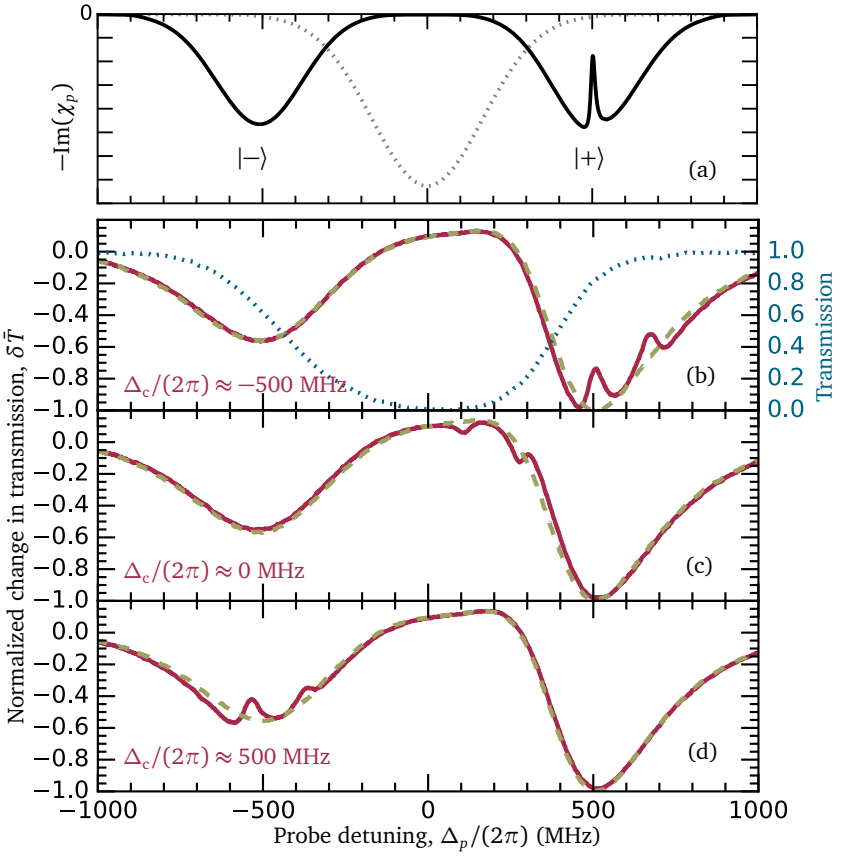

Figure 3.10: Dressed-state Doppler-free EIT in thermal vapour - theory and experiment. (a) A four-level theoretical calculation of the imaginary part of the electric susceptibility for the Doppler-broadened medium (see main text for details). The dotted (solid) line shows line profile without (with) a dressing laser beam $\Omega_d = 0$ ($\Omega_d = 2\pi \times 1$ GHz). The solid line shows EIT window in the dressed state $|+\rangle$ resonance for $\Delta_d = 0$, $\Delta_c = -2\pi \times 500$ MHz for a transit time of $\tau = 26$ ns, $(\Omega_d, \Omega_c)/(2\pi) = (1, 80)$ MHz. Experimental results in caesium thermal vapour are shown on panels (b-d). The dotted line on (b) shows the total probe transmission through the cell. Lock-in detection with the dressing-beam power modulation shows AT splitting (dashed line). Addition of the control laser opens a transparency window (solid line) when the control field is tuned to one of the dressed states [(b) and (d)]. For control laser on resonance, EIA is observed (c).

the wings of the Doppler-broadened D2 transmission spectrum. The dressing beam can be modulated by switching it on and off with an optical chopper wheel (OC1 on Fig. 3.9). Demodulating the APD signal in-phase with this dressing beam power modulation, we can obtain the change of probe transmission δT due to the presence of the dressing beam in the common interaction region. This reveals two AT peaks [Fig. 3.10(b), dashed line], the red detuned one being smaller due to the contribution of other hyperfine states ($F = 3, 4$) of the D2 transition. One also notes [Fig. 3.10(b-d)] that with the dressing beam turned on the absorption for the probe field, resonant with bare-state transition, is reduced. This can also be explained in the dressing picture, as the dressing laser shifts resonance away from the bare-stateresonance due to AT splitting. Indeed, camera images of the fluorescence from $6P_{1/2}$ state decay for the resonant probe reveal a dark spot at the location of the dressing laser in the otherwise bright fluorescence beam.

Finally, adding the control laser ($P_c = 8.8$ mW) causes a transparency peak to appear when the control field is on resonance with either of the semi-dressed states, $|+\rangle$ and $|-\rangle$ respectively on Fig. 3.10(b) and Fig. 3.10(d) (solid line). With absorption in the demodulated signal normalized with maximum absorption, we see that we can achieve transparency of $\sim 30\%$. The two observed peaks correspond to the two hyperfine states $8P_{1/2}$ $F = 3, 4$ of the final state, split by $2\pi \times 171$ MHz. Note that if the control laser is left on resonance, enhanced absorption is observed [Fig. 3.10(c) solid line], which is explained as the usual four-level ladder electromagnetically induced absorption [100, 154, 240].

To obtain further insight into the nature of the observed resonances, scans of the control laser were performed, keeping the probe laser locked, with the probe beam blue detuned by $2\pi \times 500$ MHz from the $6S_{1/2}$ $F = 4 \rightarrow 6P_{3/2}$ $F = 5$ resonance, and

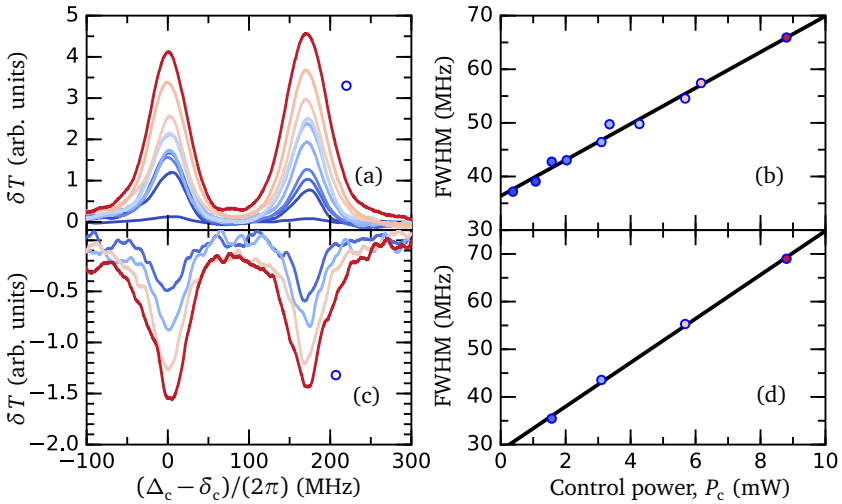

Figure 3.11: EIT and EIA of a strongly dressed state. (a) EIT resonances in probe transmission signal for off-resonant probe and control $\Delta_p = -\delta_c = 2\pi \times 500$ MHz. (b) The full-width at half-maximum (FWHM) of EIT varies linearly with control power. (c) EIA resonances are observed when probe and control fields are resonant with bare state transitions $\Delta_p = -\delta_c \approx 0$, and their FWHM also has linear scaling with control power (d).

the dressing laser locked on resonance $6P_{3/2}\ F = 5 \rightarrow 7S_{1/2}\ F = 4$. Now the optical chopper wheel OC2 (Fig. 3.9) is used to modulate the power of the control laser, while the dressing beam power is kept constant. Note that with this modulation one probes a different spatial part of the interaction region (Fig. 3.9 inset) compared to modulation with OC1, although in the present case the two regions are almost the same since $w_d \approx w_c$. The lock-in amplifier demodulated probe absorption signal is presented in Fig. 3.11(a). Analysis of the full-width at half-maximum (FWHM) extracted from the Gaussian fits of one of the resonances [marked with a dot on Fig. 3.11(a)], reveals a linear scaling of the transparency widths with control power [Fig. 3.11(b)], in accordance with the theoretical prediction [241]. Extrapolating the obtained FWHM to the limit of $\Omega_c \rightarrow 0$, we obtain a prediction for the narrowest features of about $2\pi \times 36$ MHz. A similar result with unlocked lasers, and the probe on resonance $\Delta_p \approx 0$, yields a minimum EIA linewidth of about $2\pi \times 29$ MHz [Figs. 3.11(c-d)]. Dominant contributions to the linewidth of these features are: (i) the finite time the atoms spend in the interaction region, estimated as time of flight through the probe beam, that broadens every transition by $\Gamma_t = \bar{v}/\bar{d} \approx 2\pi \times 6$ MHz, where $\bar{v}$ is the average atomic speed, and $\bar{d} = \pi D/4$ is the average transit path length through the beam of diameter D (corresponding

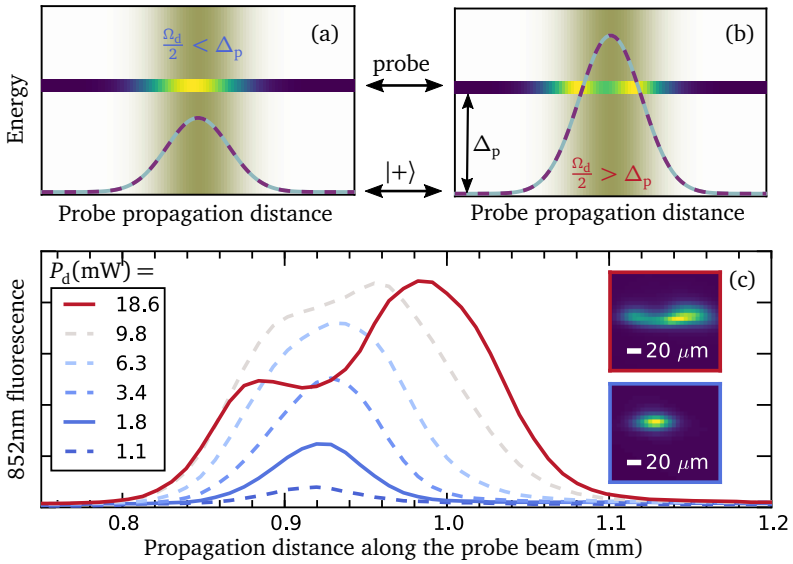

Figure 3.12: Origin of spatial averaging over dressing powers in probe transmission signal. (a) Spatially varying dressing laser power (background shading) pushes the dressed state $|+\rangle$ closer to the probe laser energy, causing increased scattering of the probe laser (colour of the horizontal line marking probe laser energy corresponds to the fluorescence rate). (b) If the peak dressing laser power causes dressed state energy to shift more than a probe detuning Δ_p, two peaks in fluorescence appears, corresponding to the wings of the dressing laser beam where probe laser and dressed state are on resonance. (c) Measured 852 nm fluorescence, integrated over vertical pixels, imaged for different dressing powers. Insets show two examples of imaged fluorescence.

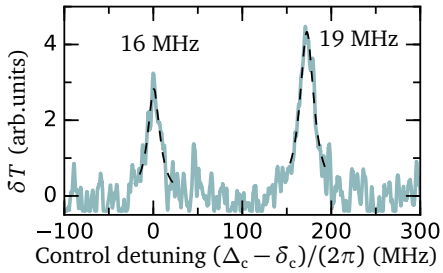

Figure 3.13: Narrowest observed EIT resonances. Less tight focusing of dressing beam compared to two other beams reduces dressing-beam power averaging, allowing narrower features to be observed. Dashed lines are Lorentzian fits, with their FWHM marked on the figure.

to the probe beam in our case); and (ii) averaging of the dressing beam power, that determines location of semi-dressed state resonance, over the region where probe and control beams intersect (Fig. 3.12). The latter can be resolved using a top-hat shaped dressing beam. Alternatively, one can select a dressing beam much wider than the control and probe beams such that overlap region of the probe and control beams probes only a small region of the dressing beam, over which the variation of the dressing beam power is much reduced. Dynamics from only that region can be conveniently extracted by modulating the control beam (with OC2 in our setup on Fig. 3.9). Under conditions like that $w_d > w_p, w_c$ (28 μm, 6 μm and 13 μm respectively), *without* astigmatism compensation, linewidths of down to $2\pi \times 16$ MHz were observed (Fig. 3.13).

Alternative possible experimental implementations

There are many suitable alternative ladder-systems that can be used for achieving the proposed dressed-state EIT. In rubidium a siutable scheme would be

$$5S_{1/2} \xrightarrow[780\text{ nm}]{5.96\ a_0 e} 5P_{3/2} \xrightarrow[1529\text{ nm}]{10.6\ a_0 e} 4D_{5/2} \xrightarrow[\sim 700\text{ nm}]{\sim 0.01\ a_0 e} nP,\ nF.$$

Here, dressing in the middle step is easily achieved since it corresponds to a strong transition in the range where erbium-doped fibre amplifiers can provide high power. Regarding the geometric constraints, while the Doppler-free condition $\sum_i \mathbf{k}_i = \mathbf{0}$ can be satisfied for many three-field transitions by orienting three beams in a plane, there are special cases where almost complete Doppler cancellation can be achieved in a collinear configuration of three driving fields. That is the case in the caesium ladder scheme

$$6S_{1/2} \xrightarrow[895\text{ nm}]{4.49\ a_0 e} 6P_{1/2} \xrightarrow[635\text{ nm}]{0.56\ a_0 e} 9S_{1/2} \xrightarrow[\sim 2.2\ \mu\text{m}]{\sim 0.01\ a_0 e} nP,$$

where almost complete Doppler cancellation is achieved in collinear regime, with wavevector mismatch corresponding to a spin-wave period of $\Lambda \approx 590$ μm. In comparison, the in-plane Doppler-free scheme in caesium, $6S_{1/2} \rightarrow 6P_{3/2} \rightarrow 7S_{1/2} \rightarrow nP$, for laser beam angles misaligned from a perfect Doppler-free condition by ~ 1 mrad, would produce a spin-wave with a comparable period of $\Lambda \approx 100$ μm. Similarly in lithium

$$2S_{1/2} \xrightarrow[671\text{ nm}]{3.4\ a_0 e} 2P_{1/2} \xrightarrow[460\ nm]{1.9\ a_0 e} 4D_{3/2} \xrightarrow[1465\text{ nm}]{\sim 0.009 a_0 e} (\sim n = 54)P$$

collinear orientation of ladder-driving fields would result in a spin-wave with period of $\Lambda \approx 1$ mm. In comparison with non-collinear schemes where driving fields are in plane, the collinear schemes restrict the choice of excitation lasers and associated dipole coupling strengths. However, they are very promising for achieving the narrowest possible spectral features of interest for electrometry [97, 199], allowing driving of big atomic volumes, resolving the problem of transit broadening due to atomic motion through small volumes. In practice for $\Lambda \sim 1$ mm in thermal vapours, in addition to finite transit time through the excitation region, additional effects like collisional broadening etc, start limiting the maximum achievable storage time and linewidth, not spin-wave motional dephasing. In cold, dense atomic clouds, the remaining dephasing mechanism that would limit storage time are Rydberg molecular interactions [123].

3.2.6 Exciting caesium 23 $P_{3/2}$ in Doppler-free configuration

The Doppler-free excitation was also used to excite the higher-lying caesium state 23 $P_{3/2}$. For this state, dressing and control driving propagation direction angles (Fig. 3.8), relative to the probe (labels as on Fig. 3.9) are 80.8° and 32.3° respectively. Three driving beams with waists $(w_p, w_d, w_c) = (12, 18, 28)$, are overlapped at their common focal points. The probe and dressing lasers are locked on resonance as in the previous section. An AOM derived probe beam is detuned by $2\pi \times 500$ MHz, to be on resonance with one of the dressed states. With the control field on, we were able to observe narrow (FWHM $\sim$ 18 MHz, Fig. 3.14) *absorption* peaks. However, detailed analysis of possible dephasing mechanisms preventing observation of transparency resonances was not performed. Rydberg excitation was confirmed via fluorescence imaging: with the control laser on resonance, fluorescence on the probe D2 transition (852 nm) was *reduced*, while fluorescence in the visible (330-750 nm) would *appear* from the common interaction point. As expected, due to the longer lifetimes of the Rydberg states, the imaged visible fluorescence occurs from a slightly bigger volume than reduced 852 nm fluorescence.

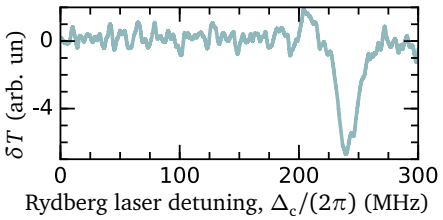

Figure 3.14: Rydberg resonance in 3-driving field ladder-scheme in Doppler-free configuration. See main text for more details.

The regime with many excited Rydberg states is also explored by increasing probe and Rydberg laser power and observing probe transmission directly. For these measurements, the optical choppers are not used in order to provide uninterrupted driving during detuning scans. Recording of the probe transmission for detuning in positive and negative direction (Fig. 3.15) reveals *bistability* of excitation in this small interaction volume, with *sharp transition* points indicating avalanche-like (de)excitation. In the hysteresis window of about $\sim$ 30 MHz, the change of transmission depends on the history of the system — i.e. from which direction in control detuning we reached that point. This is a small excitation volume demonstration of the effect first observed in Ref. [87]. Observation of this effect provides one motivation for the theoretical analysis in Chapter 4, which explores conditions under which bistability can appear.

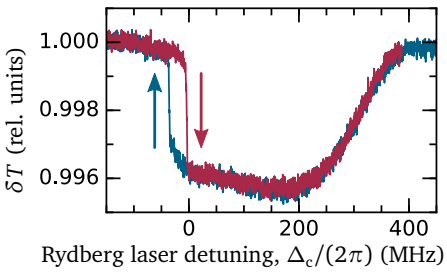

Figure 3.15: Bistability of Rydberg excitation upon control detuning Δ_c change. Measured change in probe transmission upon scans with positive and negative direction (chirp rate). Atoms are excited to 23 $P_{3/2}$ in a caesium thermal vapour at 78 °C, corresponding to the atom number density $\mathcal{N} = 3.8 \cdot 10^{12}$ cm^{-3}.

For the benefit of future experiments we note several points about the current setup that provide ideas for possible future improvements. With good, high NA collection optics and real-time image analysis for quantitative readout, fluorescence imaging provides a quick response and good signal-to-noise ratio, and presents a better method than direct measurement of probe transmission. In particular, with a selection of interference filters it is possible to observe changes in atomic population. The simplest example of this is fluorescence on the D1 transition, indicating the presence of 6 $P_{1/2}$ population due to decay from the 7 $S_{1/2}$ state excited in common interaction region. Observing real-time camera images of the fluorescence, it is possible to directly see resonances of the control laser. At the moment, extracting same information from probe transmission signals requires either averaging of multiple laser scans or use of lock-in-amplifiers, both of which have limitations, not least slow response time. Therefore software that could analyse fluorescence from different parts of the recorded camera image in real-time would be a significant improvement for future experiments. Another significant consideration in improving the signal-to-noise ratio of directly recorded transmission signals is the huge temperature gradient between the cell, heated to $50-120$ °C, and the rest of the laboratory (typically at ≈ 20 °C). This has implications on cell heater design, where thermal insulation provided by PTFE and narrow slits for the laser beams

provide some improvement. Still, with the current setup, air-current drifts that occur due to this temperature gradient, caused refraction and offsets of the beams, preventing detection of probe transmission with a balanced-photodetector. Finally, the transparency signals are sensitive to the residual magnetic field, and especially presence of permanent magnets in proximity of the cell. Magnetic shielding of cells with μ-metal can be a consideration. With these improvements the experimental setup described in this section provides a flexible platform for future exploration of non-equilibrium phase transitions, electrometry and coherent atom-light interaction phenomena in small-volumes and narrow-linewidth Doppler-free configurations.

3.3 Coherent velocity superposition of spin waves

In the previous section we discussed a special case of spin-waves where all atomic excitations have the same relative phase. The dressed-state EIT scheme was creating a Doppler-free dark state to which all the atoms, *independent of their velocity*, were contributing. Here we will discuss a case where one can do velocity selection of the excited atoms within a thermal atomic vapour ensemble. Yet it will be highly non-trivial selection, where one excites a superposition of two velocities, with both atom velocity groups being in a collectively excited (spin-wave) state. This is another example where strong dressing of states (discussed in Sec. 2.4.3) is crucial, providing selection of two velocity groups and a way of setting a well defined relative phase between them.

ACKNOWLEDGEMENTS: The theoretical model in this section was developed by the author to explain and model results of the experiment of Daniel Whiting.

3.3.1 Internal state pre-selection in a strong magnetic field

In performing qualitative modelling in the previous Section 3.2.5, we neglected the complex hyperfine structure F that was within the Doppler-broadened spectrum, as well as all the possible degenerate state projections m_F, and focused on a minimal four-level model that captured the essential physics. For closer quantitative comparison with theory, inclusion of all states would be necessary. However, even in the cases when this is possible, experimental systems requiring that are usually not reliably controllable to be readily used as a building blocks for more complex schemes for coherent control of atom-light states. The cold-atom experiments allow for state preparation and good control over dynamics, making them good systems for detailed quantitative modelling. Their current technological complexity is, however, a serious obstacle in scaling up this research for everyday applications. On the other hand, more compact solid state based systems, even with their internal dissipation controlled by cooling in cryostats, experience dephasing and resonance shifts due to impurities and sample-to-sample spread in the production process, that also makes scaling up of these systems difficult. That is why thermal atomic vapours, being a simple, easily scalable technology with reproducible atom-fixed properties, are still in the spotlight for applied research.

Vapour cells can be miniaturised [242] into compact volumes below 1 cm^3, and reproducibly manufactured. Thermal alkali vapours are already used for magnetometry [243], electrometry [97, 244], in chip-scale atomic-clocks [245] and recently even for matter-wave interferometry [246]. Various interfaces with quantum light have also been demonstrated, including single photon sources and memories [247–249], and squeezed-light sources [250, 251]. However, state preparation in atomic vapours is difficult, and usually relies on optical pumping [252]. For pumping to be efficient, atom-spin relaxation on the cell walls has to be prevented, which is difficult in small volume cells. Coatings on the cell walls can be used to prevent relaxation, or a buffer gas can be added to slow-down atom diffusion to the walls. Both approaches have important limitations. Wall-coatings are often limited to low-temperature operation (paraffin) or difficult to consistently apply (OTS [253, 254]), while buffer gases can perturb highly-excited states in collisions [220].

The alternative to state *preparation* is state *selection*, which can easily be done in high magnetic fields (Sec. 2.4.2) that can split energies of the states enough to allow individual addressing of the transitions even in presence of Doppler broadening. This

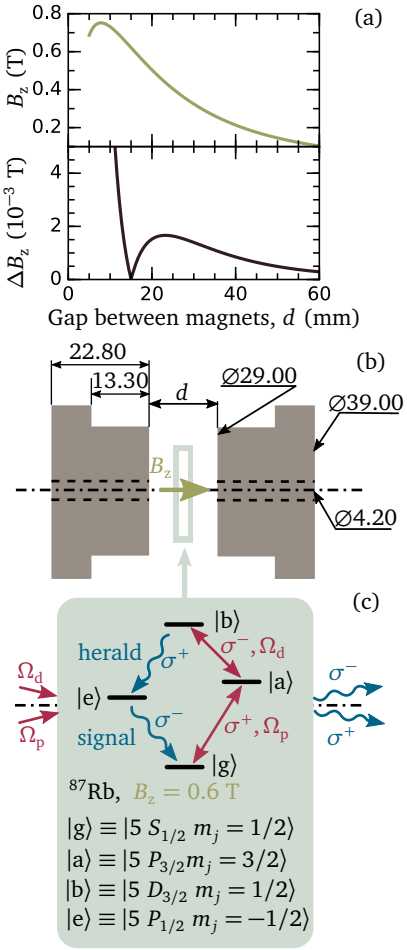

Figure 3.16: Atomic internal state pre-selection in a strong magnetic field. A pair of niobium magnets (b) creates strong magnetic field in the gap between them (a). For the given geometry (b, dimensions in mm), calculated axial field B_z and its maximal variation over 2 mm vapour cell ΔB_z is calculated on (b). The field splits energy levels of 2 mm thick rubidium vapour, placed in the gap between them, more then a Doppler-broadened transition linewidth, allowing isolation of the given four-level system (c).

old approach to achieving clean atom dynamics [255] entered into a renaissance recently thanks to the availability of compact strong permanent Neodymium magnets and several mm thick vapour cells. Compact pairs (on the ~ 1 cm scale) of these magnets [Fig. 3.16(b)] provide fields of ~ 0.6 T in the gap between them [Fig. 3.16(a)], that can split individual transitions by more than the Doppler-broadened linewidth in this hyperfine Paschen-Back regime. That allows addressing of individual transitions between $|m_J m_I\rangle$ states. The simplicity of the isolated experimental level structure allows fine *quantitative* comparisons with theory [256] and precise measurements of quantities like dipole-matrix elements between excited states [257].

In a recent experiment by Dan Whiting et.al. [96], the diamond scheme presented on Fig. 3.16(c) was isolated in a rubidium thermal vapour (for more details about experiment see Ref. [96]). Coherent laser driving of $|\mathrm{g}\rangle \leftrightarrow |\mathrm{a}\rangle \leftrightarrow |\mathrm{b}\rangle$ was supposed to initialize the system for operation as a heralded single-photon source, whereby detection of a single fluorescence photon (herald) on $|\mathrm{b}\rangle \rightarrow |\mathrm{e}\rangle$ indicates imminent emission of the second photon (signal) on the $|\mathrm{e}\rangle \rightarrow |\mathrm{g}\rangle$ transition. However close inspection of the measurements showed that the probability for detection of the signal photon at time t, conditioned on detection of the herald photon on $t = 0$, showed oscillations in time t. This was reminiscent of time-domain interference (beats) of two waves. However, what was interfering in this simple four-level system?

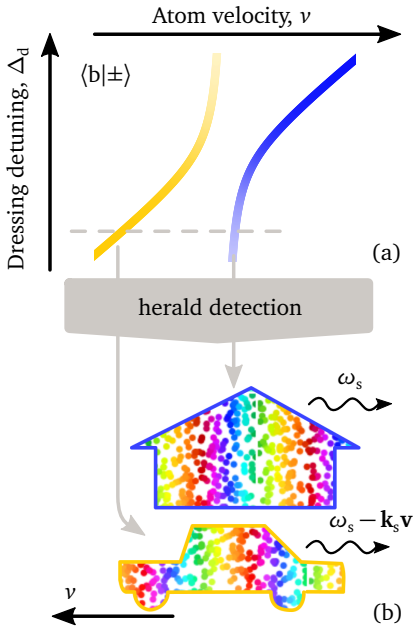

Figure 3.17: A simple model of collective beats. (a) Depending on the strength Ω_d and detuning Δ_d of the dressing, two different velocity classes v will be resonantly excited, with relative phase of excited $|\mathrm{b}\rangle$ state in each of the two dressed-state resonances $|\pm\rangle$ being π out of phase. For off resonant dressing (dashed line), one velocity class is nearly stationary, while the other moves away with velocity v. Herald detection maps that phase and velocity distribution into the spin-wave in between $|\mathrm{e}\rangle$ and $|\mathrm{g}\rangle$ states (b). Due to Doppler effect, emission between the two spins-waves, initially set out of phase, will have frequency offset of $\mathbf{k}_s\mathbf{v}$, causing beats in signal photon detection probability.

3.3.2 Coherent selection of motional state with strong dressing

In the experiments [96] with the diamond scheme presented on Fig. 3.16(c), the driving laser Ω_d was strongly dressing states $|\mathrm{a}\rangle$ and $|\mathrm{b}\rangle$. In the semi-dressed basis, as we have seen in Sec. (2.4.3), transition resonances for the two dressed states $|\pm\rangle$ that probe field sees will be split. Within atomic thermal vapour with a Boltzmann distribution of atomic velocities, two different velocity groups will have a Doppler shift that will bring them into resonance with one of the two dressed states [Fig. 3.17(a)]. Importantly, as we noted in Sec. (2.4.3), strong dressing also sets a well defined relative phase for the excitation of state $|\mathrm{b}\rangle$, which will be exactly π out of phase between the dressed-states $|+\rangle$ and $|-\rangle$.

Now we can piece together the full picture of what happens in the experiment [96]. Detection of a herald photon maps excitation initially in state $|\mathrm{b}\rangle$ into state $|\mathrm{e}\rangle$, as a collective, spin-wave excitation, as we will see in the following section. However, since we don't know which of the two atom velocity groups decayed, the excitation is stored as a superposition of the two spin-waves that move relative to each other with velocity v. This velocity is fixed by the resonance conditions for $|\pm\rangle$ states, controlled by the strength and detuning of the dressing. For off-resonant driving Δ_d the two velocity classes will correspond to one spin-wave moving with velocity v, while the other spin-wave is nearly stationary, illustrated by the car and house in Figure 3.17(b). Their initial phase is fixed to be π out of phase by strong dressing, causing destructive interference between the signal emission events from the two spin-waves. However, the relative phase of the emission events from the two classes will evolve in time as $\mathbf{k}_s \cdot \mathbf{v}$ due to the Doppler effect (or, equivalently due to relative motion of the two spin-waves), causing observed beats. With this picture in mind, we will proceed to analyse the situation quantitatively.

3.3.3 Theoretical derivation

In the following we derive a theoretical prediction for quantum beats in the single photon emission from the diamond level scheme due to spin-wave motion. The aim is to find the herald-signal joint-detection expectation value $\langle \hat{E}_{\rm s}^{\dagger}(t+\tau)\hat{E}_{\rm s}(t+\tau)\hat{E}_{\rm h}^{\dagger}(t)\hat{E}_{\rm h}(t)\rangle$ from a spatially extended atomic ensemble, where $\hat{E}_{\rm h\ldots s}^{\dagger}(t)\hat{E}_{\rm h\ldots s}(t)$ is the photon count at time t in herald and signal channels respectively.

Consider the dynamics of an ensemble of N four-level atoms, enumerated with j, located at $\mathbf{r}_j$ and moving with velocities $\mathbf{v}_j$, coupled to electromagnetic field (EM) modes (Fig. 3.18). Two of these modes are the strong pump and dressing laser fields that will be treated as classical driving fields, directed along the wave-vectors $\mathbf{k}_{\rm p}$ and $\mathbf{k}_{\rm d}$ with driving strengths given by Rabi frequencies $\Omega_{\rm p}$ and $\Omega_{\rm d}$. All the empty (vacuum) EM modes, except the two corresponding to the $\mathbf{k}_{\rm h}$ and $\mathbf{k}_{\rm s}$, will be treated as usual Markovian reservoir. Coupling to these modes gives rise to spontaneous emission with rates $\Gamma_{j,\beta}$. Dynamics of the two field modes, whose energies correspond to the $|{\rm b}\rangle \to |{\rm e}\rangle$ and $|{\rm e}\rangle \to |{\rm g}\rangle$ transitions, and whose spatial directions, labelled by the wave vectors $\mathbf{k}_{\rm h}$ and $\mathbf{k}_{\rm s}$ respectively, are defined by the directions of the single-mode inputs of the single-photon detectors used for detection of herald and signal photons in the experiment, will be considered separately. The system is analysed in the $\bigotimes_j |\alpha_j,\mathbf{r}_j,\mathbf{v}_j\rangle \bigotimes |\hat{n}_{\mathbf{k}_{\rm h}}\rangle \bigotimes |\hat{n}_{\mathbf{k}_{\rm s}}\rangle$, $\alpha \in \{{\rm g},{\rm a},{\rm b},{\rm e}\}$, basis. Dynamics of the internal degrees of freedom is described with the Hamiltonian $\bar{\mathscr{H}} = \bar{\mathscr{H}}_1 + \bar{\mathscr{H}}_2$ ($h=1$), where

$$\begin{aligned}\bar{\mathscr{H}}_1 = &\sum_j \left[\omega_{\rm a}|{\rm a}_j\rangle\langle{\rm a}_j| + \omega_{\rm b}|{\rm b}_j\rangle\langle{\rm b}_j| + \omega_{\rm e}|{\rm e}_j\rangle\langle{\rm e}_j|\right] \\ &+ \sum_j \left[\frac{\Omega_{\rm p}}{2}\,{\rm e}^{i\mathbf{k}_{\rm p}\cdot\mathbf{r}_j(t)-i\omega_{\rm p}t}\,|{\rm a}_j\rangle\langle{\rm g}_j| + \frac{\Omega_{\rm d}}{2}\,{\rm e}^{i\mathbf{k}_{\rm d}\cdot\mathbf{r}_j(t)-i\omega_{\rm d}t}\,|{\rm b}_j\rangle\langle{\rm a}_j| + {\rm H.c.}\right] \qquad (3.5)\end{aligned}$$

describes driving in the rotating wave approximation (RWA) of an ensemble of four level systems by strong probe and dressing driving fields treated as classical fields with respective frequencies $\omega_{\rm p}$ and $\omega_{\rm d}$, driving $|{\rm g}\rangle \leftrightarrow |{\rm a}\rangle$ and $|{\rm a}\rangle \leftrightarrow |{\rm b}\rangle$ transitions respectively. Energies of the states $|\alpha\rangle$ are ω_α. Additionally

$$\bar{\mathscr{H}}_2 = \sum_j \left[g_{\rm h}\,{\rm e}^{-i\mathbf{k}_{\rm h}\cdot\mathbf{r}_j+i\omega_{\rm h}t}\,\hat{a}_{\mathbf{k}_{\rm h}}^{\dagger}\,|{\rm b}_j\rangle\langle{\rm e}_j| + g_{\rm s}\,{\rm e}^{-i\mathbf{k}_{\rm s}\cdot\mathbf{r}_j+i\omega_{\rm s}t}\,\hat{a}_{\mathbf{k}_{\rm s}}^{\dagger}\,|{\rm g}_j\rangle\langle{\rm e}_j| + {\rm H.c.}\right] \qquad (3.6)$$

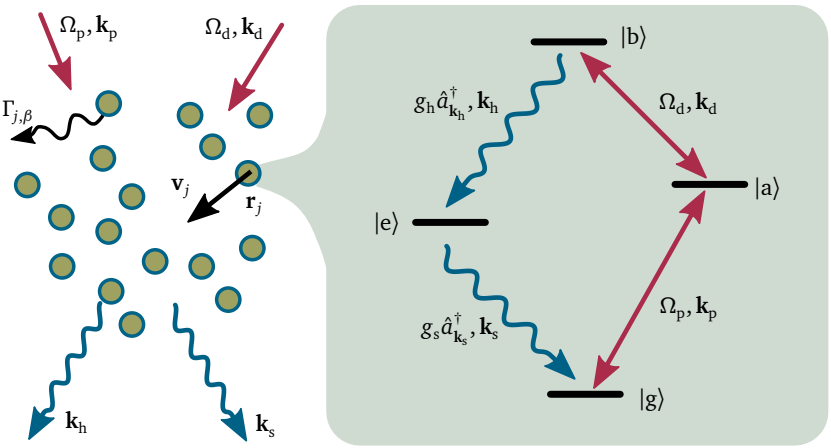

Figure 3.18: Structure of single-photon source based on diamond scheme. Spatially extended ($\max[|\mathbf{r}_i - \mathbf{r}_j|] > 2\pi/\mathbf{k}_{\rm s}$) medium containing N atoms, enumerated by j, located at $\mathbf{r}_j$, and moving with velocities $\mathbf{v}_j$. Internally (right inset) atoms have four levels, and are driven by pump and dressing fields with Rabi frequencies $\Omega_{\rm p}$ and $\Omega_{\rm d}$. Atoms can decay to the herald mode $\mathbf{k}_{\rm h}$ and the signal mode $\mathbf{k}_{\rm s}$ with under the influence of $g_{\rm h}\hat{a}_{\mathbf{k}_{\rm h}}$ and $g_{\rm p}\hat{a}_{\mathbf{k}_{\rm s}}$, or to one of the other modes β with rate $\Gamma_{j,\beta}$. The system is analysed in $\bigotimes_j |\alpha_j,\mathbf{r}_j,\mathbf{v}_j\rangle \bigotimes |\hat{n}_{\mathbf{k}_{\rm h}}\rangle \bigotimes |\hat{n}_{\mathbf{k}_{\rm s}}\rangle$, $\alpha \in \{{\rm g},{\rm a},{\rm b},{\rm e}\}$, basis coupled to the Markovian bath of other vacuum modes.

describes coupling of an ensemble of atoms in the RWA to the two vacuum modes aligned with herald and signal detector directions. Coupling strengths between atoms and the herald and signal detector field modes, g_h and g_s respectively, are formally given by $g_\mathrm{s} = \sum_{\mathbf{k}\in\mathbf{k}_\mathrm{s}\pm\Delta\mathbf{k}} g_\mathrm{be}$ (similarly for g_h) where $|\Delta\mathbf{k}| \ll |\mathbf{k}|$ defines the range of emitted photon directions that hit the detector's sensitive area, and g_be is the vacuum Rabi coupling frequency. Atom-field coupling to modes other than the herald and signal mode is described by the Lindblad superoperator $L[\hat{\rho}_N] = \sum_{j,\beta}(L_{j,\beta}\hat{\rho}_N L_{j,\beta}^\dagger - \frac{1}{2}L_{j,\beta}^\dagger L_{j,\beta}\hat{\rho}_N - \frac{1}{2}\hat{\rho}_N L_{j,\beta}^\dagger L_{j,\beta})$, acting on the system's density matrix $\hat{\rho}_N$, where $L_{j,\beta}$ are decay channels of atom j, enumerated by β. Since the atom coupling to the single spatial modes $\mathbf{k}_\mathrm{h}$ and $\mathbf{k}_\mathrm{s}$ described by $\bar{\mathscr{H}}_2$ (Eq. 3.6), is negligible compared to the coupling to all the other spatial modes with energies corresponding to decays $|\mathrm{b}\rangle \to |\mathrm{e}\rangle$ and $|\mathrm{e}\rangle \to |\mathrm{g}\rangle$, the decay of the $|\mathrm{b}\rangle$ and $|\mathrm{e}\rangle$ states is still described to an excellent approximation by the usual spontaneous decay rates Γ_b and Γ_e. Finally, evolution of the external degrees of freedom due to atomic motion, is accounted for by classical dynamics $\mathbf{r}_j(t) = \mathbf{r}_j(0) + \mathbf{v}_j t$.

Before solving the dynamics, we will choose a convenient rotating basis by applying the unitary transformation

$$\begin{aligned}\hat{U} \quad = \exp\Big(i\sum_j \quad & \Big\{\big[\omega_\mathrm{p} t - \mathbf{k}_\mathrm{p}\cdot(\mathbf{r}_j(0)+\mathbf{v}_j t)\big]\ |\mathrm{a}_j\rangle\langle\mathrm{a}_j| \\ & + \big[(\omega_\mathrm{p}+\omega_\mathrm{d})t - (\mathbf{k}_\mathrm{p}+\mathbf{k}_\mathrm{d})\cdot(\mathbf{r}_j(0)+\mathbf{v}_j t)\big]\ |\mathrm{b}_j\rangle\langle\mathrm{b}_j| \\ & + \omega_\mathrm{e} t\ |\mathrm{e}_j\rangle\langle\mathrm{e}_j|\Big\}\Big). \end{aligned} \tag{3.7}$$

In the new basis, the evolution Hamiltonian is $\mathscr{H}_1 + \mathscr{H}_2 = \hat{U}\bar{\mathscr{H}}\hat{U}^\dagger + i\frac{\mathrm{d}\hat{U}}{\mathrm{d}t}\hat{U}^\dagger$, where

$$\begin{aligned}\mathscr{H}_1 &= \sum_j \big[-\Delta_1 |\mathrm{a}_j\rangle\langle\mathrm{a}_j| - \Delta_2 |\mathrm{b}_j\rangle\langle\mathrm{b}_j|\big] \\ &\quad + \sum_j \left[\frac{\Omega_\mathrm{p}}{2}\ |\mathrm{a}_j\rangle\langle\mathrm{g}_j| + \frac{\Omega_\mathrm{d}}{2}\ |\mathrm{b}_j\rangle\langle\mathrm{a}_j| + \mathrm{H.c.}\right], \end{aligned} \tag{3.8}$$

$$\begin{aligned}\mathscr{H}_2 = \sum_j \Big\{ & g_\mathrm{h}\ \mathrm{e}^{-i(\mathbf{k}_\mathrm{h}-\mathbf{k}_\mathrm{p}-\mathbf{k}_\mathrm{d})\cdot\mathbf{r}_j(0) + i[\omega_\mathrm{h}+\omega_\mathrm{e}-\omega_\mathrm{p}-\omega_\mathrm{d}+(\mathbf{k}_\mathrm{p}+\mathbf{k}_\mathrm{d}-\mathbf{k}_\mathrm{h})\cdot\mathbf{v}_j]t}\ \hat{a}^\dagger_{\mathbf{k}_\mathrm{h}}\ |\mathrm{e}_j\rangle\langle\mathrm{b}_j| \\ & + g_\mathrm{s}\ \mathrm{e}^{-i\mathbf{k}_\mathrm{s}\cdot\mathbf{r}_j + i(\omega_\mathrm{s}-\omega_\mathrm{e})t}\ \hat{a}^\dagger_{\mathbf{k}_\mathrm{s}}\ |\mathrm{g}_j\rangle\langle\mathrm{e}_j| + \mathrm{H.c.}\Big\}, \end{aligned} \tag{3.9}$$

where $\Delta_1 \equiv \omega_\mathrm{p} - \mathbf{k}_\mathrm{p}\cdot\mathbf{v}_j - \omega_\mathrm{a}$ and $\Delta_2 \equiv \omega_\mathrm{p} + \omega_\mathrm{d} - (\mathbf{k}_\mathrm{p}+\mathbf{k}_\mathrm{d})\cdot\mathbf{v}_j - \omega_\mathrm{b}$ are the single and two-photon driving field detunings respectively.

Since we are interested in the interference of amplitudes for photon emission originating from two spatially separated locations within our medium, we solve dynamics for all N atoms in the thermal ensemble. Since $g_\mathrm{h}, g_\mathrm{s} \ll \Omega_\mathrm{p}, \Omega_\mathrm{d}$, we can treat dynamics due to $\mathscr{H}_2$ perturbatively. In the zero-order approximation ($\mathscr{H}_2 = 0$), the system density matrix evolves just under driving $\mathscr{H}_1$ and dissipation $L[\ldots]$, as described by the master equation $\frac{\mathrm{d}}{\mathrm{d}t}\hat{\rho}_N = -i[\hat{\rho}_N, \mathscr{H}_1] + L[\hat{\rho}_N] \equiv \mathscr{L}[\hat{\rho}_N]$, reaching a steady state $\hat{\rho}_N^{(0)}$ under Liouvillian $\mathscr{L}$. The system evolution under $\mathscr{H}_1$ [Eq. (3.8)] decomposes into evolution of individual atoms $\hat{\rho}_N = \bigotimes_j \hat{\rho}_j \bigotimes |0_{\mathbf{k}_\mathrm{h}} 0_{\mathbf{k}_\mathrm{s}}\rangle\langle 0_{\mathbf{k}_\mathrm{h}} 0_{\mathbf{k}_\mathrm{s}}|$, where $\hat{\rho}_j$ is the single atom density matrix for the j-th atom. In particular, atoms with the same velocity $\mathbf{v}$ at different locations will evolve under $\mathscr{H}_1$ to the same single-atom density matrix $\hat{\rho}(\mathbf{v})$. From this it seems that relative atomic positions are irrelevant. We shall see, however, that relative positions of the atoms in the ensemble play a

crucial role, imprinting important relative phase factors through the action of $\mathscr{H}_2$ (Eq. 3.9).

In order to obtain the herald-signal joint-detection correlation function $g^{(2)}_{\mathrm{h,s}}(\tau)$ we are interested in calculating $\langle \hat{E}^\dagger_{\mathrm{s}}(t+\tau)\hat{E}_{\mathrm{s}}(t+\tau)\hat{E}^\dagger_{\mathrm{h}}(t)\hat{E}_{\mathrm{h}}(t)\rangle$. The first non-zero contribution to this element originates from the second order perturbation by $\mathscr{H}_2$ (Fig. 3.19). Initially, $\mathscr{H}_2$ acts on $\hat{\rho}^{(0)}_N$, causing a herald photon emission at some time t. The system will subsequently evolve under $\mathscr{L}$ for some time τ, before a signal photon is emitted under the influence of $\mathscr{H}_2(t+\tau)$. These two emission events give

$$\langle \hat{E}^\dagger_{\mathrm{s}}(t+\tau)\hat{E}_{\mathrm{s}}(t+\tau)\hat{E}^\dagger_{\mathrm{h}}(t)\hat{E}_{\mathrm{h}}(t)\rangle = \mathrm{Tr}\left[\hat{E}^\dagger_{\mathrm{s}}(t+\tau)\hat{E}_{\mathrm{s}}(t+\tau)\hat{E}^\dagger_{\mathrm{h}}(t)\hat{E}_{\mathrm{h}}(t)\,\hat{\rho}^{(2)}_N\right], \quad (3.10)$$
$$\hat{\rho}^{(2)}_N = \mathscr{H}_2(t+\tau)\,\mathrm{e}^{-i\mathscr{L}\tau}[\mathscr{H}_2(t)\,\rho^{(0)}_N\,\mathscr{H}^\dagger_2(t)]\,\mathscr{H}^\dagger_2(t+\tau),$$

where the trace is over all atomic degrees of freedom, as well as herald and signal modes.

We will now analyse the emission process step-by-step. Looking into the time dependence of atom coupling to the herald mode, i.e. the terms containing $\hat{a}_{\mathbf{k}_{\mathrm{h}}}$ in $\mathscr{H}_2$ (Eq. 3.9), we see that for atoms with velocity $\mathbf{v}$ the dominant decay is in the mode with frequency $\omega_{\mathrm{h}} = \omega_{\mathrm{p}} + \omega_{\mathrm{d}} - \omega_{\mathrm{e}} - (\mathbf{k}_{\mathrm{p}} + \mathbf{k}_{\mathrm{d}} - \mathbf{k}_{\mathrm{h}})\cdot\mathbf{v}_j$. Starting from a steady state density matrix $\hat{\rho}^{(0)}_N$ achieved under $\mathscr{L}$, emission of a photon into a herald mode acts on the states as

$$\hat{\rho}^{(1)}_N(t) \equiv \mathscr{H}_2\hat{\rho}^{(0)}_N\mathscr{H}^\dagger_2 \propto \sum_i c_i \left[\sum_{j_1} c'_{j_1}\, g_{\mathrm{h}}\, \mathrm{e}^{-i(\mathbf{k}_{\mathrm{h}}-\mathbf{k}_{\mathrm{p}}-\mathbf{k}_{\mathrm{d}})\cdot\mathbf{r}_{j_1}(t)}|\ldots \mathrm{e}_{j_1}\ldots 1_{\mathbf{k}_{\mathrm{h}}}\rangle\right]$$
$$\cdot\left[\sum_{j_2} c'_{j_2}\, g_{\mathrm{h}}\, \mathrm{e}^{i(\mathbf{k}_{\mathrm{h}}-\mathbf{k}_{\mathrm{p}}-\mathbf{k}_{\mathrm{d}})\cdot\mathbf{r}_{j_2}(t)}\langle\ldots \mathrm{e}_{j_2}\ldots 1_{\mathbf{k}_{\mathrm{h}}}|\right]. \quad (3.11)$$

We see that emission, and subsequent detection of the herald photon, projects the system in a state where *single excitation is stored collectively as a coherent spin-wave* with a phase period variation given by the wave vector $\mathbf{k}_{\mathrm{h}} - \mathbf{k}_{\mathrm{p}} - \mathbf{k}_{\mathrm{d}}$. Since the broad-band detection scheme does not discern the frequency of the herald photon ω_{h}, we have $\hat{E}_{\mathrm{h}} = \sum_{\omega_{\mathrm{h}}} \hat{a}_{\mathbf{k}_{\mathrm{h}}}$ where the sum over ω_{h} encompasses the full Doppler broadened

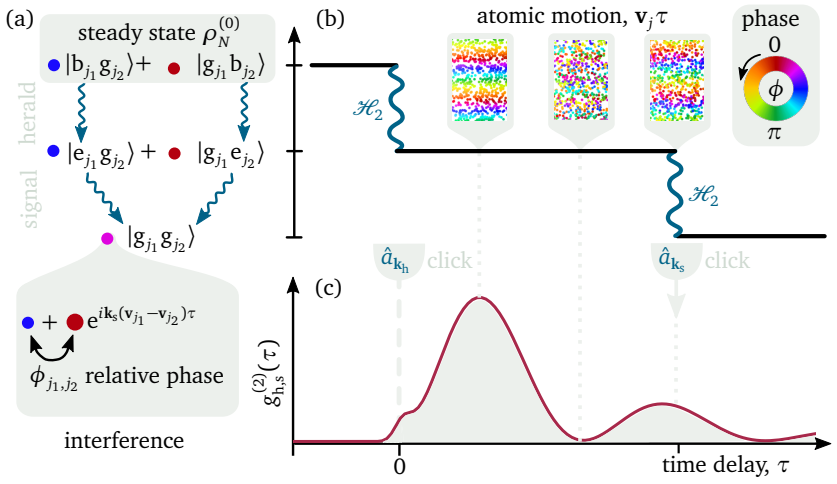

Figure 3.19: Collective decay leading to interference in signal emission amplitude. (a) Initial strong driving and spontaneous decays under $\mathscr{L}$ prepare the system in the steady state $\hat{\rho}^{(0)}_N$, part of which are states where atoms j_1 and j_2 are in the superposition of being in ground $|\mathrm{g}\rangle$ and bare state $|\mathrm{b}\rangle$. Herald detection maps the steady state amplitudes and phases into a superposition of excited states $|\mathrm{e}\rangle$. The imprinted relative phase of the medium changes due to atomic motion (b, shown in insets). Since both of these decays contribute to the amplitude of the same ground state (a, bottom inset) there appears a time-dependant factor in the collective emission amplitude. That leads to beats in the probability of signal photon emission (c) over time τ.

emission profile from the vapour, and the system state will be projected into a state where *excitation is stored in all atomic velocity classes*. In the experiment, for large dressing field detunings, two velocity groups provide dominant contributions: one nearly stationary, and the other with a narrow velocity distribution centred around non-zero velocity (Fig. 3.20). Subsequently, during time τ atoms move to new locations $\mathbf{r}_j(\tau) = \mathbf{r}_j(0) + \mathbf{v}_j\tau$. The internal system state evolves only due to the atoms in state $|\mathrm{e}\rangle$, since other atoms are already in a steady state of $\mathscr{L}$. State $|\mathrm{e}\rangle$ is decoupled from $\mathscr{H}_1$ (Eq. 3.8), but evolves due to spontaneous decay and dephasing collisions under $L[\ldots]$, resulting in the amplitude reduction of $\exp(-\gamma\tau)$ given by a rate γ. Some time τ later, a signal photon will be emitted, leaving the system in state

$$\begin{aligned}\hat{\rho}_N^{(2)} &\equiv \mathscr{H}_2(\tau)\,\hat{\rho}_N^{(1)}(t+\tau)\,\mathscr{H}_2^\dagger(\tau)\\ &\propto \exp(-2\gamma\tau)\\ &\quad\times\left\{\sum_{j_1}\exp[-i(\mathbf{k}_\mathrm{h}+\mathbf{k}_\mathrm{s}-\mathbf{k}_\mathrm{p}-\mathbf{k}_\mathrm{d})\cdot\mathbf{r}_{j_1}(t)+i(\omega_\mathrm{s}-\mathbf{k}_\mathrm{s}\cdot\mathbf{v}_{j_1}-\omega_\mathrm{e})\tau]\right.\\ &\qquad\left.\cdot|\ldots \mathrm{g}_{j_1}\ldots 1_{\mathbf{k}_\mathrm{h}}1_{\mathbf{k}_\mathrm{s}}\rangle\right\}\\ &\quad\times\left\{\sum_{j_2}\exp[i(\mathbf{k}_\mathrm{h}+\mathbf{k}_\mathrm{s}-\mathbf{k}_\mathrm{p}-\mathbf{k}_\mathrm{d})\cdot\mathbf{r}_{j_2}(t)-i(\omega_\mathrm{s}-\mathbf{k}_\mathrm{s}\cdot\mathbf{v}_{j_2}-\omega_\mathrm{e})\tau]\right.\\ &\qquad\left.\cdot\langle\ldots \mathrm{g}_{j_2}\ldots 1_{\mathbf{k}_\mathrm{h}}1_{\mathbf{k}_\mathrm{s}}|\right\}\\ &\quad+(\ldots),\end{aligned}\tag{3.12}$$

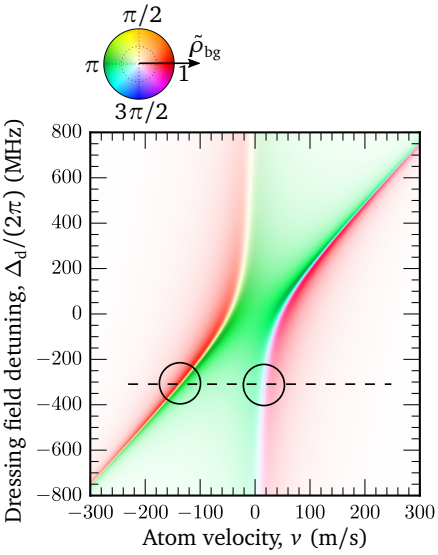

Figure 3.20: Calculation of ρ_{bg} coherence for dressed system. Parameters $\Omega_\mathrm{d} = 2\pi \times 170$ MHz, $\Omega_\mathrm{p} = 2\pi \times 30$ MHz, $\Delta_\mathrm{p} = 0$ for system shown on Fig. 3.16(c) are same as in experiment in Ref. [96]. For large dressing detunings $\Delta_\mathrm{d} \approx 2\pi \times 330$ MHz (dashed horizontal line) normalized coherence shown on plot $\tilde{\rho}_{\mathrm{bg}}(v, \Delta_\mathrm{d})$ has two peaks centred around phases $\pi/2$ and $3\pi/2$ (left and right circle respectively), that correspond to the car and house in the simple conceptual image presented in Fig. 3.17.

where omitted terms $(\ldots)$ do not contribute to the correlated emission of photons in the signal and idler channels[4]. We see that in order for this event to have significant probability at any time τ, the emitted signal photon will have frequencies centred around $\omega_\mathrm{s} = \omega_\mathrm{e} + \mathbf{k}_\mathrm{s}\cdot\mathbf{v}_j$, i.e. velocity classes differing by $\delta\mathbf{v}$ will emit photons with frequencies differing by $\mathbf{k}_\mathrm{s}\cdot\delta\mathbf{v}$, with *well defined initial relative phases and amplitudes* inherited from the initial dressed states in $\hat{\rho}_N^{(0)}$ through the emission of an initial herald photon. Crucially, since the signal detector does not discern the close energies of the emitted photons, in calculating the amplitude for the detection event $\hat{E}_\mathrm{s} = \sum_{\omega_\mathrm{s}}\hat{a}_{\mathbf{k}_\mathrm{s}}$ we have to sum over the range of ω_s corresponding to the detector bandwidth, and in this way we *do not measure which velocity class emitted the signal photon*. In order for amplitudes of *single* photon detection from different velocity classes to interfere in time causing beats in the detected signal photon count following herald detection, photons *must not leave information in the atomic medium* about which atom stored the excitation. Initial steady states that fulfil this condition are the ones in which atoms j_1 and j_2 are in a coherent superposition, where one of them is excited to $|\mathrm{b}\rangle$ and the other is in the ground state $|\mathrm{g}\rangle$, i.e. $|\ldots \mathrm{g}_{j_1}\ldots \mathrm{b}_{j_2}\ldots\rangle$ and $|\ldots \mathrm{b}_{j_1}\ldots \mathrm{g}_{j_2}\ldots\rangle$. Since after two-photon decay both of the states end up with both of the atoms in the ground state $|\ldots \mathrm{g}_{j_1}\ldots \mathrm{g}_{j_2}\ldots\rangle$, there is no which-path information left in the medium about which of the two atoms decayed, leading to interference of amplitudes for decay over different atoms [Fig. 3.19(a)]. Therefore,

[4] Omitted terms are of the form $|\ldots 2_{\mathbf{k}_\mathrm{h}}0_{\mathbf{k}_\mathrm{s}}\rangle\langle\ldots| + \mathrm{H.c.}$.

we see that in evaluating Eq. 3.10, non-zero interfering elements[5] will originate from $\langle \ldots \mathrm{g}_{j_1} \ldots \mathrm{b}_{j_2} \ldots | \hat{\rho}_N^{(0)} | \ldots \mathrm{b}_{j_1} \ldots \mathrm{g}_{j_2} \ldots \rangle$ and the corresponding conjugate. Given the decomposition of dynamics under $\mathscr{L}$ to single-atom dynamics, contributing matrix elements traced over atoms other than j_1, j_2 are equal to $\hat{\rho}_{\mathrm{gb}}(\mathbf{v}_{j_1})\, \hat{\rho}_{\mathrm{bg}}(\mathbf{v}_{j_2})$, where $\hat{\rho}(\mathbf{v})$ is the single-atom density matrix reached as a steady-state solution for evolution under $\mathscr{L}$. Therefore the relative initial phase and amplitude of the emission from state $|\mathrm{e}\rangle$ is inherited in the herald emission process from $\hat{\rho}_{\mathrm{bg}}$.

Overall, the joint detection probability (Eq. 3.10) can be written as

$$\langle \hat{E}_{\mathrm{s}}^{\dagger}(t+\tau)\hat{E}_{\mathrm{s}}(t+\tau)\hat{E}_{\mathrm{h}}^{\dagger}(t)\hat{E}_{\mathrm{h}}(t)\rangle = \left| \sum_j g_{\mathrm{s}} g_{\mathrm{h}}\, \hat{\rho}_{\mathrm{bg}}(\mathbf{v}_j)\, \exp(-\gamma\tau)\, \exp(-i\mathbf{k}_{\mathrm{s}} \cdot \mathbf{v}_j \tau) \right. \\ \left. \exp[i(\mathbf{k}_{\mathrm{p}} + \mathbf{k}_{\mathrm{d}} - \mathbf{k}_{\mathrm{h}} - \mathbf{k}_{\mathrm{s}}) \cdot \mathbf{r}_j(t)] \right|^2 . \quad (3.13)$$

In order to obtain non-zero values, summation over random atomic positions $\mathbf{r}_j$ has to produce a constant value, which gives rise to the condition $\mathbf{k}_{\mathrm{p}} + \mathbf{k}_{\mathrm{d}} - \mathbf{k}_{\mathrm{h}} - \mathbf{k}_{\mathrm{s}} = 0$ which is the usual *wave matching condition* for wave-mixing processes in extended mediums, responsible for directional emission from spin-waves. When this condition is fulfilled, the remaining time dependent part can be written as an integral over different velocity classes

$$\langle \hat{E}_{\mathrm{s}}^{\dagger}(t+\tau)\hat{E}_{\mathrm{s}}(t+\tau)\hat{E}_{\mathrm{h}}^{\dagger}(t)\hat{E}_{\mathrm{h}}(t)\rangle \propto \left| \underbrace{\int_{\mathbf{v}} \mathrm{d}\mathbf{v}\; p(\mathbf{v})\, \rho_{\mathrm{bg}}(\mathbf{v}) \exp(-\gamma\tau)\, \exp(-i\mathbf{k}_{\mathrm{s}} \cdot \mathbf{v}\tau)}_{\equiv \Psi} \right|^2 , \quad (3.14)$$

where $p(\mathbf{v})$ is the probability density function that an atom has velocity $\mathbf{v}$. Note that this calculation only includes contributions from the correlated decays. There is also a constant background of uncorrelated decays produced by other events. For example, in this derivation we neglected term proportional to $\langle \ldots \mathrm{b}_j \ldots | \hat{\rho}_N^{(0)} | \ldots \mathrm{b}_j \ldots \rangle$. Since these terms do not contribute to interference of photon-emission amplitudes from multiple atoms in space, they don't cause beats in time, nor is their emission direction enhanced in any particular direction[6]. However these terms, ultimately proportional to $\hat{\rho}_{\mathrm{bb}}(\mathbf{v}_j)$, *contribute to the background signal*, since they will cause emissions to the signal spatial mode even when the $|\mathrm{b}\rangle \rightarrow |\mathrm{e}\rangle$ decay photon is not emitted in the herald spatial mode. Also, in general, following herald emission in channels other than $\mathbf{k}_{\mathrm{h}}$, there is no clear phase matching condition for the signal emission, which can also end up in $\mathbf{k}_{\mathrm{s}}$. This processes can happen since the initial herald emission in a spatially extended medium *is not* enhanced in any particular direction, any more than the usual fluorescence directionality of single-atom σ transition decays (Sec. 2.3.4), as can be seen from Eq. 3.11 since $\mathbf{k}_{\mathrm{h}} - \mathbf{k}_{\mathrm{p}} - \mathbf{k}_{\mathrm{d}} \neq \mathbf{0}$ for nearly parallel $\mathbf{k}_{\mathrm{d}}$ and $\mathbf{k}_{\mathrm{p}}$ as in this experiment [96]. Furthermore, in collisional processes, population can be transferred non-radiatively from $|\mathrm{a}\rangle$ to $|\mathrm{e}\rangle$ (see Sec. 2.6), causing additional background emission. Due to this, the normalised signal for detection

[5] There will be other terms that don't contribute to the beat signal since they don't interfere, but add to the background level of uncorrelated emission events. See discussion following Eq. (3.14).

[6] Their radiation has the same spatial dependence as single-atom fluorescence patterns discussed in Sec. 2.3.4.

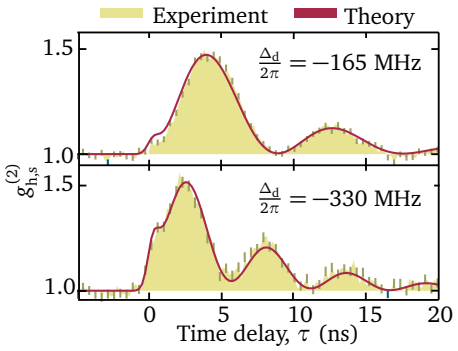

Figure 3.21: Collective beats: comparison of theory and experiment. Data and fitting by Daniel Whiting [96].

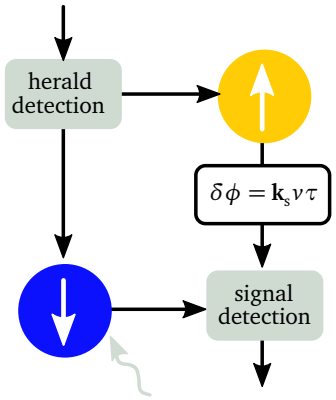

Figure 3.22: Interferometric measurement of phase between two atom velocity groups. Herald detection splits a single photon into collective excitation of the two velocity groups and measures their relative phase after recombining the excitation paths in signal detection after time τ. Relative velocity of the two collective excitations is v. External AC field (wavy line) can perturb only one of the velocity classes, imprinting a phase on it.

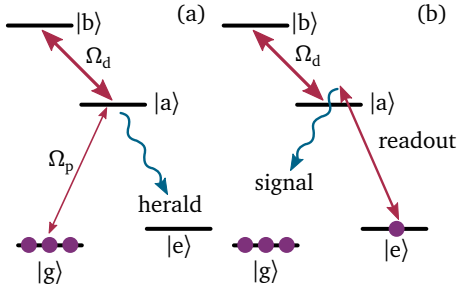

Figure 3.23: Inverted Y scheme for deterministic readout. (a) Herald detection prepares a system state where single excitation is collectively stored as spin-wave between $|g\rangle$ and $|e\rangle$ states, with *two* different spin-wave velocities set by dressing beam Ω_d. (b) After some time, readout pulse can be applied to determine relative phase, accumulated during excitation storage in two different velocity groups, by measuring the signal beats.

with low heralding efficiency will have the form

$$\frac{\langle \hat{E}_s^\dagger(t+\tau)\hat{E}_s(t+\tau)\hat{E}_h^\dagger(t)\hat{E}_h(t)\rangle}{\langle \hat{E}_s^\dagger\hat{E}_s\rangle\langle \hat{E}_h^\dagger\hat{E}_h\rangle} = 1 + c|\Psi|^2, \tag{3.15}$$

where c is a constant dependant on the background level.

3.3.4 Comparison of theory and experimental results

On Fig. (3.21) we show comparison between the theoretical prediction from the previous section and experimental results (data by Dan Whiting, for comparison over wider range of parameters see Ref. [96]). The signals match very well with theory, and exhibit coherence times on the order of the natural lifetime of $|e\rangle$. This compares positively with the pulsed four-wave mixing without a good state selection [258], where similar interference effects have been observed but with much shorter lifetimes, limited by motional dephasing.

3.3.5 Possible generalizations of the protocol

The very good agreement between data and theory raises a question whether this system can be used as a building block for quantum state manipulation, using maybe bi-chromatic single photon as a quantum resource as in Ref. [222] or for interfacing and entenglement of heterogenous systems with different resonant frequencies (see also discussion at the end of Sec. 3.2.1). We note that the setup is effectively an interferometer, where starting from an initial steady state, herald detection prepares the medium in a superposition of the two collective velocity classes. The signal detection at some time later provides recombination of these two interferometer branches and allows measurement of the relative phase. Probably the best state for interferometric measurements would be one achieved under resonant dressing $\Delta_p = \Delta_d = 0$. Then the two excited spin-waves would have equal amplitudes, and equal and opposite velocities set by the dressing laser power. Since two different velocity classes have two different, Doppler-shifted resonances, they will acquire different phase shifts upon application of, for example, off-resonant AC fields. However, with the current setup, the total time that the excitation spends split between the two spin-waves is not controlled and is limited by the lifetime of state $|e\rangle$. Effectively, the diamond scheme implements DCZL single-photon source [2] where readout, driven by the empty $\mathbf{k}_s$ mode, starts immediately after the storage of an excitation in $|e\rangle$. In principle this scheme can be made closer to the original DLCZ protocol, by using an inverted Y scheme as shown on Fig. 3.23. Dressing of the upper transition with Ω_d again provides two dressed states, which are resonantly coupled with Ω_p in two different, Doppler-shifted velocity classes. The main difference now is that detection a of herald photon, since it happens from state $|a\rangle$, will prepare two spin-waves with initially *non-shifted* (zero) relative phase, compared to π shifted relative phase in the protocol discussed above. Importantly, if $|g\rangle$ and $|e\rangle$ are selected from the ground-state hyperfine manifold, the $|e\rangle$ doesn't decay radiatively. Readout is then under experimental control, requiring application of a readout pulse [Fig. 3.23(b)]. Due to narrow velocity selection, the limited storage lifetime due to motional dephasing (Sec. 3.1) is also improved. Finally, note that the relative phase of the two velocity groups is insensitive to non-resonant perturbative

effects, since they offset atomic phases equally irrespective of atomic velocities, although they can reduce readout efficiency. Among such effects are atom-atom and atom-wall collisions, and static magnetic and electric fields.

3.3.6 Comparison of single-atom, many-atom quantum beats and Doppler superradiant beats

Beats in herald-signal joint-detection probability have many similarities with related single-atom beats [259]. Beats in herald-signal joint-detection probability are essentially many-atom beats happening due to emission-probability amplitudes from many atoms interfering, whereas in single-atoms beats, emission-probability amplitudes from several energy levels within single atom interfere. They were both discussed in a major review by S. Haroche in 1976. [259], when many-atom beats were expected to be non-observable in room-temperature atomic ensembles due to rapid atomic motion that would, as we have discussed in Sec. 3.2, dephase a spin wave in $\Lambda/\bar{v} \sim 1$ ns. At the time coherent dressing (Sec. 3.3.2) was not discussed. Here we will review single-atom quantum beats through the specific case of a recent experiment from Ref. [101]. We will then look at the simplest two models of single- and many- atom quantum beats, highlighting similarities and important differences.

An example of quantum beats observation is the recent experiment by Wade *et.al* [101], where caesium thermal vapour was exposed to a short laser pulse on D2 transition corresponding to 852 nm laser wavelength. Within the $\sim$ 1GHz bandwidth of the pulse, set by the short ($\approx$ 1 ns) pulse duration, are several hyperfine states of the 6 $P_{3/2}$ state [Fig. 3.24(a)]. Pulses are made with a Pockels cell, from a continuous (CW) laser locked to 6 $S_{1/2}$ $F = 4 \leftrightarrow$ 6 $P_{3/2}$ $F = 5$ transition with polarisation spectroscopy. In addition, a counter propagating 1470 nm CW laser, locked to 6 $P_{3/2}$ $F = 5 \leftrightarrow$ 7 $S_{1/2}$ $F = 4$ transition, is driving Rabi oscillations to the 7 $S_{1/2}$ $F = 4$ state. The fluorescence from the 6 $P_{3/2}$ excited state is monitored with a single-photon detector to the side of the cell [Fig. 3.24(b)], that provides sub-ns resolution of the photon arrival times measured relative to the 852 nm laser pulses. For more details on the experimental setup, see Ref. [101].

For the moment we will neglect the CW 1470 nm laser. The broadband 852 nm laser pulse will excite *each of the atoms* in the *superposition* of the hyperfine levels. The initial phase for the amplitudes for excitation of different states is set by the drive laser pulse and the dipole matrix-elements $\langle 6\,S_{1/2}\,F=4\,m_F|e\hat{\mathbf{r}}\cdot\varepsilon_q|6\,P_{3/2}\,F'\,m'_F\rangle$ for coupling between the relevant states . If fluorescence detection is broadband, such that it detects decay from all 6 $P_{3/2}$ hyperfine states without differentiating between them, we *don't have which path information* for the decay event. Therefore, the amplitude of decay for every *single* atom will have to be calculated as a sum of the probability amplitudes from all the excited states. During a time τ in which an atom is excited, the probability amplitudes will acquire a relative phase $\tau\Delta$ corresponding to the energy differences Δ between the hyperfine states. Therefore, the probability for the corresponding photon emission events will exhibit oscillations in time τ (beats) with frequency Δ/h. Note that there is no contribution to the beats due to interference effects for photon emission from two different atoms (sharing single excitation or having two independent excitations). This is because the broadband laser pulse excites all the atom-velocity classes in the thermal vapour, resulting in motional dephasing (Sec. 3.1) that quickly destroys any well-defined average

ACKNOWLEDGEMENTS: single-quantum beats are done in collaboration with Christopher Wade. In particular, the author discussed underlying modelling approach, and highlighted importance of polarisation selection in experiment and theoretical treatment. The author designed and assembled laser locking electronics.

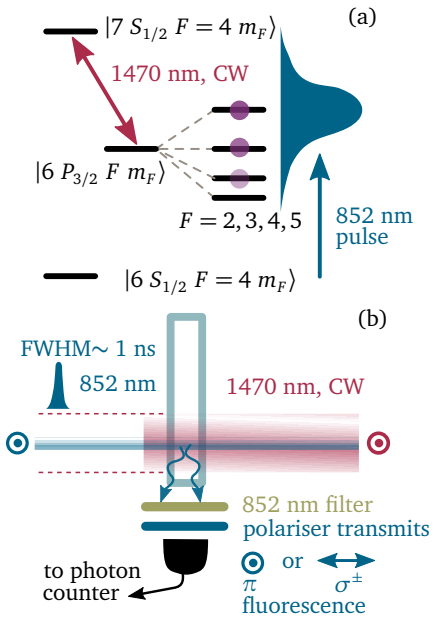

Figure 3.24: Experimental setup for observation of single-atom beats. (a) Relevant transitions in caesium. Short 852 nm pulse transfers population in superposition of hyperfine levels $|6\,P_{3/2}\,F\,m_F\rangle$, $F = 3,4,5$, while 1470 nm laser continuously (CW) drives predominantly $|6\,P_{3/2}\,F = 5\,m_F\rangle$ population to $|7S_{1/2}\,F = 4\,m_F\rangle$ state. (b) Both lasers have same linear polarisation (out of plane). With polariser on the side of the caesium filled vapour cell, one can select 852 nm fluorescence originating from π or $\sigma^{\pm}$ transitions.

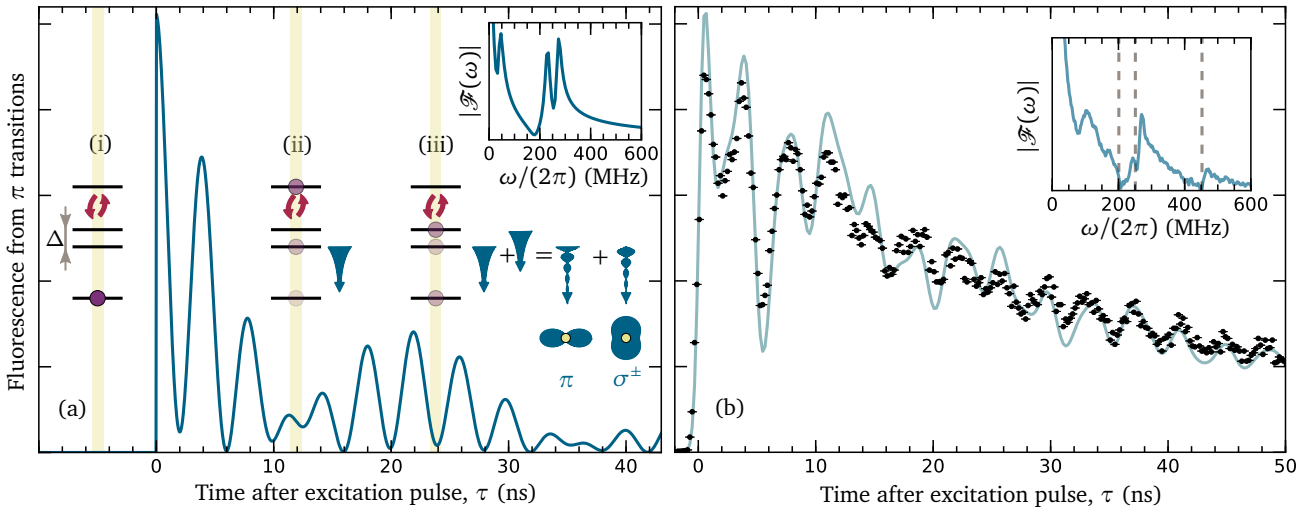

Figure 3.25: A simplified model of single-atom beats and comparison with experimental data. (a) Toy-model system of the experiment consists of four-levels (i), which excitation pulse prepares in the superposition state where two middle levels, separated in energy by Δ, are excited (iii). Fluorescence probability amplitude from both of this levels has individually exponentially decaying envelopes, however for broadband detection that cannot discern between the two frequencies, decay channels interfere, causing oscillatory fluorescence *redistribution* between π and $\sigma^{\pm}$ fluorescence channel (inset, bottom right). Constant coherent driving periodically shelves population of the upper middle level to the top level (ii), turning-off the interference of decays and associated beats temporarily. Inset shows amplitude of Fourier transform $\mathscr{F}(\omega)$ of the signal, with leftmost peak corresponding to the Rabi frequency of continuous driving Ω_{1470}, and the right peak, also split by Ω_{1470}, is centred around frequency Δ/h. (b) Full multi level model is more complicated due to m_F manifold and in total three middle levels $F = 3, 4, 5$, whose relative energy splittings are labelled on the inset with dashed lines. While the main features are captured with simplified model, ensemble averaging over all transitions and Doppler velocity classes reduces contrast. Experimental data and the multi level model fit are from Christopher Wade [101].

relative phase between different atoms.

Additionally the CW 1470 nm laser coherently drives population, preferentially from $F = 5$ state, to 7 $S_{1/2}$ state and back, through Rabi oscillations. In the simplest picture, presented on Fig. 3.25(a), this causes a periodic turn-off of the beats, whenever the probability amplitude for population of 6 $P_{3/2}$ $F = 5$ state is mapped through Rabi oscilations into amplitude of 7 $S_{1/2}$ state [Fig. 3.25(a.ii)]. Interestingly this is coherent manipulation, not a projective measurement of the atom-state, even thought photon is absorbed from the driving field which leaves information concerning whether the atom was in the $F = 5$ hyperfine state or some other state. This is because for a strong ($\alpha \gg 1$) coherent field $|\alpha\rangle = \exp(-|\alpha|^2/2)\sum_n \frac{\alpha^n}{\sqrt{n!}}|n\rangle$, overlap between states with average photon number of α and $\alpha - 1$ is essentially unity $\langle\alpha|\alpha-1\rangle \approx 1$. Single photon absorption from strong coherent field is therefore *not* measurable in a *single* shot measurement, and therefore unable to reveal atom state. Signals expected based on this simplified picture [Fig. 3.25(a)] are observed in experiments too [Fig. 3.25(b)], however due to presence of many velocity classes and m_F states, visibility is reduced, and the oscillation pattern is more complicated. Yet, the essential dynamics is the same as revealed by the Fourier transforms of the signal [insets on Fig. 3.25(a-b)]. Full modelling, accounting for fine basis manifold $|F, m_F\rangle$ can also be done. On the time-scales of the experiment ($\sim$ 30 ns) any residual magnetic fields in the lab introduce negligible state mixing through Larmor

precession[7], so we can choose to direct the quantization (z) axis along the electric field vector of the linearly polarised drive lasers, and examine each m_{F} manifold separately, since coherent dynamics driving π transitions factorises into action on individual subspaces defined by the m_{F} quantum number. The complexity of the obtained signals [full line on Fig. 3.25(b)] is another motivation for pursuing state selection as discussed in Sec. (3.3.1).

Similarities and differences of single-atom and many-atom beats, when a *single* excitation is shared among atoms, are presented and discussed in Figure. 3.26. An important thing to note is that in both cases the lifetime of the excitation (in the excited level) is neither changed nor modulated in the process. Instead, in both processes there is just interference occurring between different possible decay channels, increasing and reducing amplitudes for some of them in the process, but keeping decay in full space (4π steradians) fixed. In the single atom case, beats redistribute fluorescence between π and $\sigma^{\pm}$ decay channels, but the atomic decay is still described by a single exponential decay with lifetime Γ corresponding to the natural lifetime of the excited state (5 $P_{3/2}$ in the example above). Similarly, from the spatially extended sample discussed in section (3.3.3) the spin-wave of the form given in Eq. (3.1) *does not cause superradiance*, i.e. the atomic excitation doesn't decay faster as would be expected for the Dicke state [260]. Indeed, Dicke's argument, that a symmetric state like Eq. (3.1) for $\mathbf{k} = 0$ decays faster, is for an ensemble of dipoles *within* λ. Even in that limit of a densely localized system, in most cases it cannot directly be applied [47] as it neglects dipole-dipole interactions that are strong precisely in that limit. The problem is ultimately solvable with full diagonalization, at least for small, interacting dipolar samples, revealing sub-radiant and super-radiant modes [261, 262], however strong interactions between the dipoles play an important role in that case (i.e. the effect becomes cooperative). For *spatially-extended* systems ($\mathrm{Max}_{j_1,j_2}|\mathbf{r}_{j_1} - \mathbf{r}_{j_2}| \gg \lambda$), where we can neglect photon re-absorption (i.e. atom-atom interactions), spin-wave will have increased collective coupling *in a particular direction*, and simultaneously reduced decays in other spatial directions[8]. Overall, the decay of the stored excitation will again be described by a single non-modulated exponential, with the medium decaying equally in all spatial modes when the spin-wave is dephased, as in the case of many-atom quantum beats when signal detection probability is reduced [Fig. 3.26(b)]. Note that this is consistent with a $\sqrt{N}$ enhancement of the Rabi-driving frequency for N atoms in a blockaded volume [84], since the particular direction of the chosen field mode is that of the driving laser, and a blockaded ensemble has reduced collective coupling to the perpendicular electromagnetic field modes of the same frequency. Finally, this leads us to an important difference between the two types of beats, which is the possibility for an ensemble of atoms to emit light in a well-defined mode, whereas for a single atom in free space the choice is just between two polarisation modes with broad distribution (Fig. 2.8) in space. If the atomic superposition and state manipulation is done on the single-atom level as in Refs. [263, 264], one needs to use cavities to perform the efficient readout of the atomic state, whereas collective excitations

[7] Larmor frequency for electrons is $eg_{\mathrm{e}}B/(2m_{\mathrm{e}})$ which for residual fields of $B < 1$ G $= 10^{-4}$ T yields 2.8 MHz$\ll 1/(30$ ns).

[8] Although this in the literature is also sometimes called superradiance, it is different compared to Dicke case, since in the latter case Dicke arguments leads to faster decay of stored excitations, whereas in the former case, while we can realistically have build-up of coherence through collective decays, the ultimate result is only spatial (directional) and temporal *compression* of the emitted radiation, an interference affect that does not affect lifetime of stored excitation.

achieve that on their own, and don't require complicated setups for trapping single atoms in small EM-mode volume optical cavities.

The final important thing to note in the discussion of many-atom quantum beats is their difference between beats occurring due to a single excitation being stored collectively [as in Eq. (3.1)] and situations when many excitations are stored within a

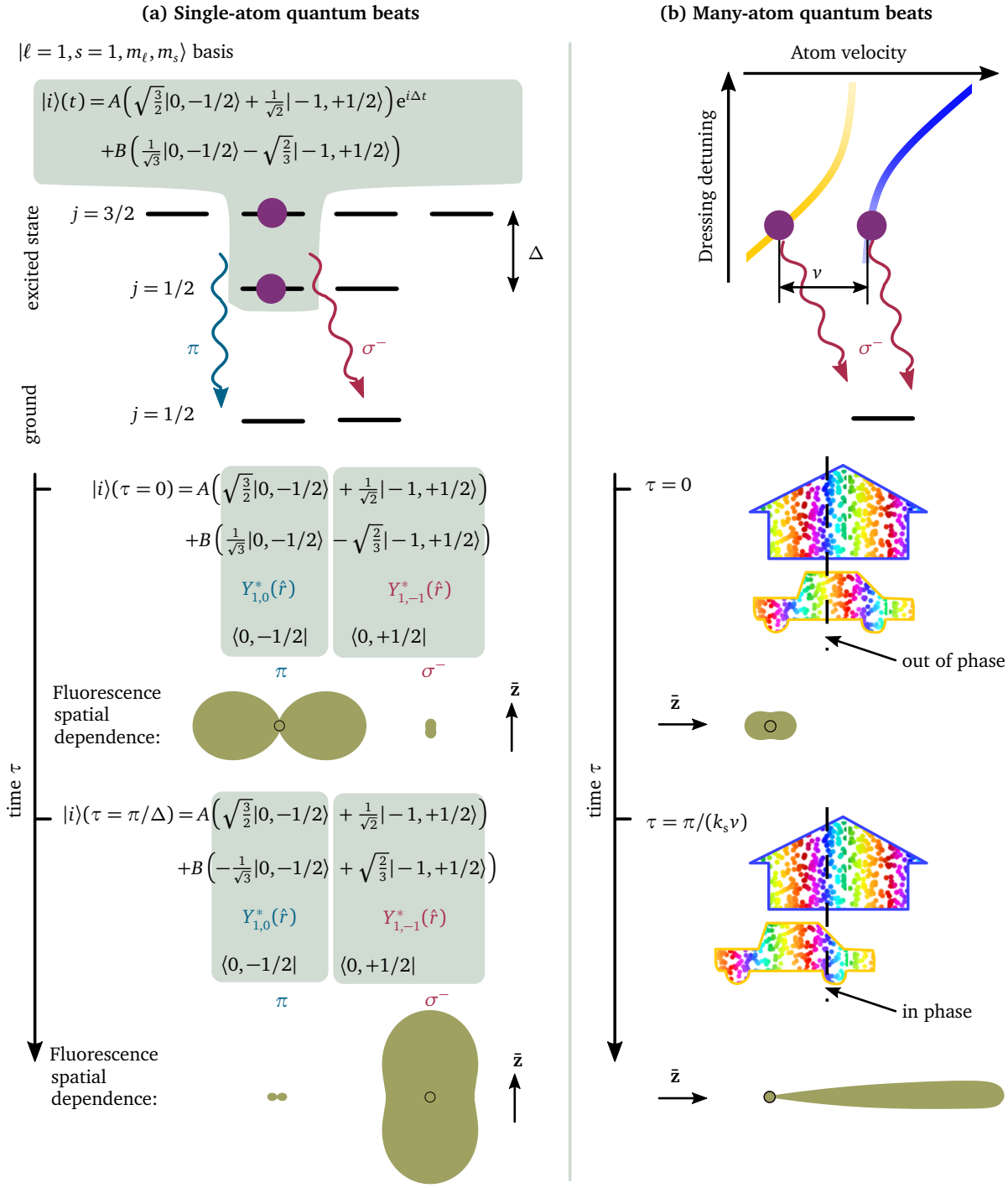

Figure 3.26: Comparison of single-atom (a) and many-atom quantum beats (b). (a) Minimal model for single-atom quantum beats demonstrating redistribution of fluorescence between the two decay channels over time. (b) Many-atom quantum beats when, when two spin waves are completely out of phase at $\tau = 0$ end up being directional in the same degree as single-atom quantum beats, however, in all other situations, radiation pattern is much more well localised in spatial direction. In both cases excitation decays over time given by individual single-atom decay.

medium. For many excitations coherent delocalization of single excitation among the states is not required and results can be understand in terms of interfering classical antennas. For example, in Ref. [265] the authors excited a caesium atomic system using the energy-level scheme presented on Fig. 3.27. The excitation was pulsed, but narrowband enough that the pulse bandwidth encompassed only one of the hyperfine states. Yet, since two hyperfine states are within the Doppler-broadened window, both states can be excited with a pulse, but they will correspond to two different velocity classes. Beats have been observed due to interference of fluorescence on $|a\rangle \rightarrow |e\rangle$ and $|b\rangle \rightarrow |e\rangle$ transitions. This looks similar to the earlier discussed beats from two spin-waves, however in Ref. [265] beats *cannot* be observed here if there is only a *single* excited atom, even though the medium can be in a superposition where one excitation is shared between two velocity classes. This is because these states don't decay to the ground state, but to state $|e\rangle$ that is initially completely empty. This effectively measures which-path information, since one could in principle measure which velocity group contains the excited state $|e\rangle$, determining which atom decayed. Interference in this case still exists, but it crucially depends on the fact that the excited spin-wave initially contains multiple excited atoms that can decay. Initially the spin wave also does not have well defined phase of emitted radiation[9], let alone phase matching condition for spatial direction of this emission[10], for decay to state $|e\rangle$. However, since initially multiple excitations are present, the gradual build-up of coherence and phase matching condition, responsible for directional emission[11], is possible under subsequent *collective* decays, described for decay in mode $\mathbf{k}$ by the action of operator $L_{\mathbf{k}} \propto \sum_j \exp(-i\mathbf{k}\cdot \mathrm{r}_j)(|e\rangle\langle a| + |e\rangle\langle b|)$. However, this *superradiant beats* scheme cannot support beats in fluorescence statistics if initially only a *single* excitation in the $\{|a\rangle, |b\rangle\}$ manifold is present, as it requires *multiple* collective decays for the build up of coherence.

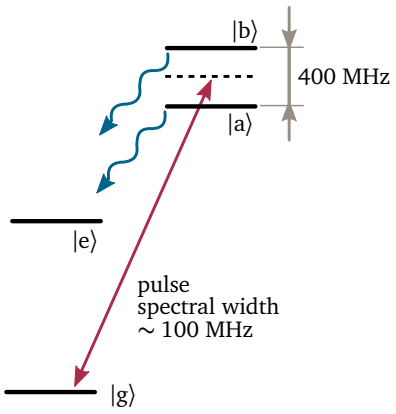

Figure 3.27: Scheme for observation of Doppler beats in superradiance. Narrowband pulse excites atoms in vapour into two hyperfine levels, $|a\rangle$ or $|b\rangle$, depending on Doppler-shifted resonance condition. Doppler beats in superradiance are observed due to interference of decays $|a\rangle \rightarrow |e\rangle$ and $|b\rangle \rightarrow |e\rangle$ happening in two *different* velocity groups of the atoms. Adopted from Ref. [265].

[9] Initially there is no spin-wave between ($|a\rangle$, $|b\rangle$) and $|e\rangle$, only between ($|a\rangle$, $|b\rangle$) and $|g\rangle$.

[10] As there is no coherence between $(|a\rangle, |b\rangle)$ and $|e\rangle$, there cannot be well-defined phase for emited radiation on that transition, and hence no interference effects and associated phase-matched directions exists.

[11] Symmetry of emitted radiation is then broken by the shape of the atomic ensemble, with the superradiant emission then directed along the longest axis of the sample, or by external seed field [266].

3.4 Summary

In this chapter we discussed two examples of controlling the motion of collective excitations (spin-waves). In the first example, we introduced a protocol for production of uniform-phase spin-waves that are insensitive to motion, through coherent four-level adiabatic-following state preparation. Uniform phase spin-waves are a universal resource for coupling multiple level schemes and different frequency fields, as they are independent of the particular field wave-vectors used in their production. For practical implementations of advanced deterministic protocols with this scheme, small scale (∼1 mm) cold-atom clouds are the most promising. In addition, narrow spectral features and good spatial localization can find applications in electrometry and selective small-volume probing and preparation. The second example is based on indeterministic state preparation through dissipative proces (spontaneous emission). There the spin-wave was sensitive to motion, but the selective, coherent preparation of this collective excitation was crucial for obtaining non-trivial dynamics. A detailed microscopic model of the dynamics was presented. It compares very well with experimental results, but also provides insights into the elementary processes involved. It highlights limitations, possible extensions for thermal-vapour based applications, and differences compared to some other schemes. Both examples discussed in this chapter relied crucially on strong state dressing in multi-step excitation schemes in order to achieve well-controllable collective excitations.

Driven-dissipative systems with power-law interactions

CHAPTER 4

This chapter explores many-body dynamics of strongly driven Rydberg atomic ensembles which contain many Rydberg excitations. In this regime we have to include inter-atomic interactions [Sec (2.5)] since they can qualitatively change the system's dynamics. There are two important properties that make dynamics of this system highly non-trivial, stimulating interest in their research. Firstly, this is a continuously driven system that releases energy through fluorescence decay, making it a many-body driven-dissipative system. Not only is this a region of non-equilibrium statistical physics[1] where we don't have powerful concepts like free energy in equilibrium statistical mechanics to provide, in principle, a recipe for finding system states, but it's also a region where we still have to appreciate which quantities are relevant, and possibly accept some new features stemming from the dynamic, driven-dissipative nature of the system. The second important property of the system is a range of interactions. In particular, dipole-dipole interactions ($\propto R^{-3}$ in 3D systems) introduce interactions that diverge logarithmically with the system size, making them long-range. Even in classical, equilibrium systems, this brings about several new features that are fundamentally changing the usual preconceptions in statistical physics: their energy no longer has to be additive, the state space is not necessarily convex, systems don't have to be ergodic, and thermodynamic ensembles are not thermodynamically equivalent [267–269]. These two elements, the range of interactions and the driven-dissipative nature of the system, make driven Rydberg atomic ensembles very interesting for studying fundamental physics in this regime. This is true even before we allow for their full quantum dynamics.

Motivated by some recent experimental observations, we will focus firstly on trying to understand predictions of simple models for driven-dissipative Rydberg ensembles. Then, in the latter part of this chapter, we will discuss more closely the connection between model and experiment. Both of these steps, from model to prediction, and from experiment to model, are highly non-trivial, and are topics of very active current research, of which the work described herein is only a small part.

[1] In this chapter we use word *non-equilibrium* in a strong sense of driven-dissipative systems, where non-thermal steady states are formed. This is different to e.g. non-driven systems brought with rapid change (quench) of external parameters out of the (equilibrium) ground state, where one can explore the system thermalisation and decay to ground state. While these situations are also often called non-equilibrium, they are usually still understandable within an equilibrium-statistical physics framework.

4.1 Introduction: observation of bistability in Rydberg gases and early theoretical work

ACKNOWLEDGEMENTS: Work described in this chapter was done in collaboration with Thomas Pohl.

In equilibrium statistical physics, the concepts of free-energy and rapid decay of many systems to the thermal equilibrium state allowed explanation of many phenomena. Excited states in these systems are of interest for exploring thermalisation, which for some, exhibiting so called glassy behaviour, can be quite long due to a rugged free-energy landscape [270] . In non-equilibrium systems, non-thermal non-equilibrium steady states can form, possibly several for the same external system parameters. Transitions between these multiple attractors are governed by the system dynamics noise, which can be very small either because the number of underlying individual spins driving the dynamics is large (simple mean-field limit) or because the spatial extent of the system prevents fluctuations from changing the whole system state (many-body limit). In the first case changes in the system's dynamics that bring about the existence of these multiple attractors are called bifurcations, while in the second case they correspond to phase transitions. Numerous examples of multi-stable behaviour (in both cases) giving rise to hysteresis in the system dynamics include coupled phonic cavities [271], biological cell decision-making [272–274], ecology [275] and economics [276].

Recent development of new experimental platforms, based on atom-light interactions, gave new momentum to research of non-equilibrium states in a driven-dissipative regime, possibly allowing the extension of research to the regime where the underlying quantum dynamics has a non-trivial impact on the states of these systems. Examples include cold atoms in cavities [277], semiconductor exciton-polariton condensates [278], trapped ion crystals [279, 280], and Rydberg gases [84]. In particular, Rydberg atomic systems are promising due to the tunability of their properties (Chapter 2). Recently bistability has been reported in this system, both for thermal [87, 102, 281] and cold ensembles [89]. We have seen example observations of small-volume thermal vapour bistability in the previous Chapter [Fig. 3.15]. Theoretically these systems are usually analysed as a model dissipative spin ensemble [77, 282–293]. We will discuss to what degree such models capture all the relevant physics in the mentioned experiments in the later part of this chapter. For the moment, we will focus on the predictions of these models. Various theoretical approaches used to extract their behaviour, employing different additional simplifying assumptions, provided inconsistent predictions. For example, a mean field description on lattices [285, 287] explains cold-atom observations [89] as the emergence of bistability, while variational approaches [290, 291] would suggest only the emergence of a first-order phase transition. While mean field predictions agree with experiments [87, 287] for one-dimensional spin-chains [282] they are in conflict with field-theoretical [292] and exact numerical results [286]. Even for 2D spin ensembles, where both mean-field and variational approaches predict antiferromagnetic phase at strong dissipation [282, 285, 291], exact numerical simulations [77] show the absence of such a phase. The exact numerical results [77] also showed that exact details of the nearest-neighbour interactions are important *qualitatively* for the phase diagram prediction, something that is also confirmed in the study described in this chapter [99], as well as other more recent studies that were done in the regime where full quantum dynamics was accounted for [294]. This

is in contrast to expectations from equilibrium statistical physics, where short-range details usually have only quantitative effect on phase diagrams, and suggest that this is characteristic of the non-equilibrium, driven-dissipative nature of the system states [294].

Differences between models occur due to different underlying assumptions, whose range of validity is yet to be precisely determined. In order to elucidate conditions that can give rise to bistability in driven-dissipative Rydberg ensemble we will use a model that allows the full interaction potential spatial dependence to be taken into account (Fig. 2.18), as well as spatial and temporal fluctuations in excited state population. Both effects are often neglected early on in the theoretical treatment with other approaches although they affect local dynamics. In particular, we would like to explore the effects of atomic motion, which is expected to have a big influence on thermal atomic vapour ensembles, smearing out spatial correlations. To do so, we will examine the system in the strong dephasing limit, where full quantum dynamics can be approximated with classical rate equations [172, 295–297]. The exact tracking of dynamics for $\sim 10^4$ atoms allows us to account for fluctuations and approach the thermodynamic limit. The latter is important in order to go away from small-sample sizes of ~ 16 two-level atoms that are the limit of Quantum Monte Carlo trajectory approaches [284, 285, 288], where Poissonian statistics inevitably introduces big shot-noise that drives transitions between any obtained steady states, preventing full characterisation of their stability in the thermodynamic limit.

4.2 Theoretical framework in the limit of strong dephasing: Rate equations

Consider an ensemble of N two-level systems with ground state $|g_i\rangle$ and excited state $|e_i\rangle$ $(i = 1,\ldots,N)$ coupled by a driving field with Rabi frequency Ω, detuned Δ in frequency from the transition resonance [Fig 4.1(a)]. Spin positions $\mathbf{r}_i$ in 3-dimensional space are randomly distributed with uniform distribution. To account for the effects of atomic motion for an ensemble at finite temperature, spins are assigned velocities $\mathbf{v}_i$ from a normal distribution characterised with (1D) speed standard deviation of $v_{\rm th}$. To model Rydberg-level interactions (Sec. 2.5.1), excited levels of spins i and j at respective locations $\mathbf{r}_i$ and $\mathbf{r}_j$ will interact with potential $V(|\mathbf{r}_i - \mathbf{r}_j|)$ introducing a level shift. The effect of interactions between the atoms on atomic motion is neglected. Unitary dynamics of the internal degrees of freedom of the system is described by the Hamiltonian ($\hbar = 1$)

$$\mathscr{H} = \frac{\Omega}{2}\sum_i (|e_i\rangle\langle g_i| + |g_i\rangle\langle e_i|) - \Delta\sum_i |e_i\rangle\langle e_i| + \sum_{i<j} V(|\mathbf{r}_i - \mathbf{r}_j|)|e_i e_j\rangle\langle e_i e_j|. \quad (4.1)$$

To account for dissipation and dephasing, the N-body density matrix $\hat{\rho}$ is evolved according to the master equation $\mathrm{d}\hat{\rho}/\mathrm{d}t = -i[\mathscr{H}, \hat{\rho}] + L[\hat{\rho}]$, where the Lindblad superoperator $L[\hat{\rho}] = \sum_{i,\alpha}(L_{i,\alpha}\hat{\rho}L_{i,\alpha}^\dagger - \frac{1}{2}L_{i,\alpha}^\dagger L_{i,\alpha}\hat{\rho} - \frac{1}{2}\hat{\rho}L_{i,\alpha}^\dagger L_{i,\alpha})$, describes dissipation due to one-body decay $L_{i,0} = \sqrt{\Gamma}|g_i\rangle\langle e_i|$ with rate Γ, and additional dephasing $L_{i,1} = \sqrt{\gamma}|e_i\rangle\langle e_i|$ due to finite drive-field linewidth γ (laser linewidth). From now on, we will use dimensionless quantities, measuring (scaling) the time in units of excited state decay rate Γ^{-1}, and the length in units of radius $r_{\rm b}$, defined as the

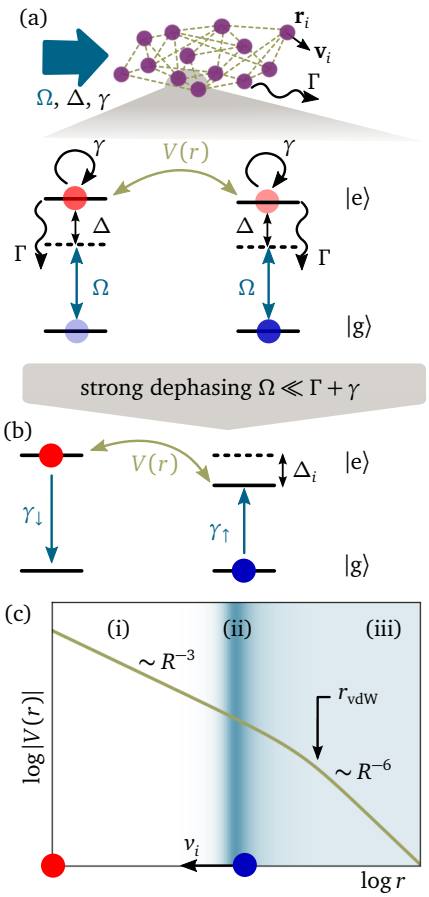

Figure 4.1: Driven-dissipative interacting system in the strong dephasing limit with rate equation modelling of dynamics. (a) Randomly distributed ensemble of two-level systems interacting with pair-potential $V(r)$, driven with field Rabi frequency Ω, dissipating energy with individual excited state decay rate Γ. In strong dephasing limit (b) dynamics can be described with rate equations. Interaction potential (c) is assumed to have cross-over between R^{-3} and R^{-6} spatial dependence at $r_{\rm vdW}$. Background shading is proportional to $\gamma_\uparrow$, indicating regions where dynamics is blockaded (i), facilitated (ii) and weakly perturbed (iii).

blockade radius for zero detuning of the drive field $V(r_{\rm b}) \equiv \Gamma + \gamma$.

The form of the interaction potential $V(r)$ [Fig 4.1(c)] is taken to match realistic interaction potentials (see Fig. 2.18 in Sec 2.5.2),

$$\frac{V(\bar{r})}{\Gamma+\gamma} = \frac{1-\sqrt{1+\xi^6/\bar{r}^6}}{1-\sqrt{1+\xi^6}}, \tag{4.2}$$

which has $V \propto r^{-3}$ distance r dependence for short inter-spin separations $r < r_{\rm vdW}$ below the van der Waals distance $r_{\rm vdW}$ (Sec. 2.5.1), and asymptotic behaviour $V \propto r^{-6}$ at long distances $r > r_{\rm vdW}$, characteristic for van der Waals interactions. Here $\bar{r} \equiv r/r_{\rm b}$, and $\xi \equiv r_{\rm vdW}/r_{\rm b}$ measures the characteristic cross-over distance between these two asymptotic regimes relative to the blockade radius, quantifying the importance of dipolar interactions for the system dynamics.

Following the approach of Refs. [172, 295–297], we derive effective rate equations in the strong dephasing limit. For a non-interacting gas, evolution of the N-body density matrix can be factorised $\hat{\rho} = \bigotimes_i \hat{\rho}_i$ into the evolution of single-spin density matrices $\hat{\rho}_i$ where individual density elements will evolve in time τ as

$$\frac{\mathrm{d}}{\mathrm{d}\tau}\hat{\rho}_{i,\mathrm{ee}} = -\frac{i\Omega}{2}(\hat{\rho}_{i,\mathrm{ge}} - \hat{\rho}_{i,\mathrm{eg}}) - \Gamma\hat{\rho}_{i,\mathrm{ee}} \quad , \tag{4.3}$$

$$\frac{\mathrm{d}}{\mathrm{d}\tau}\hat{\rho}_{i,\mathrm{ge}} = -\frac{i\Omega}{2}(2\hat{\rho}_{i,\mathrm{ee}} - 1) - i\Delta_i\hat{\rho}_{i,\mathrm{ge}} - \frac{\Gamma+\gamma}{2}\hat{\rho}_{i,\mathrm{ge}} \quad . \tag{4.4}$$

Rabi oscillations are damped on a time-scale determined by $\Gamma+\gamma$ due to the dephasing and coupling to the reservoir, and for $|\Omega| \ll \Gamma+\gamma$ the coherences ρ_{ge} will be evolving much faster than the populations, adiabatically following changes in populations. We can therefore set $\dot{\hat{\rho}}_{1,\mathrm{ge}} = 0$, to obtain the evolution of the populations

$$\frac{\mathrm{d}}{\mathrm{d}t}\hat{\rho}_{i,\mathrm{ee}} = \frac{\bar{\Omega}^2}{4\bar{\Delta}_i+1}\hat{\rho}_{i,\mathrm{gg}} - \left(\frac{\bar{\Omega}^2}{4\bar{\Delta}_i+1}+1\right)\hat{\rho}_{i,\mathrm{ee}} \quad , \tag{4.5}$$

where we introduced the scaled Rabi frequency $\bar{\Omega} \equiv \Omega/\sqrt{\Gamma(\Gamma+\gamma)}$ and scaled detuning $\bar{\Delta}_i \equiv \Delta_i/(\Gamma+\gamma)$, while time is measured in earlier introduced units of Γ^{-1}, $t = \tau\Gamma$. Importantly, note the assumption $|\Omega| \ll \Gamma+\gamma$ still permits $\bar{\Omega} \gtrsim 1$ for $\gamma \gg \Gamma$ which is typical in experiments[2]. Similar adiabatic elimination of the fast evolution of coherences can be done even in the full many-body case with interactions V turned on, giving evolution equations that depend only on diagonal elements of the density matrix. If we neglect higher-order processes, like multi-photon excitations of two or more atoms simultaneously, as discussed in Refs. [172, 295–297], we can obtain a master equation that couples only states whose excitation numbers differs by one. If we introduce vectors $\mathbf{S} \equiv (s_1, \ldots, s_N)$ labelling many-body states, with $s_i = 1$ standing for the excited i-th spin in the many-body state $|\ldots \mathrm{e}_i \ldots\rangle$, and $s_i = 0$ for the i-th spin in the ground state, and label the neighbouring vectors where the single spin i has a different state as $\mathbf{S}_i \equiv (s_1, \ldots, 1-s_i, \ldots, s_N)$, we can write the effective master equation governing evolution of the diagonal elements $\rho_{\mathbf{S},\mathbf{S}}$ of the density matrix as

[2] For example $\gamma \approx 10^3\ \Gamma$ for experimental parameters in Refs. [89, 298]

$$\frac{\mathrm{d}}{\mathrm{d}t}\rho_{\mathbf{s},\mathbf{s}} = -\sum_i \Big[s_i\gamma_\downarrow^{(i)}(\mathbf{S}) + (1-s_i)\gamma_\uparrow^{(i)}(\mathbf{S})\Big]\rho_{\mathbf{s},\mathbf{s}} + \sum_i \Big[s_i\gamma_\uparrow^{(i)}(\mathbf{S}) + (1-s_i)\gamma_\downarrow^{(i)}(\mathbf{S})\Big]\rho_{\mathbf{s}_i,\mathbf{s}_i}, \tag{4.6}$$

where the single-spin excitation rate of spin i is given by $\gamma_\uparrow^{(i)} \equiv \bar{\Omega}^2/(1+4\bar{\Delta}_i(\mathbf{S})^2)$, and the corresponding de-excitation rate is $\gamma_\downarrow^{(i)} \equiv 1+\gamma_\uparrow^{(i)}$. The interactions will now be accounted for through scaled frequency detunings $\bar{\Delta}_i(\mathbf{S}) = \Delta_i(\mathbf{S})/(\Gamma+\gamma)$ as an interaction-induced level shift $\Delta_i(\mathbf{S}) = \Delta - \sum_{j\neq i} V(r_{ij})\, s_j$ due to the presence of neighbouring excited spins [Fig 4.1(b)]. The validity of this approach for $\Omega \ll \Gamma+\gamma$ has been confirmed by comparing the rate-equation evolution (Eq. 4.6) of small systems with evolution under the full master equation accounting for the time-evolution of all the coherences and multi-photon excitations [299].

Using the dynamics explained above to find hysteresis and state bistability, the system state is continuously evolved while the drive detuning $\bar{\Delta}$ is scanned (chirped) with rate $\pm\kappa$, corresponding to increasing and decreasing drive detuning.

4.2.1 Implementation of numerical solution - serial algorithm

Evolution under Eq. (4.6) can be efficiently solved for large ensembles ($N \sim 10^4$) using Monte Carlo sampling for integration of dynamics [295, 300]. Initial atom positions are sampled uniformly within a cubic volume with periodic boundary conditions and edge L, selected in all simulations to be much larger than both r_b and r_vdW. The density of the atomic medium is given by the dimensionless density $\rho = N r_\mathrm{b}^3/L^3$, corresponding to the number of spins per blockade volume r_b^3. Observables are calculated as ensemble averages over multiple realisations of particle disorder configurations. Note however that individual realisations are also used to obtain distribution probabilities for system state variables, characterising their time-domain fluctuations. Two different algorithms are used, one for a frozen system, where atom positions $\mathbf{r}_i$ don't evolve in time, and one for hot systems, where atoms move along linear trajectories according to their velocities.

In the case of the frozen system, the transition rates $\gamma_{\uparrow,\downarrow}^{(i)}(\mathbf{S})$ for a given internal system state $\mathbf{S}$ don't change in time. This allows use of a kinetic Monte Carlo algorithm, that dynamically determines discrete time steps for the simulation, sampling directly the time required for the next change in the system to occur. The algorithm steps are

1. Initialize spin positions $\mathbf{r}_i$ from uniformly distributed random numbers
2. Calculate rates $p_i = \gamma_\uparrow^{(i)}(\mathbf{S})(1-s_i) + \gamma_\downarrow^{(i)}(\mathbf{S})\, s_i$ for flipping of spin s_i and store them in an array $[C_i]$ of cumulative spin-flip rates $C_i = \sum_{j=0}^{i} p_j$, $C_0 = 0$;
3. The probability for no spin-flips occurring during time t is $\frac{1}{C_N}\exp(-C_N t)$; Find *when* the next state change happens by sampling the time for the next spin-flip from that distribution as $\tau = \frac{1}{C_N}\ln(1/u)$, where $u \in [0,1)$ is a uniform distribution;
4. Find *which* spin i was flipped, by sampling $u' \in [0,1)$ from a uniform distribution, and then doing a binary search for i such that $C_{i-1} < u' C_N < C_i$; Flip the state of spin i ($s_i = 1-s_i$);

5. Record quantities of interest (this step is not required every time);

6. Change detuning to $\bar{\Delta} = \bar{\Delta} + \kappa\tau$. If current simulation time is smaller than the total simulation time go to step (2.), otherwise end simulation.

For hot samples, atoms move along linear paths $\mathbf{r}_i(t) = \mathbf{r}_i(0) + \mathbf{v}_i t$ according to their velocities $\mathbf{v}$ whose components are given by a normal distribution with standard deviation v_{th}. Transition rates will now depend on time, and this too has to be integrated. Numerically intensive fixed time-step δt Monte Carlo sampling is performed. The time step has to be small enough such that $C_N \delta t \ll 1$ and that atomic motion is small on the blockade radius length-scale $v_{\text{th}} \delta t \ll r_{\text{b}}$. In performed simulations, $\delta t = 10^{-4}$. In this case the algorithm steps are

1. Initialize spin positions $\mathbf{r}_i$ from uniformly distributed random numbers, and spin velocities $\mathbf{v}_i$ based on normally distributed random numbers with zero mean and v_{th} variance.

2. Calculate rates $p_i = \gamma_{\uparrow}^{(i)}(\mathbf{S})(1-s_i) + \gamma_{\downarrow}^{(i)}(\mathbf{S})\, s_i$ for flipping of spin s_i and store them in an array $[C_i]$ of cumulative spin-flip rates $C_i = \sum_{j=0}^{i} p_j$, $C_0 = 0$;

3. Sample $u' \in [0,1)$ from a uniform distribution; If $C_N \delta t < u'$, go to step (4.), otherwise find which spin i was flipped by doing a binary search for i such that $C_{i-1} < u'/\delta t < C_i$; Flip state of spin i ($s_i = 1 - s_i$);

4. Record quantities of interest (this step is not required every time);

5. Update spin positions $\mathbf{r}(t+\delta t) = \mathbf{r}(t) + \mathbf{v}\delta t$ and driving detuning $\bar{\Delta} = \bar{\Delta} + \kappa \delta t$. If current simulation time is smaller than the total simulation time go to step (2.), otherwise end simulation.

4.2.2 Implementation of numerical solution - parallel algorithm

Reaching convergence required large systems that pushed the run-times of implemented algorithms in C++ to the limits of what is realistically acceptable. For such large systems, typical execution times were of the order of a week per single trace. The total execution time on the clusters used was not calculated, but probably amounts to several years of continuous running. However, since the run-time of fixed step Monte-Carlo algorithm for the biggest explored systems was too long for serial execution, a parallel algorithm was implemented with C++ and MPI. A master node would divide the problem to worker nodes. Each worker node calculates probabilities and locations of its own subset of spins, communicating with the master only its own partial cumulative probability. In addition, in order to minimize the inter-process communication, each worker node had full list of excited spins, whose positions are calculated on each node. Given that typically only a small fraction of the medium is excited, this duplication of calculation is probably more efficient than relying on inter-process communication to obtain all the excited spin locations. The algorithm steps for the **master** node are:

1. Initialize spin positions $\mathbf{r}_i$ from uniformly distributed random numbers, and spin velocities $\mathbf{v}_i$ based on normally distributed random numbers;

2. Divide subsets of spins among worker nodes and set their initial values;

3. Request from workers the calculation of partial cumulative rates for their subset of spins (worker state 1) P_i, $i = 1, \ldots, N_\mathrm{w}$, where N_w is the number of worker nodes; Assemble meta cumulative rates $M_i = \sum_{j=1}^{i} P_j$ ($M_0 = 0$) for each of the nodes;

4. Sample $u' \in [0, 1)$ from a uniform distribution; If $M_{N_\mathrm{w}} \delta t < u'$, go to step (4.), otherwise find which node i contains the spin that changed its state by doing a binary search for i such that $M_{i-1} < u'/\delta t < M_i$; Request node i to locate the changed spin, and to change its state based on value $u'' = u'/\delta t - M_{i-1}$ (worker state 2); Wait for response and update information about the spin states;

5. Record quantities of interest (this step is not required every time);

6. Change $\bar{\Delta}$ on nodes (worker state 3), and go to step (2.) if current simulation time is smaller then the total simulation time, otherwise request worker nodes to terminate simulation (worker state 4).

The algorithm steps for **worker** nodes are oriented around several state machines. Transitions between states are prompted by the master node:

- Receive information about relevant spin subset containing N_s spins; Wait for state switch command from master node;

- **State 1**. Evolve spin positions, *including* own copy of excited spins, and calculate cumulative rates C_i , returning the last one to the master $C_{N_\mathrm{s}} \to P_i$

- **State 2**. Find which spin i within your subset was flipped based on received u'', by a binary search for i such that $C_{i-1} < u'' < C_i$; Flip state of spin i ($s_i = 1 - s_i$); Notify all nodes about changes; If new excited spin is added to the array of excited spins, add it at the end of the current array. If some spin is de-excited, remove that spin from array of excited spins, and if it is not the last spin in the array, copy into its place the last spin in array.

- **State 3**. Update the local drive detuning based on received values from the master node.

- **State 4**. Memory clean-up and exit.

To get a sense of the time-scales involved for some of the results, note that this parallelized version of the algorithm, for a *single* scan over detuning range of $\delta\bar{\Delta} = 0.75$, with scan speed $\kappa = 2.2 \times 10^{-3}$ and a system of size $L = 12$ and density $\rho = 10$ (total number of spins $N = 17280$; other parameters $\xi = 2$, $\bar{\Omega} = 0.8$), required ≈ 53 hours (wall-time) running on 32 CPUs (Intel Xeon E5 2.6 GHz) to achieve convergence on Fig. 4.2 in the following section.

4.3 Hot ensemble limit

As was noted in the introduction (Sec. 4.1), there are several examples in which mean-field theories give predictions that were inconsistent with full numerical simulations, including some done with rate equations integrated as described in Sec. 4.2.1. That is partially due to a known limitation of mean-field theory, that neglects fluctuations,

however we will see that, at least in the cases treatable with rate equations, the usual mean-field model fails but can be corrected within a framework which we introduce here.

4.3.1 Ensemble averaged mean field

The idea of the mean field in its simplest form is to consider a subspace containing only a single spin, and account for the environment in some effective manner. In the textbook case of magnetic spins in lattice geometries, described by the Ising model, one would seek to find an effective magnetisation field that a single selected spin i feels due to the spins on the nearest lattice sites. Usually at this point all correlations in the environment would be neglected, and it would be assumed that nearest neighbours have average behaviour described by some microscopic quantity like magnetisation. In very much the same spirit, finding a mean field model for a Rydberg ensemble interacting with the Hamiltonian given by Eq. (4.1) would consist of finding an average interaction $\bar{V}$ that a single spin i feels when immersed in the given ensemble. We can neglect correlations in the environment, and assume that excited spins are completely randomly distributed, giving an average interaction shift

$$\bar{V} = \int_{r_s}^{+\infty} V(r_{ij})\rho_e \cdot 4\pi r^2 \, \mathrm{d}r \tag{4.7}$$

where ρ_e is the excited state density. For random ensembles atoms can be arbitrarily close together, so we take the lower integration limit to be $r_s = 0$. This gives an indication of the problem as the result will diverge at 0 since $V \propto R^{-\alpha}$, $\alpha = 3, 6$. Related theoretical works thus far either didn't express $\bar{V}$ directly as a function of elementary interactions, or they introduce a minimum integration distance of the blockade radius $r_s = r_b$. However we note that this is not the usual failure of the mean-field, but a mathematical indication that, at least in this case, we are focusing on the wrong quantity. Typically in experiments we directly measure average Rydberg population, and that depends on the *average transition rates*. Since dynamics given by the rates $\gamma_{\uparrow,\downarrow}$ depends non-linearly on $\bar{V}$, exhibiting non-monotonic, *resonant behaviour*, it is clear that the results of averaging dynamics, which as we will see completely describe population evolution in a non-correlated system, can be very different to the dynamics obtained by inserting an average level shift into the equations for transition rates.

We will focus on a completely uncorrelated ensemble that arises due to, for example, rapid thermal motion that randomizes spatial excitation structures. Formally, if we neglect correlations between the spins we can factorise the system state as $\rho_{\mathbf{s},\mathbf{s}} = \prod_{i=1}^{N} \rho^{(i)}_{s_i,s_i}$, where $\rho^{(i)}_{s_i,s_i}$ are diagonal elements of the single spin density matrix. Inserting this in Eq. (4.6) we obtain

$$\frac{\mathrm{d}}{\mathrm{d}t}\rho^{(i)}_{1,1} = \gamma^{(i)}_{\uparrow} - (1 + 2\gamma^{(i)}_{\uparrow})\, \rho^{(i)}_{1,1} \quad . \tag{4.8}$$

From this we can find the rate of change for the excitation density $\rho_e = \frac{1}{L^3}\sum_{i=1}^{N} \rho^{(i)}_{1,1}$ as

$$\frac{\mathrm{d}}{\mathrm{d}t}\rho_{\mathrm{e}} = \frac{N}{L^3}\frac{\sum_i \gamma_\uparrow^{(i)}}{N} - \frac{1}{L^3}\sum_i (1+2\gamma_\uparrow^{(i)})\rho_{1,1}^{(i)}$$
$$= \rho\bar{\gamma}_\uparrow - \frac{1}{L^3}\sum_i \left[1+2\left(\bar{\gamma}_\uparrow+\delta\gamma_\uparrow^{(i)}\right)\right]\left(\bar{\rho}_{1,1}+\delta\rho_{1,1}^{(i)}\right), \qquad (4.9)$$

where we have introduced density $\rho \equiv N/L^3$, average excitation rate $\bar{\gamma}_\uparrow \equiv \frac{1}{N}\sum_i \gamma_\uparrow^{(i)}$ and the average excited state population element of the single-spin density matrix $\bar{\rho}_{1,1} \equiv \frac{1}{N}\sum_i \rho_{1,1}^{(i)}$, with respective spin-to-spin fluctuations of $\delta\gamma_\uparrow^{(i)}$ and $\delta\rho_{1,1}^{(i)}$. In the limit of fast motion ($v_{\mathrm{th}}/r_{\mathrm{b}} \gg \Omega$) the spin environment that determines $\gamma_\uparrow^{(i)}$ will be completely uncorrelated with the spin-state $\rho_{1,1}^{(i)}$, which allows us to set $\sum_i \delta\gamma_\uparrow^{(i)}\delta\rho_{1,1}^{(i)} \to 0$. Further using $N\bar{\rho}_{1,1}/L^3 = \rho_{\mathrm{e}}$, we obtain from Eq. (4.9)

$$\frac{\mathrm{d}}{\mathrm{d}t}\rho_{\mathrm{e}} = \rho\ \bar{\gamma}_\uparrow - (1+2\bar{\gamma}_\uparrow)\rho_{\mathrm{e}} \quad . \qquad (4.10)$$

Here the excited state population depends on the excitation rate averaged over the ensemble $\bar{\gamma}_\uparrow$, so we will refer to this model as the *ensemble averaged mean field* (eaMF). This is an exact solution of Eq. (4.6) in the limit of a hot atomic ensemble, where rapid atomic motion prevents formation of spatial patterns from excited particles. In Figure 4.2 we show comparison of the eaMF (4.10) prediction given as the colour map, and exact numerical integration as described in Sec. (4.2.1). As expected, for the hot case ($v_{\mathrm{th}} = 20$, black line in Fig. 4.2), the numerical simulation matches with eaMF, where steady states form an S-shaped curve (white part of the colour map on Fig 4.2). In the region where three equilibrium solutions ($\dot{\rho}_{\mathrm{e}} = 0$) exist, two of them are stable under small perturbations in ρ_{e}. Note that the big system size is important to capture the full hysteresis curve occurring due to the existence of two stable states. Smaller systems have stronger shot-noise, causing destabilisation of the state before the edge of the hysteresis predicted by the S-shaped curve is reached. Note that for a frozen system ($v_{\mathrm{th}} = 0$, green line in Fig. 4.2) the numerical solution is very different, and actually doesn't show bistability at all (even with expanded detuning range $\bar{\Delta}$). The frozen case will be discussed in detail in the following Section (4.4), and the important cross-over regime between the two will be explored in Section (4.5).

The prediction of the usual mean field (MF) analysis, that just uses $\bar{V}$ (Eq. 4.7) limiting integration down to the blockade distance $r_{\mathrm{s}} = r_\Delta$, $V(r_\Delta) = \bar{\Delta}$ is shown on Fig. 4.3. As expected from the introductory discussion, it completely misses both the shape of the solution and the hysteresis width. In particular MF seems to significantly underestimate fluctuations, predicting a much wider hysteresis window. This is the usual mean-field fallacy. For example, in the few-excitations branch of the bistable curve, breaking down of point-excitations to a field, and smearing them in space, effectively done by Eq. (4.7), misses the effect that a few concentrated excitations can have on their local environment. This effect is more pronounced compared to for example the mean field in magnetic materials, due to the resonant dependence of dynamics (transition rates) on V.

Introduced eaMF by averaging directly dynamics maintains fine-grained sensitivity to the point nature of excitations. Yet it keeps the computational and conceptual simplicity of the mean-field, allowing potential extensions to multi-level, multi-

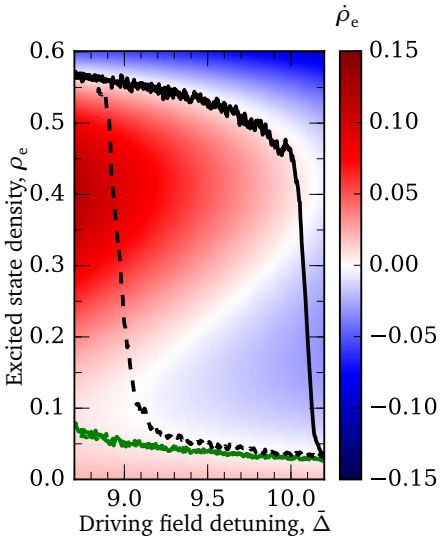

Figure 4.2: Ensemble averaged mean field (eaMF) compared with results from full numerical integration. Change in population $\dot{\rho}_{\mathrm{e}}$ for a given $(\bar{\Delta}, \rho_{\mathrm{e}})$ as calculated by eaMF (Eq. 4.10) is mapped with colour. For comparison results of numerical integration of dynamics (Eq. 4.6) for a big, hot ensemble ($L = 12$, $v_{\mathrm{th}} = 20$, $\kappa = 2.2 \times 10^{-3}$) are shown (black), for a detuning chirp in the positive (solid black) and negative (dashed black) directions. The solid green line shows results of full numerical integration of dynamics for a frozen system ($v_{\mathrm{th}} = 0$). Parameters $\bar{\Omega} = 0.8$, $\xi = 2.0$, $\rho = 10$. Unit length is r_{b}.

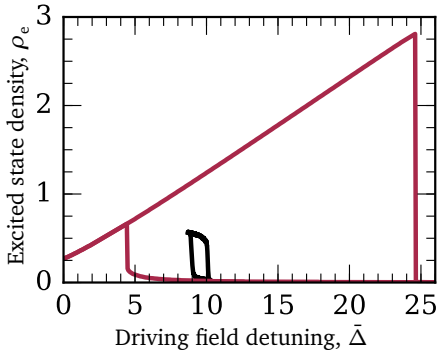

Figure 4.3: Simple mean field with cut-off at blockade radius compared with numerical results. Prediction of simple mean field (solid red) that uses average interaction (Eq. 4.7) for calculation of dynamics, with a cut-off r_{s} at blockade radius r_Δ for given detuning $V(r_\Delta) = \bar{\Delta}$. Results of numerical integration of dynamics for hot, uncorrelated ensemble are shown in solid black. Parameters as in Fig. 4.2.

component systems. The ensemble averaged rate $\bar{\gamma}_\uparrow$ can then be efficiently found by doing simple Monte Carlo sampling of the environment. In the special case of the currently considered two-level system it is also possible to derive a closed analytical solution (see Appendix A.3 for details) for the averaged transition rate

$$\bar{\gamma}_\uparrow = \frac{\bar{\Omega}}{2}\int_0^{+\infty} \mathrm{d}k\; e^{-k\{1/2+\mathrm{Re}[f(k)]\}}\; \cos\left(k\left\{\bar{\Delta}+\mathrm{Im}[f(k)]\right\}\right), \tag{4.11}$$

where $f(k) \equiv k^{-1}\rho_\mathrm{e}\int\{1-\exp[ikV(r)]\}\,\mathrm{d}\mathbf{r}$. The real and imaginary parts of $f(k)$ can be interpreted as an interaction-induced shift ($\mathrm{Im}[f]$) and broadening ($\mathrm{Re}[f]$) respectively. In the special case when interactions $V(r)$ have pure van der Waals spatial dependence r^{-6}, corresponding to $\xi \to 0$, one finds $\mathrm{Re}[f] = \mathrm{Im}[f] \propto \rho_\mathrm{e}\sqrt{k}$. This implies that the level shift will always be matched by line broadening, preventing the formation of bistable phases for pure van der Waals interactions. This will be further explored numerically in Sec. 4.4.3.

Finally, we comment on possible extensions of this approach. In a similar manner we can treat arbitrary strong driving ($\Omega > \Gamma + \gamma$) by applying a full quantum model to a single particle, and averaging over the other spins (environment) whose initial states are sampled from distributions defined by macroscopic observables, until we have a self-consistent approximation for the environment. This is possible since the full dynamics is only solved for a single atom, and the rest is treated as a self-consistent perturbing environment, which is fine as long as motion induced dephasing limits the growth of many-body coherences. Again, in contrast to usual MF analysis, this sampling of environments and direct averaging of dynamics captures the impact of fluctuations on dynamics. A related recent theoretical approach is cluster mean field in Ref. [294]. It accounts for full quantum evolution and short-range correlations in the local environment (cluster), however it still uses the usual mean-field approach for treatment of the cluster environment, partially neglecting the effect of fluctuations on dynamics.

4.3.2 Phase diagrams

Here we use the previously introduced ensemble averaged mean field to explore parameter ranges over which bistability can occur. Scans of detuning $\bar{\Delta}$ were performed, in both the positive and negative direction, and for each detuning value the excited state population density ρ_e was evolved according to Eq. (4.10), starting with an equilibrium value obtained from the previous detuning step. The local equilibrium value was found numerically, through adjustments of ρ_e until $\dot{\rho}_\mathrm{e} \to 0$, as evaluated by Eq. (4.10). For each value of ρ_e, the average rate $\bar{\gamma}_\uparrow$ was found by direct ensemble average of $\sim 10^6$ randomly generated environments, as this was found to be faster than numerical evaluation of Eq. (4.11).

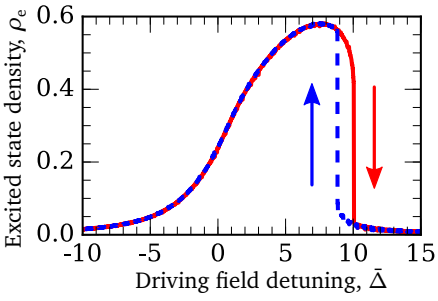

Figure 4.4: Excited state population of an uncorrelated (hot) ensemble, upon detuning scan in positive and negative direction. Calculated with eaMF for $\bar{\Omega} = 0.8$, $\xi = 2.0$, $\rho = 10$.

Example of the excitation density profile obtained is shown on Fig 4.4. The obtained hysteresis can be characterised by calculating a surface area A_0 enclosed in $(\rho_\mathrm{e}, \bar{\Delta})$ space by the excited state populations $\rho_\mathrm{e}^{\rightarrow}$ and $\rho_\mathrm{e}^{\leftarrow}$ found for detuning scans in the positive and negative direction respectively, i.e.

$$A_0 = \int_{\mathrm{Min}[\bar{\Delta}]}^{\mathrm{Max}[\bar{\Delta}]} |\rho_\mathrm{e}^{\rightarrow} - \rho_\mathrm{e}^{\leftarrow}|\,\mathrm{d}\bar{\Delta} \quad . \tag{4.12}$$

Obtained hysteresis surface areas A_0 for a range of spin densities ρ and cross-over

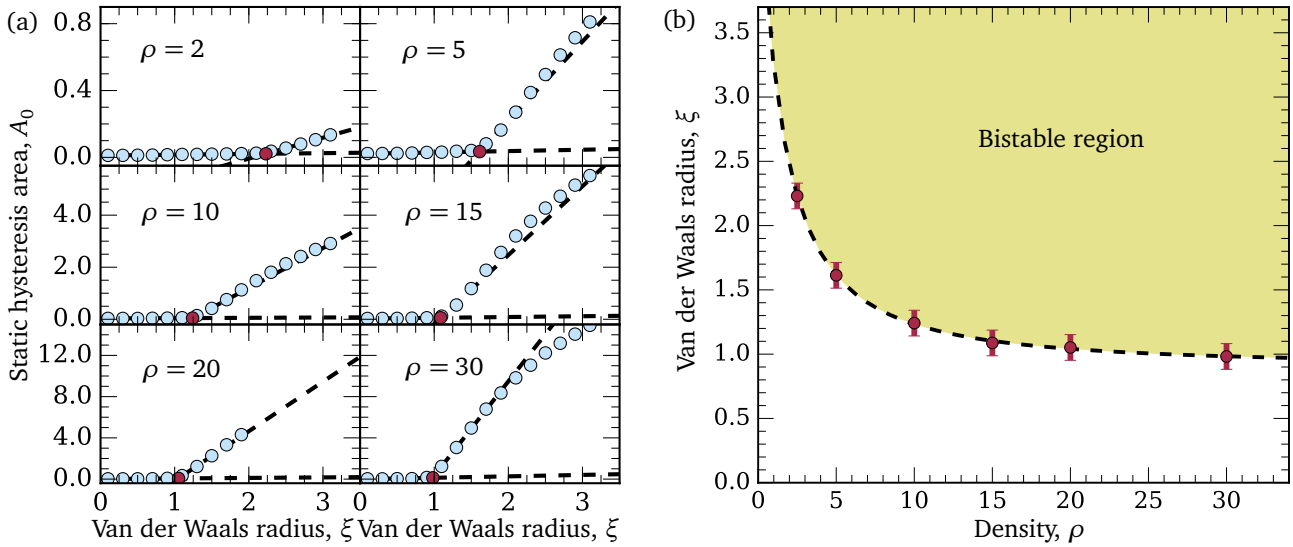

Figure 4.5: Phase diagram for hot ensemble in (ρ, ξ) plane. The phase diagram is reconstructed by integrating dynamics with eaMF and extracting hysteresis area A for each ξ [blue dots (a)]. This uncovers a second order transition into the bistable regime that occurs for critical ξ_{crit} [red dots (a)], that is extracted for each ρ as an intersection of linear fits (dashed lines) of the subsets of the data in the vincinity of transition. These critical ξ_{crit} are plotted on the phase diagram (b). Calculated for $\bar{\Omega} = 1$.

distances ξ are shown on Fig. 4.5(a). For small values of ξ there is no observable hysteresis, even though ρ_e can start to feature a sharp transition point. Approaching such a transition point means that the excited state becomes localized in a larger, shallower basin of attractor dynamics. Shallower basins require progressively more precise determination of $\bar{\gamma}_\uparrow$ in order to find a steady state. For a fixed number of sampled environments ($\sim 10^6$) this leads to increased error in the determination of the local equilibrium value of ρ_e. We can see that in the numerically extracted enclosed area A_0 that increases ever so slightly with increasing ξ [Fig. 4.5(a)], as evident from the linear fits of A_0 for small ξ. However, there is always a clear transition point in ξ when the hysteresis area experiences a second-order phase transition, and starts to rapidly grow with increasing ξ.

The critical point ξ_{crit} can be extracted from linear fits of the extracted hysteresis

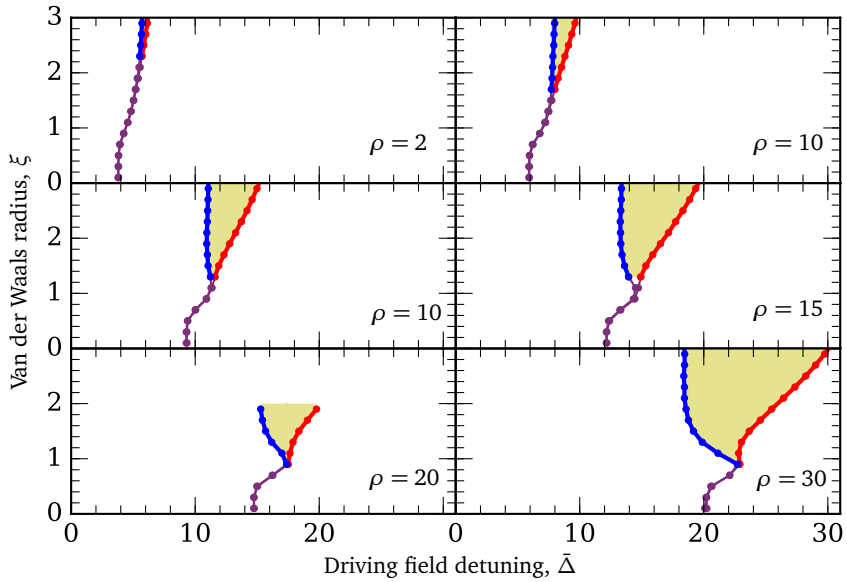

Figure 4.6: Phase diagram for hot (uncorrelated) ensemble in $(\bar{\Delta}, \xi)$ plane. Purple points show $\bar{\Delta}$ for which half of the maximum excited state is reached for blue detuned driving. With increasing dipolar core ξ, the bistability window opens (yellow shading) with separate jump-up (blue dots) and jump down (red dots) points. Parameter $\bar{\Omega} = 1$.

areas A_0 in the vicinity of the transition. Obtained values for ξ_{crit} shown as red points on Fig. 4.5(a), are represented on a bistability phase diagram in the (ρ, ξ) plane in Fig. 4.5(b). We see that numerical results indicate that bistability doesn't occur for $\xi < 1$. This confirms the conclusion reached analytically in the previous Section 4.3.1 and extends the region with no bistability to $\xi \to 1$. Changes in the location of the hysteresis, for different spin densities ρ and cross-overs ξ are shown on Fig. 4.6. There we recorded driving field detunings $\bar{\Delta}$ for which half-maximum value of ρ_{e} is crossed on the blue-detuned side, marking turn-on (blue circles) and turn-off (red circles) point of the hysteresis.

4.4 Frozen ensemble

In the previous chapter we have shown how bistability can arise in a hot atomic ensemble if a finite dipolar core is present ($\xi = 2$ for simulations in Fig. 4.2). Two non-equilibrium steady states identified in the bistable loop are stable under small fluctuations, but transitions between these two attractors of dynamics can easily occur in finite systems due to occasional big fluctuations, making them metastable. The size of fluctuations can be simply reduced by considering big systems, which makes states infinitely long-lived in the limit of $L, N \to \infty$. This is very similar to the usual cavity bistability extensively explored both theoretically and experimentally [301–304] for the last forty years, where an all-to-all mean interaction field in an atomic medium is provided by the cavity-trapped field.

Bistability in the frozen, spatially extended, locally interacting many-body system would be of a fundamentally different nature. For finite systems, similarly as discussed in the eaMF picture, switching between two states is inevitable. However, for spatially extended systems the question whether two states, metastable in finite systems, can become stable in the thermodynamic limit, and if so, under which conditions, is very complicated. In contrast to eaMF bistability, this is a non-trivial question since local fluctuations of dynamics cannot be prevented. The local fluctuations in spatially extended systems can cause inhomogeneities, that can act as a nucleation centre for an avalanche that spreads and changes the state of the system. In thermal equilibrium systems, mechanisms like this usually prevent observation of metastable phases [305], like superheated water and supercooled vapour in gas-liquid transitions. Thermal equilibrium systems in a metastable state are stable under small perturbations, and the states are well defined by the current external parameters (unlike in the glassy systems), however, once the system leaves the metastable state, the probability of returning is very low [306]. Inhomogenuities, local nucleation and phase separation followed by an avalanche, prevents easy calculation of metastable state lifetimes based on mean-field based estimates for crossing free-energy barriers between states [306–308]. A fact that complicates analysis of metastable states in driven-dissipative systems even more, and a reason for caution when drawing comparisons to thermal-equilibrium systems, is the lack of a formally defined equivalent to free energy. However, transitions can still be seen occurring due to local, fluctuation induced changes of state, if such changes can spread and span the whole system size.

There are two types of question one can ask about metastability/bistability in the discussed spin system (Eq. 4.1). The first one is a fundamental question: can two

states become infinitely long lived in the thermodynamic limit, and how that can be understood? The second is pragmatic, asking if we have any long-lived states, which on experimental time-scales are effectively stable and completely dominate the dynamics, how can we identify and characterise these states? For the former question we cannot provide a definitive answer, but we can highlight two frameworks within which one can understand the origin of bistability. Within the Liouvillian formalism (Sec. 2.4.3), for the bistable regime to occur an eigenstate of the Liouvillian should have a real part[3] that vanishes in the thermodynamic limit, making that state also exactly infinitely long-lived, as discussed in Refs. [271, 309]. However, since the rate equation model is fully classical, we should be also able to understand the occurrence of the two phases from the point of view of percolation and changes in percolation tresholds with detuning and system state, required for apperance of (non)excited clusters that span the whole system size on the hysteresis edges where sharp changes in excited state population occur. These should provide a transparent way of understanding the occurrence of dynamic phase transitions in spatially extended systems. In order to answer the latter question, we introduced a number of precisely defined quantities, that can be directly measured experimentally. We showed that clear transition points can be identified with them. Intensive numerical efforts allowed reconstruction of phase diagrams, identification of bistable states, and identification of persistent state switching, a separate phenomena from transient bistability. We also analysed a microscopic basis for the importance of short-range potential form which, in contrast to expectations based on equilibrium statistical physics, has a qualitative influence on phase diagrams in these non-equilibrium situations. We showed that it has a profound influence on the size of dynamics fluctuations, which bears some resemblance to the influence that temperature has on equilibrium systems.

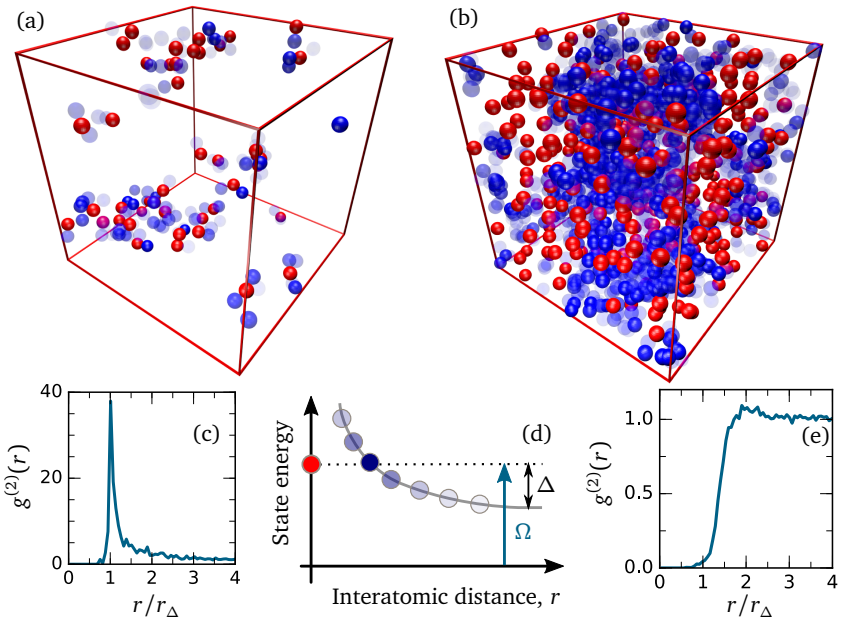

Figure 4.7: Snapshot of low (a) and high (b) excited state density phase of a frozen non-equilibrium bistable system. Two non-equilibrium steady states are shown in space, with wire-frame marking limits of periodic-boundary simulation space. Low excited state density phase (a) features small clusters [correlation function shown on (c)] of excited spins (red spheres), that facilitate excitation of other neighbouring spins as indicated by the shading (d) of the ground state spins (blue spheres). High excited state density phase (b) features a cluster that spans the whole system. The cluster consists of excited spins (red) and ground state spins whose dynamics is highly facilitated (strong blue) being brought into resonance with off-resonant driving due to interactions with excited spins. The phase has liquid like correlations (e). Note that both (a) and (b) have same number of spins, with the same spatial distribution, however on (a) a majority of them is invisible, just as it would be for off-resonant driving field, since they are far detuned from the driving resonance.

4.4.1 Hysteresis scaling: static v.s. dynamic hysteresis

For a finite dipolar core, as measured by ξ, we were able to find regions where hysteresis in the excited state density ρ_e opens upon a detuning $\bar{\Delta}$ scan, where two well defined states [Fig 4.7(a-b)] persisted for a long time. The low-excitation density state [Fig 4.7(a)] features small clusters of excitation, indicated also in the excitation density correlation function [Fig. 4.7(c)] that shows pairs of hard-core spheres being formed. The short-range exclusion zone corresponds to the blockade (Sec. 2.5.2), where the level shift caused by interactions between two excited states decouples states featuring two or more excitations from the driving field, effectively freezing dynamics at short distances. The peak in the correlation function corresponds to the facilitation radius r_Δ (Sec. 2.5.2) where the presence of a single excitation compensates driving detuning Δ through an interaction induced level shift $V(r_\Delta) = \Delta$ of the spins, bringing them into resonance with the driving field [Fig. 4.7(d) for shading]. The high-density phase consists of one giant excited cluster that spans the whole system. Note that Fig. 4.7(b) shows a snapshot of such a cluster in time. This is a non-equilibrium steady state, and for maintenance of the cluster its structure, consisting of interleaved excited spins (red) and ground-state spins whose states are brought into resonance with driving (blue), is of crucial importance. In subsequent time steps excited spins will decay, and somewhere in their neighbourhood some resonant spins will be excited, maintaining the total excited state density ρ_e. Note that each blockaded volume in the figure contains multiple spins whose dynamics is effectively frozen due to interactions. In such a dynamically grown cluster there is nothing that would maintain long-range ordering over a length-scale r_Δ, and this is indeed seen in the correlation function on Fig. 4.7(e), which resembles a liquid of hard core particles.

To determine the nature of hysteresis, we observed a scaling of hysteresis area for different chirp rates κ of detuning $\bar{\Delta}$. If the external parameters are changed very quickly, faster than the characteristic response time of the system, hysteresis will always occur. In the region of first-order phase transitions, hysteresis can occur due to the existence of meta-stable states. If one waits for long-enough, the system should find its equilibrium state, and the hysteresis usually closes. Indeed, we can see on Fig. 4.8(a) that hysteresis becomes smaller for slower chirp rates. However, we consider whether, in addition to this inevitable dynamic hysteresis, one can identify appearance of long-lived states giving time-persistent static hysteresis and bistability. To this end we fitted numerically obtained hysteresis areas $A(\kappa)$ for different chirp rates κ to

$$A(\kappa) = A_0 + a\kappa^{-b}, \tag{4.13}$$

where a, b and A_0 are free parameters. Dynamic hysteresis corresponds to $a\kappa^{-b}$, while A_0 corresponds to static hysteresis, that persists in the limit of infinitely slow (adiabatic) sweep rates $\kappa \to 0$. As shown on Fig. 4.8(b), below the critical point ξ_{crit} hysteresis completely closes for infinitely slow scans. However for $\xi > \xi_{\text{crit}}$ we see persistence of non-zero static hysteresis. The dependence of static hysteresis on cross-over radius $A_0(\xi)$ can be used for determining ξ_{crit} and bistability regions in a similar method as the one used for hot ensemble in Sec. (4.3.2). The obtained

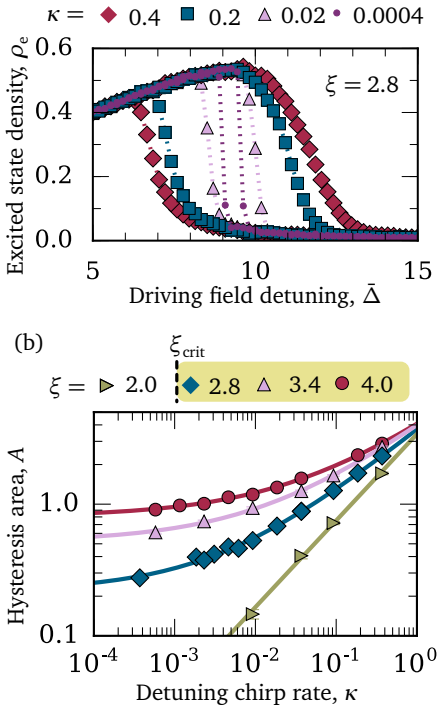

Figure 4.8: Scaling of hysteresis size for different chirp (drive detuning scan) rates κ. While hysteresis becomes smaller for slower chirp rates (a), below critical value of the van der Waals radius ξ_{crit} there is non-zero static hysteresis A_0 (b). Parameters: $\rho = 10, \bar{\Omega} = 0.8$.

[3] this characterises lifetime of the state, see Sec. 2.4.3

phase diagrams will be explored in Sec. (4.4.3).

4.4.2 Divergence of transition time between bistable states

To examine closely the emergence of static hysteresis, the characteristic times for leaving the state corresponding to the metastable part of the hysteresis loop, in the region of detunings where hysteresis is dynamic and closes for $\kappa \to 0$, are measured. The system is prepared in the high- or low- excited state density ρ_e regime, and with a fast detuning chirp it is brought to some detuning $\bar{\Delta}$ within the metastable part of the curve. The time for switching to the other state is then measured. This closely follows the experimental protocol used to measure switching times between bistable states in Ref. [87].

Above the critical van der Waals radius $\xi > \xi_{crit}$, times for the jump-up from low to high density regime $\langle T_\uparrow \rangle$ and vice versa $\langle T_\downarrow \rangle$ are found to diverge with a power law

$$T = c \cdot |\bar{\Delta} - \bar{\Delta}_c|^\alpha, \tag{4.14}$$

where c, α and $\bar{\Delta}_c$ are fit parameters. Importantly, the critical detunings $\bar{\Delta}_c^\uparrow$ and $\bar{\Delta}_c^\downarrow$ at which jump-up and jump-down times diverge were different [Fig. 4.9], indicating the existence of two long-lived states in the window $(\bar{\Delta}_c^\uparrow, \bar{\Delta}_c^\downarrow)$ of driving field detunings. The width of the static hysteresis window obtained in this way matches with the estimated static hysteresis surface area A_0 obtained with the finite-time scaling of hysteresis areas in previous Section (4.4.1).

It is possible to hypothesise that in the identified bistable regime the system switches to some new scaling of the state lifetime, and eventually still decays. This relates back to the question raised in the introduction of this section about the possibility that many-body character stabilises multiple non-equilibrium steady states in driven-dissipative states. We do not see evidence for slow-decay of obtained states in the current numerical simulations, and for practical system description this question is irrelevant since the obtained state lifetimes $> 10^4\ \Gamma^{-1}$ are many times longer than the characteristic single-excitation lifetime Γ^{-1}, exceeding the experimental observation time-scale in any cold or hot atomic ensembles to date.

Regarding the decay of metastable states in the dynamic hysteresis, there are several important differences of this many-body meta-stable state decay compared to the mean field results. In contrast to mean field results [287, 310], we don't find

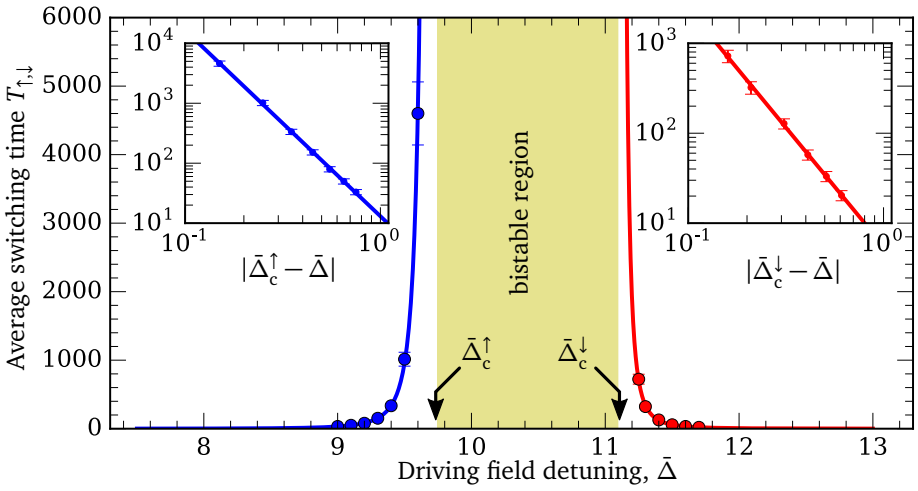

Figure 4.9: Divergence of lifetimes for high and low excited state density phase. For a system initialised in low (high) excited state density phase average switching time $T_\uparrow$ ($T_\downarrow$) to the high (low) excited state density phase are measured and shown in blue (red). Insets show that these diverge with a power-law dependence, indicating critical detuning $\bar{\Delta}_c^\uparrow$ ($\bar{\Delta}_c^\downarrow$) at which transitions to the high (low) excited state density stop. In-between two critical detunings (yellow shading), system has two long-lived non-equilibrium steady states, i.e. it is bistable. Parameters $\rho = 10$, $\bar{\Omega} = 0.8$, $\xi = 4.0$.

a single, universal value for the jump time scaling exponent α. A difference with MF is also seen in predicted transition paths $\rho_e(t)$ during the time of transition t. Transitions between the states in a frozen sample are stochastic events, defined by a single average jump time $\langle T_{\uparrow,\downarrow}\rangle$. This is in contrast to the mean field [287] that predicts deterministic trajectories with a well defined transition after some initial, *deterministic* time delay. The fact that the universal mean field exponent of $\alpha = 0.5$ was observed in experiments [87], as well as measured transition paths having a well defined initial delay, is a strong indication that motional effects, often neglected in treatment of the systems, brought the system into the mean field (eaMF) regime, as described in Sec. (4.3).

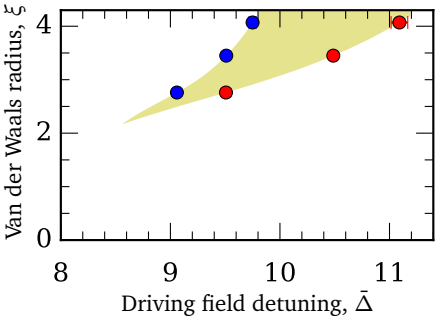

Figure 4.10: Phase diagram for a frozen system in $(\bar{\Delta},\xi)$ plane, reconstructed from switching times of non-equilibrium steady states. Critical detunings at which state lifetime diverges $\bar{\Delta}_c^{\uparrow}$ (blue circles) and $\bar{\Delta}_c^{\downarrow}$ (blue circles) delineate bistable area (yellow shading). Parameters $\bar{\Omega} = 0.8$, $\rho = 10$.

4.4.3 Phase diagrams

With the well defined transition points to bistable behaviour based on determination of a static hysteresis through hysteresis scaling (Sec. 4.4.1) and identification of the divergent switching times (Sec. 4.4.2), we can now explore a range of parameters to determine the phase diagram of the frozen system.

Extracting critical switching times $\bar{\Delta}_{\uparrow,\downarrow}$ for a range of van der Waals radii ξ allows identification of the bistable regime in the $(\bar{\Delta},\xi)$ plane, as shown on Fig. 4.10. However, this approach is slightly harder to implement automatically for a wide range of parameters, since it requires some previous knowledge of the range of detuning $\bar{\Delta}$ over which hysteresis occurs. Therefore, in the remaining part of this section we will focus on results obtained through hysteresis scaling.

For each choice of (ξ,ρ), multiple simulations are done to determine the dynamic hysteresis area A, and then the procedure is repeated for a range of sweep rates κ. The static hysteresis area is then obtained from hysteresis scaling analysis (Sec. 4.4.1). This can be repeated for a range of van der Waals radii ξ, revealing a clear continuous transition to the bistable regime. Similarly to the hot case (Sec 4.3.2), critical ξ_{crit} for which a non-zero static hysteresis area occurs can be identified. This is labelled as a *single* blue point on Fig. 4.11. Repeating this procedure for a range of densities ρ reveals the bistable phase in the (ρ,ξ) plane. The intensive numerical calculations required for this were done by Thomas Pohl using computational resources of MPIPKS

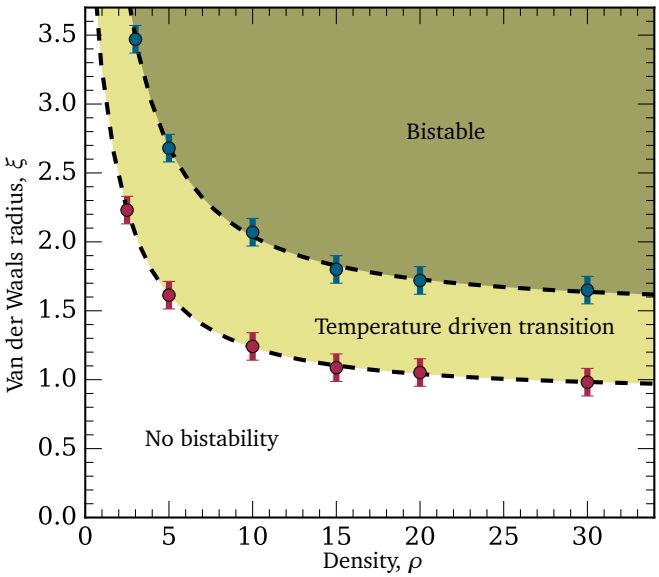

Figure 4.11: Phase diagram of the driven dissipative spin system in (ρ,ξ) plane. Blue solid circles delineate the area where frozen system is bistable, as obtained from numerical integration of dynamics (Eq. 4.6). Red solid circles delineate the area when completely uncorrelated, infinitely hot system (external degrees of freedom), is bistable, as obtained from eaMF (Sec. 4.3). In between, whether the system is bistable or not depends on the temperature of its external degrees of freedom (i.e. spin motion). Data for frozen system is from simulations by T. Pohl [99]. Parameters $\bar{\Omega} = 1$, $\rho = 10$.

in Dresden. We note that both the eaMF prediction (red circles) which is an exact solution in the limit of very hot atomic ensembles (Sec. 4.3.2), and the numeric solution for the case of a frozen gas which maintains all spatial correlations and fluctuations of local dynamics (blue circles), predict the same qualitative behaviour. In particular, critical ξ_{crit} initially decreases with increasing density ρ, only to saturate for high densities, indicating no bistability for pure van der Waals interactions $\xi \to 0$. As expected, there are quantitative differences, with the two bistable regions being shifted relative to each other. The behaviour in the gap arising from this offset will be explored in detail in Sec. (4.5).

We can obtain further insight into nature of the identified non-equilibrium phase transition into the bistable state by observing the system state for individual realizations of the disorder. The ensemble average over several very slow scans ($\kappa = 10^{-8}$) produces the phase diagram shown on Fig. 4.12(a). We can identify three regions of ξ on this phase diagram. Below the critical point (marked with open circle) there is no discontinuity in the excited state density ρ_{e}. What can be noted, however, by observing the probability distribution of ρ_{e} [shown as shading on Fig. 4.12(b-d)] obtained from recording population oscillations in time, is that the system experiences pronounced fluctuations. This is reminiscent of the thermal-equilibrium system's approach to the second order phase transition.

In the region $1.8 \lesssim \xi \lesssim 2$, just above the critical point, the system experiences a first order phase transition, indicated by the dashed line in Fig. 4.12(a), but there is still no discontinuity in ρ_{e}. This is due to time-averaging of a single system trajectory, as shown on Fig. 4.12(c) (line). The transition can be seen however if one observes the probability distribution for ρ_{e} that now separates into two well-defined attractors of dynamics. The system doesn't spent significant time between these two attractors. Keeping in mind that red and blue shading corresponds to the probability density (single realisation, time averaged) functions of ρ_{e} for positive and negative chirp rates κ, we see that the system persistently switches between these two attractors of dynamics, as indicated by the purple colour of the probability density distribution. This is very different behaviour to the usual metastable states in thermal equilibrium, for which the probability of re-entry once the system leaves the state to the stable equilibrium state, is very low [306]. Although the switching

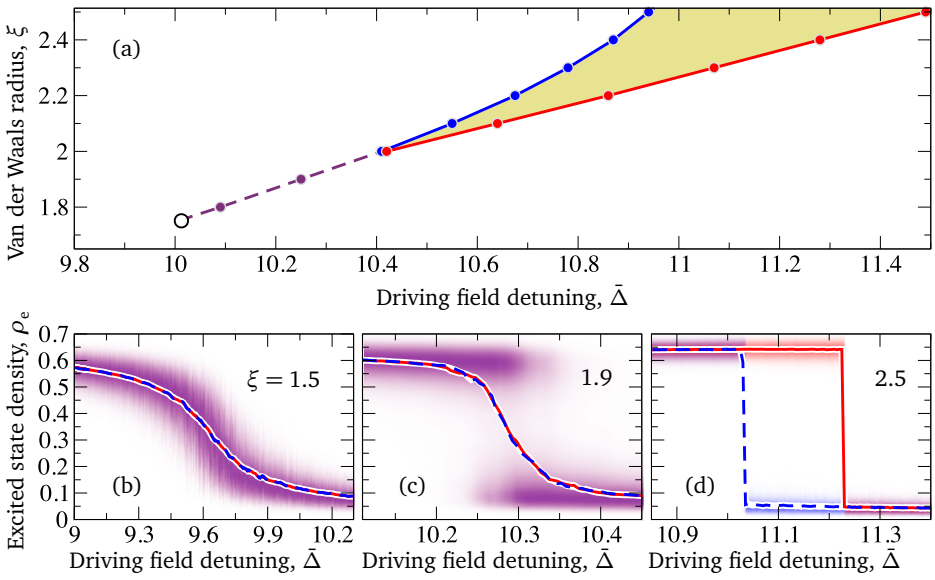

Figure 4.12: Phase diagram for the frozen system in $(\bar{\Delta}, \xi)$ plane and individual transition trajectories. Phase diagram (a) obtained from ensemble average of multiple slow scans ($\kappa = 10^{-8}$) with critical point marked with open white circle, and bistable regime with yellow shading. Individual slow-scan trajectories (b-d) show time-averaged populations for scans in positive (solid red) and negative (dashed blue) direction, while shading shows probability density function for system state obtained from time evolution of the single realisation of the system for slow scans for positive (red) and negative (blue) direction. Persistent switching between the two non-equilibrium steady states is obtained near the dashed purple line. Data from numerical simulations by T. Pohl [99]. Parameters $\bar{\Omega} = 1$, $\rho = 10$.

between states is happening on long time scales, the fact that there is constant intermittent switching between them underlines the need for describing *both* states within the theoretical framework for modelling of the system. This driven-dissipative aspect is in contrast to the usual thermal-equilibrium situations, where knowledge only of a single lowest energy state is often sufficient. In this case that is not true even after infinite time. Note also that this *persistent* bimodality in the ρ_e distribution is very different to the *transient* bimodality, theoretically discussed in Ref. [299, 311] and experimentally observed in off-resonant excitation of Rydberg atoms [89, 298]. The transient bimodality occurs purely due to the slow initial relaxation of the system, which requires creation of the first Rydberg excitation, usually a stochastic process in time, to act as an initial nucleus driving further Rydberg excitation. If one waits for a long time, there won't be bimodality in the excitation number. Finally, going back to the phase diagram [Fig. 4.12(a)], for $\xi \gtrsim 2$, fluctuations are reduced and the system exhibits a sharp transition between the high and low excited state density ρ_e state, with a clear hysteresis window.

4.4.4 Importance of short range interactions for non-equilibrium phase diagrams of driven-dissipative systems

Both eaMF results in Section (4.3.2), and results in the frozen system in the previous Section (4.4.3), highlighted the crucial impact of short-range details of the interaction potential. Although the asymptotic long-range behaviour of the potential is always $V \sim R^{-6}$, the inner dipolar-core characterized by the van der Waals radius ξ introduced qualitative new features on the non-equilibrium phase diagram. This is very much in contrast to the expectations based on thermal-equilibrium statistical physics, where short-range details of interactions usually have only quantitative impact on details of phase-diagrams. This characteristic of driven-dissipative systems has been recently noted [294] even in the case where full quantum dynamics is accounted for in system evolution. In the strong decoherence limit, the importance of extended range of the interactions (i.e. beyond nearest-neighbour interactions) on non-equilibrium phase diagrams was also highlighted in Ref. [77].

The reason for the importance of short-range potential details in the present study can be seen by considering the effect of the interaction potential form $V(r)$ on energy level fluctuations, which through flip rates $\gamma_{\uparrow,\downarrow}$ causes fluctuations in spin dynamics.

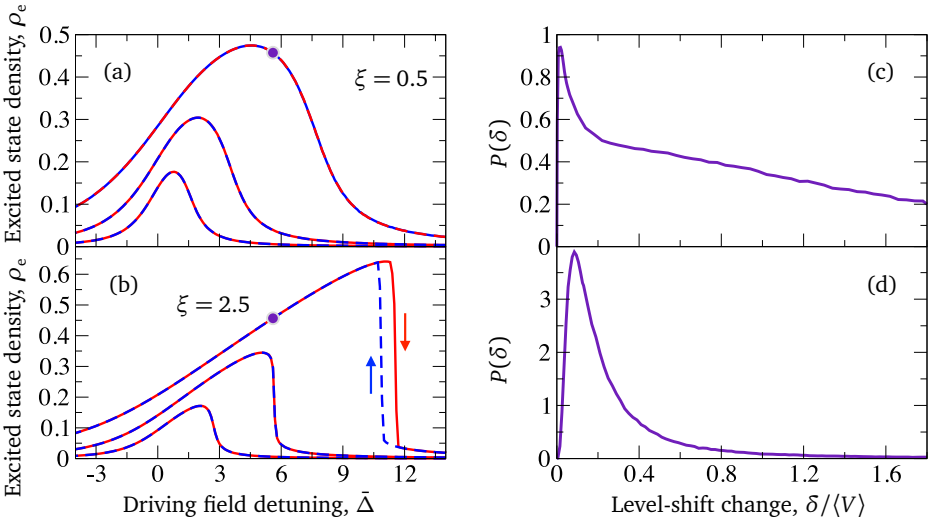

Figure 4.13: Fluctuations in the non-equilibrium dynamics controlled by the short range potential shape. (a-b) Excited state density upon drive detuning scans in positive (solid red) and negative (dashed blue) direction for $\bar{\Omega} = 1, 0.5, 0.25$. For finite dipolar core $\xi = 2.5$ (b) bistability window opens. Distribution $P(\delta)$ of maximal fluctuations in the level shift δ of the excited states due to spin de-excitation for $\xi = 0.5$ (c) and $\xi = 2.5$ (d) calculated for system in the state marked with solid purple circle (a-b). Data from numerical simulations by T. Pohl [99]. Parameter $\rho = 10$.

Individual spin decays, due to inevitable spontaneous decay or driving accounted for in $\gamma_\downarrow$, cause level shifts $\bar{\Delta}_i$ of the neighbouring spins i. For $\xi \lesssim 1$, a level shift $\bar{\Delta}_i$ of every spin is dominated by a small number of excited spins in its immediate neighbourhood. De-excitation of a single spin from that neighbourhood will cause a large change in $\bar{\Delta}_i$, causing corresponding fluctuations in excitation rates $\gamma^{(i)}_{\uparrow,\downarrow}$. The resulting large density fluctuations seen on Fig. 4.12(b) prevent the formation of the bistable phase. For large ξ, the total level shift $\bar{\Delta}_i$ depends on a number of excited spins within distance $\lesssim \xi$. Single spin decays will therefore have a much smaller influence on level detuning. This effective averaging of dynamics over a volume of $\sim \xi^3$ reduces variance in $\bar{\Delta}_i$ and fluctuations in corresponding dynamics.

This qualitative description can be quantified by observing the maximum level shift δ of excited spins caused by de-excitation of a single excited spin. This can be obtained by following the time dynamics of a non-equilibrium steady state for fixed detuning. For example, Fig. 4.13(a–b) show the selected point at which measurements are done. In both cases the system is in the same state $(\rho_e, \bar{\Delta})$. However we see that while for $\xi = 2.5$ the probability distribution $P(\delta)$ for a maximum level shift δ of the excited states has a well localized peak at small values $\delta \ll \langle V \rangle$ [Fig. 4.13(d)], for $\xi = 0.5$ it exhibits a pronounced long tail [Fig. 4.13(c)], with significant level shifts even on the scale of the ensemble averaged level shift $\langle V \rangle$ of the excited states.

Finally, we note how the initial surprise regarding the importance of the detailed shape of the short-range interaction potential can be reconciled with thermal statistical physics intuition. While formally temperature is not defined for driven-dissipative non-equilibrium steady states, we note that in these non-equilibrium situations ξ plays a similar role to the temperature in equilibrium systems. Both parameters determine relative fluctuations in dynamics, one in the driven-dissipative case, the other in the thermal-equilibrium case. Indeed, even the transition shown on Fig. 4.12(a), is in many ways reminiscent of changes in magnetisation upon temperature tuning in the Ising model of magnetics. We stop short of formally pursuing this analogy, because finding formal mapping of non-equilibrium system parameters to temperature alone is of questionable use for practical system description without formal mapping of the free energy potential concept.

4.5 Temperature driven non-equilibrium phase transitions

In Section 4.4.3 (Fig. 4.11), we noted a gap between the bistable phase in the hot atom limit (eaMF predictions) and simulations for frozen systems. Numerically solving the dynamics of the system (Sec. 4.2.1) we can continuously interpolate between these two limits by changing the velocity of the spins in the simulations. Under the assumption that inter-atomic interactions have negligible influence on the spin motion, we can completely decouple the evolution of external and internal degrees of freedom. This allows us to assign temperature to the external degrees of freedom of the spin ensemble even in the presence of driving of its internal degrees of freedom, and use a normal velocity distribution defined by mean velocity v_{th}.

On Fig. 4.14 we show hysteresis areas A obtained for slow $\kappa = 2.2 \times 10^{-3}$ evolution of the system. For slow motion, the hysteresis areas don't change, and the

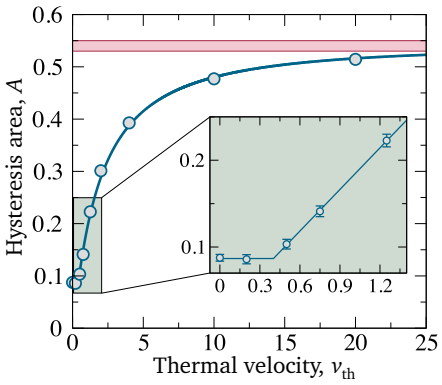

Figure 4.14: Non-equilibrium phase transition into the bistable phase driven by the temperature of the external degrees of freedom (spin motion). Blue dots are results of full numerical integration of Eq. 4.6 for $L = 12$, $\rho = 10$, $\kappa = 2.2 \times 10^{-3}$. Red line shows prediction of the eaMF for the corresponding system size and chirp rate.

extrapolated static hysteresis area goes to zero, indicating closing of the hysteresis loop. However at $v_{\text{th}} \approx 0.4$, measured in units of $r_b\Gamma$, a continuous transition to non-zero hysteresis occurs, which then gradually saturates to the eaMF value which is the exact solution for $v_{\text{th}} \to \infty$. To account for finite scan speed and finite system size, introducing inevitable fluctuations, eaMF prediction is based on evolution of the same number of particles ρL^3 under Eq. (4.10), accounting for the expected reduction in hysteresis area due to the finite size of the simulated system. Taking the typical cold-atom experimental parameters from Ref. [89], with $r_b \approx 11$ μm and $\Gamma^{-1} \approx 200$ μs, the unit velocity $r_b\Gamma^{-1}$ would correspond to an atom temperature of only ~ 30 μK, indicating that motion and the predicted temperature induced phase-transition can be observed even in cold atom systems.

4.6 Comparison with experiments

Up to now we've been focusing on a link between a spin-description of the system and predictions that can be derived under strong dephasing conditions. Now we will discuss a link between the spin-model and the realistic driven-dissipative Rydberg atomic ensemble. In order to draw conclusions based on the theoretical predictions so far, it is important to discuss how closely the initial spin model (Eq. 4.1) matches the experiments. The spin-description introduced here in Section (4.2), accounting for the full potential in spin interactions and allowing for motion, is the most complicated model used so far, and provides important insight in various effects (i.e. of atomic motion). Yet, it is still a very simplified picture of the real system. In particular, the complex Rydberg state manifold, population redistribution under collisions and black-body radiation, corresponding strong resonant dipole-dipole interactions and possible ionization (Chapter 2) have all been neglected. This is a common weakness in relating any spin models directly to observations in Rydberg experiments. We will try to estimate the influence of these additional effects, and also discuss the cleanest possible preparation for direct observation of the predictions exposed herein.

In Ref. [89] bimodal counting statistics of cold rubidium atoms excited to the 70 $S_{1/2}$ state has been reported. The quoted laser linewidth of $\gamma/(2\pi) \approx 500$ kHz and Rabi driving frequencies $\Omega < \Gamma + \gamma$ are within the range of validity of the present theory. The scaled van der Waals radius $\xi \approx 0.3$ implies that the bistable state cannot be observed according to the results of this model. The observed bimodality is not then caused by the emergence of bistability [285, 288] or a phase transition [290] in the steady state of the system. However, in the transient regime, for the finite excitation time τ it can emerge due to the finite relaxation time of the system, dominated by the creation of the initial Rydberg "seed" excitation. On long time-scales, black-body radiation induced population of the neighbouring levels (Sec. 2.3.2) can significantly affect excitation dynamics, as was seen in recent experiments [37, 312, 313].

In Ref. [311] cold Rubidium atoms were prepared in a three-dimensional optical lattice, with a single atom per lattice site, and atoms were excited to the 25 $P_{3/2}$ state. No bistability was observed. Again the quoted laser linewidth of $\gamma/(2\pi) \approx 300$ kHz and Rabi frequency $\Omega/(2\pi) = 77$ kHz are within the range of validity of the rate equation model. With the calculated interaction potential $V \propto R^{-9}$, which has faster decay than that of pure van der Waals interactions for which $\xi \to 0$, no bistability

is predicted within the model presented in this chapter, which is consistent with experimental observations. Also, the low density per blockade volume would prevent observation of bistability (see phase diagram on Fig. 4.11). The density is further reduced during the experimental sequence due to additional loss of the atoms from the lattice due to ionization. This problem is less pronounced in atomic clouds, and completely absent in thermal vapours.

Finally, we turn our attention to thermal vapour experiments where bistability *has* been observed [87, 102, 281, 314]. Based on the sign of the van der Waals shift and the side on which the bistability is observed experimentally, it was concluded in recent study [281] that bistability is not due to van der Waals interactions, which is in agreement with the presented model. It was also argued that bistability originates purely from the creation of ions. Ion creation is inevitable in thermal vapours due to collisional processes, and since Coloumb potential is even longer range then potential $V(r)$ considered here even in the limit of $\xi \to \infty$, it could produce bistability. However, we note that in experiments in Ref. [314] bistability for both positive and negative detunings was observed. Also for low-lying 12 $P_{3/2}$ states in caesium, sharp turn-on is observed for both positive and negative detunings at equal but opposite detunings from the line centre (C. Wade private communication), allowing for some parameters even double bistability, for both red and blue detunings, to be observed. Also, fluorescence for nearby 11 D states (ibid.), that provides readout of relative population in this state, also has a symmetric profile around the centre of the line. These symmetric features, sometimes allowing observation of double bistability, cannot be explained purely with an ion-induced shift that shifts energy levels only in one direction, and suggest contribution of dipole-dipole interactions [315].

Putting thermal vapour experiments in the context of the presented theory requires checks of both the domain of validity of rate equations and questioning of the form of potential $V(r)$. The strong dephasing limit required for validity of the rate equations is easily satisfied due to rapid thermal motion which introduces collisional and other effects [88] that result in rapid dephasing of the excited states. The system is treatable within the ensemble averaged mean-field model (eaMF). However, since low-lying states don't have van der Waals interactions with $\xi > 1$, this would indicate the absence of bistability in our model. We note however that collisional processes (Sec. 2.6) quickly populate neighbouring opposite parity states. The same is true for black-body induced transitions (Sec. 2.3.2), which happen even in the absence of collisions, leading to fast avalanche excitation as seen in the off-resonant excitation of lattices [37, 38]. These give rise to resonant dipole-dipole interactions, which would be effectively modelled as level shifts due to $V(r)$ for $\xi \gg 1$, that would produce bistability. The important difference is that for resonant dipole-dipole interactions, levels are split, i.e. shifted in both positive and negative detuning direction. This can be easily accounted for with the jump-up rate

$$\gamma_{\uparrow}^{\mathrm{dd}} \to \frac{\bar{\Omega}^2}{1+4\bar{\Delta}_i^{+}(\mathbf{S})^2} + \frac{\bar{\Omega}^2}{1+4\bar{\Delta}_i^{-}(\mathbf{S})^2}, \tag{4.15}$$

and corresponding $\gamma_{\downarrow}^{\mathrm{dd}} = \gamma_{\uparrow}^{\mathrm{dd}} + 1$, where $\Delta_i^{\pm}(\mathbf{S}) = \Delta \pm \sum_{j\neq i} V(r_{ij})\, s_j$. This excitation rate now produces a symmetric lineshape and bistability. The presence of ions, neglected so far, can introduce additional uni-directional energy level shifts $\Delta_i^{\pm}(\mathbf{S}) \to \Delta_i^{\pm}(\mathbf{S}) + \sum_{k\neq i} \alpha/r_{ik}^2$, where k is a sum over all ions in the environment, and α is proportional to the scalar polarizability of the state (Sec. 2.4.1). This would explain

why in high-densities of high-lying states, only one branch of bistability is visible. Yet for states with lower polarizability, like 12 P, the ion induced shift is not strong enough to completely wash-away strong turn-on at a particular detuning, sometimes allowing even observation of double bistability.

Therefore, it seems likely that at least for some thermal vapour experiments, the bistability occurs due to dipole-dipole interactions, which themselves occur due to the excitation of states of opposite parity within the Rydberg manifold. This is indicated by the symmetric turn-on points of excited 12 P states, and symmetric fluorescence for neighbouring opposite parity 11 D states in caesium (C. Wade private communication). For highly polarizable states, an ion-induced shift would make one branch of the bistable curve more pronounced as in Ref. [314], consistent with the sign of state polarizability, while for a high-density of excitations the ion-induced shift dominates allowing only a single bistable curve to be seen [87, 281]. Finally, dephasing effects [102] can reduce the effective driving strength $\bar{\Omega}$ closing the bistability.

Finally we note that possible direct realization of the $V(r)$ potential [Eq. (4.2)], and tuning of the ξ value can be achieved experimentally by selecting states with different energy defects (Sec. 2.5.1) or by selective admixing of other states through AC and DC applied fields (Sec. 2.5.3).

4.7 Summary

In this chapter we explored a spin model of driven-dissipative Rydberg atomic ensembles. Being particularly interested in fluctuations and correlations in dynamics, controlled both though the inter-atomic interaction potential dependence on distance as well as atomic motion, we solved the model in the strong dephasing case. That allowed us to track the large number of atoms necessary to capture these effects. In the limit of a very hot ensemble, where atomic motion destroys any spatial correlations among excited particles, we have introduced a new exact solution of the ensemble averaged mean field (eaMF). By correctly accounting for the resonant nature of excitation dynamics, eaMF does not suffer from the divergences of simple early mean field treatments. Directly averaging the dynamics, eaMF also captures the effects of temporal fluctuations in the excitation dynamics. This solution was benchmarked against the full dynamics from numerical simulation of hot ensembles, providing a very good agreement. It also showed that for the emergence of bistability, and indeed associated phase transitions, the dipolar core of the interaction potential has to be taken into account, as pure van der Waals interactions do not produce bistability.

For frozen ensembles that keep correlations among created excitations, we introduced hysteresis scaling and observed changes in jump times that allowed us to provide clear criteria for the emergence of long-lived bistable solutions. No universal features in transition dynamics were observed, indicating that atomic motion is crucial for the emergence of universal mean-field exponents seen in experiments. Reconstructed phase diagrams show transition through a critical point into a first order phase-transition, where the system does not have a unique steady state but exhibits persistent switching between a high-excitation density and low-excitation density branch, which can be detected as persistent bistability in the full counting distribution. Persistent switching and lack of a unique steady state highlights the need that any practical theoretical treatment of these systems has to account for the existence of both of these states to be a sufficient system description. This first-order transition region then continues into region where long-lived bistable solution exists. Qualitatively, phase diagrams of both frozen and infinitely hot systems are the same. In the region where they differ, temperature-driven non-equilibrium phase transition was detected.

Experiments have been discussed in view of these results. While a simple interpretation of cold atom experiments is possible, at least before the black-body radiation induced processes start to have a crucial role, for thermal vapour experiments analysis is harder due to the collisional and black-body induced redistribution of the initial Rydberg state. At the moment, it seems that the resonant dipolar interactions that arise in this processes can play a crucial role in the appearance of bistability.

This work highlighted the importance of potential shape at short-range for phase diagrams of driven-dissipative systems. Although the considered potential always had the same short-range form ($\sim R^{-6}$) at long distances, the short range details control the impact of fluctuations on non-equilibrium dynamics, playing a similar role to temperature in thermal equilibrium systems, and have significant *qualitative* impact on the non-equilibrium phase diagrams.

Outlook and conclusion

CHAPTER 5

In this chapter we show two simple ideas that can be used in the future short-term development of work described in this thesis. One of them is technological, as a way forward to laser locking in high magnetic fields, that as we will see, might be used in special cases even for Rydberg state excitation. The second is an interesting phenomena that illustrates another way in which the dynamical nature of the dephasing and noise, e.g. due to atomic motion, can actually recover coherent quantum behaviour. Building on these ideas, and other results exposed in the thesis, we will conclude by looking at possible long-term developments.

5.1 Short term outlook

Here we show some immediate extensions of experimental and theoretical work presented in the thesis.

5.1.1 Drift-free atomic frequency reference with ~ 30 GHz of continuous tuning

The experiment in strong magnetic fields outlined in Sec. 3.3.4 didn't use active laser locking, and the dressed-state EIT (Sec. 3.2) also didn't have a frequency reference for locking the last control laser. We recently demonstrated that usual saturation spectroscopy can be easily extended in the hyperfine Paschen-Back regime, providing both a solution for laser locking in strong-magnetic fields and possibly a frequency reference for at least one particular Rydberg state transition. On Fig. 5.2(a-b) we see a theoretical prediction for the D1 transition frequencies of rubidium in a variable magnetic field, that can be easily tuned by adjusting the distance between the two permanent magnets (see Fig. 3.16). Of course, Doppler broadening still produces ~ 300 MHz wide features. However if a probe light is used in conjunction a with circularly polarised counter-propagating pump [Fig. 5.1(a)], it is possible to perform saturation spectroscopy, generating a frequency comb of clear narrow peaks [Fig. 5.1(b)]. Using a standard frequency modulation setup [316], side-bands can be added to the probe laser which is then detected on a fast avalanche photodiode (APD). The differential absorption of the light at side-band frequencies can be extracted by phase-sensitive detection, implemented by simple probe signal mixing with the local oscillator signal from which a near DC component is extracted by a low-pass filter [Fig. 5.1(a)]. This generates narrow (~ 10 MHz) dispersive features suitable for laser locking [Fig. 5.1(c)]. Similar dispersive features can also be formed by polarisation-spectroscopy [317] [Fig. 5.1(b)].

ACKNOWLEDGEMENTS: Work described in this section was done in collaboration with Massayuki Kondo.

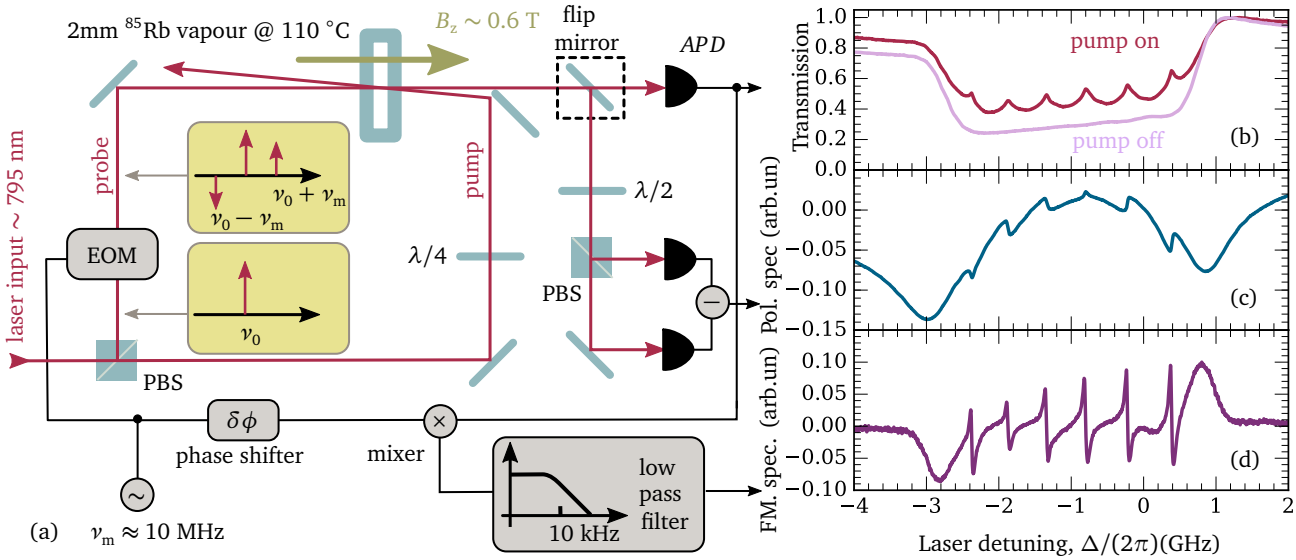

Figure 5.1: Saturation spectroscopy in the hyperfine Paschen-Back regime. (a) Schematics of optical setup and electronics. Probe light is split on polarising beam splitter (PBS) into weak probe and stronger pump beam. Electro-optic modulator (EOM) adds side-bands to the probe frequency, as indicated on insets (yellow). Pump, whose polarisation can be adjusted with quarter wave-plate ($\lambda/4$), is overlapped with counter-propagating probe inside the Rubidium vapour filled cell. The cell is inside the magnets [not shown, same as in Fig. 3.16(b)] whose distance can be adjusted to provide variable magnetic field B_z. Probe signal is analysed with saturation spectroscopy (b), polarisation spectroscopy (c) and frequency modulation spectroscopy (d).

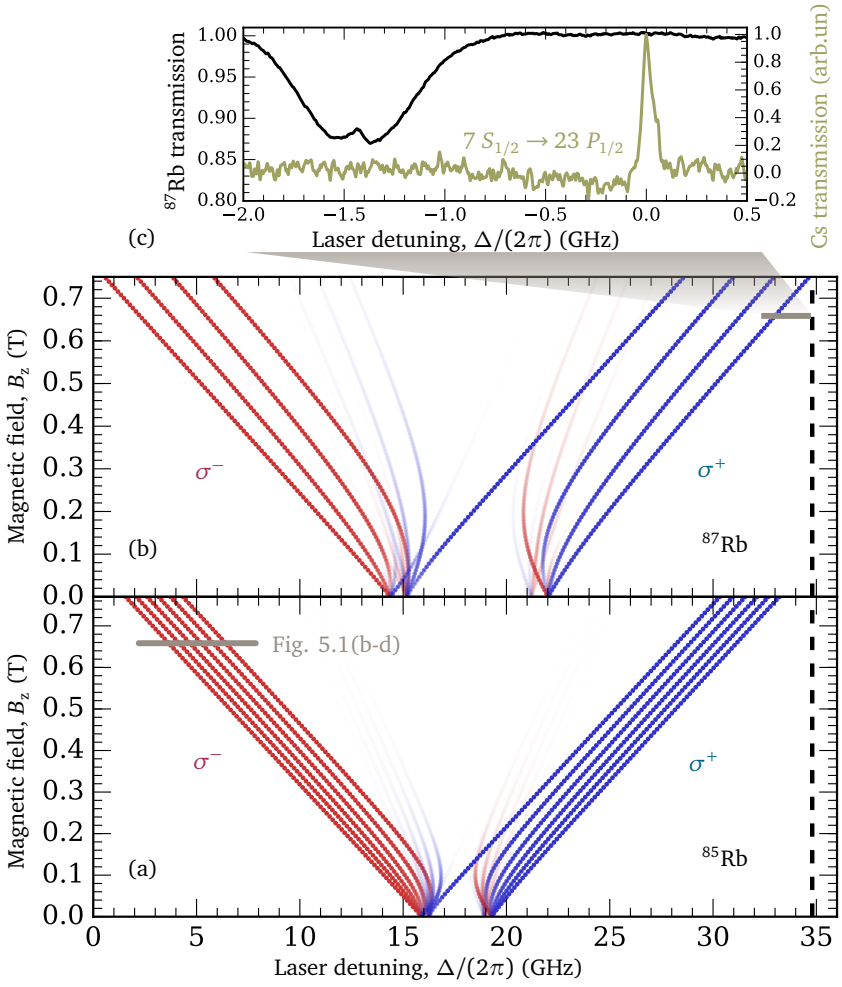

Figure 5.2: D1 transitions in ^{85}Rb (a) and ^{87}Rb (b) in a magnetic field of up to 0.75 T. Calculated with ElecSus [318]. Colour intensity is linear maping of normalized relative strength $\propto \Omega^2$ of $\sigma^{\pm}$ transitions. Dashed vertical line marks transition in caesium $7\,S_{1/2} \leftrightarrow 23\,P_{1/2}$ for which rubidium ground state transition might provide a frequency reference (c).

In contrast to Faraday rotation spectroscopy [319] that is an alternative locking method for off-resonant locking and for use in strong magnetic fields, this approach is insensitive to atom-vapour number density [see Sec (2.8)], and is thus insensitive to any temperature drifts. The location of the atomic spectral features is set only by the strength of the magnetic field, determined by the mechanical position of permanent magnets, providing an essentially drift-free atomic reference. The location of the peaks can be, in principle, tuned continuously over more than ~ 30 GHz by moving permanent magnets. If the magnetic field used is pre-calibrated, one can calculate the transmission spectrum from the ElecSus [318] program package, easily achieving ~ 1 MHz frequency calibrated laser scan covering this whole range. We expect that this will find use in future experiments in the hyperfine Paschen-Back regime. In the experiment, the tuning range was limited purely by the maximum field we could reach with the given permanent magnets. Since the strength of the transition lines doesn't show signs of weakening [Fig. 5.2], we can expect that one can use incidental near resonance of rubidium-87 $5S_{1/2} \rightarrow 5P_{1/2}$ transition with transition caesium transition to Rydberg states $7S_{1/2} \rightarrow 23P_{1/2}$, providing a simple way to lock the Rydberg laser on resonance, or at an arbitrary detuning. The results achieved with the current magnets [Fig. 5.2(c)] show that we can tune the Rubidium transition to be 1.4 GHz from the transition in caesium, with the reference beam shifted $2\pi \times 0.5$ GHz closer to the Rubidium transition with an AOM. With slightly bigger magnets, providing a stronger field of about ~ 0.7 T, we should be able to lock on resonance, providing a resource for future caesium Rydberg thermal vapour experiments.

5.1.2 Coherent dynamics under fast, low-drift noise

In chapter 3 we've seen how atomic motion dephases collective excitations. It is also interesting to consider how atomic motion can influence single-atom excitation dynamics, e.g. due to changing level-shifts as an atom travels through an atomic medium filled with other atoms with whom it interacts [Fig 5.3(a)]. One motivation for considering such a system is the dynamics of an atom as it flies through the facilitation sphere during off-resonant excitation (Sec. 2.5.2). To get some insight into this problem, we will consider the simplest model, where motion induces a dynamic change of the excited state detuning $\Delta(t) = \Delta + f(t)$, where Δ is driving field detuning and $f(t)$ is a noise term, effectively reproducing the interaction contribution to the level shift from the rapidly changing atom's environment. We will consider Gaussian noise, with zero-mean[1] $\langle f \rangle_t = 0$, and standard deviation σ_N [5.3(b)] . The noise has a correlation time of τ, which is implemented numerically by sampling a new value for f at time steps τ from the corresponding normal distribution.

Let's consider the regime $\Omega/\Gamma = 0.2$, which is within the domain of validity of the rate equations. We will evolve single atom dynamics both under the rate equations, and under full quantum dynamics, implemented with the Monte Carlo wavefunction (QMC) approach [320]. The QMC approach results are shown on Fig 5.4(a), for different correlation times τ. For static atoms, $1/\tau \rightarrow 0$, an atomic ensemble will have just a broadened line, which can be accounted for by adding some additional

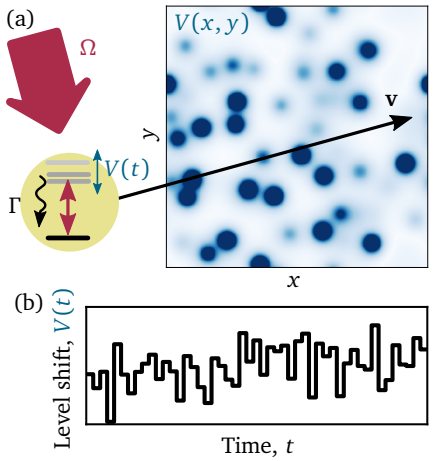

Figure 5.3: Driven two-level system in rapidly varying environment. (a) Two-level system, whose upper level decays with rate Γ is driven with field whose Rabi frequency is Ω. As the system travels through the environment with speed $\mathbf{v}$, environment will induce time-varying level shift $V(t)$. The simple model for this shift $V(t)$ is Gaussian distributed process (b), where each value of the noise lasts some time τ that would depend on the speed v that characterises system motion.

[1] we'll do calculations for noise with fixed mean value, but in principle similar considerations apply for slowly-drifting mean value

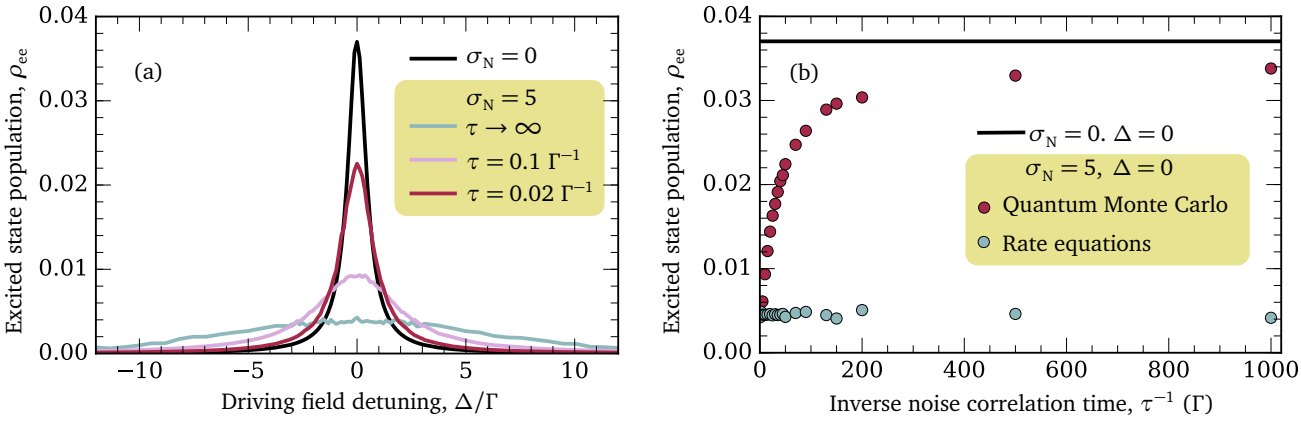

Figure 5.4: Motional averaging of single-spin dynamics. (a) Resonance lines for system driven with Rabi frequency $\Omega/\Gamma = 0.2$. Unperturbed line (black) is broadened after introducing level shifts (blue), but, fast dynamic level shifts recover narrow linewidths (red). Results of ensemble average over multiple Quantum Monte Carlo (QMC) simulations. (b) Comparison of excited state population for resonant driving $\Delta = 0$, for dynamics under QMC and rate equations. Solid black line is population for unperturbed state.

inhomogeneous dephasing $\gamma \sim \sigma_N$. In this limit, rate-equations will also give the correct prediction, as seen on Fig. 5.4(b). If we now introduce dynamic noise, the results are however very different. We will see that QMC predicts significant line narrowing, approaching an unperturbed line.

This can be understood to be a consequence of the fundamentally *continuous* nature of quantum evolution. Changes in detuning Δ with correlation time-scales τ much faster than the internal dynamics $\tau \ll \Omega^{-1}, \Gamma^{-1}$ cannot be recorded in the system's internal state. In the Bloch-sphere picture of two-level system evolution, the system cannot react instantaneously to rapid changes in direction of the driving vector $\mathbf{\Omega}$, and instead the effective evolution will be around some driving vector $\langle \mathbf{\Omega} \rangle_t$ averaged over time $t \sim \mathrm{Max}[\Omega^{-1}, \Gamma^{-1}]$. Indeed, this phenomena has been discussed by P. W. Anderson [321] in the 1950's in the context of motional narrowing in nuclear magnetic resonance spectra.

Rate equations, as derived in Sec. (4.2), depend only on instantaneous detunings, and thus always predict the same population on resonance, independent of the correlation time τ of any noise. This is of course un-physical, and the reason is that we must now consider an additional time scale τ when we assume that coherences in Eq. (4.3) have evolved to their steady states. For $\tau < \gamma + \Gamma$, we cannot assume that coherence is following fast changes in detuning. In this example the *dynamical* nature of inhomogeneities in environment-induced detuning shifts exposes continuous evolution of the two-state system, and prevents description purely in terms of a single parameter σ_N describing a *static* image of environment induced dephasing.

Similarly, in many-body systems, the dynamic nature of the noise in coupling strengths (or, equivalently, detunings) can reduce their effect on dephasing coherent dynamics of the system. To see this we can consider a simple example of an excitation travelling in a spin chain $|e_1, g_2, \ldots, g_N\rangle \to |g_1, e_2, \ldots, g_N\rangle$ of N two-level ($|e_i\rangle$ and $|g_i\rangle$) spins, coupled with nearest neighbour interactions $\hat{V} = \sum_{i<N} V(|g_i e_{i+1}\rangle\langle e_i g_{i+1}| + \mathrm{h.c.})$. We account for the noise in spin levels due to for example different AC Stark shifts of individual atoms trapped in optical tweezers, or similarly for noise in coupling strength due to disorder in exact spin locations

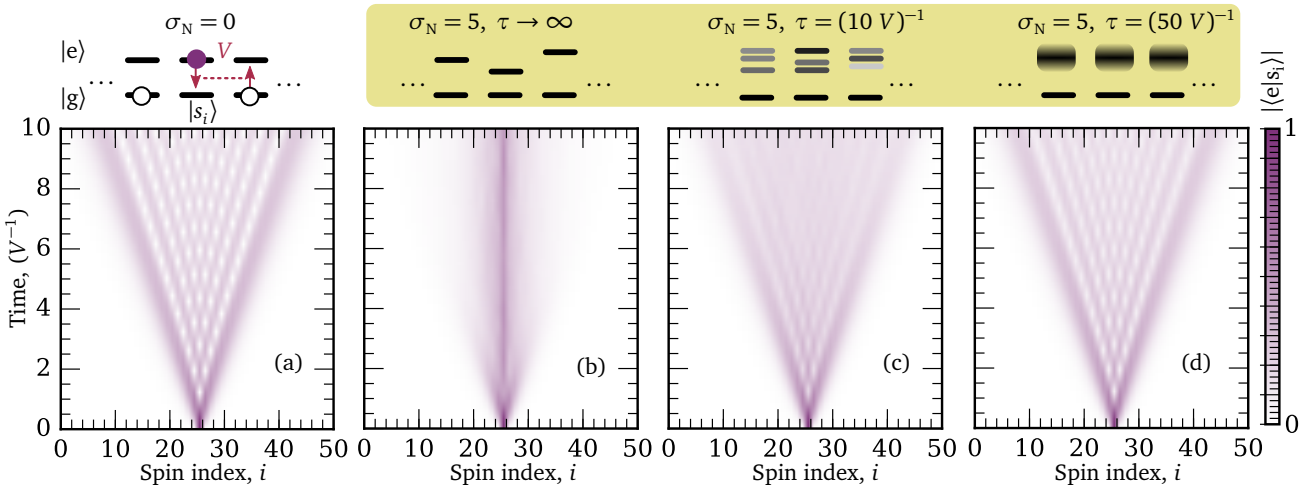

Figure 5.5: Motional averaging of many-body dynamics. A spin-chain with nearest-neighbour coupling that induces hopping of excitation initially located in the middle spin [schematics above (a)]. Evolution under coherent dynamics produces quantum random walk with characteristic interference in probability amplitude and characteristic ballistic expansion of the excitation. Static noise in the spin levels (b) localises excitation, preventing also observation of interference in probability amplitude. However dynamic noise, recovers characteristic coherent transport (c-d).

in the potential wells of 1D optical tweezer chain, by the same Gaussian noise as described in the previous paragraph. We see on Fig. 5.5 that while static noise on spin detunings completely destroys coherent transport of excitation [Fig. 5.5(b)], if dynamic changes are fast, with zero mean, the coherence time of the system is longer, increasing the time over which coherent transport can be seen [Fig. 5.5(c-d)].

Two simple models discussed here showed two interesting cases where system induced dephasing *cannot* be accounted for with an additional parameter describing static dephasing, but actually recover more coherent dynamics than what one expects from such a static description of dephasing. This can motivate further exploration of the dynamic nature of various fluctuations, and their influence on the quantum evolution of the systems. The mechanism described here, most closely described in Ref. [321], is effectively the same mechanism that brings about spin-exchange narrowing [322] in dense thermal vapours used in magnetometry, exchange narrowing in paramagnetic resonance [323], and Dicke narrowing [324] under fast collisions. This mechanism can be interesting to explore further in context of atomic motion in both off-resonantly (van der Waals) and resonantly (dipolar) coupled Rydberg ensembles, as well as dense dipolar samples achieved in high-density thermal vapours.

5.2 Conclusion: long term outlook

The tunability of Rydberg states (Chapter 2), combined with control of dissipation, dephasing, and good spatial localization, provides a good test of our understanding of single- and many-body aspects of atom-light interactions. Equally, if not more importantly, they can provide an insight into deficiencies of the current models. The sometimes unwanted, incidental knowledge in the current era of quantum simulators, about various dissipation and dephasing mechanisms, can be our biggest future asset in building atomic-physics technology. This is because it will allow better understanding and thus much better control of atomic vapours (Chapter 3), that already have production-ready, widely-deployable real-world applications. In particular, for advanced future applications of dense thermal vapours, we have to develop better understanding of atom-light interactions in the presence of strong atom-atom interactions.

For the long-lived states of driven-dissipative many body system, regardless of their origin, be it dissipation gap closing in the thermodynamic limit or emergence of high dynamical barriers for transitioning between the states, identification of good quantities and concepts through which we can quantify their behaviour, and predict their occurrence and dynamics is important. We don't have to look far to new technologies to see this. In fact, we have to look no further than ourselves to be persuaded of this: life is a transient dynamical driven-dissipative phenomena. And this is not meant in poetic way, but in a deeply technical one. Cell decision making and function in our bodies is determined by the noisy chemical circuits and their dynamics attractors, as well as it is evolution on the longer scale. Similarly, the critical and metastable nature of our neural circuitry allows the very thoughts we have. In all of them attractors of many-body dynamics and their metastable nature is the very reason for what on a macroscopic scale we recognise as well-defined functioning. We are trying to build frameworks for understanding of driven-dissipative processes, and develop more precise understanding of limits of various simplifying assumptions (Chapter 4). At the end, better understanding of these processes might also allow for building fundamentally new types of hardware for adaptable and responsive ("smart") future technology. The current development of so-called Artificial Intelligence looks impressive, but is mainly based on patter recognition (through Deep Learning in Neural networks) and Natural Language Processing algorithms. While both of these extend previous applications, technology is still based around old-style, deterministic, sequential electronics hardware. Taking inspiration from the functioning of the human brain, it would be interesting to explore what can be done with hardware that can exhibit criticality, avalanches, multiple stochastic attractors and similar complex dynamics in a strongly parallel way. Can such hardware provide more interesting, original responses to various environmental inputs? The answer is uncertain, but to even try to respond to that we need new ideas since the language (i.e. concepts for thinking about) used for building and programming old electronics hardware is not best suited for new systems. While it seems unlikely that Rydberg atoms will be the ultimate implementation of such a hardware, it is certain that we need to develop new concepts for better, easier understanding of driven-dissipative non-equilibrium systems.

Appendix

CHAPTER A

A.1 Numerov numeric integration of radial wavefunctions

Here we describe a simple way of radial wavefunction integration with Numerov method.

Equation for the radial wavefunction (Eq. 2.4) can be writen in terms of $u(r) \equiv rR(r)$ as

$$\begin{aligned} \frac{\mathrm{d}^2}{\mathrm{d}r^2}u(r) &= -[2\mu(E-V)-\ell(\ell+1)/r^2]\,u(r) \\ &\equiv -g(r)\,u(r). \end{aligned} \tag{A.1}$$

This is a purely second order differential equation, that can be integrated using a Numerov[119, 120] approach as

$$u(r-\delta r) = \frac{2\left[1-\frac{5}{12}\delta r^2\ g(r)\right]\ u(r) - \left[1+\frac{1}{12}\delta r^2\ g(r+\delta r)\right]u(r+\delta r) + \mathcal{O}(\delta r^6)}{1+\frac{1}{12}\delta r^2\ g(r-\delta r)}. \tag{A.2}$$

If required, non-linear mesh can be used for integration points, see e.g. Refs. [121, 325].

A.2 Derivation of equations for propagation of electromagnetic field in a slowly varying amplitude approximation

Here we derive Maxwell eqution for medium where both electric field and medium polarisability are slowly varying.

Starting from the Maxwell equations for electric field **E** propagation in space without free charges

$$\nabla^2\mathbf{E} - \frac{1}{c^2}\frac{\partial^2\mathbf{E}}{\partial t^2} = \frac{1}{\varepsilon_0 c^2}\frac{\partial^2\mathbf{P}}{\partial t^2}, \tag{A.3}$$

we can factor out fast oscilations of electric field **E** and polarisation **B** around some center frequency $\bar{\omega}$ with corresponding wave vector $\bar{k} = \bar{\omega}/c$

$$\mathbf{E} = \frac{\mathcal{E}}{2} e^{i\bar{k}z - i\bar{\omega}t} + \text{c.c.}, \tag{A.4}$$

$$\mathbf{P} = \mathscr{P} e^{i\bar{k}z - i\bar{\omega}t} + \text{c.c.}, \tag{A.5}$$

and find equations govering dynamics of envelope of these oscilations $\mathcal{E}(r,t)$, $\mathscr{P}(r,t)$, which is slowly changing in the propagation direction and in time compared to the factored out part

$$\left|\frac{\partial \mathcal{E}}{\partial z}\right| \ll |\bar{k}\mathcal{E}|, \qquad \left|\frac{\partial \mathcal{E}}{\partial t}\right| \ll |\bar{\omega}\mathcal{E}|, \qquad \left|\frac{\partial \mathscr{P}}{\partial z}\right| \ll |\bar{k}\mathscr{P}|, \qquad \left|\frac{\partial \mathscr{P}}{\partial t}\right| \ll |\bar{\omega}\mathscr{P}|. \tag{A.6}$$

Replacing factored electric field **E** (Eq. A.4) and polarisability **P** (Eq. A.5) into Maxwell equations (Eq. A.3), and keeping only the first order terms (in expansion in terms of small values from Eq. A.6)

$$\frac{1}{2i\bar{k}}\left(\frac{\partial^2}{\partial x^2} + \frac{\partial^2}{\partial y^2}\right)\mathcal{E} + \frac{\partial \mathcal{E}}{\partial z} + \frac{1}{c}\frac{\partial \mathcal{E}}{\partial t} = \frac{i\bar{k}}{\varepsilon_0}\mathscr{P}. \tag{A.7}$$

For plane-wave we can neglect first part of this equaiton characterising field variation in transverse diraction to the propagation ($x-y$ plane), and we obtain Eq. 2.20.

A.3 Derivation of analytical solution for ensamble averaged Mean Field

Here we present derivation of analyitical closed form of excitation rate $\bar{\gamma}_\uparrow$ averaged over completely uncorrelated ensemble. This derivation follows closely original derivation by T. Pohl (private communication) and it is stated here for completeness.

Average excitation rate can be calculated as

$$\bar{\gamma}_\uparrow = \bar{\Omega}^2 \int \frac{P(W)\,\mathrm{d}W}{1+4(\Delta-W)^2}, \tag{A.8}$$

where $P(W)$ is probability density for the interaction-induced level shift of W in uniform, uncorrelated ensamble

$$P(W) = \left\langle \delta\left[W - \sum_i V(r_i)\right]\right\rangle_{\text{ensemble}} \tag{A.9}$$

$$= \frac{1}{L^{3N_\mathrm{e}}} \int \delta\left[W - \sum_i V(r_i)\right] \mathrm{d}\mathbf{r}_1 \ldots\ \mathrm{d}\mathbf{r}_{N_\mathrm{e}}, \tag{A.10}$$

where $\langle \ldots \rangle$ denotes average over ensemble, and N_e is number of excited spins. Using Fourier transformed form of δ function, we obtain

$$\begin{aligned} P(W) &= \frac{1}{L^{3N_\mathrm{e}}} \int \frac{1}{2\pi} \int e^{-i[W-\sum_i V(r_i)]k} \mathrm{d}k\ \mathrm{d}\mathbf{r}_1 \ldots \mathrm{d}\mathbf{r}_{N_\mathrm{e}} \\ &= \frac{1}{2\pi} \int \mathrm{d}k\ e^{-iWk} \left[\frac{1}{L^3}\int e^{iV(r)k}\mathrm{d}\mathbf{r}\right]^{N_\mathrm{e}} \\ &= \frac{1}{2\pi} \int \mathrm{d}k\ e^{-iWk} \left\{1 + \frac{\rho_\mathrm{e}}{N_\mathrm{e}} \int \left[e^{iV(r)k} - 1\right]\mathrm{d}\mathbf{r}\right\}^{N_\mathrm{e}}, \end{aligned} \tag{A.11}$$

where we have introduced desity of excited states $\rho_\mathrm{e} \equiv N_\mathrm{e}/L^3$. Going into the limit $L^3, N_\mathrm{e} \to \infty$, we obtain

$$P(W) = \frac{1}{2\pi} \int \mathrm{d}k\ e^{-iWk}\ \exp\left\{\rho_\mathrm{e} \int [e^{iV(r)k} - 1]\mathrm{d}\mathbf{r}\right\} \tag{A.12}$$

$$\frac{1}{2\pi} \int \mathrm{d}k\ e^{-iWk}\ \exp[-kf(k)], \tag{A.13}$$

where we have defined $f(k) \equiv \rho_\mathrm{e} k^{-1} \int \{1 - \exp[ikV(r)]\}\ \mathrm{d}\mathbf{r}$. Note that real and imaginary part of the $f(k)$ have odd and even parity respectively, $\mathrm{Re}[f(k)] = -\mathrm{Re}[f(k)]$, $\mathrm{Im}[f(k)] = \mathrm{Im}[f(-k)]$. Inserting obtained probability density (Eq. A.13) into expression for average rate (Eq. A.8) we obtain

$$\bar{\gamma}_{\uparrow} = \frac{\bar{\Omega}^2}{2\pi} \int \mathrm{d}k \; e^{-kf(k)} \underbrace{\int \frac{e^{-ikW}\mathrm{d}W}{1+4(\Delta-W)^2}}_{=\pi \exp(-i\Delta k - |k|/2)/2}$$

$$= \frac{\bar{\Omega}^2}{4} \int \mathrm{d}k \; \underbrace{\exp\{-|k|/2 - k\mathrm{Re}[f(k)]\}}_{\equiv A}$$

$$\cdot \left[\underbrace{\cos(-k\{\Delta + \mathrm{Im}[f(k)]\})}_{\equiv B} + i \underbrace{\sin(-k\{\Delta + \mathrm{Im}[f(k)]\})}_{\equiv C} \right]. \tag{A.14}$$

In integration over k from $-\infty$ to $+\infty$ imaginary part dissapears, as expected, due to odd parity of $A \cdot C$. Real part we can write, using even parity of $A \cdot B$, as

$$\bar{\gamma}_{\uparrow} = \frac{\bar{\Omega}^2}{2} \int_0^{+\infty} \mathrm{d}k \; e^{-k\{1/2 + \mathrm{Re}[f(k)]\}} \cos(k\{\Delta + \mathrm{Im}[f(k)]\}). \tag{A.15}$$

Bibliography

[1] Sui Huang, Ingemar Ernberg and Stuart Kauffman, "Cancer attractors: a systems view of tumors from a gene network dynamics and developmental perspective." *Semin. Cell Dev. Biol.* **20**, 869 (2009) (p. 1).

[2] L.-M. Duan, M. D. Lukin, J. I. Cirac and P. Zoller, "Long-distance quantum communication with atomic ensembles and linear optics." *Nature* **414**, 413 (2001) (pp. 1, 44, 66).

[3] M. D. Lukin and A. Imamoğlu, "Nonlinear optics and quantum entanglement of ultraslow single photons", *Phys. Rev. Lett.* **84**, 1419 (2000) (p. 1).

[4] M. Fleischhauer and M. D. Lukin, "Quantum memory for photons: Dark-state polaritons", *Phys. Rev. A* **65**, 022314 (2002) (pp. 1, 44, 50).

[5] C. Monroe, "Quantum information processing with atoms and photons." *Nature* **416**, 238 (2002) (p. 1).

[6] Markus Müller, Sebastian Diehl, Guido Pupillo and Peter Zoller, Engineered Open Systems and Quantum Simulations with Atoms and Ions, *Adv. At. Mol. Opt. Phys.* Ed. by Paul R. Berman, Ennio Arimondo and Chun C. Lin, Academic Press, 2011, 1–80, arXiv: 1203.6595 (p. 1).

[7] A. Micheli, G. K. Brennen and P. Zoller, "A toolbox for lattice spin models with polar molecules", *Nat. Phys.* **2**, 341 (2006) (pp. 1, 2).

[8] Immanuel Bloch, "Ultracold quantum gases in optical lattices", *Nat. Phys.* **1**, 23 (2005) (p. 1).

[9] David D. Awschalom, Lee C. Bassett, Andrew S. Dzurak, Evelyn L. Hu and Jason R. Petta, "Quantum Spintronics : Engineering and Manipulating Atom-Like Spins in Semiconductors", *Science* **339**, 1174 (2013) (p. 1).

[10] Ronald Hanson and David D. Awschalom, "Coherent manipulation of single spins in semiconductors." *Nature* **453**, 1043 (2008) (p. 1).

[11] Hugues De Riedmatten and Mikael Afzelius, Quantum Light Storage in Solid State Atomic, *Eng. Atom-phot. Interact.* Ed. by Ana Predojević and Morgan W Mitchell, Springer International Publishing, 2015, 241–273, arXiv: 1502.00307 (pp. 1, 45).

[12] R. J. Schoelkopf and S. M. Girvin, "Wiring up quantum systems." *Nature* **451**, 664 (2008) (p. 1).

[13] K. Hennessy, A. Badolato, M. Winger, D. Gerace, M. Atatüre, S. Gulde, S. Fält and A. Imamoğlu, "Quantum nature of a strongly coupled single quantum dot-cavity system", *Nature* **445**, 896 (2007) (p. 1).

[14] J. Denschlag, J. E. Simsarian, D. L. Feder, Charles W. Clark, L. A. Collins, J. Cubizolles, L. Deng, E. W. Hagley, K. Helmerson, W. P. Reinhardt, S. L. Rolston, B. I. Schneider and W. D. Phillips, "Generating Solitons by Phase Engineering of a Bose-Einstein Condensate", *Science* **287**, 97 (2000) (p. 1).

[15] Markus Greiner, Olaf Mandel, Tilman Esslinger, Theodor W. Hänsch and Immanuel Bloch, "Quantum phase transition from a superfluid to a Mott insulator in a gas of ultracold atoms", *Nature* **415**, 39 (2002) (pp. 1, 6).

[16] Daniel Kleppner, "Inhibited spontaneous emission", *Phys. Rev. Lett.* **47**, 233 (1981) (pp. 2–4).

[17] Eli Yablonovitch, "Inhibited Spontaneous Emission in Solid-State Physics and Electronics", *Phys. Rev. Lett.* **58**, 2059 (1987) (pp. 2–4).

[18] Serge Haroche and Daniel Kleppner, "Cavity Quantum Electrodynamics", *Phys. Today* January, 24 (1989) (p. 2).

[19] J. M. Raimond, M. Brune and S. Haroche, "Colloquium: Manipulating quantum entanglement with atoms and photons in a cavity", *Rev. Mod. Phys.* **73**, 565 (2001) (p. 2).

[20] S. T. Dawkins, R. Mitsch, D. Reitz, E. Vetsch and A. Rauschenbeutel, "Dispersive optical interface based on nanofiber-trapped atoms", *Phys. Rev. Lett.* **107**, 243601 (2011) (p. 2).

[21] R. F. Cregan, B. J. Mangan, J. C. Knight, T. A. Birks, P. St. J. Russel, P. J. Roberts and D. C. Allan, "Single-mode photonic band gap guidance of light in air", *Science* **285**, 1537 (1999) (p. 2).

[22] J. S. Douglas, H. Habibian, C.-L. Hung, A. V. Gorshkov, H. J. Kimble and D. E. Chang, "Quantum many-body models with cold atoms coupled to photonic crystals", *Nat. Photonics* **9**, 326 (2015) (p. 2).

[23] M. Saffman, T. G. Walker and K. Mølmer, "Quantum information with Rydberg atoms", *Rev. Mod. Phys.* **82**, 2313 (2010) (pp. 2, 6, 12).

[24] W. Dür, G. Vidal and J. I. Cirac, "Three qubits can be entangled in two inequivalent ways", *Phys. Rev. A* **62**, 062314 (2000) (pp. 2, 44).

[25] Iacopo Carusotto and Cristiano Ciuti, "Quantum fluids of light", *Rev. Mod. Phys.* **85**, 299 (2013) (p. 2).

[26] E. L. Hahn, "Spin echoes", *Phys. Rev.* **80**, 580 (1950) (p. 3).

[27] Lorenza Viola and Seth Lloyd, "Dynamical suppression of decoherence in two-state quantum systems", *Phys. Rev. A* **58**, 2733 (1998) (pp. 3, 45).

[28] G. de Lange, Z. H. Wang, D. Riste, V. V. Dobrovitski and R. Hanson, "Universal Dynamical Decoupling of a Single Solid-State Spin from a Spin Bath", *Science* **330**, 60 (2010) (p. 3).

[29] Y. O. Dudin, L. Li and A. Kuzmich, "Light storage on the time scale of a minute", *Phys. Rev. A* **87**, 031801(R) (2013) (pp. 3, 45).

[30] Randall G. Hulet, Eric S. Hilfer and Daniel Kleppner, "Inhibited Spontaneous Emission by a Rydberd Atom", *Phys. Rev. Lett.* **55**, 2137 (1985) (pp. 3, 4).

[31] M. D. Leistikow, A. P. Mosk, E. Yeganegi, S. R. Huisman, A. Lagendijk and W. L. Vos, "Inhibited spontaneous emission of quantum dots observed in a 3D photonic band gap", *Phys. Rev. Lett.* **107**, 193903 (2011) (pp. 3, 4).

[32] J. C. H. Chen, Y. Sato, R. Kosaka, M. Hashisaka, K. Muraki and T. Fujisawa, "Enhanced electron-phonon coupling for a semiconductor charge qubit in a surface phonon cavity." *Sci. Rep.* **5**, 15176 (2015) (pp. 3, 4).

[33] M. Brune, S. Haroche, V. Lefevre, J. M. Raimond and N. Zagury, "Quantum Nondemolition Measurement of Small Photon Numbers by Rydberg-Atom Phase-Sensitive Detection", *Phys. Rev. Lett.* **65**, 976 (1990) (p. 3).

[34] G. Nogues, A. Rauschenbeutel, S. Osnaghi, M. Brune, J. M. Raimond and S. Haroche, "Seeing a single photon without destroying it", *Nature* **400**, 239 (1999) (p. 3).

[35] Sébastien Gleyzes, Stefan Kuhr, Christine Guerlin, Julien Bernu, Samuel Deléglise, Ulrich Busk Hoff, Michel Brune, Jean-Michel Raimond and Serge Haroche, "Quantum jumps of light recording the birth and death of a photon in a cavity." *Nature* **446**, 297 (2007) (p. 3).

[36] Vera Bendkowsky, Björn Butscher, Johannes Nipper, James P. Shaffer, Robert Löw and Tilman Pfau, "Observation of ultralong-range Rydberg molecules." *Nature* **458**, 1005 (2009) (pp. 3, 6, 14).

[37] E. A. Goldschmidt, T. Boulier, R. C. Brown, S. B. Koller, J. T. Young, A. V. Gorshkov, S. L. Rolston and J. V. Porto, "Anomalous Broadening in Driven Dissipative Rydberg Systems", *Phys. Rev. Lett.* **116**, 113001 (2016) (pp. 4, 18, 92, 93).

[38] Johannes Zeiher, Rick Van Bijnen, Peter Schauß, Sebastian Hild, Jae-yoon Choi, Thomas Pohl, Immanuel Bloch and Christian Gross, "Many-body interferometry of a Rydberg-dressed spin lattice", *Nat. Phys.* **12**, 1095 (2016) (pp. 4, 18, 19, 22, 93).

[39] Jian-Wei Pan, Dik Bouwmeester, Harald Weinfurter and Anton Zeilinger, "Experimental Entanglement Swapping: Entangling Photons That Never Interacted", *Phys. Rev. Lett.* **80**, 3891 (1998) (p. 4).

[40] Marlan O. Scully and Kai Drühl, "Quantum eraser: A proposed photon correlation experiment concerning observation and "delayed choice" in quantum mechanics", *Phys. Rev. A* **25**, 2208 (1982) (p. 4).

[41] P. Zanardi and M. Rasetti, "Noiseless Quantum Codes", *Phys. Rev. Lett.* **79**, 3306 (1997) (p. 4).

[42] Lu-Ming Duan and Guang-Can Guo, "Preserving Coherence in Quantum Computation by Pairing Quantum Bits", *Phys. Rev. Lett.* **79**, 1953 (1997) (p. 4).

[43] D. A. Lidar, I. L. Chuang and K. B. Whaley, "Decoherence-Free Subspaces for Quantum Computation", *Phys. Rev. Lett.* **81**, 2594 (1998) (p. 4).

[44] S. Diehl, A. Micheli, A. Kantian, B. Kraus, H. P. Büchler and P. Zoller, "Quantum states and phases in driven open quantum systems with cold atoms", *Nat. Phys.* **4**, 878 (2008) (p. 4).

[45] Frank Verstraete, Michael M. Wolf and J. Ignacio Cirac, "Quantum computation and quantum-state engineering driven by dissipation", *Nat. Phys.* **5**, 633 (2009) (p. 4).

[46] Alexander I. Lvovsky, Barry C. Sanders and Wolfgang Tittel, "Optical quantum memory", *Nat. Photonics* **3**, 706 (2009) (p. 5).

[47] M. Gross and S. Haroche, "Superradiance: an essay on the theory of collective spontaneous emission", *Phys. Rep.* **93**, 301 (1982) (pp. 5, 69).

[48] Theodore W. Ducas, William P. Spencer, A. Ganesh Vaidyanathan, William H. Hamilton and Daniel Kleppner, "Detection of far-infrared radiation using Rydberg atoms", *Appl. Phys. Lett.* **35**, 382 (1979) (pp. 5, 39–41).

[49] Harold J. Metcalf, "Highly excited atoms", *Nature* **284**, 127 (1980) (p. 5).

[50] H. Figger, G. Leuchs, R. Straubinger and H. Walther, "A photon detector for submillimetre wavelegths using Rydberg atoms", *Opt. Commun.* **33**, 37 (1980) (pp. 5, 39, 40).

[51] Daniel Kleppner, Michael G. Littman and Myron L. Zimmerman, "Highly excited atoms", *Sci. Am.* May, 108 (1981) (p. 5).

[52] P. Goy, J. M. Raimond, S. Haroche and M. Gross, "Small and sensitive systems interacting with millimeter and submillimeter waves: Rydberg atoms in a cavity", *J. Appl. Phys.* **56**, 627 (1984) (pp. 5, 39).

[53] Martin C. Gutzwiller, "Quantum Chaos", *Sci. Am.* **266**.January, 78 (1992) (p. 5).

[54] Randall G. Hulet and Daniel Kleppner, "Rydberg Atoms in "Circular" States", *Phys. Rev. Lett.* **51**, 1430 (1983) (p. 5).

[55] Theodor W. Hänsch, "Repetitively Pulsed Tunable Dye Laser for High Resolution Spectroscopy", *Appl. Opt.* **11**, 895 (1972) (pp. 5, 6).

[56] Theodore W. Ducas, Michael G. Littman, Richard R. Freeman and Daniel Kleppner, "Stark Ionization of High-Lying States of Sodium", *Phys. Rev. Lett.* **35**, 366 (1975) (pp. 6, 21).

[57] A. B. Arons and M. B. Peppard, "Einstein's Proposal of The Photon Concept - a Translation of the Annalen der Physik Paper of 1905", *Am. J. Phys.* **33**.5 (1965) (p. 6).

[58] Arthur L. Schawlow, "Lasers and physics: a pretty good hint", *Phys. Today* **35**, 46 (1982) (p. 6).

[59] Carl E. Wieman and Leo Hollberg, "Using diode lasers for atomic physics", *Rev. Sci. Instrum.* **62**, 1 (1991) (p. 6).

[60] A. Imamoğlu and S. E. Harris, "Lasers without inversion: interference of dressed lifetime-broadened states." *Opt. Lett.* **14**, 1344 (1989) (p. 6).

[61] S. E. Harris, J. E. Field and A. Imamoğlu, "Nonlinear Optical Processes Using Electromagnetically Induced Transparency", *Phys. Rev. Lett.* **64**, 1107 (1990) (p. 6).

[62] M. D. Lukin and A. Imamoğlu, "Controlling photons using electromagnetically induced transparency." *Nature* **413**, 273 (2001) (p. 6).

[63] K. J. Weatherill, J. D. Pritchard, R. P. Abel, M. G. Bason, A. K. Mohapatra and C. S. Adams, "Electromagnetically induced transparency of an interacting cold Rydberg ensemble", *J. Phys. B At. Mol. Opt. Phys.* **41**, 201002 (2008) (pp. 6, 22).

[64] E. Urban, T. A. Johnson, T. Henage, L. Isenhower, D. D. Yavuz, T. G. Walker and M. Saffman, "Observation of Rydberg blockade between two atoms", *Nat. Phys.* **5**, 110 (2009) (pp. 6, 43).

[65] Daniel Comparat and Pierre Pillet, "Dipole blockade in a cold Rydberg atomic sample", *J. Opt. Soc. Am. B* **27**, A208 (2010) (p. 6).

[66] J. D. Pritchard, D. Maxwell, A. Gauguet, K. J. Weatherill, M. P. A. Jones and C. S. Adams, "Cooperative atom-light interaction in a blockaded Rydberg ensemble", *Phys. Rev. Lett.* **105**, 193603 (2010) (pp. 6, 22, 31, 44).

[67] M. D. Lukin, M. Fleischhauer, R. Cote, L. M. Duan, D. Jaksch, J. I. Cirac and P. Zoller, "Dipole Blockade and Quantum Information Processing in Mesoscopic Atomic Ensembles", *Phys. Rev. Lett.* **87**, 037901 (2001) (pp. 6, 31, 52).

[68] Thibault Peyronel, Ofer Firstenberg, Qi-Yu Liang, Sebastian Hofferberth, Alexey V. Gorshkov, Thomas Pohl, Mikhail D. Lukin and Vladan Vuletić, "Quantum nonlinear optics with single photons enabled by strongly interacting atoms", *Nature* **488**, 57 (2012) (pp. 6, 44).

[69] Ofer Firstenberg, Thibault Peyronel, Qi-Yu Liang, Alexey V. Gorshkov, Mikhail D. Lukin and Vladan Vuletić, "Attractive photons in a quantum nonlinear medium", *Nature* **502**, 71 (2013) (pp. 6, 44).

[70] Jeff D. Thompson, Travis L. Nicholson, Qi-Yu Liang, Sergio H. Cantu, Aditya V. Venkatramani, Soonwon Choi, Ilya A. Fedorov, Daniel Viscor, Thomas Pohl, Mikhail D. Lukin and Vladan Vuletić, "Symmetry-protected collisions between strongly interacting photons", *Nature* **542**, 206 (2017) (p. 6).

[71] H. Gorniaczyk, C. Tresp, P. Bienias, A. Paris-Mandoki, W. Li, I. Mirgorodskiy, H. P. Büchler, I. Lesanovsky and S. Hofferberth, "Enhancement of Rydberg-mediated single-photon nonlinearities by electrically tuned Förster resonances", *Nat. Commun.* **7**, 12480 (2016) (pp. 6, 32, 33, 45).

[72] Hannes Busche, Paul Huillery, Simon W. Ball, Teodora Ilieva, Matthew P. A. Jones and Charles S. Adams, "Contactless nonlinear optics mediated by long-range Rydberg interactions", *Nat. Phys.* (2017) (pp. 6, 43, 45, 50).

[73] W. Li, T. Pohl, J. M. Rost, Seth T. Rittenhouse, H. R. Sadeghpour, J. Nipper, B. Butscher, J. B. Balewski, V. Bendkowsky, R. Löw and T. Pfau, "A Homonuclear Molecule with a Permanent Electric Dipole Moment", *Science* **334**, 1110 (2011) (pp. 6, 14).

[74] Heiner Saßmannshausen and Johannes Deiglmayr, "Observation of Rydberg-atom macrodimers : micrometer-sized diatomic molecules", *Phys. Rev. Lett.* **117**, 083401 (2016) (pp. 6, 30).

[75] R. M. W. van Bijnen and T Pohl, "Quantum Magnetism and Topological Ordering via Rydberg Dressing near Förster Resonances", *Phys. Rev. Lett.* **114**, 243002 (2015) (pp. 6, 32, 34).

[76] T. Pohl, E. Demler and M. D. Lukin, "Dynamical crystallization in the dipole blockade of ultracold atoms", *Phys. Rev. Lett.* **104**, 043002 (2010) (pp. 6, 35).

[77] Michael Hoening, Wildan Abdussalam, Michael Fleischhauer and Thomas Pohl, "Antiferromagnetic long-range order in dissipative Rydberg lattices", *Phys. Rev. A* **90**, 021603(R) (2014) (pp. 6, 74, 90).

[78] Alexander W. Glaetzle, Marcello Dalmonte, Rejish Nath, Christian Gross, Immanuel Bloch and Peter Zoller, "Designing frustrated quantum magnets with laser-dressed Rydberg atoms", *Phys. Rev. Lett.* **114**, 173002 (2015) (p. 6).

[79] P. Schauß, J. Zeiher, T. Fukuhara, S. Hild, M. Cheneau, T. Macrì, T. Pohl, I. Bloch and C. Gross, "Crystallization in Ising quantum magnets", *Science* **347**, 1455 (2015) (pp. 6, 35).

[80] Christof Weitenberg, Manuel Endres, Jacob F. Sherson, Marc Cheneau, Peter Schauß, Takeshi Fukuhara, Immanuel Bloch and Stefan Kuhr, "Single-spin addressing in an atomic Mott insulator." *Nature* **471**, 319 (2011) (pp. 6, 52).

[81] Silvia Bergamini, Benoît Darquié, Matthew Jones, Lionel Jacubowiez, Antoine Browaeys and Philippe Grangier, "Holographic generation of micro-trap arrays for single atoms", *J. Opt. Soc. Am. B* **21**, 1889 (2004) (p. 6).

[82] F. Nogrette, H. Labuhn, S. Ravets, D. Barredo, L. Béguin, A. Vernier, T. Lahaye and A. Browaeys, "Single-atom trapping in holographic 2D arrays of microtraps with arbitrary geometries", *Phys. Rev. X* **4**, 021034 (2014) (p. 6).

[83] Henning Labuhn, Sylvain Ravets, Daniel Barredo, Lucas Béguin, Florence Nogrette, Thierry Lahaye and Antoine Browaeys, "Single-atom addressing in microtraps for quantum-state engineering using Rydberg atoms", *Phys. Rev. A* **90**, 023415 (2014) (pp. 6, 52).

[84] Henning Labuhn, Daniel Barredo, Sylvain Ravets, Sylvain de Léséleuc, Tommaso Macrì, Thierry Lahaye and Antoine Browaeys, "Tunable two-dimensional arrays of single Rydberg atoms for realizing quantum Ising models", *Nature* **534**, 667 (2016) (pp. 6, 22, 31, 69, 74).

[85] Manuel Endres, Hannes Bernien, Alexander Keesling, Harry Levine, Eric R. Anschuetz, Alexandre Krajenbrink, Crystal Senko, Vladan Vuletic, Markus Greiner and Mikhail D. Lukin, "Atom-by-atom assembly of defect-free one-dimensional cold atom arrays", *Science* **354**, 1024 (2016) (pp. 6, 22).

[86] Daniel Barredo, Sylvain de Léséleuc, Vincent Lienhard, Thierry Lahaye and Antoine Browaeys, "An atom-by-atom assembler of defect-free arbitrary two-dimensional atomic arrays", *Science* **354**, 1021 (2016) (pp. 6, 22).

[87] C. Carr, R. Ritter, C. G. Wade, C. S. Adams and K. J. Weatherill, "Nonequilibrium Phase Transition in a Dilute Rydberg Ensemble", *Phys. Rev. Lett.* **111**, 113901 (2013) (pp. 6, 52, 57, 74, 87, 88, 93, 94).

[88] A. Urvoy, F. Ripka, I. Lesanovsky, D. Booth, J. P. Shaffer, T. Pfau and R. Löw, "Strongly correlated growth of Rydberg aggregates in a vapour cell", *Phys. Rev. Lett.* **114**, 203002 (2015) (pp. 6, 30, 93).

[89] N. Malossi, M. M. Valado, S. Scotto, P. Huillery, P. Pillet, D. Ciampini, E. Arimondo and O. Morsch, "Full Counting Statistics and Phase Diagram of a Dissipative Rydberg Gas", *Phys. Rev. Lett.* **113**, 023006 (2014) (pp. 6, 74, 76, 90, 92).

[90] H. Schempp, G. Günter, M. Robert-de Saint-Vincent, C. S. Hofmann, D. Breyel, A. Komnik, D. W. Schönleber, M. Gärttner, J. Evers, S. Whitlock and M. Weidemüller, "Full Counting Statistics of Laser Excited Rydberg Aggregates in a One-Dimensional Geometry", *Phys. Rev. Lett.* **112**.1, 013002 (2014) (p. 6).

[91] A. K. Mohapatra, T. R. Jackson and C. S. Adams, "Coherent Optical Detection of Highly Excited Rydberg States Using Electromagnetically Induced Transparency", *Phys. Rev. Lett.* **98**, 113003 (2007) (pp. 7, 22).

[92] Ashok K. Mohapatra, Mark G. Bason, Björn Butscher, Kevin J. Weatherill and Charles S. Adams, "A giant electro-optic effect using polarizable dark states", *Nat. Phys.* **4**, 890 (2008) (pp. 7, 22).

[93] H. Kübler, J. P. Shaffer, T. Baluktsian, R. Löw and T. Pfau, "Coherent excitation of Rydberg atoms in micrometre-sized atomic vapour cells", *Nat. Photonics* **4**, 112 (2010) (p. 7).

[94] B. Huber, T. Baluktsian, M. Schlagmüller, A. Kölle, H. Kübler, R. Löw and T. Pfau, "GHz Rabi Flopping to Rydberg States in Hot Atomic Vapor Cells", *Phys. Rev. Lett.* **107**, 243001 (2011) (p. 7).

[95] N. Šibalić, J. D. Pritchard, C. S. Adams and K. J. Weatherill, "ARC: An open-source library for calculating properties of alkali Rydberg atoms" (2016), arXiv: 1612.05529 (pp. 9, 36).

[96] D. J. Whiting, N. Šibalić, J. Keaveney, C. S. Adams and I. G. Hughes, "Single-Photon Interference due to Motion in an Atomic Collective Excitation", *Phys. Rev. Lett.* **118**, 253601 (2017) (pp. 9, 60, 64–66).

[97] C. G. Wade, N. Šibalić, N. R. de Melo, J. M. Kondo, C. S. Adams and K. J. Weatherill, "Real-time near-field terahertz imaging with atomic optical fluorescence", *Nat. Photonics* **11**, 40 (2017) (pp. 9, 39–41, 56, 59).

[98] N. Šibalić, J. M. Kondo, C. S. Adams and K. J. Weatherill, "Dressed-state electromagnetically induced transparency for light storage in uniform-phase spin waves", *Phys. Rev. A* **94**, 033840 (2016) (pp. 9, 22).

[99] N. Šibalić, C. G. Wade, C. S. Adams, K. J. Weatherill and T. Pohl, "Driven-dissipative many-body systems with mixed power-law interactions: Bistabilities and temperature-driven nonequilibrium phase transitions", *Phys. Rev. A* **94**, 011401(R) (2016) (pp. 9, 32, 74, 88–90).

[100] Jorge M. Kondo, Nikola Šibalić, Alex Guttridge, Christopher G. Wade, Natalia R. De Melo, Charles S. Adams and Kevin J. Weatherill, "Observation of interference effects via four photon excitation of highly excited Rydberg states in thermal cesium vapor", *Opt. Lett.* **40**, 5570 (2015) (pp. 9, 19, 22, 54).

[101] C. G. Wade, N. Šibalić, J. Keaveney, C. S. Adams and K. J. Weatherill, "Probing an excited-state atomic transition using hyperfine quantum-beat spectroscopy", *Phys. Rev. A* **90**, 033424 (2014) (pp. 9, 67, 68).

[102] Natalia R. de Melo, Christopher G. Wade, Nikola Šibalić, Jorge M. Kondo, Charles S. Adams and Kevin J. Weatherill, "Intrinsic optical bistability in a strongly driven Rydberg ensemble", *Phys. Rev. A* **93**, 063863 (2016) (pp. 9, 74, 93, 94).

[103] B. Zlatković, A. J. Krmpot, N. Šibalić, M. Radonjić and B. M. Jelenković, "Efficient parametric non-degenerate four-wave mixing in hot potassium vapor", *Laser Phys. Lett.* **13**, 015205 (2016) (p. 9).

[104] Michael Fleischhauer, Atac Imamoglu and Jonathan P. Marangos, "Electromagnetically induced transparency: Optics in coherent media", *Rev. Mod. Phys.* **77**, 633 (2005) (pp. 12, 25).

[105] C. Murray and T. Pohl, Quantum and Nonlinear Optics in Strongly Interacting Atomic Ensembles, *Adv. At. Mol. Opt. Phys.* Ed. by Ennio Arimondo, Chun C. Lin and Susanne F. Yelin, Advances I, Academic Press, 2016, chap. 7, 321–372 (p. 12).

[106] C.-J. Lorenzen and K. Niemax, "Quantum Defects of the $n^2P_{1/2,3/2}$ Levels in ^{39}K I and ^{85}Rb I", *Phys. Scr.* **27**, 300 (1983) (p. 13).

[107] K.-H. Weber and Craig J. Sansonetti, "Accurate energies of nS, nP, nD, nF, and nG levels of neutral cesium", *Phys. Rev. A* **35**, 4650 (1987) (p. 13).

[108] Wenhui Li, I. Mourachko, M. W. Noel and T. F. Gallagher, "Millimeter-wave spectroscopy of cold Rb Rydberg atoms in a magneto-optical trap: Quantum defects of the ns, np, and nd series", *Phys. Rev. A* **67**, 052502 (2003) (p. 13).

[109] Jianing Han, Yasir Jamil, D. V. L. Norum, Paul J. Tanner and T. F. Gallagher, "Rb nf quantum defects from millimeter-wave spectroscopy of cold ^{85}Rb Rydberg atoms", *Phys. Rev. A* **74**, 054502 (2006) (p. 13).

[110] Markus Mack, Florian Karlewski, Helge Hattermann, Simone Höckh, Florian Jessen, Daniel Cano and József Fortágh, "Measurement of absolute transition frequencies of ^{87}Rb to nS and nD Rydberg states by means of electromagnetically induced transparency", *Phys. Rev. A* **83**, 052515 (2011) (p. 13).

[111] K. Afrousheh, P. Bohlouli-Zanjani, J. A. Petrus and J. D. D. Martin, "Determination of the ^{85}Rb ng-series quantum defect by electric-field-induced resonant energy transfer between cold Rydberg atoms", *Phys. Rev. A* **74**, 062712 (2006) (p. 13).

[112] P. Goy, J. Liang, M. Gross and S. Haroche, "Quantum defects and specific-isotopic-shift measurements in ns and np highly excited states of lithium: Exchange effects between Rydberg and core electrons", *Phys. Rev. A* **34**, 2889 (1986) (p. 13).

[113] Johannes Deiglmayr, Holger Herburger, Heiner Saßmannshausen, Paul Jansen, Hansjürg Schmutz and Frédéric Merkt, "Precision measurement of the ionization energy of Cs I", *Phys. Rev. A* **93**, 013424 (2016) (p. 13).

[114] C.-J. Lorenzen and K. Niemax, "Precise Quantum Defects of nS, nP and nD Levels in Cs I", *Zeitschrift für Phys. A Atoms Nucl.* **315**, 127 (1984) (p. 13).

[115] B. Sanguinetti, H. O. Majeed, M. L. Jones and B. T. H. Varcoe, "Precision measurements of quantum defects in the $nP_{3/2}$ Rydberg States of ^{85}Rb", *J. Phys. B At. Mol. Phys.* **42**, 165004 (2009) (p. 13).

[116] Atreju Tauschinsky, Richard Newell, H. B. Van Linden Van Den Heuvell and R. J. C. Spreeuw, "Measurement of ^{87}Rb Rydberg-state hyperfine splitting in a room-temperature vapor cell", *Phys. Rev. A* **87**, 042522 (2013) (pp. 13, 23, 24).

[117] P. Goy, J. M. Raimond, G. Vitrant and S. Haroche, "Millimeter-wave spectroscopy in cesium Rydberg states. Quantum defects, fine-and hyperfine-structure measurements", *Phys. Rev. A* **26**, 2733 (1982) (p. 13).

[118] M. Marinescu, H. R. Sadeghpour and A. Dalgarno, "Dispersion coefficients for alkali-metal dimers", *Phys. Rev. A* **49**, 982 (1994) (pp. 13, 14).

[119] B. V. Numerov, "A method of extrapolation of pertubations", *Mon. Not. R. Astron. Soc.* **84**, 592 (1924) (pp. 14, 103).

[120] B. V. Numerov, "Note on the numerical integration of $\mathrm{d}^2x/\mathrm{d}r^2 = f(x,t)$", *Astron. Nachrichten* **230**, 359 (1927) (pp. 14, 103).

[121] Myeon L. Zimmerman, Michael G. Littman, Michaeil M. Kash and Daniel Kleppner, "Stark structure of the Rydberg states of alkali-metal atoms", *PRA* **20**, 2251 (1979) (pp. 14, 23, 103).

[122] Chris H. Greene, A. S. Dickinson and H. R. Sadeghpour, "Creation of Polar and Nonpolar Ultra-Long-Range Rydberg Molecules", *Phys. Rev. Lett.* **85**, 2458 (2000) (p. 14).

[123] A. Gaj, A. T. Krupp, J. B. Balewski, R. Löw, S. Hofferberth and T. Pfau, "From molecular spectra to a density shift in dense Rydberg gases." *Nat. Commun.* **5**, 4546 (2014) (pp. 14, 56).

[124] Edward U. Condon and G. H. Shortley, *The Theory of Atomic Spectra.* Cambridge: Cambridge University Press, 1970 (p. 16).

[125] J. J. Sakurai and J. Napolitano, *Modern Quantum Mechanics*, 2nd ed., San Francisco: 978-0805382914, 2011 (p. 16).

[126] L. Béguin, A. Vernier, R. Chicireanu, T. Lahaye and A. Browaeys, "Direct Measurement of the van der Waals Interaction between Two Rydberg Atoms", *Phys. Rev. Lett.* **110**, 263201 (2013) (p. 16).

[127] Daniel Barredo, Henning Labuhn, Sylvain Ravets, Thierry Lahaye, Antoine Browaeys and Charles S. Adams, "Coherent Excitation Transfer in a Spin Chain of Three Rydberg Atoms", *Phys. Rev. Lett.* **114**, 113002 (2015) (pp. 16, 19).

[128] N. Thaicharoen, A. Schwarzkopf and G. Raithel, "Measurement of the van der Waals interaction by atom trajectory imaging", *Phys. Rev. A* **92**, 040701(R) (2015) (pp. 16, 22).

[129] M. S. Safronova, W. R. Johnson and A. Derevianko, "Relativistic many-body calculations of energy levels, hyperfine constants, electric-dipole matrix elements and static polarizabilities for alkali-metal atoms", *Phys. Rev. A* **60**, 4476 (1999) (p. 16).

[130] M. S. Safronova, Carl J. Williams and Charles W. Clark, "Relativistic many-body calculations of electric-dipole matrix elements, lifetimes and polarizabilities in rubidium", *Phys. Rev. A* **69**, 022509 (2004) (p. 16).

[131] I. I. Beterov, I. I. Ryabtsev, D. B. Tretyakov and V. M. Entin, "Quasiclassical calculations of blackbody-radiation-induced depopulation rates and effective lifetimes of Rydberg nS, nP, and nD alkali-metal atoms with $n \leq 80$", *Phys. Rev. A* **79**, 052504 (2009) (p. 17).

[132] T. F. Gallagher and W. E. Cooke, “Interactions of Blackbody Radiation with Atoms”, *Phys. Rev. Lett.* **42**, 835 (1979) (p. 18).

[133] E. J. Beiting, G. F. Hildebrandt, F. G. Kellert, G. W. Foltz, K. a. Smith, F. B. Dunning and R. F. Stebbings, “The effects of 300 K background radiation on Rydberg atoms”, *J. Chem. Phys.* **70**.7, 3551 (1979) (p. 18).

[134] W. E. Cooke and T. F. Gallagher, “Effects of blackbody radiation on highly excited atoms”, *Phys. Rev. A* **21**, 588 (1980) (p. 18).

[135] William P. Spencer, A. Ganesh Vaidyanathan, Daniel Kleppner and Theodore W. Ducas, “Temperature dependence of blackbody-radiation-induced transfer among highly excited states of sodium”, *Phys. Rev. A* **25**, 380 (1982) (p. 18).

[136] I. I. Beterov, D. B. Tretyakov, I. I. Ryabtsev, V. M. Entin, A. Ekers and N. N. Bezuglov, “Ionization of Rydberg atoms by blackbody radiation”, *New J. Phys.* **11**, 013052 (2009) (p. 18).

[137] William P. Spencer, A. Ganesh Vaidyanathan, Daniel Kleppner and Theodore W. Ducas, “Photoionization by blackbody radiation”, *Phys. Rev. A* **26**, 1490 (1982) (p. 18).

[138] G. Vitrant, J. M. Raimond, M. Gross and S. Haroche, “Rydberg to plasma evolution in a dense gas of very excited atoms”, *J. Phys. B At. Mol. Phys.* **15**, L49 (1982) (pp. 18, 35).

[139] M. G. Boshier, D. Berkeland, E. A. Hinds and V. Sandoghdar, “External-cavity frequency-stabilization of visible and infrared semiconductor lasers for high resolution spectroscopy”, *Opt. Commun.* **85**, 355 (1991) (p. 19).

[140] L. Ricci, M. Weidemüller, T. Esslinger, A. Hammerich, C. Zimmerman, V. Vuletic, W. König and T. W. Hänsch, “A compact grating-stabilized diode laser system for atomic physics”, *Opt. Commun.* **117**, 541 (1995) (p. 19).

[141] Kurt R. Vogel, Timothy P. Dinneen, Alan Gallagher and John L. Hall, “Narrow-line Doppler cooling of strontium to the recoil limit”, *IEEE Trans. Instrum. Meas.* **48**, 618 (1999) (pp. 19, 20).

[142] Elizabeth M. Bridge, Niamh C. Keegan, Alistair D. Bounds, Danielle Boddy, Daniel P. Sadler and Matthew P. A. Jones, “Tunable cw UV laser with <35 kHz absolute frequency instability for precision spectroscopy of Sr Rydberg states”, *Opt. Express* **24**, 2281 (2016) (p. 19).

[143] Sadaf Sultana and M. Suhail Zubairy, “Effect of finite bandwidth on refractive-index enhancement and lasing without inversion”, *Phys. Rev. A* **49**, 438 (1994) (p. 19).

[144] M. G. Bason, A. K. Mohapatra, K. J. Weatherill and C. S. Adams, “Narrow absorptive resonances in a four-level atomic system”, *J. Phys. B At. Mol. Opt. Phys.* **42**, 075503 (2009) (p. 19).

[145] Jun Ye and John L. Hall, “Optical phase locking in the microradian domain: potential applications to NASA spaceborne optical measurements”, *Opt. Lett.* **24**, 1838 (1999) (p. 19).

[146] R. W. P. Drever, J. L. Hall, F. V. Kowalski, J. Hough, G. M. Ford, A. J. Munley and H. Ward, “Laser phase and frequency stabilization using an optical resonator”, *Appl. Phys. B* **31**, 97 (1983) (p. 20).

[147] Mark Notcutt, Long-Sheng Ma, Jun Ye and John L. Hall, "Simple and compact 1-Hz laser system via an improved mounting configuration of a reference cavity." *Opt. Lett.* **30**, 1815 (2005) (p. 20).

[148] David J. Griffiths, *Introduction to Electrodynamics*, London: Prentice-Hall, 1999 (p. 20).

[149] Julio Gea-Banacloche, Yong-qing Li, Shao-zheng Jin and Min Xiao, *Electromagnetically induced transparency in ladder-type inhomogeneously broadened media: Theory and experiment*, 1995 (p. 21).

[150] F. Gounand, M. Hugon, P. R. Fournier and J. Berlande, "Superradiant cascading effects in rubidium Rydberg levels", *J. Phys. B At. Mol. Opt. Phys.* **12**, 547 (1979) (p. 21).

[151] C. Fabre, P. Goy and S. Haroche, "Millimetre resonances in Na Rydberg levels detected by field ionization: quantum defects and Stark-effect studies", *J. Phys. B At. Mol. Phys.* **10**, L183 (1977) (p. 21).

[152] A. Schwarzkopf, R. E. Sapiro and G. Raithel, "Imaging spatial correlations of Rydberg excitations in cold atom clouds", *Phys. Rev. Lett.* **107**, 103001 (2011) (p. 22).

[153] R. Faoro, C. Simonelli, M. Archimi, G. Masella, M. M. Valado, E. Arimondo, R. Mannella, D. Ciampini and O. Morsch, "Van der Waals explosion of cold Rydberg clusters", *Phys. Rev. A* **93**, 030701(R) (2016) (p. 22).

[154] Christopher Carr, Charles S. Adams and Kevin J. Weatherill, "Polarization spectroscopy of an excited state transition." *Opt. Lett.* **37**, 118 (2012) (pp. 22, 52, 54).

[155] G. Günter, M. Robert-De-Saint-Vincent, H. Schempp, C. S. Hofmann, S. Whitlock and M. Weidemüller, "Interaction enhanced imaging of individual Rydberg atoms in dense gases", *Phys. Rev. Lett.* **108**, 013002 (2012) (p. 22).

[156] G. Günter, H. Schempp, M. Robert-de Saint-Vincent, V. Gavryusev, S. Helmrich, C. S. Hofmann, S. Whitlock and M Weidemüller, "Observing the dynamics of dipole-mediated energy transport by interaction-enhanced imaging." *Science* **342**, 954 (2013) (p. 22).

[157] Jens Grimmel, Markus Mack, Florian Karlewski, Florian Jessen, Malte Reinschmidt, Nóra Sándor and József Fortágh, "Measurement and numerical calculation of Rubidium Rydberg Stark spectra", *New J. Phys.* **17**, 053005 (2015) (p. 23).

[158] T. F. Gallagher, *Rydberg atoms*, Cambridge University Press, 1994 (p. 24).

[159] K.-J. Boller, A. Imamoğlu and S. E. Harris, "Observation of electromagnetically induced transparency", *Phys. Rev. Lett.* **66**, 2593 (1991) (p. 25).

[160] M. Tanasittikosol, J. D. Pritchard, D. Maxwell, A. Gauguet, K. J. Weatherill, R. M. Potvliege and C. S. Adams, "Microwave dressing of Rydberg dark states", *J. Phys. B At. Mol. Phys.* **44**, 184020 (2011) (pp. 25, 34, 39).

[161] S. Sevinçli and T. Pohl, "Microwave control of Rydberg atom interactions", *New J. Phys.* **16**, 123036 (2014) (pp. 25, 34).

[162] A. Urvoy, C. Carr, R. Ritter, C. S. Adams, K. J. Weatherill and R. Löw, "Optical coherences and wavelength mismatch in ladder systems", *J. Phys. B At. Mol. Opt. Phys.* **46**, 245001 (2013) (p. 27).

[163] Lene Vestergaard Hau, S. E. Harris, Zachary Dutton and Cyrus H. Behroozi, "Light speed reduction to 17 metres per second in an ultracold atomic gas", *Nature* **397**, 594 (1999) (p. 27).

[164] D. Phillips, A. Fleischhauer, A. Mair, R. L. Walsworth and M. D. Lukin, "Storage of Light in Atomic Vapor", *Phys. Rev. Lett.* **86**, 783 (2001) (pp. 27, 44, 45).

[165] A. Dalgarno and W. D. Davison, The Calculation of Van der Waals Interactions, *Adv. At. Mol. Phys.* **2**, London-New York: Academic Press, 1966, 1–32 (p. 28).

[166] M. E. Rose, "The electrostatic interaction of two arbitrary charge distributions", *J. Math. Phys.* **37**, 215 (1958) (p. 28).

[167] Robert J. Le Roy, "Long-Range Potential Coefficients From RKR Turning Points: C_6 and C_8 for $B(^3\Pi_{Ou}^+)$-State Cl_2, Br_2, and I_2", *Can. J. Phys.* **52**, 246 (1974) (p. 29).

[168] R. B. Lehoucq, D. C. Sorensen and C. Yang, *ARPACK Users' Guide: Solution of Large Scale Eigenvalue Problems with Implicitly Restarted Arnoldi Methods*. Philadelphia: SIAM Publications, 1998 (p. 30).

[169] Travis E. Oliphant, "Python for Scientific Computing", *Comput. Sci. Eng.* **9**, 10 (2007) (pp. 30, 37).

[170] Johannes Deiglmayr, Heiner Saßmannshausen, Pierre Pillet and Frédéric Merkt, "Observation of Dipole-Quadrupole Interaction in an Ultracold Gas of Rydberg Atoms", *Phys. Rev. Lett.* **113**, 193001 (2014) (pp. 30, 32).

[171] D. Tong, S. M. Farooqi, J. Stanojevic, S. Krishnan, Y. P. Zhang, R. Côté, E. E. Eyler and P. L. Gould, "Local Blockade of Rydberg Excitation in an Ultracold Gas", *Phys. Rev. Lett.* **93**, 063001 (2004) (p. 31).

[172] C. Ates, T. Pohl, T. Pattard and J. M. Rost, "Strong interaction effects on the atom counting statistics of ultracold Rydberg gases", *J. Phys. B At. Mol. Opt. Phys.* **39**.11, L233 (2006) (pp. 31, 75, 76).

[173] Andrei Derevianko, Péter Kómár, Turker Topcu, Ronen M. Kroeze and Mikhail D. Lukin, "Effects of molecular resonances on Rydberg blockade", *Phys. Rev. A* **92**, 063419 (2015) (p. 32).

[174] Heiner Saßmannshausen, Frédéric Merkt and Johannes Deiglmayr, "Pulsed excitation of Rydberg-atom-pair states in an ultracold Cs gas", *Phys. Rev. A* **92**, 032505 (2015) (p. 32).

[175] Heiner Saßmannshausen, Johannes Deiglmayr and Frédéric Merkt, "Long-range Rydberg molecules, Rydberg macrodimers and Rydberg aggregates in an ultracold Cs gas", 1–29 (2016), arXiv: 1607.04060 (p. 32).

[176] John Weiner, Vanderlei S. Bagnato, Sergio Zilio and Paul S. Julienne, "Experiments and theory in cold and ultracold collisions", *Rev. Mod. Phys.* **71**, 1 (1999) (p. 32).

[177] Truman M. Wilson and Jacob L. Roberts, "Enhanced light-assisted-collision rate via excitation to the long-lived $5S_{1/2} - 5D_{5/2}$ molecular potential in an ^{85}Rb magneto-optical trap", *Phys. Rev. A* **83**, 033419 (2011) (p. 32).

[178] T. F. Gallagher, K. A. Safinya, F. Gounand, J. F. Delpech, W. Sandner and R. Kachru, "Resonant Rydberg-atom - Rydberg-atom collisions", *Phys. Rev. A* **25**, 1905 (1982) (p. 32).

[179] Thibault Vogt, Matthieu Viteau, Jianming Zhao, Amodsen Chotia, Daniel Comparat and Pierre Pillet, "Dipole Blockade at Förster Resonances in High Resolution Laser Excitation of Rydberg States of Cesium Atoms", *Phys. Rev. Lett.* **97**, 083003 (2006) (p. 32).

[180] A. Reinhard, T. Cubel Liebisch, K. C. Younge, P. R. Berman and G. Raithel, "Rydberg-Rydberg Collisions: Resonant Enhancement of State Mixing and Penning Ionization", *Phys. Rev. Lett.* **100**, 123007 (2008) (p. 32).

[181] Sylvain Ravets, Henning Labuhn, Daniel Barredo, Lucas Béguin, Thierry Lahaye and Antoine Browaeys, "Coherent dipole-dipole coupling between two single atoms at a Förster resonance", *Nat. Phys.* **10**, 914 (2014) (p. 32).

[182] I. I. Beterov and M. Saffman, "Rydberg blockade, Förster resonances, and quantum state measurements with different atomic species", *Phys. Rev. A* **92**, 042710 (2015) (p. 32).

[183] N. Henkel, R. Nath and T. Pohl, "Three-Dimensional Roton Excitations and Supersolid Formation in Rydberg-Excited Bose-Einstein Condensates", *Phys. Rev. Lett.* **104**, 195302 (2010) (p. 33).

[184] M. Born and V. Fock, "Beweis des Adiabatensatzes", *Zeitschrift für Phys.* **51**, 165 (1928) (p. 35).

[185] Dorit Aharonov, Wim van Dam, Julia Kempe, Zeph Landau, Seth Lloyd and Oded Regev, "Adiabatic Quantum Computation Is Equivalent to Standard Quantum Computation", *Siam Rev.* **50**, 755 (2008) (p. 35).

[186] L. D. Landau, "Zur Theorie der Energieübertragung. II", *Phys. Zeitschrift der Sowjetunion* **2**, 46 (1932) (p. 35).

[187] Clarence Zener, "Non-Adiabatic Crossing of Energy Levels", *Proc. Roy. Soc. A* **137**, 696 (1932) (p. 35).

[188] J. S. Cabral, J. M. Kondo, L. F. Gonçalves, V. A. Nascimento, L. G. Marcassa, D. Booth, J. Tallant, A. Schwettmann, K. R. Overstreet, J. Sedlacek and J. P. Shaffer, "Effects of electric fields on ultracold Rydberg atom interactions", *J. Phys. B At. Mol. Opt. Phys.* **44**, 184007 (2011) (p. 35).

[189] Paul J. Tanner, Jianing Han, E. S. Shuman and T. F. Gallagher, "Many-body ionization in a frozen Rydberg gas", *Phys. Rev. Lett.* **100**, 043002 (2008) (p. 35).

[190] Martin Kiffner, Davide Ceresoli, Wenhui Li and Dieter Jaksch, "Quantum mechanical calculation of Rydberg-Rydberg Auger decay rates", *J. Phys. B At. Mol. Opt. Phys.* **49**, 204004 (2015) (p. 35).

[191] H. P. Büchler, A. Micheli and P. Zoller, "Three-body interactions with cold polar molecules", *Nat. Phys.* **3**, 726 (2007) (p. 35).

[192] K. Younge, A. Reinhard, T. Pohl, P. R. Berman and G. Raithel, "Mesoscopic Rydberg ensembles: Beyond the pairwise-interaction approximation", *Phys. Rev. A* **79**, 043420 (2009) (p. 35).

[193] T. Pohl and P. R. Berman, "Breaking the Dipole Blockade: Nearly Resonant Dipole Interactions in Few-Atom Systems", *Phys. Rev. Lett.* **102**, 013004 (2009) (p. 35).

[194] R. Faoro, B. Pelle, A. Zuliani, P. Cheinet, E. Arimondo and P. Pillet, "Borromean three-body FRET in frozen Rydberg gases", *Nat. Commun.* **6**, 8173 (2015) (p. 35).

[195] J. H. Gurian, P. Cheinet, P. Huillery, A. Fioretti, J. Zhao, P. L. Gould, D. Comparat and P. Pillet, "Observation of a resonant four-body interaction in cold cesium rydberg atoms", *Phys. Rev. Lett.* **108**, 023005 (2012) (p. 35).

[196] C. B. Alcock, V. P. Itkin and M. K. Horrigan, "Vapor Pressure of the Metallic Elements", *Can. Metall. Q.* **23**, 309 (1984) (p. 36).

[197] Nikola Šibalić, Jonathan D. Pritchard, Charles S. Adams and Kevin J. Weatherill, *ARC GitHub page*, `https://github.com/nikolasibalic/ARC-Alkali-Rydberg-Calculator` (p. 36).

[198] N. Šibalić, J. D. Pritchard, C. S. Adams and K. J. Weatherill, *Alkali Rydberg Calculator (ARC) documentation*, `http://arc-alkali-rydberg-calculator.readthedocs.io` (p. 36).

[199] Jonathon A. Sedlacek, Arne Schwettmann, Harald Kübler, Robert Löw, Tilman Pfau and James P. Shaffer, "Microwave electrometry with Rydberg atoms in a vapour cell using bright atomic resonances", *Nat. Phys.* **8**, 819 (2012) (pp. 39, 56).

[200] Christopher L. Holloway, Joshua A. Gordon, Andrew Schwarzkopf, David A. Anderson, Stephanie A. Miller, Nithiwadee Thaicharoen and Georg Raithel, "Sub-wavelength imaging and field mapping via electromagnetically induced transparency and Autler-Townes splitting in Rydberg atoms", *Appl. Phys. Lett.* **104**, 244102 (2014) (pp. 40, 41).

[201] M. Naftaly and R. E. Miles, "Terahertz time-domain spectroscopy of silicate glasses and the relationship to material properties", *J. Appl. Phys.* **102**, 043517 (2007) (p. 40).

[202] Yun-sik Jin, Geun-ju Kim and Seok-gy Jeon, "Terahertz Dielectric Properties of Polymers", *J. Korean Phys. Soc.* **49**, 513 (2006) (p. 40).

[203] L Weller, R. J. Bettles, C. L. Vaillant, M. A. Zentile, R. M. Potvliege, C. S. Adams and I. G. Hughes, "Cooperative Enhancement of Energy Transfer in a High-Density Thermal Vapor" (2013), arXiv: `1308.0129` (p. 40).

[204] LIGO Open Science Center, *IPython notebook: SIGNAL PROCESSING WITH GW150914 OPEN DATA*, `https://losc.ligo.org/s/events/GW150914/GW150914_tutorial.html` (p. 42).

[205] Sebastian Weber, Christoph Tresp, Henri Menke, Alban Urvoy, Ofer Firstenberg, Hans Peter Büchler and Sebastian Hofferberth, "Tutorial: Calculation of Rydberg interaction potentials" (2016), arXiv: `1612.08053` (p. 42).

[206] M. Fleischhauer and M. D. Lukin, "Dark-state polaritons in electromagnetically induced transparency", *Phys. Rev. Lett.* **84**, 5094 (2000) (pp. 44, 50).

[207] Alexey V. Gorshkov, Johannes Otterbach, Michael Fleischhauer, Thomas Pohl and Mikhail D. Lukin, "Photon-Photon Interactions via Rydberg Blockade", *Phys. Rev. Lett.* **107**, 133602 (2011) (p. 44).

[208] Alexey V. Gorshkov, Axel André, Michael Fleischhauer, Anders S. Sørensen and Mikhail D. Lukin, "Universal Approach to Optimal Photon Storage in Atomic Media", *Phys. Rev. Lett.* **98**, 123601 (2007) (p. 44).

[209] M. M. Müller, A. Kölle, R. Löw, T. Pfau, T. Calarco and S. Montangero, "Room-temperature Rydberg single-photon source", *Phys. Rev. A* **87**, 053412 (2013) (pp. 44, 49).

[210] Emanuele Distante, Pau Farrera, Auxiliadora Padrón-Brito, David Paredes-Barato, Georg Heinze and Hugues de Riedmatten, "Storing single photons emitted by a quantum memory on a highly excited Rydberg state", *Nat. Commun.* **8**, 14072 (2017) (p. 44).

[211] Y. O. Dudin and A. Kuzmich, "Strongly Interacting Rydberg Excitations of a Cold Atomic Gas." *Science* **336**, 887 (2012) (pp. 45, 46).

[212] D. Maxwell, D. J. Szwer, D. Paredes-Barato, H. Busche, J. D. Pritchard, A. Gauguet, K. J. Weatherill, M. P. A. Jones and C. S. Adams, "Storage and Control of Optical Photons Using Rydberg Polaritons", *Phys. Rev. Lett.* **110**, 103001 (2013) (pp. 45, 46).

[213] H. Gorniaczyk, C. Tresp, J. Schmidt, H. Fedder and S. Hofferberth, "Single-photon transistor mediated by interstate Rydberg interactions", *Phys. Rev. Lett.* **113**, 053601 (2014) (p. 45).

[214] F. Bariani, Y. O. Dudin, T. A. B. Kennedy and A. Kuzmich, "Dephasing of Multiparticle Rydberg Excitations for Fast Entanglement Generation", *Phys. Rev. Lett.* **108**, 030501 (2012) (pp. 45, 49).

[215] J. J. Longdell, E. Fraval, M. J. Sellars and N. B. Manson, "Stopped Light with Storage Times Greater than One Second Using Electromagnetically Induced Transparency in a Solid", *Phys. Rev. Lett.* **95**, 063601 (2005) (p. 45).

[216] Georg Heinze, Christian Hubrich and Thomas Halfmann, "Stopped Light and Image Storage by Electromagnetically Induced Transparency up to the Regime of One Minute", *Phys. Rev. Lett.* **111**, 033601 (2013) (p. 45).

[217] Nathaniel B. Phillips, Alexey V. Gorshkov and Irina Novikova, "Optimal light storage in atomic vapor", *Phys. Rev. A* **78**, 023801 (2008) (p. 45).

[218] M. Hosseini, B. M. Sparkes, G. Campbell, P. K. Lam and B. C. Buchler, "High efficiency coherent optical memory with warm rubidium vapour." *Nat. Commun.* **2**, 174 (2011) (p. 45).

[219] Fabian Ripka, Yi-Hsin Chen, Robert Löw and Tilman Pfau, "Rydberg polaritons in a thermal vapor", *Phys. Rev. A* **93**, 053429 (2016) (pp. 45, 49).

[220] Wan-Ü.L. Brillet and A. Gallagher, "Inert-gas collisional broadening and shifts of Rb Rydberg states", *Phys. Rev. A* **22**, 1012 (1980) (pp. 46, 59).

[221] M. D. Lukin, S. F. Yelin, M. Fleischhauer and M. O. Scully, "Quantum interference effects induced by interacting dark resonances", *Phys. Rev. A* **60**, 3225 (1999) (p. 47).

[222] Stéphane Clemmen, Alessandro Farsi, Sven Ramelow and Alexander L. Gaeta, "Ramsey Interference with Single Photons", *Phys. Rev. Lett.* **117**, 223601 (2016) (pp. 48, 66).

[223] Yan Jiang, Jun Rui, Xiao-Hui Bao and Jian-Wei Pan, "Freezing motion-induced dephasing in an atomic-ensemble quantum memory", *Phys. Rev. A* **93**, 063819 (2016) (p. 49).

[224] H J Kimble, "The quantum internet", *Nature* **453**, 1023 (2008) (p. 49).

[225] David A. Smith and Ifan G. Hughes, "The role of hyperfine pumping in multilevel systems exhibiting saturated absorption", *Am. J. Phys.* **72**, 631 (2004) (p. 49).

[226] I. I. Ryabtsev, I. I. Beterov, D. B. Tretyakov, V. M. Entin and E. A. Yakshina, "Doppler- and recoil-free laser excitation of Rydberg states via three-photon transitions", *Phys. Rev. A* **84**, 053409 (2011) (p. 50).

[227] J. Deiglmayr, M. Reetz-Lamour, T. Amthor, S. Westermann, A. L. de Oliveira and M. Weidemüller, "Coherent excitation of Rydberg atoms in an ultracold gas", *Opt. Commun.* **264**, 293 (2006) (p. 50).

[228] Vladimir S. Malinovsky and David J. Tannor, "Simple and robust extension of the stimulated Raman adiabatic passage technique to N-level systems", *Phys. Rev. A* **56**, 4929 (1997) (p. 50).

[229] P. A. Ivanov, N. V. Vitanov and K. Bergmann, "Spontaneous emission in stimulated Raman adiabatic passage", *Phys. Rev. A* **72**, 053412 (2005) (p. 50).

[230] David Petrosyan and Klaus Mølmer, "Stimulated adiabatic passage in a dissipative ensemble of atoms with strong Rydberg-state interactions", *Phys. Rev. A* **87**, 033416 (2013) (pp. 51, 52).

[231] Andrew Horsley, Guan-Xiang Du and Philipp Treutlein, "Widefield microwave imaging in alkali vapor cells with sub-100 μm resolution", *New J. Phys.* **17**, 112002 (2015) (p. 51).

[232] E. A. Hinds, K. S. Lai and M. Schnell, "Atoms in micron-sized metallic and dielectric waveguides", *Philos. Trans. R. Soc. A Math. Phys. Eng. Sci.* **355**, 2353 (1997) (p. 51).

[233] Jiteng Sheng, Yuanxi Chao and James P. Shaffer, "Strong coupling of Rydberg atoms and surface phonon polaritons on piezoelectric superlattices", *Phys. Rev. Lett.* **117**, 103201 (2016) (p. 51).

[234] C. Ates, I. Lesanovsky, C. S. Adams and K. J. Weatherill, "Fast and quasi-deterministic single ion source from a dipole-blockaded atomic ensemble", *Phys. Rev. Lett.* **110**, 213003 (2013) (p. 52).

[235] T. Xia, M. Lichtman, K. Maller, A. W. Carr, M. J. Piotrowicz, L. Isenhower and M. Saffman, "Randomized benchmarking of single-qubit gates in a 2D array of neutral-atom qubits", *Phys. Rev. Lett.* **114**, 100503 (2015) (p. 52).

[236] Yang Wang, Xianli Zhang, Theodore A. Corcovilos, Aishwarya Kumar and David S. Weiss, "Coherent Addressing of Individual Neutral Atoms in a 3D Optical Lattice", *Phys. Rev. Lett.* **115**, 043003 (2015) (p. 52).

[237] Philipp M. Preiss, Ruichao Ma, M. Eric Tai, Alexander Lukin, Matthew Rispoli, Philip Zupancic, Yoav Lahini, Rajibul Islam and Markus Greiner, "Strongly correlated quantum walks in optical lattices", *Science* **347**, 1229 (2015) (p. 52).

[238] C. P. Pearman, C. S. Adams, S. G. Cox, P. F. Griffin, D. A. Smith and I. G. Hughes, "Polarization spectroscopy of a closed atomic transition: applications to laser frequency locking", *J. Phys. B At. Mol. Opt. Phys.* **35**, 5141 (2002) (p. 52).

[239] James C. Wyant and Katherine Creath, Basic Wavefront Aberration Theory for Optical Metrology, *Appl. Opt. Opt. Eng.* **XI**, Academic Press, 1992, 1–53 (p. 52).

[240] C. Y. Ye, A. S. Zibrov, Yu. V. Rostovtsev and M. O. Scully, "Unexpected Doppler-free resonance in generalized double dark states", *Phys. Rev. A* **65**, 043805 (2002) (p. 54).

[241] Michael Erhard and Hanspeter Helm, "Buffer-gas effects on dark resonances: Theory and experiment", *Phys. Rev. A* **63**, 043813 (2001) (p. 55).

[242] Li-Anne Liew, Svenja Knappe, John Moreland, Hugh Robinson, Leo Hollberg and John Kitching, "Microfabricated alkali atom vapor cells", *Appl. Phys. Lett.* **84**, 2694 (2004) (p. 59).

[243] Dmitry Budker and Michael Romalis, "Optical magnetometry", *Nat. Phys.* **3**, 227 (2007) (p. 59).

[244] Haoquan Fan, Santosh Kumar, Jonathon Sedlacek, Harald Kübler, Shaya Karimkashi and James P Shaffer, "Atom based RF electric field sensing", *J. Phys. B At. Mol. Opt. Phys.* **48**.20, 202001 (2015) (p. 59).

[245] S. Knappe, P. D. D. Schwindt, V. Shah, L. Hollberg, J. Kitching, L. Liew and J. Moreland, "A chip-scale atomic clock based on ^{87}Rb with improved frequency stability", *Opt. Express* **13**, 1249 (2005) (p. 59).

[246] G. W. Biedermann, H. J. McGuinness, A. V. Rakholia, Y. Y. Jau, D. R. Wheeler, J. D. Sterk and G. R. Burns, "Atom Interferometry in a Warm Vapor", *Phys. Rev. Lett.* **118**, 163601 (2017) (p. 59).

[247] Brian Julsgaard, Jacob Sherson, J. Ignacio Cirac, Jaromír Fiurášek and Eugene S. Polzik, "Experimental demonstration of quantum memory for light." *Nature* **432**, 482 (2004) (p. 59).

[248] M. D. Eisaman, A. André, F. Massou, M. Fleischhauer, A. S. Zibrov and M. D. Lukin, "Electromagnetically induced transparency with tunable single-photon pulses." *Nature* **438**, 837 (2005) (p. 59).

[249] K. F. Reim, J. Nunn, V. O. Lorenz, B. J. Sussman, K. C. Lee, N. K. Langford, D. Jaksch and I. A. Walmsley, "Towards high-speed optical quantum memories", *Nat. Photon.* **4**, 218 (2010) (p. 59).

[250] C. F. McCormick, A. M. Marino, V. Boyer and P. D. Lett, "Strong low-frequency quantum correlations from a four-wave-mixing amplifier", *Phys. Rev. A* **78**, 043816 (2008) (p. 59).

[251] A. MacRae, T. Brannan, R. Achal and A. I. Lvovsky, "Tomography of a High-Purity Narrowband Photon from a Transient Atomic Collective Excitation", *Phys. Rev. Lett.* **109**, 033601 (2012) (p. 59).

[252] William Happer, "Optical pumping", *Rev. Mod. Phys.* **44**, 169 (1972) (p. 59).

[253] S. J. Seltzer and M. V. Romalis, "High-temperature alkali vapor cells with antirelaxation surface coatings", *J. Appl. Phys.* **106**, 114905 (2009) (p. 59).

[254] Y. W. Yi, H. G. Robinson, S. Knappe, J. E. Maclennan, C. D. Jones, C. Zhu, N. A. Clark and J. Kitching, "Method for characterizing self-assembled monolayers as antirelaxation wall coatings for alkali vapor cells", *J. Appl. Phys.* **104**, 023534 (2008) (p. 59).

[255] Hyatt M. Gibbs, "Incoherent Resonance Fluorescence from a Rb Atomic Beam Excited by a Short Coherent Optical Pulse", *Phys. Rev. A* **8**, 446 (1973) (p. 60).

[256] Daniel J. Whiting, Erwan Bimbard, James Keaveney, Mark A. Zentile, Charles S. Adams and Ifan G. Hughes, "Electromagnetically induced absorption in a nondegenerate three-level ladder system", *Opt. Lett.* **40**, 4289 (2015) (p. 60).

[257] Daniel J. Whiting, James Keaveney, Charles S. Adams and Ifan G. Hughes, "Direct measurement of excited-state dipole matrix elements using electromagnetically induced transparency in the hyperfine Paschen-Back regime", *Phys. Rev. A* **93**, 043854 (2016) (p. 60).

[258] B. Huber, A. Kölle and T. Pfau, "Motion-induced singnal revival in pulsed Rydberg four-wave mixing beyond the frozen-gas limit", *Phys. Rev. A* **90**, 053806 (2014) (p. 66).

[259] Serge Haroche, Quantum Beats and Time-Resolved Fluorescence Spectroscopy, *High-Resolution Laser Spectrosc.* Ed. by K. Shimoda, Springer-Verlag, 1976, 253–313 (p. 67).

[260] R. H. Dicke, "Coherence in Spontaneous Radiation Processes", *Phys. Rev.* **93**, 99 (1954) (p. 69).

[261] Robert J. Bettles, Simon A. Gardiner and Charles S. Adams, "Cooperative ordering in lattices of interacting two-level dipoles", *Phys. Rev. A* **92**, 063822 (2015) (p. 69).

[262] B. Zhu, J. Schachenmayer, M. Xu, F. Herrera, J. G. Restrepo, M. J. Holland and A. M. Rey, "Synchronization of interacting quantum dipoles", *New J. Phys.* **17**, 083063 (2015) (p. 69).

[263] B. Weber, H. P. Specht, T. Müller, J. Bochmann, M. Mücke, D. L. Moehring and G. Rempe, "Photon-photon entanglement with a single trapped atom", *Phys. Rev. Lett.* **102**, 030501 (2009) (p. 69).

[264] D. G. Norris, L. A. Orozco, P. Barberis-Blostein and H. J. Carmichael, "Observation of ground-state quantum beats in atomic spontaneous emission", *Phys. Rev. Lett.* **105**, 123602 (2010) (p. 69).

[265] M. Gross, J. M. Raimond and S. Haroche, "Doppler beats in superradiance", *Phys. Rev. Lett.* **40**, 1711 (1978) (p. 71).

[266] N. W. Carlson, D. J. Jackson, A. L. Schawlow, M. Gross and S. Haroche, "Superradiance triggering spectroscopy", *Opt. Commun.* **32**, 350 (1980) (p. 71).

[267] Thierry Dauxois, Stefano Ruffo, Ennio Arimondo and Martin Wilkens, Dynamics and Thermodynamics of Systems with Long Range Interactions: an Introduction, *Dyn. Thermodyn. Syst. with Long Range Interact.* Ed. by T. Dauxois, S. Ruffo, E. Arimondo and M. Wilkens, Berlin Heidelberg: Springer-Verlag, 2002, 1–19, arXiv: 0208455 [cond-mat] (p. 73).

[268] Alessandro Campa, Thierry Dauxois and Stefano Ruffo, "Statistical mechanics and dynamics of solvable models with long-range interactions", *Phys. Rep.* **480**, 57 (2009) (p. 73).

[269] David Mukamel, "Notes on the Statistical Mechanics of Systems with Long-Range Interactions" (2009), arXiv: 0905.1457 (p. 73).

[270] K. Binder and A. P. Young, "Spin glasses: Experimental facts, theoretical concepts, and open questions", *Rev. Mod. Phys.* **58**, 801 (1986) (p. 74).

[271] Ryan M. Wilson, Khan W. Mahmud, Anzi Hu, Alexey V. Gorshkov, Mohammad Hafezi and Michael Foss-Feig, "Collective phases of strongly interacting cavity photons", *Phys. Rev. A* **94**, 033801 (2016) (pp. 74, 85).

[272] Ertugrul M. Ozbudak, Mukund Thattai, Han N. Lim, Boris I. Shraiman and Alexander van Oudenaarden, "Multistability in the lactose utilization network of Escherichia coli", *Nature* **427**, 737 (2004) (p. 74).

[273] Tetsuya Shiraishi, Shinako Matsuyama and Hiroaki Kitano, "Large-scale analysis of network bistability for human cancers." *PLoS Comput. Biol.* **6**, e1000851 (2010) (p. 74).

[274] Guang Yao, Cheemeng Tan, Mike West, Joseph R. Nevins and Lingchong You, "Origin of bistability underlying mammalian cell cycle entry", *Mol. Syst. Biol.* **7**, 485 (2011) (p. 74).

[275] Marten Scheffer, Jordi Bascompte, William A. Brock, Victor Brovkin, Stephen R. Carpenter, Vasilis Dakos, Hermann Held, Egbert H. van Nes, Max Rietkerk and George Sugihara, "Early-warning signals for critical transitions." *Nature* **461**, 53 (2009) (p. 74).

[276] Matthias Göcke, "Various Concepts of Hysteresis Applied in Economics", *J. Econ. Surv.* **16**, 167 (2002) (p. 74).

[277] Helmut Ritsch, Peter Domokos, Ferdinand Brennecke and Tilman Esslinger, "Cold atoms in cavity-generated dynamical optical potentials", *Rev. Mod. Phys.* **85**, 553 (2013) (p. 74).

[278] Tim Byrnes, Na Young Kim and Yoshihisa Yamamoto, "Exciton–polariton condensates", *Nat. Phys.* **10**, 803 (2014) (p. 74).

[279] Joseph W. Britton, Brian C. Sawyer, Adam C. Keith, C.-C. Joseph Wang, James K. Freericks, Hermann Uys, Michael J. Biercuk and John J. Bollinger, "Engineered two-dimensional Ising interactions in a trapped-ion quantum simulator with hundreds of spins", *Nature* **484**, 489 (2012) (p. 74).

[280] Justin G. Bohnet, Brian C. Sawyer, Joseph W. Britton, Michael L. Wall, Ana Maria Rey, Michael Foss-Feig and John J. Bollinger, "Quantum spin dynamics and entanglement generation with hundreds of trapped ions", *Science* **352**, 1297 (2016) (p. 74).

[281] Daniel Weller, Alban Urvoy, Andy Rico, Robert Löw and Harald Kübler, "Charge-induced optical bistability in thermal Rydberg vapor", *Phys. Rev. A* **94**, 063820 (2016) (pp. 74, 93, 94).

[282] Tony E. Lee, H. Häffner and M. C. Cross, "Antiferromagnetic phase transition in a nonequilibrium lattice of Rydberg atoms", *Phys. Rev. A* **84**, 031402(R) (2011) (p. 74).

[283] Tony E. Lee, Sarang Gopalakrishnan and Mikhail D. Lukin, "Unconventional Magnetism via Optical Pumping of Interacting Spin Systems", *Phys. Rev. Lett.* **110**, 257204 (2013) (p. 74).

[284] Tony E. Lee, H. Häffner and M. C. Cross, "Collective Quantum Jumps of Rydberg Atoms", *Phys. Rev. Lett.* **108**, 023602 (2012) (pp. 74, 75).

[285] Anzi Hu, Tony E. Lee and Charles W. Clark, "Spatial correlations of one-dimensional driven-dissipative systems of Rydberg atoms", *Phys. Rev. A* **88**, 053627 (2013) (pp. 74, 75, 92).

[286] Michael Höning, Dominik Muth, David Petrosyan and Michael Fleischhauer, "Steady-state crystallization of Rydberg excitations in an optically driven lattice gas", *Phys. Rev. A* **87**, 023401 (2013) (p. 74).

[287] Matteo Marcuzzi, Emanuele Levi, Sebastian Diehl, Juan P. Garrahan and Igor Lesanovsky, "Universal non-equilibrium properties of dissipative Rydberg gases", *Phys. Rev. Lett.* **113**, 210401 (2014) (pp. 74, 87, 88).

[288] Cenap Ates, Beatriz Olmos, Juan P. Garrahan and Igor Lesanovsky, "Dynamical phases and intermittency of the dissipative quantum Ising model", *Phys. Rev. A* **85**, 043620 (2012) (pp. 74, 75, 92).

[289] Igor Lesanovsky and Juan P. Garrahan, "Out-of-equilibrium structures in strongly interacting Rydberg gases with dissipation", *Phys. Rev. A* **90**, 011603(R) (2014) (p. 74).

[290] Hendrik Weimer, "Variational Principle for Steady States of Dissipative Quantum Many-Body Systems", *Phys. Rev. Lett.* **114**, 040402 (2015) (pp. 74, 92).

[291] Hendrik Weimer, "Variational analysis of driven-dissipative Rydberg gases", *Phys. Rev. A* **91**, 063401 (2015) (p. 74).

[292] Mohammad F. Maghrebi and Alexey V. Gorshkov, "Nonequilibrium many-body steady states via Keldysh formalism", *Phys. Rev. B* **93**, 014307 (2016) (p. 74).

[293] J. J. Mendoza-Arenas, S. R. Clark, S. Felicetti, G. Romero, E. Solano, D. G. Angelakis and D. Jaksch, "Beyond mean-field bistability in driven-dissipative lattices: Bunching-antibunching transition and quantum simulation", *Phys. Rev. A* **93**, 023821 (2016) (p. 74).

[294] Jiasen Jin, Alberto Biella, Oscar Viyuela, Leonardo Mazza, Jonathan Keeling, Rosario Fazio and Davide Rossini, "Cluster mean-field approach to the steady-state phase diagram of dissipative spin systems", *Phys. Rev. X* **6**, 031011 (2016) (pp. 74, 75, 82, 90).

[295] Amodsen Chotia, Matthieu Viteau, Thibault Vogt, Daniel Comparat and Pierre Pillet, "Kinetic Monte Carlo modeling of dipole blockade in Rydberg excitation experiment", *New J. Phys.* **10**, 045031 (2008) (pp. 75–77).

[296] C. Ates, T. Pohl, T. Pattard and J. M. Rost, "Many-body theory of excitation dynamics in an ultracold Rydberg gas", *Phys. Rev. A* **76**, 013413 (2007) (pp. 75, 76).

[297] C. Ates, T. Pohl, T. Pattard and J. M. Rost, "Antiblockade in Rydberg Excitation of an Ultracold Lattice Gas", *Phys. Rev. Lett.* **98**, 023002 (2007) (pp. 75, 76).

[298] M. M. Valado, C. Simonelli, M. D. Hoogerland, I. Lesanovsky, J. P. Garrahan, E. Arimondo, D. Ciampini and O. Morsch, "Experimental observation of controllable kinetic constraints in a cold atomic gas", *Phys. Rev. A* **93**, 040701(R) (2016) (pp. 76, 90).

[299] David W. Schonleber, Martin Gärttner and Jörg Evers, "Coherent versus incoherent excitation dynamics in dissipative many-body Rydberg systems", *Phys. Rev. A* **89**, 033421 (2014) (pp. 77, 90).

[300] Kristen A. Fichthorn and W. H. Weinberg, "Theoretical Foundations of Dynamical Monte Carlo Simulations", *J. Chem. Phys.* **95**, 1090 (1991) (p. 77).

[301] H. M. Gibbs, S. L. McCall and T. N. C. Venkatesan, "Differential Gain and Bistability Using a Sodium-Filled Fabry-Perot Interferometer", *Phys. Rev. Lett.* **36**, 1135 (1976) (p. 84).

[302] W. Lange, F. Mitschke, R. Deserno and J. Mlynek, "Study of fluctuations in transient optical bistability", *Phys. Rev. A* **32**, 1271 (1985) (p. 84).

[303] C. M. Savage and H. J. Carmichael, "Single-Atom Optical Bistability", *IEEE J. Quantum Electron.* **24**, 1495 (1988) (p. 84).

[304] G. Rempe, R. J. Thompson, R. J. Brecha, W. D. Lee and H. J. Kimble, "Optical bistability and photon statistics in cavity quantum electrodynamics", *Phys. Rev. Lett.* **67**, 1727 (1991) (p. 84).

[305] J.S. Langer, "Metastable states", *Physica* **73**, 61 (1974) (p. 84).

[306] O. Penrose and J. L. Lebowitz, "Rigorous treatment of metastable states in the van der Waals-Maxwell theory", *J. Stat. Phys.* **3**, 211 (1971) (pp. 84, 89).

[307] Robert B. Griffiths, Chi-Yuan Weng and James S. Langer, "Relaxation Times for Metastable states in the Mean-Field model of a ferromagnet", *Phys. Rev.* **149**, 301 (1966) (p. 84).

[308] J. S. Langer, "Statistical Theory of the Decay of Metastable States", *Ann. Phys. (N. Y).* **54**, 258 (1969) (p. 84).

[309] E. M. Kessler, G. Giedke, A. Imamoglu, S. F. Yelin, M. D. Lukin and J. I. Cirac, "Dissipative phase transition in a central spin system", *Phys. Rev. A* **86**, 012116 (2012) (p. 85).

[310] G Grynberg and S Cribier, "Critical exponents in dispersive optical bistability", *J. Phys. Lettres* **44**, L–449 (1983) (p. 87).

[311] F. Letscher, O. Thomas, T. Niederprüm, M. Fleischhauer and H. Ott, "Bistability vs. Metastability in Driven Dissipative Rydberg Gases", *Phys. Rev. X* **7**, 021020 (2017) (pp. 90, 92).

[312] T. Amthor, M. Reetz-Lamour, S. Westermann, J. Denskat and M. Weidemüller, "Mechanical effect of van der waals interactions observed in real time in an ultracold rydberg gas", *Phys. Rev. Lett.* **98**, 023004 (2007) (p. 92).

[313] B. J. DeSalvo, J. A. Aman, C. Gaul, T. Pohl, S. Yoshida, J. Burgdörfer, K. R. A. Hazzard, F. B. Dunning and T. C. Killian, "Rydberg-blockade effects in Autler-Townes spectra of ultracold strontium", *Phys. Rev. A* **93**, 022709 (2016) (p. 92).

[314] D. S. Ding, C. S. Adams, B. S. Shi and G. C. Guo, "Non-equilibrium phase-transitions in multi-component Rydberg gases" (2016), arXiv: 1606.08791 (pp. 93, 94).

[315] A. Reinhard, K. C. Younge, T. Cubel Liebisch, B. Knuffman, P. R. Berman and G. Raithel, "Double-resonance spectroscopy of interacting Rydberg-atom systems", *Phys. Rev. Lett.* **100**, 233201 (2008) (p. 93).

[316] J. L. Hall, L. Hollberg, T. Baer and H. G. Robinson, "Optical heterodyne saturation spectroscopy", *Appl. Phys. Lett.* **39**, 680 (1981) (p. 97).

[317] C. Wieman and T. W. Hänsch, "Doppler-free laser polarization spectroscopy", *Phys. Rev. Lett.* **36**, 1170 (1976) (p. 97).

[318] Mark A. Zentile, James Keaveney, Lee Weller, Daniel J. Whiting, Charles S. Adams and Ifan G. Hughes, "ElecSus: A program to calculate the electric susceptibility of an atomic ensemble", *Comput. Phys. Commun.* **189**, 162 (2015) (pp. 98, 99).

[319] Anna L Marchant, Sylvi Händel, Timothy P. Wiles, Stephen A. Hopkins, Charles S. Adams and Simon L. Cornish, "Off-resonance laser frequency stabilization using the Faraday effect." *Opt. Lett.* **36**, 64 (2011) (p. 99).

[320] Klaus Mølmer, Yvan Castin and Jean Dalibard, "Monte Carlo wave-function method in quantum optics", *J. Opt. Soc. Am. B* **10**, 524 (1993) (p. 99).

[321] P. W. Anderson, "A mathematical model for the narrowing of spectral lines by exchange or motion", *J. Phys. Soc. Japan* **9**.3, 316 (1954) (pp. 100, 101).

[322] W. Happer and H. Tang, "Spin-Exchange Shift and Narrowing of Magnetic Resonance Lines in Optically Pumped Alkali Vapors", *Phys. Rev. Lett.* **31**, 273 (1973) (p. 101).

[323] P. W. Anderson and P. R. Weiss, "Exchange narrowing in paramagnetic resonance", *Rev. Mod. Phys.* **25**, 269 (1953) (p. 101).

[324] R. H. Dicke, "The Effect of Collisions upon the Doppler Width of Spectral Lines", *Phys. Rev.* **89**, 472 (1953) (p. 101).

[325] S. A. Bhatti, C. L. Cromer and W. E. Cooke, "Analysis of the Rydberg character of the $5d7d\ ^1D_2$ state of barium", *Phys. Rev. A* **24**, 161 (1981) (p. 103).